

# **Performance of Na-based Liquid Metal Batteries and related Corrosion Issues**

Zur Erlangung des akademischen Grades eines

**Doktors der Ingenieurwissenschaften (Dr.Ing.)**

von der KIT-Fakultät für **Elektrotechnik und Informationstechnik** des  
Karlsruher Instituts für Technologie (KIT)

genehmigte

**Dissertation**

von

**M.Sc. ZHANG Tianru**

aus Hebei, China

Tag der mündlichen Prüfung:

24. Juli 2023

Hauptreferent:

Prof. Dr.-Ing. Georg Müller

Korreferent:

Prof. Dr. Kangli Wang

# Contents

<b>Acknowledgements</b>	<b>vi</b>
<b>Abstract</b>	<b>viii</b>
<b>Zusammenfassung</b>	<b>x</b>
<b>List of Abbreviations</b>	<b>xii</b>
<b>1 Introduction</b>	<b>1</b>
1.1 Motivation . . . . .	1
1.2 Electrical energy storage systems . . . . .	4
1.2.1 Basic concepts of batteries and cells . . . . .	5
1.2.2 Pros and cons of lithium-ion batteries (LIBs) . . . . .	6
1.3 Aim and objectives . . . . .	7
1.4 Structure of thesis . . . . .	8
<b>2 State of the Art</b>	<b>9</b>
2.1 History of liquid metal batteries . . . . .	9
2.2 Concept of liquid metal batteries . . . . .	10
2.3 Advantages and disadvantages of Na-based liquid metal battery . . . . .	11
2.4 Development of a positive electrode for liquid metal batteries . . . . .	14
2.5 Key issues on Na-based liquid metal battery . . . . .	17
2.5.1 Electrolyte with low melting point and low sodium solubility . . . . .	17
2.5.2 Electrode couple with low melting point but high voltage . . . . .	18

2.5.3	Corrosion . . . . .	19
<b>3</b>	<b>Fundamentals</b>	<b>24</b>
3.1	Working principle of liquid metal batteries . . . . .	24
3.2	General designs of LMB cells . . . . .	26
3.3	Equilibrium voltage and terminal voltage . . . . .	26
3.3.1	Ohmic overpotential . . . . .	28
3.3.2	Mass transport overpotential . . . . .	28
3.3.3	Charge transfer overpotential . . . . .	29
3.4	Electrochemical methods . . . . .	29
3.4.1	Galvanostatic Intermittent Titration Technique (GITT) . . . . .	29
3.4.2	Galvanostatic Cycling with Potential Limitation (GCPL) . . . . .	31
3.4.3	Electrochemical Impedance Spectroscopy (EIS) . . . . .	33
3.5	Material characterization methods . . . . .	38
3.5.1	X-Ray diffraction (XRD) . . . . .	38
3.5.2	Inductively coupled plasma optical emission spectroscopy (ICP-OES)	39
3.5.3	Laser-induced breakdown spectroscopy (LIBS) . . . . .	41
3.5.4	Scanning electron microscope (SEM) with energy-dispersive X-ray spectroscopy (EDS) . . . . .	42
<b>4</b>	<b>Material compatibility</b>	<b>46</b>
4.1	Static corrosion tests for NCC and electrical insulator materials . . . . .	46
4.1.1	Material selection . . . . .	46
4.1.2	Experiments . . . . .	48
4.1.3	Results . . . . .	51

4.1.4	Discussion . . . . .	66
4.1.5	Short summary . . . . .	67
4.2	Static corrosion tests for PCC materials in positive electrode at fully-charged state . . . . .	68
4.2.1	Material selection . . . . .	68
4.2.2	Experiments . . . . .	69
4.2.3	Results . . . . .	73
4.2.4	Discussion . . . . .	104
4.2.5	Short summary . . . . .	107
4.3	Static corrosion tests for PCC materials in positive electrode at fully-discharged state . . . . .	107
4.3.1	Material selection . . . . .	107
4.3.2	Experiments . . . . .	108
4.3.3	Results . . . . .	111
4.3.4	Discussion . . . . .	124
4.3.5	Short summary . . . . .	125
4.4	Static corrosion tests for PCC materials in electrolyte . . . . .	125
4.4.1	Material selection . . . . .	125
4.4.2	Experiments . . . . .	126
4.4.3	Results . . . . .	127
4.4.4	Discussion . . . . .	136
4.4.5	Short summary . . . . .	138
<b>5</b>	<b>Cell performance</b>	<b>139</b>
5.1	Preparation of cell active components . . . . .	139

5.1.1	Preparation of negative electrode . . . . .	139
5.1.2	Preparation of electrolyte . . . . .	139
5.1.3	Preparation of positive electrode . . . . .	139
5.2	Cell assembly . . . . .	140
5.2.1	Cell with a Ni-foam . . . . .	140
5.2.2	Cell without foam . . . . .	142
5.3	Cell testing . . . . .	143
5.4	Unexpected problems . . . . .	144
5.4.1	Side reactions in electrolyte . . . . .	144
5.4.2	Short-circuit . . . . .	148
5.5	Electrochemical performance . . . . .	149
5.5.1	GITT measurements . . . . .	149
5.5.2	GCPL tests . . . . .	157
5.5.3	EIS measurements . . . . .	164
5.5.4	Discussion . . . . .	171
5.5.5	Short summary . . . . .	173
5.6	Post-evaluation of cell cases . . . . .	174
5.6.1	Results . . . . .	175
5.6.2	Discussion . . . . .	187
5.6.3	Short summary . . . . .	188
<b>6</b>	<b>Conclusion and outlook</b>	<b>190</b>
6.1	Conclusion . . . . .	190
6.2	Outlook . . . . .	192

References	194
List of publications	212

# Acknowledgements

This PhD dissertation represents the work I have carried out over the past four years, I could not have undertaken this journey without the expertise and support from my colleagues from GESA (Gepulste ElektronenstrahlAnlage) group at the Institute for Pulsed Power and Microwave Technology (IHM). Additionally, this endeavor would not have been possible without the financial support from DFG (Deutsche Forschungsgemeinschaft).

First and foremost, I would like to express my sincere gratitude to my supervisor Prof. Dr.-Ing. Georg Müller for giving me the opportunity to work on this project at IHM, providing unconditional guidance and challenging me to grow as a scientist. In addition, I could not imagine that he enabled my business travel back to China during the COVID pandemic, I know how hard it is during the pandemic. I would express my heartfelt appreciation to Prof. Dr. Kangli Wang for kindly accepting to be my second reviewer. I would like to give my deepest thanks to my advisor, Dr. Alfons Weisenburger for his invaluable advice and consistent support all the time. I would like to offer special thanks to my colleagues, especially Dr. Annette Heinzl and Dr. Renate Fetzner for their great expertise, all the academic suggestions and scientific comments throughout my PhD study.

I would like to extend my appreciation to everyone I've collaborated with: Prof. Dr. Kangli Wang, Prof. Dr. Kai Jiang at Huazhong University of Science and Technology (HUST) for their kind reception in Wuhan and the scientific cooperation from their whole research group during my stay there; Dr. Wenjin Ding and Qing Gong at Deutsches Zentrum für Luft- und Raumfahrt (DLR) for conducting the exposure test in molten salts; Dr. Chongchong Tang (IAM-AWP/KIT) for his help on MAX-phases; Dr. Thomas Bergfeldt (IAM-AWP/KIT) for his contribution on ICP-OES measurement and analysis; Dr. Adrian Jianu for his help on arc-melting; Dipl.-Ing. Faiban Lang for his technical support and help in the labors; Florian Lindner for constructing the heating facilities and his assistance in battery cell assembly; Kai Schäfer, Alexander Sivkovich, Davide Quattrocchi at the mechanical workshop (IHM/KIT) for manufacturing all needed cell components; Klaus Baumann and Kevin Paulus at the electrical engineering laboratory (IHM/KIT) for fabricating the sodium sink and reconstructing the electrochemical workstation.

I am also grateful to all the members at IHM for creating a good working atmosphere and harmonious interpersonal relationship, including but not limited to Prof. Dr.-Ing. John Jelonnek, Prof. Dr. Manfred Thumm, Bertsch Gabriela, Melanie Mai, Natascha Zidek, Dr. An Waldimir, Dr. Hao Shi, Dr. Zhen Wang, Dr. Martin Hochberg, Dr. Martin Sack, Dr. Ivan Vorotiahin, Louis Müller, Luis Orellana and Anisa Purwitasari.

Lastly, I would be remiss in not mentioning my parents and my girlfriend for their support and encouragements not only throughout my PhD stage but also for all the times.

ZHANG Tianru

Karlsruhe, June, 2023

# Abstract

Liquid metal batteries (LMBs) are discussed as promising candidates for large-scale stationary storage of electrical energy at comparatively moderate costs. They have a number of advantages over solid-state batteries, such as lower manufacturing costs and a basically unlimited number of cycles due to the absence of microstructural changes and dendrite growth. Superior safety performance and lower thermal management requirements are further advantages.

The focus on the work was on the compatibility of the structural materials with the active cell components (molten salts electrolyte and two liquid metal electrodes) and the performance of the assembled cells, including post-mortem studies of the structural materials of the cell. LiCl-NaCl-KCl was selected as electrolyte, Na and Sb-Bi or Sb-Sn as electrode materials.

The static corrosion tests of negative current collector (NCC) and electrical insulator materials combined with the cost factor verify that most appropriate candidates for electrical insulator materials are oxide ceramics ( $\text{Al}_2\text{O}_3$  and  $\text{MgO}$ ) while the best selection for NCC materials are Cu and Invar alloy.

The static corrosion tests of positive current collector (PCC) materials not only confirm that the severest corrosion attack was triggered by the positive electrode, but also manifest that Sb-Sn alloys are more aggressive and corrosive than Sb-Bi alloy. Besides, the results also reveal that the application of steels as PCC might be feasible for short term application while the best choice for PCC are Mo metal and MAX-phases coatings. However, considering about the cost factor, coating of pure Mo metal or MAX-phases on a suitable substrate might be the most economically reasonable and feasible method.

Two cell designs (cells with Ni-foam as Na-host and without foam) of Na || SbBi<sub>9</sub> cells were successfully realized, the electrochemical properties of those Na-based LMB cells were evaluated by several measurements.

Galvanostatic Intermittent Titration Technique (GITT) tests manifest at least five orders of magnitude larger diffusion coefficient (in the range of  $10^{-6}$  to  $10^{-4}$   $\text{cm}^2 \text{s}^{-1}$ ) of Na-based LMB cells when compared with sodium-ion-batteries (SIBs).

The extremely low charge-transfer resistance (maximum value:  $9\text{ m}\Omega$ ) of Na-based LMB cells is verified by Electrochemical Impedance Spectroscopy (EIS) measurements.

Galvanostatic Cycling with Potential Limitation (GCPL) tests reveal that both cells with Ni-foam and without foam exhibit a small self-discharge rate (self-discharge current in the range between 13 and 16.5 mA) during the whole test time. In addition, the application of this type of LMB cell in the field of power supply might be restricted due to its maximal applicable discharge current density of  $600\text{ mA}/\text{cm}^2$ .

Since both cell designs could only maintain normal operation for up to 1200 h and a clear capacity degradation could be observed on both cell designs, the corrosion attack on cell cases (Fe-Cr-Ni steel) after cell operation was investigated. The results show that the corrosion attack is mainly caused by the positive electrode. Both the corrosion rate ( $0.037\text{ }\mu\text{m}/\text{h}$ ) and the corrosion products on the cell case bottom coincide with the results on Fe-Cr-Ni steels during static corrosion tests in Sb-Bi alloys.

In order to investigate the corrosion influence on the cell performance, cells with Mo-crucible as PCC material were built. Comparing the long-term cycling tests and the cell case post-evaluation of cells without Mo-crucible with that of cells with Mo-crucible as corrosion mitigation method, it is easy to find out that the corrosion attack on PCC results in adverse consequences on cell performance (much faster capacity degradation rate). Therefore, the corrosion on PCC materials of LMB cells should be avoided by technical corrosion protection methods for long-term industrial application.

To conclude, in order to meet the increasingly serious challenge to find proper alternatives for energy storage system in grid-scale, Na-based LMBs are worth of being further studied.

# Zusammenfassung

Flüssigmetallbatterien (LMBs) werden als vielversprechende Kandidaten für die stationäre Speicherung elektrischer Energie in großem Maßstab zu vergleichsweise moderaten Kosten diskutiert. Sie haben eine Reihe von Vorteilen gegenüber Festkörperbatterien, wie z.B. geringere Herstellungskosten und eine grundsätzlich unbegrenzte Zyklenanzahl aufgrund des Fehlens von Mikrostrukturveränderungen und Dendritenwachstum. Weitere Vorteile sind die höhere Sicherheit und die geringeren Anforderungen an das Wärmemanagement.

Der Schwerpunkt der Arbeiten lag auf der Kompatibilität der Strukturmaterialien mit den aktiven Zellkomponenten (Salzschmelze-Elektrolyt und zwei Flüssigmetall-Elektroden) und der Leistungsfähigkeit der zusammengebauten Zellen, einschließlich Post-Mortem-Studien der Strukturmaterialien der Zelle. Als Elektrolyt wurde LiCl-NaCl-KCl gewählt, als Elektrodenmaterialien Na und Sb-Bi oder Sb-Sn.

Die statischen Korrosionstests von negativen Stromkollektor- (NCC) und elektrischen Isolatormaterialien bestätigen in Verbindung mit dem Kostenfaktor, dass die geeignetsten Kandidaten für elektrische Isolatormaterialien Oxidkeramik ( $\text{Al}_2\text{O}_3$  und  $\text{MgO}$ ) sind, während Cu und Invar-Legierungen die beste Wahl für NCC-Materialien darstellen.

Die statischen Korrosionstests der positiven Stromkollektormaterialien (PCC) bestätigen nicht nur, dass der schwerste Korrosionsangriff von der positiven Elektrode ausgelöst wurde, sondern zeigen auch, dass Sb-Sn-Legierungen aggressiver und korrosiver sind als Sb-Bi-Legierungen. Außerdem zeigen die Ergebnisse, dass Stähle als PCC für Kurzzeitanwendung möglich sein könnten, während Mo-Metall und MAX-Phasen-Beschichtungen die beste Wahl für PCC sind. Unter Berücksichtigung des Kostenfaktors könnte jedoch die Beschichtung von reinem Mo-Metall oder MAX-Phasen auf einem geeigneten Substrat die wirtschaftlich vernünftigste und praktikabelste Methode sein.

Zwei Zelldesigns (Zellen mit Ni-Schaum als Na-Wirt und ohne Schaum) von  $\text{Na} \parallel \text{SbBi}_9$  Zellen wurden erfolgreich realisiert, die elektrochemischen Eigenschaften dieser Na-basierten LMB-Zellen wurden durch verschiedene Messungen bewertet.

Galvanostatische intermittierende Titrationstests (GITT) zeigen, dass der Diffusionskoeffizient von Na-basierten LMB-Zellen (im Bereich von  $10^{-6}$  bis  $10^{-4} \text{ cm}^2 \text{ s}^{-1}$ ) im Vergleich zu Natrium-Ionen-Batterien (SIBs) um mindestens fünf Größenordnungen größer ist.

Der extrem niedrige Ladungstransferwiderstand (Maximalwert:  $9 \text{ m}\Omega$ ) von Na-basierten LMB-Zellen wurde durch elektrochemische Impedanzspektroskopie (EIS) nachgewiesen.

Galvanostatische Zyklen mit Potentialbegrenzung (GCPL)-Tests zeigen, dass sowohl Zellen mit Ni-Schaum als auch ohne Schaum eine geringe Selbstentladungsrate (Selbstentladestrom im Bereich zwischen  $13$  und  $16.5 \text{ mA}$ ) während der gesamten Testzeit aufweisen. Darüber hinaus könnte die Anwendung dieser Art von LMB-Zellen im Bereich der Stromversorgung aufgrund ihrer maximalen anwendbaren Entladestromdichte von  $600 \text{ mA/cm}^2$  eingeschränkt sein.

Da beide Zelldesigns einen normalen Betrieb nur bis zu  $1200 \text{ h}$  aufrechterhalten konnten und bei beiden Zelldesigns ein deutlicher Kapazitätsabbau zu beobachten war, wurde der Korrosionsangriff auf die Zellgehäuse (Fe-Cr-Ni-Stahl) nach dem Zellbetrieb untersucht. Die Ergebnisse zeigen, dass der Korrosionsangriff hauptsächlich durch die positive Elektrode verursacht wird. Sowohl die Korrosionsrate ( $0,037 \text{ }\mu\text{m/h}$ ) als auch die Korrosionsprodukte auf dem Zellengehäuseboden stimmen mit den Ergebnissen für Fe-Cr-Ni-Stähle bei statischen Korrosionstests in Sb-Bi-Legierungen überein.

Um den Einfluss der Korrosion auf die Leistungsfähigkeit der Zelle zu untersuchen, wurden Zellen mit Mo-Tiegel als PCC-Material gebaut. Vergleicht man die Langzeitzyklentests und die Nachbewertung des Zellgehäuses von Zellen ohne Mo-Tiegel mit denen von Zellen mit Mo-Tiegel als Korrosionsschutzmethode, lässt sich leicht feststellen, dass der Korrosionsangriff auf PCC nachteilige Auswirkungen auf die Zelleistung hat (viel schnellere Kapazitätsabbaurate). Daher sollte die Korrosion an PCC-Materialien von LMB-Zellen für eine langfristige industrielle Anwendung durch technische Korrosionsschutzmaßnahme vermieden werden.

Zusammenfassend lässt sich sagen, dass Na-basierte LMBs weiter untersucht werden sollten, um der immer ernster werdenden Herausforderung zu begegnen, geeignete Alternativen für Energiespeichersysteme im Netzmaßstab zu finden.

# List of Abbreviations

**$\beta$ -Al<sub>2</sub>O<sub>3</sub>** beta-alumina.

**AC** alternating current.

**AE** auger electron.

**AES** atomic emission spectroscopy.

**Ah** ampere-hour.

**Alcoa** Aluminum Company of America.

**APS** Announced Pledges Scenario.

**BASE**  $\beta$ -Al<sub>2</sub>O<sub>3</sub> solid electrolyte.

**BSE** back-scattered electron.

**CCUS** carbon capture, utilisation and storage.

**CL** cathodoluminescence.

**CPE** constant phase element.

**CSP** concentrating solar power.

**CTE** coefficient of thermal expansion.

**CV** Cyclic Voltammetry.

**DLR** Deutsches Zentrum für Luft- und Raumfahrt.

**DoD** depth of discharge.

**EDS** energy-dispersive X-ray spectroscopy.

**EEC** equivalent electrical circuit.

**EES** electrical energy storage.

**EIS** Electrochemical Impedance Spectroscopy.

**EMF** electromotive force.

**EV** electric vehicle.

**GCPL** Galvanostatic Cycling with Potential Limitation.

**GHG** greenhouse-gas.

**GITT** Galvanostatic Intermittent Titration Technique.

**Gt** gigatonnes.

**HTF** heat transfer fluid.

**ICP** inductively coupled plasma.

**ICP-AES** inductively coupled plasma atomic emission spectroscopy.

**ICP-OES** inductively coupled plasma optical emission spectroscopy.

**IEA** International Energy Agency.

**LIB** lithium-ion battery.

**LIBS** laser-induced breakdown spectroscopy.

**LIPS** laser-induced plasma spectroscopy.

**LMB** liquid metal battery.

**LMFBR** liquid metal fast-breeder reactors.

**LOD** limit of detection.

**LSS** laser spark spectroscopy.

**MIT** Massachusetts Institute of Technology.

**NCC** negative current collector.

**NZE** Net Zero Emission.

**OCV** open-circuit voltage.

**PCC** positive current collector.

**PITT** Potentiostatic Intermittent Titration Technique.

**PM** particulate matter.

**PPI** pores per inch.

**ppm** parts-per-million.

**PV** photovoltaics.

**RF** radio frequency.

**SB** secondary battery.

**SBB** sodium-beta battery.

**SDGs** Sustainable Development Goals.

**SE** secondary electron.

**SEI** solid electrolyte interface.

**SEM** scanning electron microscope.

**SHE** standard hydrogen electrode.

**SIB** sodium-ion battery.

**SoC** state of charge.

**STEPS** Stated Policies Scenario.

**TRES** thermally regenerative electrochemical system.

**TWh** terawatt-hours.

**UN** United Nations.

**XRD** X-ray diffraction.

**ZEBRA** ZEolite Battery Research Africa.

# 1 Introduction

## 1.1 Motivation

Since the industrial revolution in the mid-eighteenth century and the technological revolution, especially the electrification from the late nineteenth century into the early twentieth century, both the world's population and economy have grown rapidly, which brought enormous additional demands on energy supply, predominantly and particularly on electrical energy [1].

From 1800 to 2011, the worldwide economy expanded massively and the world population increased sevenfold, both expansions were evoked by technological revolutions [2]. The world population is expected to achieve 8.0 billion in mid-November 2022 from an estimated value of 2.5 billion in 1950. According to the latest projections from United Nations (UN), this value is projected to reach 8.5 billion in 2030, 9.7 billion in 2050, and 10.4 billion in 2100. This rapid growth in world population have already put additional pressure on already strained resources and brought huge challenges to the achievement of the Sustainable Development Goals (SDGs) [3].

Since electricity is at the heart of modern lives and economies, powering residence, transportation, industrial production, healthcare services and so on, the demand for electricity keeps increasing further as the world is getting wealthier and more developed. As shown in Table 1.1, according to International Energy Agency (IEA), all three scenarios exhibit a remarkable increase in global electricity demand by 2050, which is projected to grow from 24700 terawatt-hours (TWh) in 2021 by about 80 % in the Stated Policies Scenario (STEPS), by 120 % in the Announced Pledges Scenario (APS) and by 150 % in the Net Zero Emission (NZE).

**Table 1.1:** Global electricity demand and supply by scenario (TWh) [4]

	STEPS				APS		NZE	
	2010	2021	2030	2050	2030	2050	2030	2050
Buildings	9637	12594	15383	21940	14889	19623	13293	15850
Industry	7450	10166	12036	15073	112471	18332	13776	21697
Transport	295	441	1169	3607	1570	7845	2236	10243
Hydrogen production	–	2	159	663	879	5714	2464	11433
<b>Global electricity demand</b>	<b>18548</b>	<b>24700</b>	<b>30621</b>	<b>43672</b>	<b>31752</b>	<b>53810</b>	<b>33733</b>	<b>62159</b>
Unabated coal	8670	10201	9044	5892	8076	1580	4666	0
Unabated natural gas	4855	6552	6848	6658	6100	3577	4977	82
Unabated oil	969	682	432	312	363	175	180	3
Fossil fuels with CCUS	–	1	5	133	75	1338	282	1317
Nuclear	2756	2776	3351	4260	3547	5103	3896	5810
Hydropower	3449	4327	5078	6809	5213	7543	5725	8251
Wind	342	1870	4604	10691	5816	17416	7840	23486
Solar PV	32	1003	4011	12118	4838	18761	7551	27006
Other renewables	411	859	1380	2833	1707	5153	1948	5762
Hydrogen and ammonia	–	–	9	44	79	567	603	1467
<b>Global electricity supply</b>	<b>21539</b>	<b>28334</b>	<b>34834</b>	<b>49845</b>	<b>35878</b>	<b>61268</b>	<b>37723</b>	<b>73232</b>
Renewables share	20 %	28 %	43 %	65 %	49 %	80 %	61 %	88 %

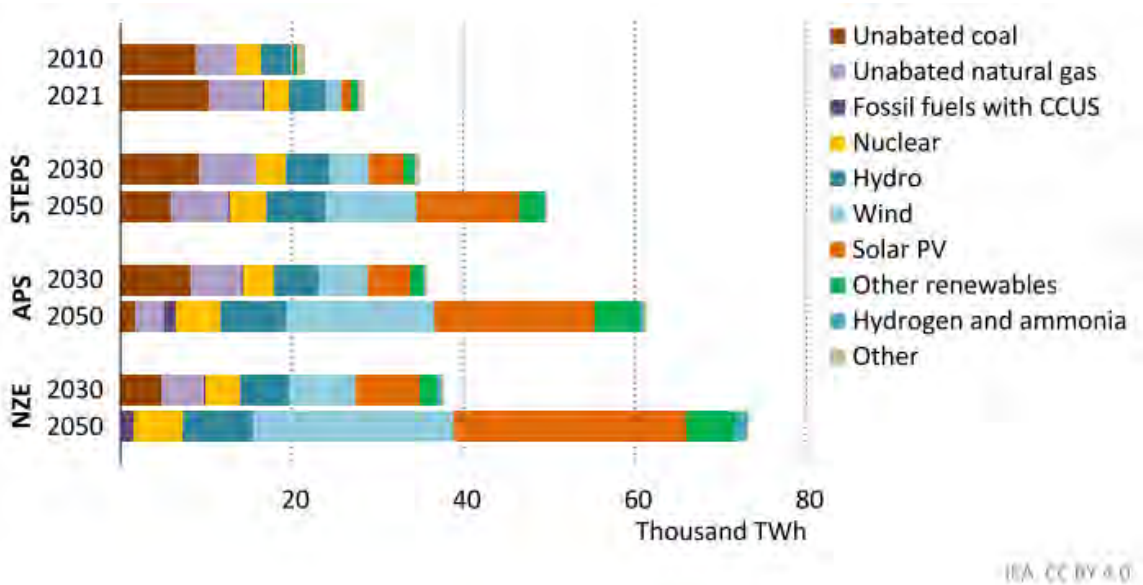
Notes: TWh = terawatt-hours; CCUS = carbon capture, utilisation and storage; PV = photovoltaics. STEPS = Stated Policies Scenario, APS = Announced Pledges Scenario; NZE = Net Zero Emission by 2050 Scenario. Electricity demand is defined as total gross electricity generated less own use generation, plus imports, less exports and transmission and distribution losses. Other sources are included in electricity supply.

Table 1.1 illustrates that the global share of fossil fuels in electricity generation declined from around 67 % in 2010 to 62 % in 2021 reflects a certain extent of growth of renewable energy in electricity generation over the past decade, which is mostly led by solar and wind [4]. Nevertheless, currently, a huge amount of global electricity is still provided by fossil fuels, which followed by several huge problems: the resulting emission of CO<sub>2</sub>, other greenhouse-gas (GHG), other environmental pollutants and particulate matter (PM). The energy-related CO<sub>2</sub> emission exhibited the largest ever annual growth in 2021, rebounded

to 36.6 gigatonnes (Gt), which may drive the global climate change and global warming in the future [4].

Underlying the environmental issues over the use of fossil fuels, combined with concerns on their resource constraints, energy security and price stability, many see the necessity and importance of clean energy transitions, in which energy is generated from renewable sources [4–8].

Among all the renewable energy sources, solar and wind energy are the most abundant and potentially readily available. As shown in Figure 1.1, so far, approximately 30 % of electricity generation is provided by renewables, mainly led by solar photovoltaics (PV) and wind. Besides, the share of renewables in global electricity generation exhibits a continuous and rapid scale-up tendency in all scenarios. This value is projected to increase to 43 % by 2030 and to 65 % by 2050 in the STEPS, the APS presents even a higher growth than that in the STEPS and the NZE Scenario projects the highest increment of their share of generation: this value rises to over 60 % in 2030 and to nearly 90 % in 2050 [4].



**Figure 1.1:** Global electricity generation by source and scenario, 2010-2050. [4]

However, both solar and wind are not constant and reliable power sources. The intermittent nature of renewables raises significant challenges for the electrical power generator to compensate for the variability and discontinuity. Another concern brought by renewables is the fact that almost all renewables with power generating facilities are

localized and commonly away from load centers or consumers' locations, which sometimes may lead to higher risks of an interruption in electricity power supply and potentially influence wide areas [7, 9–11]. Therefore, electrical energy storage (EES) systems are playing a crucial role for future society. Accessible, affordable, sustainable and reliable electrical energy storage (EES) systems have been considered as a key enabler of overall electric systems, including integrating renewables to power market to continuously and reliably provide electrical power to consumers, reducing CO<sub>2</sub> emission brought by electrical production and enabling the smart grid or green grid technology [7, 9, 12].

## 1.2 Electrical energy storage systems

As indicated in Figure 1.2, electrical energy storage (EES) systems can be classified into five main types: mechanical, thermal, chemical, electrochemical and electrical [10–12].

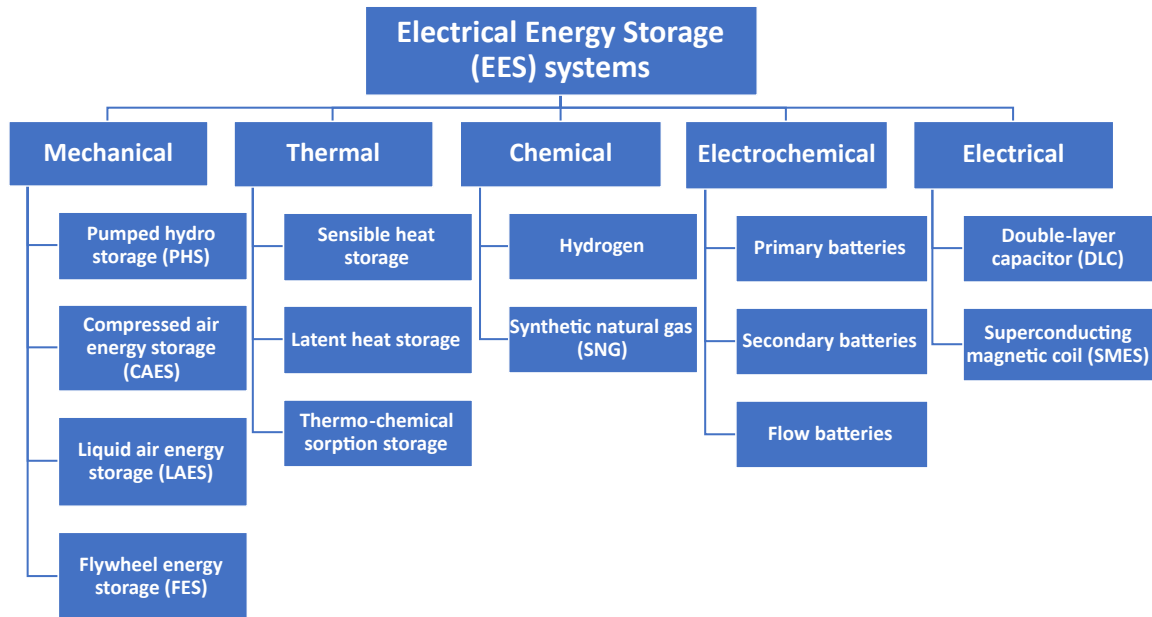


**Figure 1.2:** Classification of electrical energy storage (EES) systems.

Electrochemical storage systems, widely known as batteries, in which electricity is stored in the form of chemical energy and delivered on demand through a electrochemical oxidation-reduction (redox) reaction, are playing the crucial role among all above-mentioned EES systems [7, 10, 12, 13].

Generally, secondary batteries (SBs), in which the batteries can be recharged by a

reversal of the foregoing process (energy transformation from electrical energy into chemical energy), present a number of desirable characteristics, including high energy density, high power density, high round-trip efficiency, long cycle life, low maintenance and pollution-free operation. Hence they represent a captivating and excellent energy storage technology for the integration of renewables. Besides, the compact size of SBs enables their suitable application at distributed locations. Moreover, they are able to provide frequency control to reduce variations and mitigate fluctuations in renewable energy output. Considering about those advantages, they have been applied in widespread fields including portable electronic devices, transport vehicles and stationary energy storage during the past decades and will increasingly gain intense importance in the future [12–16].

### 1.2.1 Basic concepts of batteries and cells

Although the term “battery” is commonly used, in fact, the basic electrochemical unit being referred to as is “cell”. Generally speaking, a battery is composed of one or more of these cells, which are connected either in series or parallel, or both, depending on the desired output voltage and capacity [15].

A cell is composed of three major components [15]:

- (1) An anode (the reducing electrode) or negative electrode, which is oxidized during discharging and hence releases electrons into the external circuit.
- (2) A cathode (the oxidizing electrode) or positive electrode, which is reduced during charging and receives electrons provided by anode from the external circuit.
- (3) An electrolyte, which acts as ionic conductor, and provides the medium for transfer of charge (ions) inside the cell between anode and cathode. An electrolyte is typically liquid (water-based or organic solvents with suitable solutes to impart ionic conductivity), however, solids can be applied as electrolyte (solid electrolyte) as well.

In the literature, the negative electrode is commonly referred to as anode while the positive electrode as cathode owing to the function of the respective electrode during discharging.

However, for SBs, during charging, the functions of cathode and anode are reversed, i.e., cathode is reduced and anode is oxidized during charging. Therefore, for the clarity of expression, the use of “anode” and “cathode” is avoided throughout this dissertation, and “negative electrode” and “positive electrode” are used instead [17].

### 1.2.2 Pros and cons of lithium-ion batteries (LIBs)

As one of the most widely applied commercial SBs, lithium-ion batteries (LIBs), which utilize Li-intercalation (or insertion) compounds as electrode materials, possess a number of advantages, including high gravimetric and volumetric capacity with high power density owing to the low molecular weight and small ionic radius of lithium, high possible cell voltage level thanks to the low redox potential ( $E_{(\text{Li}^+/\text{Li})}^\circ = -3.04 \text{ V vs. SHE}$ ), low self-discharge rate and no memory effect. Hence LIBs have become the most important and dominant energy storage technology since its first commercialization by Sony in 1991. Up to now, billions of LIBs have been produced because of its widespread applications in various areas and the demand for LIBs is predicted to expand sustainably in the future owing to their potential application in portable electronics and especially in electric vehicles (EVs) [7, 11–15, 18–21].

However, lithium is not an abundant element. There are considerable concerns about the rare natural lithium resource in Earth’s crust (only 17 ppm), uneven lithium global distribution (predominantly in Chile, Bolivia, Argentina and China) and the expected increasing cost of lithium-ion-containing mineral ( $\text{Li}_2\text{CO}_3$ ), which is today mostly fabricated by mining [22–27]. Besides, the use of cobalt (Co) as commercial positive electrode material in LIBs is also of major concern due to its rarity (around 26.6 ppm in Earth’s crust) and the increasing cost of natural cobalt resource [18, 22, 23, 28].

Moreover, LIBs, as other SBs, use an electrochemical process known as Faradaic process, a process where the charged particles (in this case, lithium-ions) are reduced or oxidized, migrate through electrolyte, enter and leave electrodes (so-called lithiation and de-lithiation) during charging and discharging [29–31]. The redox reactions may change the molecular or crystalline structure of electrode materials, together with the formation and decomposition of solid electrolyte interface (SEI) layers damages the stability of

electrodes and hence significantly affects the cycle life of cell. Therefore LIBs need to be replaced after a certain number of charge-discharge cycles [20, 32–34].

All those above-mentioned factors have severely limited the widespread application of LIBs for large-scale stationary energy storage in the long-term future, where cost per unit of energy storage capacity ( $\$/\text{kWh}^{-1}$ ), voltage and cycle stability instead of energy density and power density are the superior metrics [7, 35]. Therefore, liquid metal batteries (LMBs) have drawn increasing attention to be applied for stationary energy storage. Additionally, taking both the rarity and high fabrication cost of Li into consideration, Na-based LMBs have the potential to be the most promising candidate among those LMBs as a more sustainable, affordable, reliable and scalable alternative to LIBs for deployment as large-scale stationary energy storage system.

### **1.3 Aim and objectives**

The aim of this dissertation is first to investigate the material compatibility of construction materials on Na-based liquid metal battery (LMB) cells, including negative current collector (NCC), electrical insulator and positive current collector (PCC) materials with cell active components (negative electrode, electrolyte and positive electrode).

Another goal of this dissertation is the assembly of Na-based LMB cells with approximate 5 Ah or larger capacity. After cell assembly, the electrochemical properties of those cells were characterized by studying the discharge-charge voltage curves and cycle efficiencies at different current densities cooperating with the corrosion mechanism occurred during cell operation to verify the feasibility of Na-based LMBs to be applied as sustainable, affordable, reliable and scalable energy storage system in grid-scale. Additionally, if possible, the electrochemical performance and even the cell design of our Na-based LMBs cells will also be improved during the research stage.

## 1.4 Structure of thesis

Above, the basic introduction of this dissertation was presented in Section 1, which starts with the motivation of this research project.

The state of the art of LMBs is reviewed in Section 2, including the history of LMBs, the concept of LMBs, advantages and disadvantages of Na-based LMB, the development of positive electrode in LMBs and the key issues in Na-based LMB need to be solved for grid-scale, long-term application, especially the material challenges on corrosion.

Section 3 briefly introduces the basic working principle of LMB cells, concisely describes the fundamentals of all used material characterization methods and electrochemical methods.

Section 4 not only presents the general designs of LMB cells, but also shortly discusses the material selection criterion for different parts in LMB cells. Moreover, the corrosion performance of those parts, including negative current collector (NCC), electrical insulator and positive current collector (PCC) in Na-based LMB cells are investigated and analyzed in this section as well.

The preparation of cell active components, the cell assembly procedure and the electrochemical tests of both designs of Na-based LMB cells form the heart of Section 5. In addition, considering about the distinct cell capacity degradation found by long-term Galvanostatic Cycling with Potential Limitation (GCPL) tests, cells with foam were disassembled for further analysis.

Section 6 makes the conclusion and a short summary of this dissertation.

## 2 State of the Art

### 2.1 History of liquid metal batteries

The timeline of LMBs is shown in Figure 2.1, the birth of all-liquid electrochemical cells can be traced back to the turn of last century with roots in the progress of classical electrometallurgy: the three-liquid-layer “Hoopes cell” invented and developed by Aluminum Company of America (Alcoa) in the 1920s for the electrolytic production of ultrahigh-pure aluminum [35, 36].

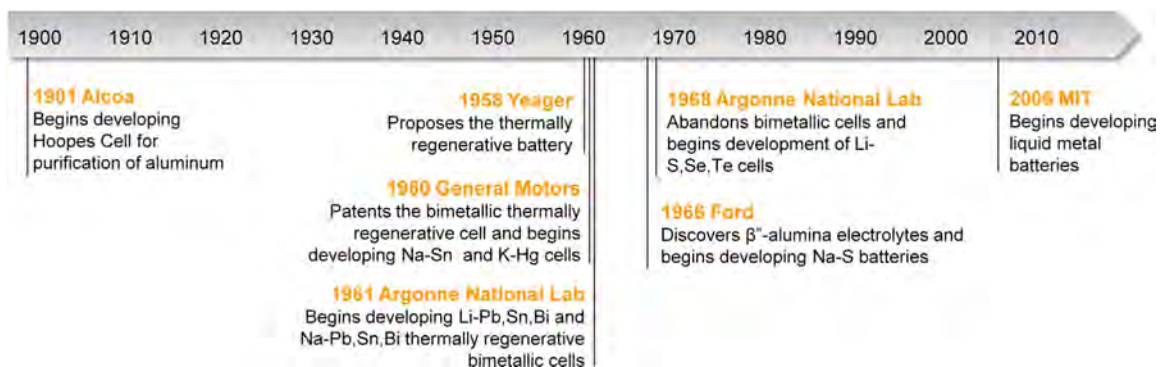


**Figure 2.1:** Timeline of the development of three-liquid-layer electrochemical cells and LMBs [35].

“Thermally regenerative electrochemical systems (TRESs)” are closed systems that convert heat into chemical stored energy then into electricity in an electrochemical heat engine whose efficiency is limited by Carnot cycle. In the late 1950s, under the concept of “TRESs”, the three-liquid-layer electrochemical cell named “thermally regenerative cells” regained people’s interest as one of the varieties for energy storage and conversion applications, and therefore was massive studied [35, 37, 38].

From then on, two types of thermally regenerative cells have emerged: metal hydride or metal halide cells and bimetallic cells, the latter possess the same three-liquid-layer self-segregating structure as the LMB cells discussed in this dissertation. In the 1960s, the bimetallic cells had been intensively studied, however, at the end of 1960s, bimetallic cells have lost its attraction to be applied for portable applications because of its low specific energy density [35].

Since 2006, Professor Sadoway’s group at MIT restarted to research and develop novel rechargeable those galvanic cells, the liquid metal batteries (LMBs), with the aim of deploying them as an accessible, affordable, sustainable and reliable grid-scale energy storage device for an efficient utilization of renewable resources like solar and wind. Since then, LMBs have experienced a renaissance [35].

## 2.2 Concept of liquid metal batteries

It can be seen from Figure 2.2 that a LMB cell consists of three liquid layers (two liquid metal electrodes and one molten salts electrolyte) as electroactive components, which are self-segregated on the basis of their density differences and mutual immiscibility: a liquid metal with low electronegativity and low density (alkaline or alkaline earth metal) as negative electrode, which floats on top; another liquid metal (transition metals, post-transition metals or metalloids) with high electronegativity and high density as positive electrode, which pools at bottom; and a molten salts electrolyte with intermediate density sandwiched in between the two liquid metal electrodes [35, 39–45].

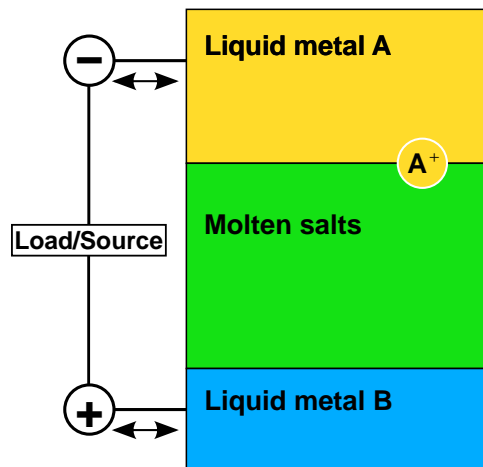


**Figure 2.2:** Schematic diagram of the active components in a liquid metal battery cell [35].

The periodic table (see Figure 2.3) highlights all possible candidates for negative electrode materials (yellow) and positive electrode materials (blue) for LMBs.

1																	18
H	2											13	14	15	16	17	He
Li	Be											B	C	N	O	F	Ne
Na	Mg	3	4	5	6	7	8	9	10	11	12	Al	Si	P	S	Cl	Ar
K	Ca	Sc	Ti	V	Cr	Mn	Fe	Co	Ni	Cu	Zn	Ga	Ge	As	Se	Br	Kr
Rb	Sr	Y	Zr	Nb	Mo	Tc	Ru	Rh	Pd	Ag	Cd	In	Sn	Sb	Te	I	Xe
Cs	Ba		Hf	Ta	W	Re	Os	Ir	Pt	Au	Hg	Tl	Pb	Bi	Po	At	Rn

**Figure 2.3:** Possible candidates for negative electrode materials (yellow) and positive electrode materials (blue) for LMBs [35].

The selection criteria of the liquid metal electrode materials are listed below, basically, there are three main requirements on electrode material candidates [35]:

- (1) Electrode need to be liquid at operating temperature, as a rule of thumb, the melting point of electrode need to be greater than 25 °C while its boiling point should be less than 1000 °C ( $T_m > 25 \text{ °C}$ ,  $T_b < 1000 \text{ °C}$ ).
- (2) Electrode must be electrically conductive, whose minimum electronic conductivity should be greater than the ionic conductivity of a typical molten salts electrolyte ( $\sigma > 1 \text{ S cm}^{-1}$ ).
- (3) For safety concerns, those candidates also must be non-radioactive, i.e., they must be in the form of a naturally occurring, stable isotope.

### 2.3 Advantages and disadvantages of Na-based liquid metal battery

Taking the concerns about LIBs referred to in Section 1.2.2 into account, in contrast to lithium, sodium is the sixth most abundant element and fourth most abundant metal in the Earth's crust (around 2.36 wt.%), whose resources are almost inexhaustible and much cheaper than lithium [22, 46–49]. Moreover, sodium is the next metal after lithium in the alkali metal group (second-lightest and -smallest alkali metal), which not

only possesses similar physical and chemical characteristics as lithium, but also exhibits promising electrochemical properties ( $E_{(\text{Na}^+/\text{Na})}^\circ = -2.71 \text{ V vs. SHE}$ ) [47–49]. In combination of those aforementioned factors, sodium-ion batteries (SIBs) have also been regarded as an auspicious alternative to the commercial LIBs for the next-generation battery albeit the energy density of SIBs is lower than that of LIBs.

When compared with SIBs, sodium-based LMBs have some unique strengths:

- (1) All components in LMBs are liquid, which endows LMBs with superior kinetics and transport properties. The liquid-liquid electrode-electrolyte interface in LMB cells not only makes rapid charge transfer possible, but also enable ultrafast mass transport of reactants and products to and from the electrode-electrolyte interface by full liquid-state diffusion. Hence LMBs have low voltage losses, i.e., weak polarizations, which enables LMBs to achieve high voltage efficiencies at high current densities [35, 50, 51].
- (2) In contrast to conventional ion battery cells, in which a microporous membrane is required as separator between negative electrode and positive electrode, which increases the manufacturing costs remarkably and complicates the cell fabrication, LMB cells are easy to assembly and the fabrication costs can be reduced to some extent [20, 50, 51].
- (3) Unlike common ion battery cells, whose capacity and cycle life are usually limited by the degradation of the electrode microstructure and decomposition of the electrolyte solution during cell cycling, for LMB cells, the continuous creation and annihilation of the liquid metal electrodes during charge-discharge cycling immunize the electrodes from the aforementioned degradation mechanism. Hence, grants LMB cells the potential for unprecedented cycle life. This characteristic also makes LMB cells immune to the dendrite formation which causes short-circuit and even leads battery cells to catastrophic failures like catching fire [15, 20, 48, 49, 52–54].
- (4) The relatively higher operating temperature of LMBs liberates itself from complicated thermal management system, which is essential for conventional ion battery cells. This is due to the fact that heat is generated during the operation of

LIBs, which is associated with charge transfer and chemical reactions during charge-discharging cycling [55] and LIBs are usually connected as cell stack and installed in the battery housing [20]. It is well known that the optimum operating temperature for conventional LIBs ranges from 20 to 40 °C, their performance characteristics (e.g., raising internal resistance by lower temperatures) and service life (e.g., cell aging at higher temperatures) are strongly dependent on the ambient temperature [20, 55]. The required thermal management system for LMBs is a simple heating system, which could utilize the heat from the surroundings, heat generated during its operation and the waste heat from other industrial activities. This characteristic of LMBs enables its application in rugged surroundings, such as tropics and other high-temperature regions.

Except for those room-temperature SIBs, high-temperature sodium-based batteries, also known sodium-beta batteries (SBBs), with the representative of sodium-sulfur (Na-S) battery and sodium-metal halides battery with the nickname of ZEolite Battery Research Africa (ZEBRA) battery also have been intensively investigated and even commercially applied for grid integration. Compared with LMBs, both the Na-S and the ZEBRA batteries have the same drawback: a beta-alumina ( $\beta$ -Al<sub>2</sub>O<sub>3</sub>) ceramic, the so-called  $\beta$ -Al<sub>2</sub>O<sub>3</sub> solid electrolyte (BASE) serves as a sodium-ion selective membrane.  $\beta$ -Al<sub>2</sub>O<sub>3</sub> is regarded as the key element in determining the manufacturing cost for both high-temperature Na-based batteries. Moreover,  $\beta$ -Al<sub>2</sub>O<sub>3</sub> is a solid electrolyte, which limits the ion transport. Additionally,  $\beta$ -Al<sub>2</sub>O<sub>3</sub> is brittle, the fracture of  $\beta$ -Al<sub>2</sub>O<sub>3</sub> during cell operation will lead to cell failure. Especially for the Na-S battery, a broken  $\beta$ -Al<sub>2</sub>O<sub>3</sub> will potentially cause fire and even explosion [7, 14, 15, 42, 56, 57].

Those aforementioned demerits of sodium batteries with solid electrolyte have drawn great interest and attention on Na-based LMBs.

Nevertheless, Na-based LMBs, under the concept of LMBs, own some specific disadvantages, including all-liquid configuration, relatively higher operating temperature (generally > 200 °C), low theoretical specific energy density (typically < 200 Wh kg<sup>-1</sup>) and comparatively low equilibrium cell voltage (typically < 1.0 V), which make it impossible for portable applications. As a result, its application has been restricted to stationary energy storage. Additionally, its high operating temperature together with

high corrosive active cell components brings great challenges on high temperature sealing, high temperature insulation and high temperature corrosion issues on cell construction materials [35, 51].

## 2.4 Development of a positive electrode for liquid metal batteries

Among all transition metals, post-transition metals and metalloids, antimony (Sb) is regarded as a competitive and promising candidate for positive electrode for LMBs because of its higher anticipated cell voltage when coupled with an alkali or alkaline earth negative electrode (e.g. the equilibrium cell voltage of Li-Sb electrode couple at fully-charged state is  $\sim 0.92$  V) [35, 43, 44] and its low cost (average price over the past 5 years: \$ 0.993 mol<sup>-1</sup>) [23].

In 2012, Bradwell et al. built LMB cells with magnesium (Mg) negative electrode and antimony (Sb) positive electrode, which utilized MgCl<sub>2</sub>-NaCl-KCl (50-30-20 mol.%) as electrolyte [43]. High Coulombic efficiencies (over 94 %) were achieved when cycled at the current densities from 50 to 200 mA/cm<sup>2</sup>, however, low energy efficiencies (under 70 %) were obtained as well in consequence of a relatively low electrolyte conductivity ( $\sim 0.8$  S cm<sup>-1</sup>). Moreover, the cell voltage is quite low ( $\sim 0.21$  V under galvanostatic discharging with the current density of 200 mA/cm<sup>2</sup>). Additionally, due to high melting points of magnesium (650 °C) and antimony (631 °C), the Mg || Sb cell must be operated near 700 °C, which exacerbates the corrosion issues and reduces the overall energy efficiency. Considering about the high operating temperature, low cell voltage and high cost of electrode materials (estimated \$ 170 kWh<sup>-1</sup> and realized \$ 230 kWh<sup>-1</sup>, respectively), Mg-Sb cells were abandoned for commercial application in large-scale grid energy storage [35, 43, 51].

Take the high melting point of antimony (631 °C) into consideration, alloying antimony (Sb) with other lower-melting point metals might be an effective approach to decrease the melting point of positive electrode as well as the operating temperature of LMB cell. However, this is generally accompanied by an undesirable decline in cell voltage [35, 44, 58, 59].

In 2014, Wang et al. developed Sb-Pb positive electrode for Li-based LMB cells, which utilized LiF-LiCl-LiI (20-50-30 mol.%) as electrolyte [44]. The operating temperature of this Li || Sb-Pb cell was successfully decreased to 450 °C. A high nominal discharge voltage (0.73 V) and a high Coulombic efficiency (98 %) were reached at the current density of 275 mA/cm<sup>2</sup>. Moreover, after 450 full charge-discharge cycles, 94 % of its initial capacity was maintained, which demonstrate its good cycle performance. Alloying antimony with lead lowers the cell operating temperature by decreasing the melting point of the positive electrode without an attendant decline in cell voltage at the initial discharge state. Additionally and more important, alloying antimony with lead also reduces the cost of cells (electrode materials costs:  $\sim$  \$ 65 kWh<sup>-1</sup>), which enables the potential application of Li || Sb-Pb LMB cell in large-scale grid energy storage [44, 51].

Nevertheless, since the underlying mechanism for alloying antimony (Sb) with lead (Pb) without a decline in cell voltage is still undefined and the large-scale utilization of lead may bring severe environmental concerns, Sb-Sn positive electrode for Li-based LMB cells with LiF-LiCl-LiBr (22-31-47 mol.%) electrolyte was researched by Li et al. in 2016 [60]. The reported Li || Sb-Sn cell was operated at 500 °C, which exhibited a relatively high discharge voltage ( $\sim$  0.8 V at the current density of 100 mA/cm<sup>2</sup>), a high Coulombic efficiency (about 98 %) and superior rate capability (only 13 % capacity loss from the current density of 100 mA/cm<sup>2</sup> to 1000 mA/cm<sup>2</sup>). Moreover, at the current density of 300 mA/cm<sup>2</sup>, after 3500 h operation (more than 430 full charge-discharge cycles), 96.7 % of the initial capacity was maintained, which also revealed the excellent cycle performance at a low materials cost ( $\sim$  \$ 73 kWh<sup>-1</sup>). Additionally, the predominant role of antimony in achieving a higher cell voltage and the inert “solvent” role of Sn in lowering the melting point and reducing the positive electrode material cost were also proven by no remarkable differences in the charge/discharge voltage plateau among different Sb-Sn alloy compositions in this paper [60].

Although alloying antimony (Sb) with lead (Pb) and tin (Sn) could reduce cell operation temperature by decreasing the melting point of positive electrode and reduce the cost of positive electrode materials [44, 51, 60], both Pb and Sn are not able to enhance the energy density of LMB cells.

Considering that bismuth (Bi) is a post-transition metal with a low melting point

(271.5 °C) and high electronegativity, with has similar thermodynamic properties as antimony (Sb) [51, 61], Dai et al. extended the above-mentioned concept by developing a novel Li-based LMB cell, which employs Sb-Bi alloy as positive electrode and eutectic LiF-LiCl (69.6-30.4 mol.%) as electrolyte [62]. The operating temperature of Li || Sb-Bi cell is located in the range of 450 °C – 550 °C. The addition of bismuth (Bi) to antimony (Sb) possesses several advantages: First, bismuth (Bi) also has a lower melting point (271.5 °C), alloying of bismuth (Bi) with antimony (Sb) lowers the cell operating temperature by decreasing the melting point of positive electrode. Secondly, compared with lead (Pb), bismuth (Bi) is more environmentally friendly. Thirdly, although the cost of bismuth (Bi) is a little bit more expensive, the cost of positive electrode can still be reduced by adjusting the mole fractions of antimony (Sb) and bismuth (Bi). Finally and most importantly, both antimony (Sb) and bismuth (Bi) could participate in the reaction and hence contribute to the overall cell capacity [62].

The results showed that during discharging, lithium (Li) first reacts with antimony (Sb) to form Li-Sb intermetallic compounds, at a deeper level of discharging, Li starts to react with Bi. Moreover, Li || Sb-Bi cell with 40 : 60 mol.% Sb-Bi alloy as positive electrode presents the highest average discharge voltage (ca. 0.83 V), an extremely high Coulombic efficiency (99 %) and a very high overall energy efficiency (89 %) (under galvanostatic cycling with the current density of 150 mA/cm<sup>2</sup>) after 160 cycles. Additionally, the cost per unit energy (\$68 kWh<sup>-1</sup>) for this cell is comparable to that of Li || Sb-Pb and Li || Sb-Sn LMB cells. Therefore, Sb-Bi alloy holds great promise to be applied as positive electrode in LMB cells for grid-scale applications [62].

Recently, Sb-Bi positive electrode was also investigated in Na-based LMB cells which utilized a multic-cationic ternary chloride salt mixture of LiCl-NaCl-KCl (59-5-36 mol.%) as electrolyte. The operating temperature of this Na || Sb-Bi was decreased to 450 °C. At the current density of 100 mA/cm<sup>2</sup>, a high Coulombic efficiency (97 %) and a high active material utilization (about 80 %) were achieved after 700 cycles [63].

The comparison of basic cell parameters of some Sb-based LMB systems is shown in Table 2.1.

**Table 2.1:** Comparison of basic cell parameters of some Sb-based LMB systems.

Electrode couple	Electrolyte	Working temperature (°C)	Average discharge voltage (V)	Electrode material cost (\$ kWh <sup>-1</sup> )	Ref.
Mg    Sb	MgCl <sub>2</sub> -NaCl-KCl (50-30-20 mol.%)	≈ 700	0.21 (at 200 mA/cm <sup>2</sup> )	375	[43]
Li    Sb-Pb	LiF-LiCl-LiI (20-30-30 mol.%)	450	0.73 (at 275 mA/cm <sup>2</sup> )	69	[44]
Li    Sb-Sn	LiF-LiCl-LiBr (22-31-47 mol.%)	500	≈ 0.8 (at 100 mA/cm <sup>2</sup> )	73	[60]
Li    Sb-Bi	LiF-LiCl (69.6-30.4 mol.%)	450 ~ 550	≈ 0.83 (at 150 mA/cm <sup>2</sup> )	68	[62]
Na    Sb-Bi	LiCl-NaCl-KCl (59-5-36 mol.%)	450	≈ 0.7 (at 100 mA/cm <sup>2</sup> )	0.029	[63]

## 2.5 Key issues on Na-based liquid metal battery

Although LMBs have been intensively studied by a large number of researchers, its commercial application for grid-scale energy storage is still accompanied with several serious challenges or issues to be solved. The first and most important issue is to keep the cell operating temperature as low as possible. This is due to the fact that a relatively high operating temperature may bring numerous detrimental effects on LMBs cells from different perspectives, including low cell efficiencies brought by a higher sodium solubility in electrolyte with higher ohmic losses, severe corrosion on cell construction materials triggered by cell active components, adverse impact on sealing, high temperature management, etc..

### 2.5.1 Electrolyte with low melting point and low sodium solubility

Bimetallic cells with liquid Na as electrode, for example, Na-Bi, Na-Sn and Na-Pb cells were devised by Argonne National Laboratory in the 1960s [35, 51, 64].

Owing to the higher theoretical cell voltage of Na-Bi, Na-Bi cells were preferred as secondary cells, which are cited here as an example. In Na-Bi cells, the ternary eutectic composition of all-sodium salts mixture NaF-NaCl-NaI (15-32-53 mol.%) was utilized as electrolyte, and the cells were operated between 535 °C and 650 °C. Although one of those cells had been continuously operated for more than 17 months without appreciable

cell performance degradation, the formation of intermetallic Na-Bi species at electrode-electrolyte interface during discharging at high current densities impedes the diffusion of Na-ions, thereby prevents the cell from achieving its theoretical cell capacity. Moreover, both a low Coulombic efficiency (less than 80 %) at the current density of 665 mA/cm<sup>2</sup> and an obvious dropping of open-circuit voltage (OCV) ( $\approx$  0.12 V within 30 min) indicate a high self-discharge rate of this cell, which is mainly caused by the solubility of Na in the molten salts electrolyte [35, 51, 64].

The relatively large self-discharge rate can be observed in all bimetallic cells equipped with liquid Na electrode because of the high solubility of Na in molten salts electrolyte. Hence, suppressing the solubility of Na in molten salts electrolyte is the crucial factor for Na-based LMBs to achieve higher efficiencies.

The selection of low-melting sodium-cation electrolytes for cells with liquid Na electrode have been restricted to halides due to the fact that all the other anions are regarded either unstable with respect to liquid Na or react with Na and form compounds with high melting points [64]. There are two ways to decrease the solubility of Na in molten salts. The simplest way is to reduce the operating temperature of Na-based LMBs while the other one is to adjust and optimize the composition of halide molten salts. The solubility of metals can be suppressed by utilizing multi-cation halide molten salts [35, 51, 65]. Therefore, a suitable electrolyte (low-cost, lowest possible melting point and lowest possible Na solubility) is determinative for the progress in the development of Na-based LMBs. The eutectic mixture of LiCl-NaCl-KCl (55-9-36 mol.%) with a melting point of approximate 350 °C is considered as an appropriate electrolyte for Na-based LMBs cells due to its low melting point, low Na solubility but high stability and sufficient sodium ion conductivity [50, 63, 66–68].

### **2.5.2 Electrode couple with low melting point but high voltage**

Another challenge for Na-based LMBs is the development of low melting point, low-cost but high voltage electrode couple.

The minimum operating temperature of LMBs cells is determined by the melting point of electrolyte and electrode materials. A reduced cell operating temperature decreases

detrimental effects triggered by corrosion and self-discharge [35]. Since the negative electrode (Na, melting point: 98 °C) and halide salts electrolyte (e.g., eutectic mixture of LiCl-NaCl-KCl, melting point:  $\approx$  350 °C) are relatively low, positive electrode with high melting points should be abandoned.

According to previous studies, alloying LMB electrodes with another metal or with other metals not only achieve the aim of reducing the melting point and cost of electrode, but also reach the goal of maintaining a high cell voltage [35, 44, 51, 60, 62], this broadens the material selection on positive electrode materials for LMBs.

### **2.5.3 Corrosion**

As mentioned before, an elevated operating temperature of LMBs cells not only affects cell efficiency by increasing Na solubility in electrolyte, but also brings serious corrosion issues on cell construction materials and exerts an adverse impact on cell sealing [35].

In contrast to conventional batteries, all-liquid components of LMB cells provides several advantages including superior kinetics and immunity to microstructural degradation on electrodes. Despite that, the main concern for the long-term performance of LMBs is the corrosion on cell construction materials (negative current collector (NCC), positive current collector (PCC), electrical insulator and seal) brought by the high operating temperature and high reactivity of cell active components. To be more precise, the corrosion attacks on LMB cells not only bring safety concerns on its long service lifetime, the corrosion products generated by the reaction between cell active components and cell construction materials may change the composition of cell active components, hence have adverse effects on cell performance, including undesirable side-reactions, increased cell internal resistance and reduced cell capacity [35, 69, 70]. Therefore, corrosion-resistant cell construction materials are essential for LMB cells to maintain an excellent cell performance for long terms.

#### **NCC and electrical insulator materials**

So far, liquid Na is known as the most effective coolants in high-temperature applications such as liquid metal fast-breeder reactors (LMFBR) and concentrating solar power (CSP) systems [71, 72]. Halides eutectic mixture are becoming more competitive to be applied

as high temperature heat transfer fluid (HTF) for CSP systems owing to their low melting point (200 °C) but high boiling point ( $> 1000$  °C), low cost and high thermal stability at higher temperature [73]. Hence, for the past decades, the compatibility of construction materials in liquid Na and in liquid molten salts have been intensively investigated.

It is to be expected that a very large proportion of the published studies concerned with corrosion of stainless steels and nickel-based alloys in liquid Na since these alloys are favored construction materials and their properties can be varied quite widely by change the composition [74]. As early as 1950, Argonne has published a report about the compatibility of liquid Na with various construction materials, which revealed that iron (Fe) dissolves in Na at a very slow rate resulting in extremely long times to achieve equilibrium solubility, oxygen accelerates both the attack by Na on most metals and the decarburization rate of carbon steels [75].

Recently, several works on corrosion behavior of stainless steel and nickel-based alloys in molten chloride salts have been performed by many investigators.

Corrosion behavior of nickel-containing alloys in eutectic molten LiCl-KCl was performed by Ravi Shankar et al., and the results showed that when compared to Inconel 625 and 800H, Ni-based alloys Inconel 600 and 690 possess better corrosion resistance at high temperatures in the presence of air because the presence of Mo in Inconel 625 is not beneficial for molten salts environment in air. Moreover, the corrosion mechanism of those alloys seems to be the formation of Cr-rich and Ni-rich layers of chromium oxide ( $\text{Cr}_2\text{O}_3$ ), nickel oxide (NiO) and spinel oxides at the surface and subsequent spallation [76]. Abramov et al. investigated stainless steel corrosion in equimolar NaCl-KCl melt at 750 °C and found that the main corrosion products are iron, manganese and chromium species. Additionally, prolongation of anodic dissolution results in increasing chromium-to-iron ratio in the melt [77]. As evidenced by Lai, the major corrosion type occurred on alloys exposed in molten chlorides under oxidizing atmosphere is the intergranular corrosion [78]. Porcayo-Calderon et al. found that when exposed in  $\text{ZnCl}_2$ -KCl (at the molar ratio of 1:1) in air, Ni20Cr coatings present better corrosion resistance than SS304 owing to its high Ni content, which is beneficial to improve the corrosion resistance while SS304 exhibits poor corrosion resistance, which is attributed to the low stability of Fe and Cr, their oxides and chlorides in the used corrosive media [79]. The corrosion behavior of

Fe-Cr, Fe-Al and Ni-Al alloys in NaCl-KCl (1:1 mole ratio) melt was studied by Li et al. and the results showed that Cr presents a detrimental effect on the corrosion performance of Fe-Cr alloys while Al is advantageous to improve the corrosion resistance of Fe-Al alloys with increasing Al content. Besides, metallic Ni remains relatively stable after exposure, hence Ni-Al alloy exhibits the best corrosion resistance among all test materials [80]. It has been reported that the corrosion of materials in molten salts was clarified with the respect to the different thermal-chemical stability of the metallic elements, their oxides and chlorides in the molten salts, therefore, the worse performance of Cr is owing to the high reactivities (solubilities) of Cr and  $\text{Cr}_2\text{O}_3$  in alkali chloride molten salts while the good corrosion resistance of Ni and Al can be contributed to the high thermodynamic stabilities of their chlorides or oxides [79, 80].

However, the corrosion phenomena of dielectric ceramics and metallic materials in sodium vapor and in molten salts vapor are not well elucidated. For all we know, hot corrosion of  $\text{Al}_2\text{O}_3$  and SiC ceramics by KCl-NaCl molten salt was reported by Nagaoka et al. at high temperatures (700 °C and 800 °C) under air by immersing in molten salts and exposing in salts vapor, respectively. They found out that neither corrosion products nor a significant roughness of  $\text{Al}_2\text{O}_3$  particles can be observed after corrosion tests. Moreover, no significant strength decrease could be detected. As for SiC,  $\text{SiO}_2$  emerged as the corrosion product, and a considerable roughness can be observed at the surface of the immersed sample, which became more pronounced as the corrosion temperature and time increased. Additionally, no significant strength decrease was observed on both ceramics [81].

## **PCC materials**

Liquid metals have been considered as coolants in nuclear plants [82] and heat transfer fluid (HTF) in concentrating solar power (CSP) systems [83–85]. Therefore, in the past, studies on corrosion of structural materials in liquid metals have also been intensively performed, and the main corrosion mechanisms between solid structural materials and liquid metals have been established. The principal identified corrosion mechanisms include direct dissolution of components of structural materials in liquid metal, formation of intermetallic compounds at the interface between solid structural materials and liquid

metal as a consequence of direct alloying process, intergranular penetration or depletion of a dissolved component of the solid caused by selective reaction of liquid metals with the minor constituents of structural materials [83, 84, 86].

Up to now, published works investigated the corrosion issues mainly in pure liquid antimony (Sb), tin (Sn) or bismuth (Bi). Corrosion tests in liquid Bi were performed and the results showed that ferritic iron, low-carbon steels and low-alloy steels all have good resistance against attack by liquid Bi up to their transformation temperatures (about 700 °C) [75, 86]. Chromium (Cr) has good resistance against attack by liquid Bi at 730 °C and limited resistance at 1010 °C [75, 86]. Molybdenum (Mo) has good resistance against attack by liquid Bi at temperature up to 1010 °C and higher while nickel (Ni) and high-nickel alloys have poor resistance against attack by liquid Bi at temperatures above its melting point (271 °C) [75, 86]. Armco iron, cast iron, low-carbon steel (0.13 wt.% C), cast steel were also investigated and proven to have poor resistance against attack by antimony (Sb) at 630 °C and higher temperatures due to the formation of Fe-Sb compounds [75, 86, 87]. Moreover, both chromium (Cr) and nickel (Ni) are excluded from container materials for liquid Sb due to their appreciable solubility in liquid Sb at low temperatures [75, 86]. To the contrary, tin (Sn) forms intermetallic phases with iron (Fe), chromium (Cr) and nickel (Ni) and hence is the most aggressive liquid metal towards steels or Ni-based alloys [84, 88–90]. Sn attacks stainless steel strongly already at temperature of only 300 °C [88, 89]. Besides, Ni exhibits appreciable solubility in liquid Sn at low temperatures while Cr shows no signs of attack by liquid Sn at the melting point of Sn (231.9 °C) and may exhibit good corrosion resistance at considerable higher temperatures [75, 86]. Even niobium (Nb) and molybdenum (Mo) which are regarded as resistant against most other liquid metals due to their generally low solubility and have been suggested for use with liquid Sn [75, 86], they may substantially corroded in the presence of liquid Sn as a result of the formation of intermetallic compounds [75, 86, 90, 91].

Even so, only very few reports concerned on the corrosion between positive electrode in LMB cells and stainless steel. The corrosion of low carbon steel 1018, SS301 and SS430 as positive current collector (PCC) in Li || Sb-Pb LMBs was investigated by Ouchi and Sadoway, the results showed that Sn dominantly alloys with Ni, Fe and Cr in Sb-Pb alloys,

the thickness of intermetallic layers ranks  $\text{Ni} > \text{Fe} > \text{Cr}$ . Despite that, cell performance is not adversely affected by Fe or Ni dissolution but rather Ni. Moreover, the in-situ formation of protective Fe-Cr-Sb layer inhibits the corrosion on SS430 [69]. Cui et al. studied the corrosion of SS304 as PCC in Li || Sb-Sn LMBs, the results manifested that Fe and Ni of SS304 dissolve easily in liquid Sb-Sn alloy rather than Cr, forming the Fe-Ni-Sb-Sn corrosion products. Owing to the prominent solubility of Fe in liquid Sb-Sn alloy and high concentration of Fe in SS304, the dissolution of Fe is decisive, which leads to the formation of Fe-Sb and Fe-Sn corrosion products. Sn in positive electrode accelerates the diffusion of dissolved elements hence exacerbates the corrosion of PCC [70]. Liu et al. investigated the corrosion behaviors of Fe, Ni, Cr and several steels in liquid antimony-tin for a shorter time (160 h), the results showed that among Fe, Ni and Cr, Cr possesses the lowest corrosion rate due to the formation of a relatively stable Cr-Sb layer while Ni has the highest corrosion rate due to the formation of Ni-Sb and Ni-Sn compounds, which are soluble in liquid Sb-Sn. Besides, among A3 (98 wt.% Fe), SS304, SS316L, SS410 and SS430, SS430 has the lowest corrosion rate of 0.19  $\mu\text{m}$  owing to its relatively high Cr content and low Ni content, which indicates the principle for Sb-Sn resistant materials [92].

### 3 Fundamentals

In this section, the basic working principle of LMB cells is briefly introduced. Moreover, all the material characterization methods and electrochemical methods, which have been used in the present dissertation are concisely presented and described.

#### 3.1 Working principle of liquid metal batteries

A LMB cell is a simple concentration cell, during discharging, as indicated in Figure 3.1 (a), the negative electrode (liquid metal A at top) is oxidized to  $A^{z+}$ , and the  $A^{z+}$  cations migrate through the molten salts electrolyte to the positive electrode at the bottom as electrons are released from negative current collector (NCC) into the external circuit. As a result, negative electrode layer reduces in thickness; simultaneously, the positive electrode layer increases in thickness, the  $A^{z+}$  cations are reduced to neutral metal A which alloys with positive electrode (liquid metal B at the bottom) and forms a liquid A-B alloy. As shown in Figure 3.1 (b), this process is reversed when the cell is under charging: the liquid A-B alloy at the bottom is oxidized and generates  $A^{z+}$  cations, which transit across the molten salts electrolyte back to the negative electrode at top and are reduced to neutral liquid metal A (named as de-alloying process). Concurrently, electrons are released from positive current collector (PCC) into the external circuit and return to the cell via NCC [35, 40, 41, 51].

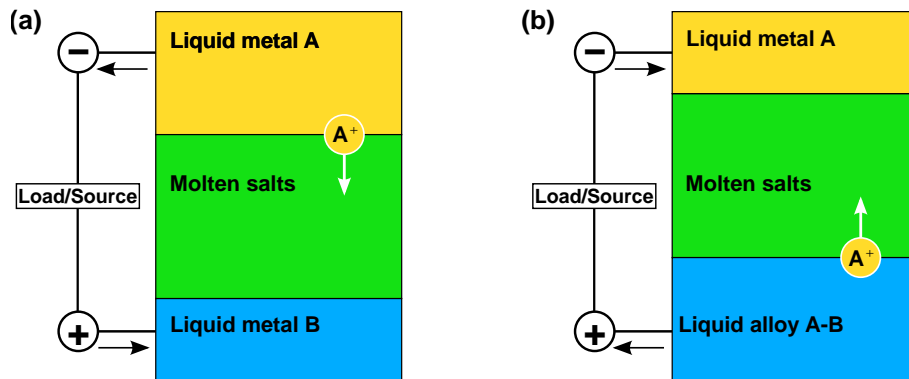


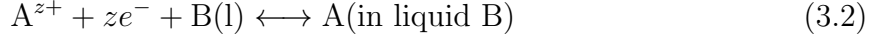
**Figure 3.1:** Schematic diagram of a liquid metal battery cell during (a) discharging and (b) charging.

The electrode reactions and overall cell reaction can be represented as follows [35, 50].

Negative electrode reaction:



Positive electrode reaction:



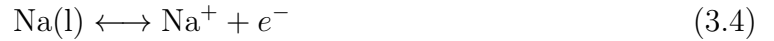
where  $z$  is the valency or the number of transferred electrons (1 for alkali metals and 2 for alkali earth metals).

The overall cell reaction:

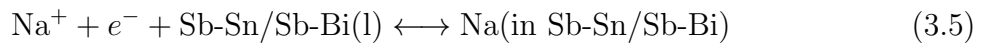


In this dissertation, the Na-based LMB cells employ liquid Na as negative electrode atop, liquid antimony-tin (Sb-Sn)/antimony-bismuth (Sb-Sn) (low melting point and high electronegativity and relatively low-cost) as positive electrode at bottom of the cell, LiCl-NaCl-KCl (61-3-36 mol.%) molten salts as electrolyte between the negative and positive electrode. The negative and positive reactions of our Na-based LMB cells can be expressed in the following.

Negative electrode reaction:



Positive electrode reaction:



The overall cell reaction:



The theoretical capacity  $Q_{\text{theoretical}}$  (Ah) of the Na-based LMB cells is based on the mass of Na used as negative electrode in cell, which can be calculated with the following formula:

$$Q_{\text{theoretical}} = \left( \frac{m_{Na}}{M_{Na}} \right) \left( \frac{N_A e}{3600} \right) \quad (3.7)$$

where  $m_{Na}$  (g) is the mass of used Na,  $M_{Na}$  (22.990 g/mol) is the molar mass of Na,  $N_A$  is the Avogadro constant ( $6.02 \times 10^{23} \text{ mol}^{-1}$ ) and  $e$  is the elementary charge ( $1.602 \times 10^{-19} \text{ C}$ ).

### 3.2 General designs of LMB cells

As shown in Figure 3.2, basically, there are two design types of the LMB cell, which were both investigated in this work. The cell case serves as positive current collector (PCC) for both designs. In Figure 3.2 (a), a metallic foam, which is connected to the negative current collector (NCC), is immersed in molten salts electrolyte to host the negative electrode by surface tension. The dielectric break and NCC are exposed to electrolyte (molten salts) vapor. In Figure 3.2 (b), with the aim of increasing the cell capacity, no metallic foam is applied as negative electrode host and the liquid negative electrode directly floats on top of electrolyte. In this case, an insulating sheath of ceramic is needed to insulate the negative electrode from the PCC. Both dielectric break and NCC are exposed to negative electrode (in this case, liquid Na). In both designs of the LMB cell, one dielectric break (electrical insulator) is needed to insulate the negative electrode from the positive electrode and to provide a hermetic seal [35].

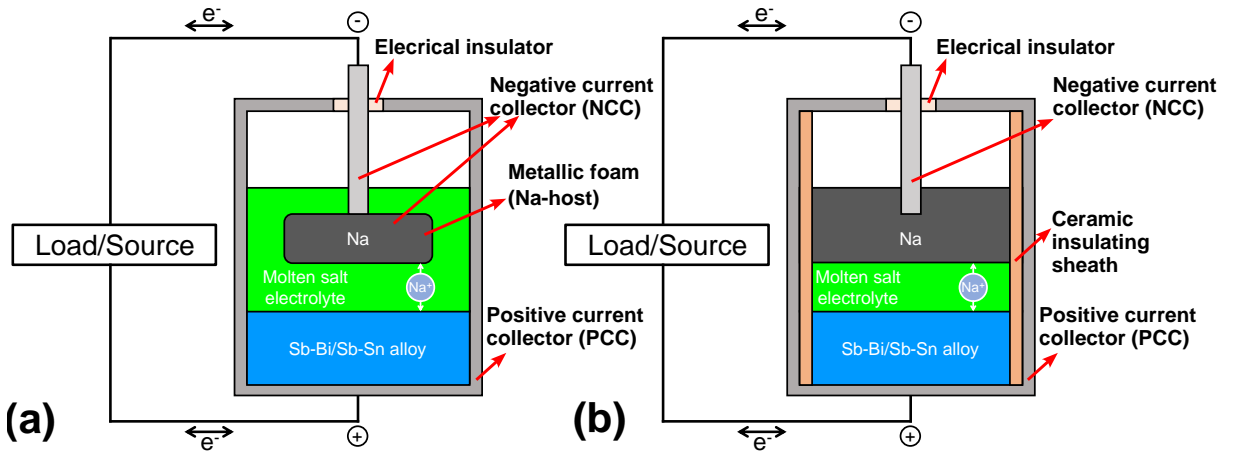


**Figure 3.2:** Schematic of liquid metal battery cell designs (a) without insulating sheath on the inner wall of PCC but one metallic foam is connected to NCC and immersed in molten salts electrolyte to host liquid Na by surface tension and (b) with an insulating sheath but without a metallic foam.

### 3.3 Equilibrium voltage and terminal voltage

The thermodynamic driving force or the so-called electromotive force (EMF) of a LMB cell is solely determined by the change in partial molar Gibbs free energy, as shown in

equation below [35, 40, 50]:

$$\Delta\bar{G}_{\text{cell}} = \bar{G}_{\text{A(in liquid B)}} - \bar{G}_{\text{A(l)}} \quad (3.8)$$

where the partial molar Gibbs free energy  $\bar{G}_i$  of component  $i$  is given by:

$$\bar{G}_{\text{A(in liquid B)}} = G_{\text{A(l)}}^{\circ} + RT \ln a_{\text{A(in liquid B)}} \quad (3.9)$$

$$\bar{G}_{\text{A(l)}} = G_{\text{A(l)}}^{\circ} + RT \ln a_{\text{A(l)}} \quad (a_{\text{A(l)}} = 1) \quad (3.10)$$

where  $a_i$  is the activity of component  $i$  at different states,  $G_{\text{A(l)}}^{\circ}$  is the standard Gibbs free energy of the metal A in the pure (liquid) state,  $R$  is the universal gas constant and  $T$  is the temperature. The Nernst equation links the change in partial molar Gibbs free energy to the equilibrium cell voltage:

$$\Delta\bar{G}_{\text{cell}} = -zFE_{\text{cell,eq}} \quad (3.11)$$

Together with Equation 3.8, 3.9 and 3.10, the equilibrium voltage/open-circuit voltage (OCV) of the cell  $E_{\text{cell,eq}}$  at fully charged-state is given by the change in partial molar Gibbs free energy, thereby given by the activity of negative electrode material in positive electrode [35, 40, 50]:

$$E_{\text{cell,eq}} = -\frac{\Delta\bar{G}_{\text{cell}}}{zF} = -\frac{RT}{zF} \ln a_{\text{A(in liquid B)}} \quad (3.12)$$

where  $F$  is the Faraday constant and  $z$  is the valency or the number of transferred electrons.

Conceptually, the thermodynamic driving force/EMF for the cell is provided by the strong interaction between metal A and B. Since the activity of A in B  $a_{\text{A(in liquid B)}}$  can be extremely low (as low as  $10^{-10}$ ), LMB cells can achieve a high equilibrium voltage/OCV [35].

However, the potential of a cell through which a current flows differs from its equilibrium potential  $E_{\text{cell,eq}}$ , this phenomenon is termed as polarization and the difference is defined as overpotential (overvoltage)  $\eta$ . A positive and negative current always generates a positive and negative overpotential, respectively. In the majority of electrochemical cells, the overpotential can be classified into three main categories: ohmic overpotential ( $\eta_{\text{ohm}}$ ), mass

transport overpotential ( $\eta_{\text{mt}}$ ) and charge transfer overpotential ( $\eta_{\text{ct}}$ ). The overpotential of the cell is the summation of those three contributions. Therefore, the terminal voltage of cell  $E_{\text{cell}}$  can be expressed as [35, 50, 93–98]:

$$E_{\text{cell}} = E_{\text{cell,eq}} + \eta_{\text{ohm}} + \eta_{\text{mt}} + \eta_{\text{ct}} \quad (3.13)$$

### 3.3.1 Ohmic overpotential

Every electrochemical cell has an ohmic internal resistance, which consists of the resistance of the electrolyte  $R_{\text{E}}$ , the resistance of the current collector  $R_{\text{cc}}$  and the resistance of the leads  $R_{\text{leads}}$  [35, 95]. Thus, an electric current passing through a cell results in an ohmic overpotential and heat production. The ohmic overpotential of a cell is typically dominated by the electrolyte [96, 97].

The ohmic overpotential  $\eta_{\text{ohm}}$  follows Ohm’s Law, and it can be expressed as [97]:

$$\eta_{\text{ohm}} = IR_{\text{E}} + IR_{\text{cc}} + IR_{\text{leads}} \quad (3.14)$$

### 3.3.2 Mass transport overpotential

Mass transport overpotential  $\eta_{\text{mt}}$  is caused by the concentration gradient of the reactants and/or the products in the bulk electrolyte and at the positive electrode-electrolyte interface. This overpotential usually occurs at high current densities, when the cell reaction is sufficiently rapid while the mass transport is relatively slow [95, 96]. For LMB cells, the mass transport limitations in molten salts electrolyte is generally neglected due to the strong mixing induced by the internally heated convection in this region [97, 98]. In contrast, the concentrations at the positive electrode-electrolyte interface is influenced by the alloying and de-alloying of the negative electrode in positive electrode [97].

Nevertheless, considering the rapid mass transport rate owing to the LMB cells’ high operating temperature, even at high current densities, the mass transport overpotential of LMB cells is quite small and it is overshadowed by the relatively high ohmic overpotential brought by the electrolyte [98].

### 3.3.3 Charge transfer overpotential

Charge transfer overpotential  $\eta_{ct}$  occurs because of the potential energy barrier to the interfacial reaction. Since charge transfer in LMB cells is very fast thanks to the liquid-liquid interfaces, the charge transfer overpotential in LMB cells can be usually neglected ( $\eta_{ct} \approx 0$ ) [94–99].

## 3.4 Electrochemical methods

### 3.4.1 Galvanostatic Intermittent Titration Technique (GITT)

For batteries including LIBs, SIBs and our Na-based LMBs, during charging and discharging, Li-ions or Na-ions are transported from one electrode, through the electrolyte, to the other electrode. At the electrode surface, redox reaction of electroactive materials (Li-ions or Na-ions) with the electrode occurs and the products diffuse into the bulk electrode. Hence the battery performance primarily depends on the diffusion coefficient of electroactive materials in the electrode, which is of extreme importance.

Galvanostatic Intermittent Titration Technique (GITT) combines both transient and steady-state measurements to obtain both kinetic and thermodynamic parameters of electrode materials, e.g. diffusion coefficient. When compared to Potentiostatic Intermittent Titration Technique (PITT), GITT eliminates the customary problem of interference due to resistance polarization generated when potentiostatic technique is applied [100, 101].

As shown in Figure 3.3 (a), the GITT procedure is comprised of a series of constant current pulse steps (positive during charging and negative during discharging), each followed by a relaxation step, in which no current passes through the cell. Take charging (positive current pulse) as example, as illustrated in Figure 3.3 (b), when a positive current pulse is employed, the cell potential immediately jumps by a value equal to the  $iR$  drop, where  $R$  is the total internal resistance (ohmic resistance  $R_{ohm}$  and charge transfer resistance  $R_{ct}$ ). Afterwards, since the galvanostatic current pulse generates a concentration gradient

at the electrode-electrolyte interface, the cell potential slowly increases with time. When the current pulse is interrupted (at relaxation step), the composition of the electrode tends to become homogeneous by diffusion of electroactive species. Consequently, the cell potential first suddenly falls by a value equal to the  $iR$  drop, then it slowly decreases until the electrode is again in equilibrium (i.e., when  $dE/dt \sim 0$ ) and the open-circuit voltage (OCV) of the cell is reached. After that, the galvanostatic current pulse is applied again, followed by current interruption and the sequence of current pulse followed by a relaxation step is repeated until the cell is fully charged [101].

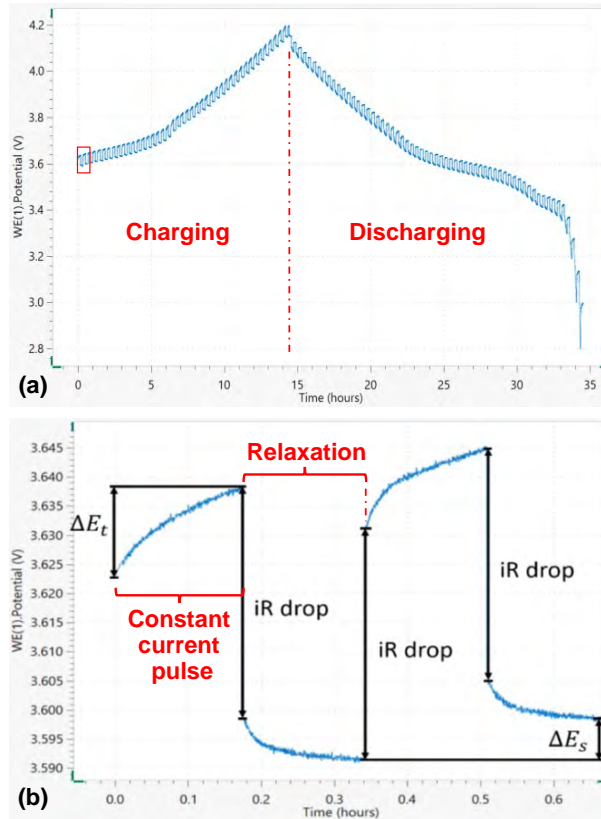


**Figure 3.3:** (a) Schematic illustration of a Galvanostatic Intermittent Titration Technique (GITT) curve vs. time, (b) Zoom-in shows the enlarged first two steps of GITT curve.

The chemical diffusion coefficient at each step can be calculated by the following formula:

$$D = \frac{4}{\pi} \left( \frac{IV_M}{z_A F S} \right)^2 \left[ \frac{dE}{d\delta} / \frac{dE}{d\sqrt{t}} \right]^2 \quad (3.15)$$

where  $I$  (A) is the applied current,  $V_M$  ( $\text{cm}^3/\text{mol}$ ) is the molar volume of the electrode,  $z_A$  is the charge number of electroactive species (for both Li-ions and Na-ions,  $z_A = 1$ ),  $F$  ( $9.648\,533\,212 \times 10^4$  C/mol) is the Faraday's constant and  $S$  ( $\text{cm}^2$ ) is the

electrode/electrolyte contact area (active reaction area),  $dE/d\delta$  is the slope of the coulometric titration curve, which can be obtained by plotting the steady-state equilibrium voltage  $E$  (V) against the electroactive material composition or the stoichiometric parameter after each galvanostatic titration step  $\delta$  and  $dE/d\sqrt{t}$  is the slope of the voltage versus the square root of the time during constant current pulse [100–102].

If a sufficiently small current is employed for short time intervals, the change of the steady-state equilibrium voltage over a single galvanostatic titration step  $\delta$  is small, hence  $dE/d\sqrt{t}$  can be considered linear, namely  $dE/d\sqrt{t} = \Delta E_t/\Delta\sqrt{t}$ , the coulometric titration curve can also be regarded as linear over the composition range involved in the titration step, in other words,  $dE/d\delta = \Delta E_s/\Delta\delta$ , therefore Equation 3.15 can be simplified into:

$$D = \frac{4}{\pi\tau} \left( \frac{n_M V_M}{S} \right)^2 \left( \frac{\Delta E_s}{\Delta E_t} \right)^2 \quad (3.16)$$

where  $\tau$  (s) is the duration of the current pulse,  $n_M$  (mol) is the number of moles,  $V_M$  (cm<sup>3</sup>/mol) is the molar volume of the electrode,  $S$  (cm<sup>2</sup>) is the electrode/electrolyte contact area (active reaction area),  $\Delta E_s$  is the change of the steady-state voltage over a single galvanostatic titration step due to the current pulse and  $\Delta E_t$  is the voltage change for applied constant current pulse for time  $\tau$ , eliminating the  $iR$  drop [100, 101, 103–105].

### 3.4.2 Galvanostatic Cycling with Potential Limitation (GCPL)

One of the most important behavior of batteries is the amount of charge stored and delivered during cycling, which is determined as a function of its charging and discharging conditions: a given current rate within a given potential range.

The Galvanostatic Cycling with Potential Limitation (GCPL), also referred to as cyclic chronopotentiometric technique, is the most widely applied technique to study battery behavior. A GCPL experiment is performed by applying a controlled-current between negative and positive electrodes, which is reversed after reaching the defined potential limit, the potential between the negative and positive electrodes as a function of time are recorded and the potential against capacity are plotted as well. It is important to note that, in a battery, in order to avoid irreversible processes like electrolyte

decomposition, the potential limitation must be carefully set. This limitation (electrochemical stability window) should be determined by other electrochemical methods such as Cyclic Voltammetry (CV). Additionally, the plot of potential against time can be effectively used to characterize multi-step redox reactions during the charging and discharging processes [105, 106].

With regards to galvanostatic cycling of batteries, the charge or discharge current is usually expressed as C-rate (C/h), at which a battery is completely charged or discharged, relatively to its nominal capacity. For example, a C-rate of 1 C is defined as the current to fully complete charging or discharging in one hour. A C-rate higher than 1 C/h means a faster charge or discharge while a C-rate smaller than 1 C/h means a slower charge or discharge. Except for C-rate, the applied current in GCPL measurement is commonly normalized to the mass of active materials or the area of the electrodes, depending on whether gravimetric ( $\text{mA h cm}^{-2}$ ) or areal capacity ( $\text{mA h g}^{-1}$ ) is emphasized. Gravimetric capacity ( $\text{mA h g}^{-1}$ ) is more commonly used in battery tests, and the current is normalized to specific current ( $\text{A g}^{-1}$ ) [105].

The capacity  $Q$  (Ah) during charging and discharging can be calculated by multiplying the current  $I$  (A) by the duration  $t$  (s) of a single charging or discharging step, and divided by the conversion factor between seconds and hours 3600 (s/h):

$$Q = \frac{I \cdot t}{3600} \quad (3.17)$$

Efficiency values are of high interest to evaluate the lifetime of a battery in respect of the charge sustainability. Coulombic efficiency  $\eta_C$ , also called faradaic efficiency or current efficiency is the ratio between the discharge capacity and the former charge capacity:

$$\eta_C = \frac{Q_{\text{discharge}}}{Q_{\text{charge}}} \times 100 \% \quad (3.18)$$

The voltaic efficiency  $\eta_V$  is associated with the average discharge voltage  $E_{\text{discharge}}$  and the average charge voltage  $E_{\text{charge}}$ :

$$\eta_V = \frac{E_{\text{discharge}}}{E_{\text{charge}}} \times 100 \% \quad (3.19)$$

The round-trip efficiency or the energy efficiency  $\eta_E$  is defined as the ratio of the total

energy output to the total energy input, i.e., the product of those two efficiencies [105]:

$$\eta_E = \frac{\text{Total energy output}}{\text{Total energy input}} \times 100 \% = \frac{E_{\text{discharge}} Q_{\text{discharge}}}{E_{\text{charge}} Q_{\text{charge}}} \times 100 \% \quad (3.20)$$

### 3.4.3 Electrochemical Impedance Spectroscopy (EIS)

Like resistance  $R$  ( $\Omega$ ), impedance  $Z$  ( $\Omega$ ) is a measure of an electrical system's ratio of voltage to the electrical current, however, unlike resistance, it is not limited by ideal resistor under Ohm's Law (for example, no phase-shift and independence of frequency).

Electrochemical Impedance Spectroscopy (EIS) is usually performed by applying an alternating signal (voltage or current) over a wide frequency range with a single and small amplitude to an electrochemical cell as excitation and measuring the cell response (voltage signal: current response; current signal: voltage response) to the applied excitation signal at steady-state as a function of the excitation frequency. An example of voltage excitation and current response is illustrated in Figure 3.4, in order to simplify the impedance analysis, the amplitude of the applied excitation signal should be small enough so that the response signal is pseudo-linear. If a sinusoidal voltage excitation is applied, the response to this voltage signal is an AC signal, which can be analyzed as a sum of sinusoidal functions (a Fourier series). In a linear (or pseudo-linear) system, the current response to a sinusoidal voltage is sinusoidal at the same frequency but with a phase-shift (Figure 3.5) [105–107].

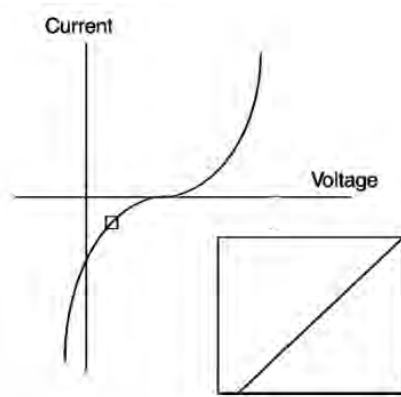


**Figure 3.4:** Current-voltage curve; Zoom-in shows the pseudo-linearity of an electrochemical cell with a small voltage excitation.

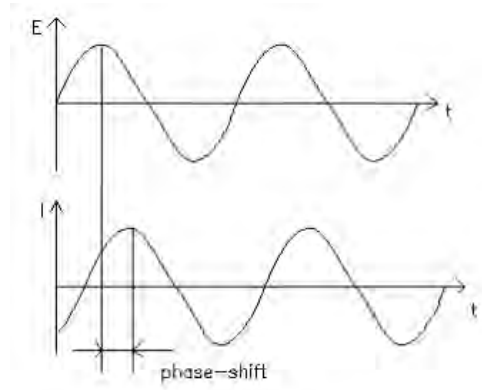


**Figure 3.5:** Sinusoidal current response to a sinusoidal voltage excitation in a linear (or pseudo-linear) system.

The sinusoidal voltage excitation as a function of time  $t$  can be expressed as:

$$E_t = E_0 \sin(\omega t) \quad (3.21)$$

where  $E_t$  is the voltage at time  $t$ ,  $E_0$  is the amplitude of the excitation signal and  $\omega$  (rad/s) is the angular frequency (also known as radial frequency or circular frequency), which equals  $2\pi$  times the conventional frequency (Hz).

The response current signal  $I_t$  can be represented as:

$$I_t = I_0 \sin(\omega t - \phi) \quad (3.22)$$

The impedance  $Z_t$  can be expressed analogous to Ohm's Law, in terms of a magnitude  $Z_0$  and a phase shift  $\phi$ :

$$Z_t = \frac{E_t}{I_t} = \frac{E_0 \sin(\omega t)}{I_0 \sin(\omega t - \phi)} = Z_0 \frac{\sin(\omega t)}{\sin(\omega t - \phi)} \quad (3.23)$$

With Euler's formula ( $j = \sqrt{-1}$ ):

$$\exp(j\phi) = \cos \phi + j \sin \phi \quad (3.24)$$

The impedance as a function of frequency  $\omega$ , which is composed of a real part and an imaginary part, can be expressed as a complex function:

$$Z(\omega) = \frac{E_t}{I_t} = Z_0 \exp(j\phi) = \frac{E_0 \exp(j\omega t)}{I_0 \exp(j\omega t - \phi)} = Z_0(\cos \phi + j \sin \phi) \quad (3.25)$$

Generally, EIS data are displayed in two ways: Nyquist plot and Bode plot. In a Nyquist plot, the data from each frequency point is plotted by the real part of impedance on the abscissa and the negative imaginary part of impedance on the ordinate. The impedance can be illustrated as a vector with length  $|Z|$  in Nyquist plot, the angle  $\phi$  between this vector and X-axis is the phase-shift (see Figure 3.6). However, Nyquist plot has one major drawback, namely the applied frequency on each point is missing [105–107].

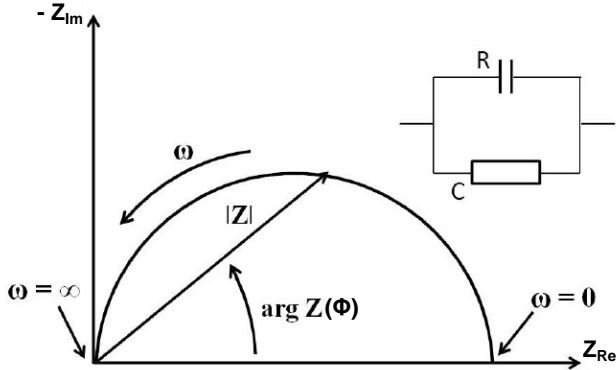


**Figure 3.6:** Nyquist plot with impedance vector and the corresponding equivalent electrical circuit with one time constant.

By contrast, another common plot method, Bode plot (seen in Figure 3.7), in which the absolute value of the amplitude  $|Z|$  and phase-shift  $\phi$  of impedance are plotted against the logarithm of frequency, shows the frequency information [105–107].

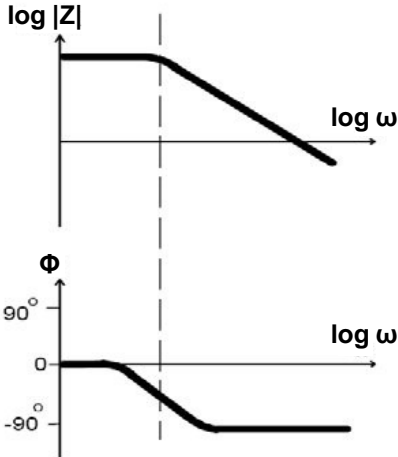


**Figure 3.7:** Bode plot with one time constant.

Generally speaking, EIS data are analyzed by fitting an equivalent electrical circuit (EEC) model (as the electrical circuit in Figure 3.6), which consists of a combination of common

circuit elements including resistors, capacitors and inductors [105–107]. The properties of those common circuit elements are listed in Table 3.1.

**Table 3.1:** Properties of common circuit elements.

Components	Current vs. Voltage	Impedance
Resistor	$E = IR$	$Z = R$
Inductor	$E = LdI/dt$	$Z = j\omega L$
Capacitor	$I = CdE/dt$	$Z = 1/j\omega C$

EEC models are comprised of combinations of those elements in series and/or in parallel. The total impedance of the circuit elements in series is the sum of their individual values (Equation 3.26), as the calculation of overall resistance for ideal resistors in electrical circuit. And for elements in parallel, the inverse of the total impedance is the sum of the reciprocals of each individual impedance (Equation 3.27) [106].

$$Z_{\text{total}} = Z_1 + Z_2 + Z_3 + \dots \quad (3.26)$$

$$\frac{1}{Z_{\text{total}}} = \frac{1}{Z_1} + \frac{1}{Z_2} + \frac{1}{Z_3} + \dots \quad (3.27)$$

Moreover, those elements should correspond to physical and electrochemical processes of the system, such as electrolyte resistance, double layer capacitance formed at electrode-electrolyte interface, polarization resistance, charge transfer resistance and etc.. Other elements which are not analogous to ideal electrical circuit elements, are not listed in Table 3.1. However, those elements including constant phase elements (CPEs) and Warburg impedance, which models the behavior of imperfect capacitor and the linear diffusion of active species, respectively, can still be employed to analyze EIS data [105–107].

The impedance of a constant phase element (CPE) can be expressed as:

$$Z_{\text{CPE}} = \frac{1}{(j\omega)^n Y_0} \quad (3.28)$$

where  $0 < n < 1$  is an exponent (for capacitors,  $n = 1$ ) and  $Y_0$  (additance parameter) is the numerical value of admittance  $Y$  (inverse impedance,  $Y = 1/Z$ ) at  $\omega = 1$  rad/s [107].

As for Warburg impedance, whose value strongly depends on the frequency of the applied signal, its value is quite small at high frequencies ( $\omega \rightarrow \infty$ ) because of the insufficient

time for diffusion, by contrast, it increases at lower frequencies (longer time for farther diffusion).

For “infinite” diffusion (diffusion layer thickness  $\delta \rightarrow \infty$ ), the “infinite” Warburg impedance can be represented as:

$$Z_W = \frac{1}{Y_0 \sqrt{j\omega}} \quad (3.29)$$

However, the diffusion in reality usually possesses an finite thickness, hence the Warburg impedance is finite, and the “finite” Warburg impedance can be expressed as:

$$Z_W = \frac{\tanh B \sqrt{j\omega}}{Y_0 \sqrt{j\omega}} \quad (3.30)$$

where  $Y_0$  is the addittance parameter (as in Equation 3.28) [107] and  $B$  is a parameter which is related to the diffusion layer thickness  $\delta$ , active species’ diffusion coefficients  $D$  and frequency  $\omega$ :

$$B = \tanh \left( \delta \sqrt{\frac{j\omega}{D}} \right) \quad (3.31)$$

One of the most frequently used equivalent electrical circuit (EEC) for EIS data analysis, the Randles circuit, is shown in Figure 3.8 (a), where  $R_\Omega$  is the internal resistance,  $C_{dl}$  is the double layer capacitance,  $R_{ct}$  is the charge transfer resistance and  $Z_W$  is Warburg impedance, which is generated due to the linear diffusion (mass transfer) of electroactive species and is inversely proportional to the square root of frequency. Due to the fact that the diffusion of electroactive species is not an instantaneous process, when the frequency of applied signal is high enough, the concentration of electroactive species can be considered as constant, thereby the Warburg impedance makes almost no contribution to the total impedance [105–107]. On a Nyquist plot, the Warburg impedance appears as a diagonal line with a slope of  $45^\circ$  (Figure 3.8 (b)). On a Bode plot, the Warburg impedance exhibits a phase shift of  $45^\circ$ .

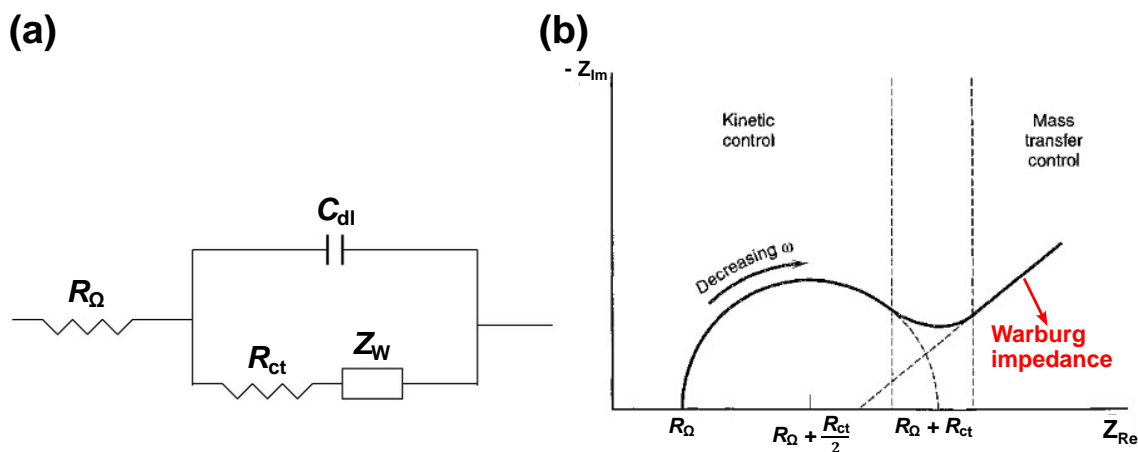


**Figure 3.8:** Schematic of (a) Randles circuit and (b) its corresponding EIS data [106, 107].

### 3.5 Material characterization methods

#### 3.5.1 X-Ray diffraction (XRD)

X-ray diffraction (XRD) is a rapid, non-destructive, analytical technique to investigate the fine structure of matter based on the wave-particle duality of X-rays [108–110].

The working principle of XRD is the well known Bragg's Law for constructive interference (Figure 3.9):

$$n\lambda = 2d \sin \theta \quad (3.32)$$

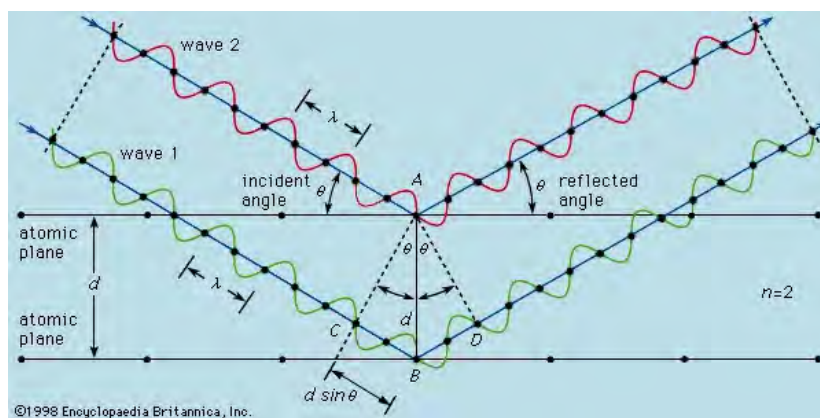


**Figure 3.9:** Bragg' Law for constructive interference.

where  $n$  is a positive integer,  $\lambda$  is the wavelength of incident X-rays,  $d$  is the interplanar distance of the crystal and  $\theta$  is the angle of incidence of the X-ray (between the incident beam and the particular crystal planes) [108–110].

An X-ray diffractometer consists of three main components: an X-ray tube (as X-ray source), a sample stage (to hold sample) and an X-ray detector. In a Bragg-Brentano reflection geometry (see Figure 3.10), the X-ray source is fixed and focused on the sample's surface at the angle of  $\theta$ , while the detector opposite the source is set at the angle of  $2\theta$ . During the XRD tests, both the stage and detector rotate about an axis through the center of diffractometer precisely to maintain the  $\theta/2\theta$  geometry. The increase of incident angle of X-ray may cause diffraction happening on dedicated crystal planes [108].

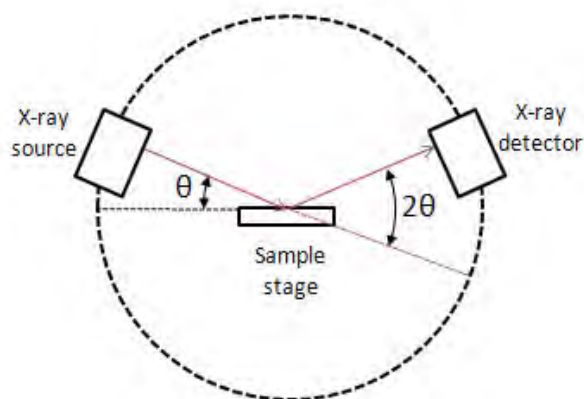


**Figure 3.10:** Schematic arrangement of XRD diffractometer components.

### 3.5.2 Inductively coupled plasma optical emission spectroscopy (ICP-OES)

Inductively coupled plasma optical emission spectroscopy (ICP-OES), also known as inductively coupled plasma atomic emission spectroscopy (ICP-AES), is one of the most powerful analytical technique to determine the trace elements in a myriad of sample types, which utilizes the spontaneous emission of photons from atoms and ions that have been excited in a radio frequency (RF) discharge [111].

A representation of the layout of a typical ICP-OES instrument is depicted in Figure 3.11. Liquid and gas samples can be injected directly into the torch tube by the pump through the nebulizer and the spray chamber with the help of argon gas while solid samples require extraction or acid digestion so that the analytes can be present in a solution, which is converted into an aerosol (known as nebulization) and directed into the central channel of the plasma [111, 112].



selectivity, reproducibility, long-term stability, limit of detection (LOD) and accuracy. Almost all naturally occurring elements can be determined by ICP-OES except for hydrogen (H), oxygen (O), fluorine and inert gases [111].

### 3.5.3 Laser-induced breakdown spectroscopy (LIBS)

Laser-induced breakdown spectroscopy (LIBS), also referred to as laser-induced plasma spectroscopy (LIPS) or laser spark spectroscopy (LSS), is one method of atomic emission spectroscopy (AES) which utilizes a highly energetic laser pulse as the excitation source to determine the elemental composition of a sample [113–116].

The schematic LIBS set-up is shown in Figure 3.12. A short duration laser pulse (ca. 5 ns or shorter) of sufficient energy is generated and focused onto the surface of a sample. The generation of the plasma only begins when the energy of the laser pulse achieves a certain threshold (breakdown energy), which generally depends on the environment and the target material. As a result, in the first instant, the atomic or molecular structure of the sample is heated and broken by the plasma, and a small amount of the materials (from hundreds of ng to a few  $\mu\text{g}$ , which may contain free neutral atoms, ions, molecular fragments and free electrons) is vaporized. The high temperature plasma ( $> 10000$  K) in which the vaporized species can be excited, is maintained by the continuous incoming energy of the same laser pulse. The excited species will by electromagnetic radiation come back to their less energetic non-excited status. A portion of the electromagnetic radiation, whose wavelengths is characterisitc for a specific species and whose intensity is proportional to their content in the sample, is collected and detected [113–116]. Each firing of the laser produces a single LIBS measurement, however, the signals from many laser pulse are generally added or averaged in order to increase accuracy and precision of the measurement and to average out non-uniformities in sample composition [114].

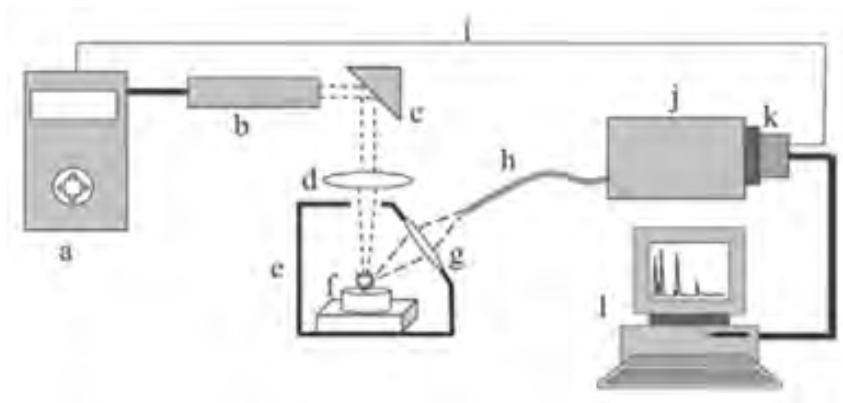


**Figure 3.12:** Schematic set-up of a LIBS system. Here (a) = laser source and cooler, (b) = pulsed laser head, (c) = mirror, (d) = focusing lens, (e) = excitation chamber, (f) = sample, (g) = collecting optics, (h) = optical fiber, (i) = detector trigger signal, (j) = wavelength selector, (k) = detector array and (l) = PC.

When compared with many other types of elemental analysis, LIBS is a relatively appealing technique which possesses many advantages including no need for sample preparation, which avoids further contamination of the sample to be analyzed, fast analysis process, a wide range of applications for both conductive and non-conductive samples, regardless of their physical states, i.e., aerosols, gases, liquids or solids. Especially, LIBS is applicable to the analysis of extremely hard materials which are difficult to digest or dissolve, such as ceramics and semi-/superconductors as well as biological samples. Its capability of simultaneous multielement determination, localized microanalysis and surface analysis is of great importance as well [115, 116].

#### 3.5.4 Scanning electron microscope (SEM) with energy-dispersive X-ray spectroscopy (EDS)

The schematic representation of a scanning electron microscope (SEM) is illustrated in Figure 3.13, a typical SEM consists of several systems including vacuum pump, electron gun, several electromagnetic lenses and relevant signal detectors [117].

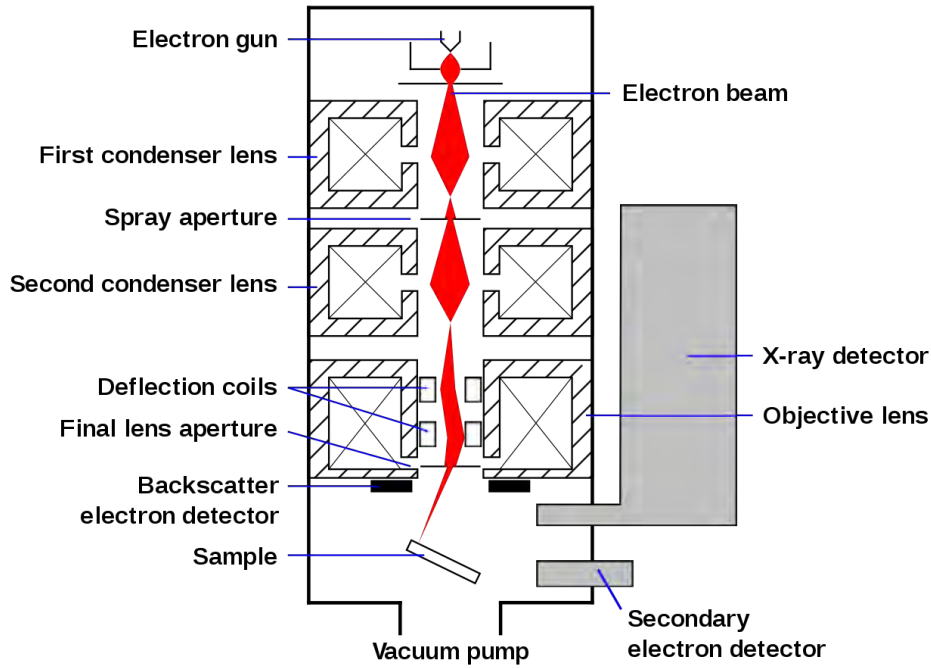


**Figure 3.13:** Schematic representation of a SEM.

A SEM investigates the surface morphology and composition of the sample through different types of signals generated by the interactions of the incident electron beam with atoms at various depths within the sample [117].

The electron beam has a kinetic energy ranging from 0.2 to 40 keV and interacts with the matter at different depths in a teardrop-shape (Figure 3.14), which results in the generation of various signals including secondary electrons (SEs), reflected or back-scattered electrons (BSEs), auger electrons (AEs), characteristic energy-dispersive X-ray spectroscopy (EDS), cathodoluminescence (CL), transmitted electrons and so on [117, 118].

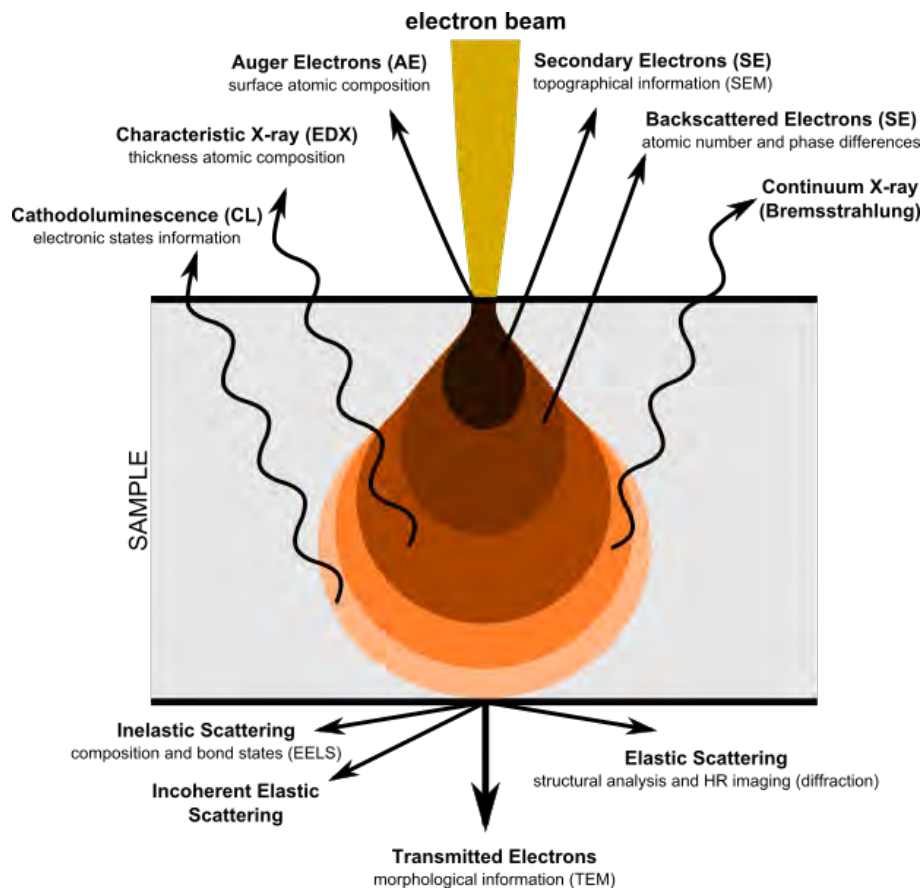


**Figure 3.14:** Electron-matter interactions: various types of signals generated at different depths in a SEM.

Since the SEs are generated only within a very small depth ( $< 2$  nm) below the matter's surface, SE image mainly reveals the surface topography whereas BSE image shows contrast due to the variations in chemical composition of the sample. BSE image exhibit high sensitivity to differences in atomic number: the higher the atomic number, the brighter the material appears in the image [117, 118].

Information about the elemental composition of the sample can be obtained by detecting the characteristic energy-dispersive X-ray spectroscopy (EDS), usually called as EDX or EDXS as well, which is a technique carried out in the SEM to identify the elemental composition of materials based on the energy spectrum of the characteristic X-rays (see Figure 3.9) generated by electron beam irradiation [117, 118].

EDS is a very useful technique, however, it still has some shortcomings, including the inability for elements with a low atomic number (detection limits), such as hydrogen (H) and lithium (Li) due to its detection limits [119].

For conventional samples in SEM, they should be electrically conductive, or at least conductive at the surface to avoid scanning faults and other image artifacts. One solution to the charging problem of those non-conductive samples is the coating of the sample surface with an ultra-thin film of metal, such as gold (Au) or platinum (Pt) or conductive carbon [118].

All specimens obtained in the following sections were cut, embedded in epoxy resin, ground and polished in order to get the cross-sections. Afterwards, those cross-sections were coated by a thin gold film for the analysis in SEM with EDS.

## 4 Material compatibility

### 4.1 Static corrosion tests for NCC and electrical insulator materials

#### 4.1.1 Material selection

As illustrated in Figure 3.2, in both designs of a LMB cell, the electrical insulator between NCC and PCC has no direct contact to any active cell components. Nevertheless, it is exposed either to molten salts electrolyte vapor (Figure 3.2 (a)) or to negative electrode (Na) vapor (Figure 3.2 (b)).

The direct contact between NCC and negative electrode or molten salts electrolyte atop can be easily avoided by adding another conductive connecting part in between. Thus, in the ideal case, NCC will like the electrical insulator, be merely exposed to the molten salts electrolyte vapor (Figure 3.2 (a)) or to the negative electrode (in this case, Na) vapor (Figure 3.2 (b)).

Since the active cell components (especially Na and salts) are sensitive to oxygen and moisture, the dielectric sealing material and its bond to the NCC material need to be gas-tight [35, 51]. The hermetic sealing needs to be thermally/chemically stable and thermo-mechanically robust. Moreover, dielectric break and NCC material need to be corrosion resistant to vapors from molten salts electrolyte (design in Figure 3.2 (a)) and from sodium (design in Figure 3.2 (b)). Additionally, for grid-scale application, their cost must be moderate, or at least acceptable [35].

Considering about all the criteria mentioned before, obviously, the most appropriate candidates for electrical insulator are dielectric ceramics, the possibly suitable candidates for NCC are conductive metallic materials (metal, steels and alloys). However, for bonds between dissimilar materials (in this case, a ceramic-metal joint), it is well known that a coefficient of thermal expansion (CTE) mismatch may result in detrimental influence on joint strength and cause joint reliability issues through the formation of residual stresses upon cooling [120, 121].

The level of residual stresses in the close vicinity of the interface between two adjacent materials 1 and 2 can be roughly expressed by Equation 4.1, provided that the materials only deform elastically (reasonable for ceramics) and the stresses generated on both sides of the reaction layer do not interfere with each other [120–122]:

$$\sigma_1 = -\sigma_2 = \frac{E_1 E_2}{E_1 + E_2} (\alpha_1 - \alpha_2) (T_B - T_0) \quad (4.1)$$

where  $E$  is Young's modulus,  $\alpha$  the coefficient of thermal expansion,  $T_B$  the brazing temperature and  $T_0$  the temperature of the surroundings (normally the room temperature).

Considering that the coefficients of thermal expansion of ceramics are generally much lower than metals and steels, following methods are usually utilized to reduce the residual stress between a ceramic-metal joint [121, 123]:

- (1) Using metallic materials whose coefficients of thermal expansion are close to ceramics.
- (2) Using soft metallic materials, which possess low Young's modulus.
- (3) Using composite interlayer consisting of a softer metal with low Young's modulus and another metal with a coefficient of thermal expansion close to that of ceramic, which is a combination of merits of (1) and (2).
- (4) Joining under low temperature.
- (5) Heat treatment after joining.
- (6) Appropriate configuration of the joint.

Table 4.1 lists the Young's modulus  $E$  and coefficients of thermal expansion  $\alpha$  of various dielectric ceramics and metallic materials. It can be seen from this table that in contrast with common iron and stainless steels, copper (Cu), Invar alloy and Kovar alloy are much more promising candidates to be applied in a ceramic-metal joint.

**Table 4.1:** Young’s modulus  $E$  and coefficients of thermal expansion  $\alpha$  of various dielectric ceramics and metallic materials [120, 124–127].

	Material	Young’s modulus (GPa)	Coefficient of thermal expansion ( $10^{-6}/^{\circ}\text{C}$ )
Dielectric ceramics	$\text{Al}_2\text{O}_3$	380	7.2 – 8.1
	MgO	83 – 205	13.3 – 13.5
	BN	34 – 76	7.5
	AlN	317 – 346	4.2 – 5.3
	$\text{Si}_3\text{N}_4$	250 – 294	2.3 – 3.7
Metals, steels and alloys	Iron	210	12.1 – 12.6
	Stainless steel 304	190 – 200	17.3
	Cu	110	16.4 – 17.2
	Invar alloy	147	2.0
	Kovar alloy	147	6.0

Due to the lack of knowledge, the corrosion behavior of the five electrical insulator materials ( $\text{Al}_2\text{O}_3$ , MgO, BN, AlN and  $\text{Si}_3\text{N}_4$ ) and three conductive materials (Cu, Ni42 Invar alloy and 4J33 Kovar alloy) were studied in Na vapor and in molten salts vapor (LiCl-NaCl-KCl: 61-3-36 mol.%) at the temperature of 450 °C up to 750 h, respectively, in order to investigate their potential to be applied as electrical insulator and NCC of a ceramic-metal joint for Na-based LMBs, with the aim of realizing low-temperature and low-cost Na-based LMBs with good electrochemical performance and long lifetime.

#### 4.1.2 Experiments

##### Materials and preparation of specimens

The test specimens in this experiment were  $\text{Al}_2\text{O}_3$  (8 mm in diameter, Friedrichsfeld GmbH), MgO (2 mm thick, 99 %, SITUS Technicals GmbH), BN (15 mm in diameter, ESK Ceramics GmbH & Co.KG), AlN (2 mm thick, Gieß-Technische-Sonderkeramik GmbH & Co. KG) and  $\text{Si}_3\text{N}_4$  (2 mm thick, Gieß-Technische-Sonderkeramik GmbH & Co.KG), Cu (2 mm thick, Workshop/KIT), Ni42 Invar alloy (5 mm in diameter, KYOCERA Fin ceramics Solutions GmbH) and 4J33 Kovar alloy (2 mm thick,

Dongguan Saijing special alloy Co. Ltd.).

The composition of Ni42 Invar alloy and 4J33 Kovar alloy are listed in Table 4.2.

**Table 4.2:** Composition of Ni42 Invar alloy and 4J33 Kovar alloy (in wt.%).

Material	C	Co	Cr	Ni	Mn	Si	P	S	Fe
Ni42	$\leq 0.05$	/	$\leq 0.30$	41.00 – 43.00	$\leq 0.80$	$\leq 0.30$	$\leq 0.02$	$\leq 0.02$	Bal.
4J33	$\leq 0.05$	14.00 – 15.20	/	32.10 – 33.60	$\leq 0.50$	$\leq 0.30$	$\leq 0.02$	$\leq 0.02$	Bal.

All specimens were cut into appropriate size; particularly, before exposure, all metallic specimens were ground by sandpaper with a grid size of 800 and 1200, successively, then cleaned in ethanol and distilled water.

### Test facility

The corrosion tests were done in a stainless steel container as shown in Figure 4.1. To evaluate the corrosion behavior of those specimens, all specimens were fixed on a stainless steel fastening disc by Mo-wires. After that, the fastening disc was screwed to a stainless steel cover, which was sealed to the stainless steel container which containing liquid Na and liquid salts mixture, respectively.

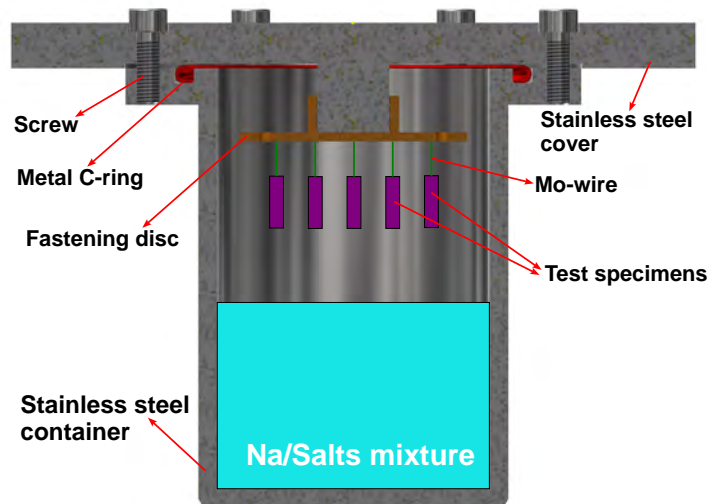


**Figure 4.1:** Schematic illustration of test specimens in a stainless steel container for corrosion tests for NCC materials.

## **Pre-treatment of test medium**

The used sodium was gained by melting the elementary Na block (99.8 % purity) delivered by Haines & Maassen Metallhandels-gesellschaft GmbH. To purify the liquid Na used for corrosion test, a stainless steel sink equipped with heating system and temperature regulator was used. Considering that both sodium oxide and sodium peroxide are denser than liquid Na, the spout of the sink is installed in the middle to ensure that only purest liquid Na can flow out of the sink for the corrosion test.

After melting the sodium blocks at 130 °C in the sodium sink in order to minimize the oxygen content in liquid Na [72, 128], 56.7 g liquid Na was poured into the stainless steel container for corrosion tests in Na vapor.

The LiCl-NaCl-KCl salts mixture was prepared with the composition of 61-3-36 mol.%, which was gained by mixing the individual salts LiCl (anhydrous, purity: 99.9 %, Apollo Scientific), NaCl (anhydrous, free-flowing, purity:  $\geq 99.0$  %, Honeywell) and KCl (purity:  $\geq 99.5$  %, Sigma-Aldrich) in their power form. 150 g LiCl-NaCl-KCl (61-3-36 mol.%) salts were mixed in a stainless steel-crucible for the corrosion test, followed by dehydration at 110 °C and 300 °C for 30 min each. After that, the salts mixture (covered by a ceramic cover) was heated to 600 °C until the salts mixture totally melted.

## **Test procedures**

The pre-treatment of both Na and the molten salts, the assembly of the test container and the implementation of corrosion tests were performed in a glovebox under argon atmosphere, whose oxygen level and moisture level were both less than 0.1 ppm.

The sealed stainless steel container was then heated by a heating sleeve with temperature regulator to a constant temperature of 500 °C and isothermally hold for 750 h.

First of all, the vapor pressure of Na and molten salts at test temperature must be determined to ensure that the specimens were actually exposed in vapor from Na and in vapor from molten salts, respectively.

According to the research of J.K. Fink and L. Leibowitz [129], the vapor pressure of Na

was measured as 0.79 Torr and 7.05 Torr at 427 °C and at 527 °C, respectively. Hence, the vapor pressure of Na should fall in between those two values.

As for molten salts, the vapor pressure of LiCl was determined as  $1.690 \times 10^{-3}$  Torr at 527 °C [130], the vapor pressure of NaCl was measured as  $8.003 \times 10^{-4}$  Torr at 587 °C [131] and the vapor pressure of KCl was measured as  $6.98 \times 10^{-4}$  Torr at 626 °C [132]. Neither vapor pressure of each alkali halide salt nor the vapor pressure of LiCl-NaCl-KCl mixture (61-3-36 mol.%) at 500 °C is available to us.

### **Post-test analysis**

After 750 h exposure, all specimens were extracted from the stainless steel container, cleaned by distilled water and ethanol, then dried by compressed air. The phase composition of specimens was analysed by X-ray diffraction (XRD) analysis. The surface morphology and cross-sections of specimens were analysed by scanning electron microscope (SEM) with energy-dispersive X-ray spectroscopy (EDS).

#### **4.1.3 Results**

The appearance of all specimens after exposure in Na vapor and in molten salts vapor at 750 °C for 750 h, respectively, are shown in Table 4.3. To present the results better, the materials are classified by their chemical compositions.

Obviously, as shown in Table 4.3, regardless of exposure in Na vapor or in molten salts vapor, all test specimens' surface was more or less darkened. The surface appearance change verified the existence of Na vapor and molten salts vapor, which was confirmed by the surface morphology of specimens in the following text. Compared with the specimens exposed in molten salts vapor, after exposure, the color change of the specimens in Na vapor is much severer.

**Table 4.3:** Appearance of all specimens after exposure in sodium vapor and in molten salts vapor at 450 °C for 750 h.

Group	Specimen	Raw material before exposure	After exposure in sodium vapor	After exposure in molten salts vapor
Oxide ceramics	Al <sub>2</sub> O <sub>3</sub>			
	MgO			
Nitride ceramics	BN			
	AlN			
	Si <sub>3</sub> N <sub>4</sub>			
Pure metal	Cu			
Alloys	Ni42 Invar alloy			
	4J33 Kovar alloy			

## XRD analysis

The XRD analysis results of all specimens before exposure, after exposure in sodium vapor and after exposure in molten salts vapor of all test specimens are shown in Figure 4.2.

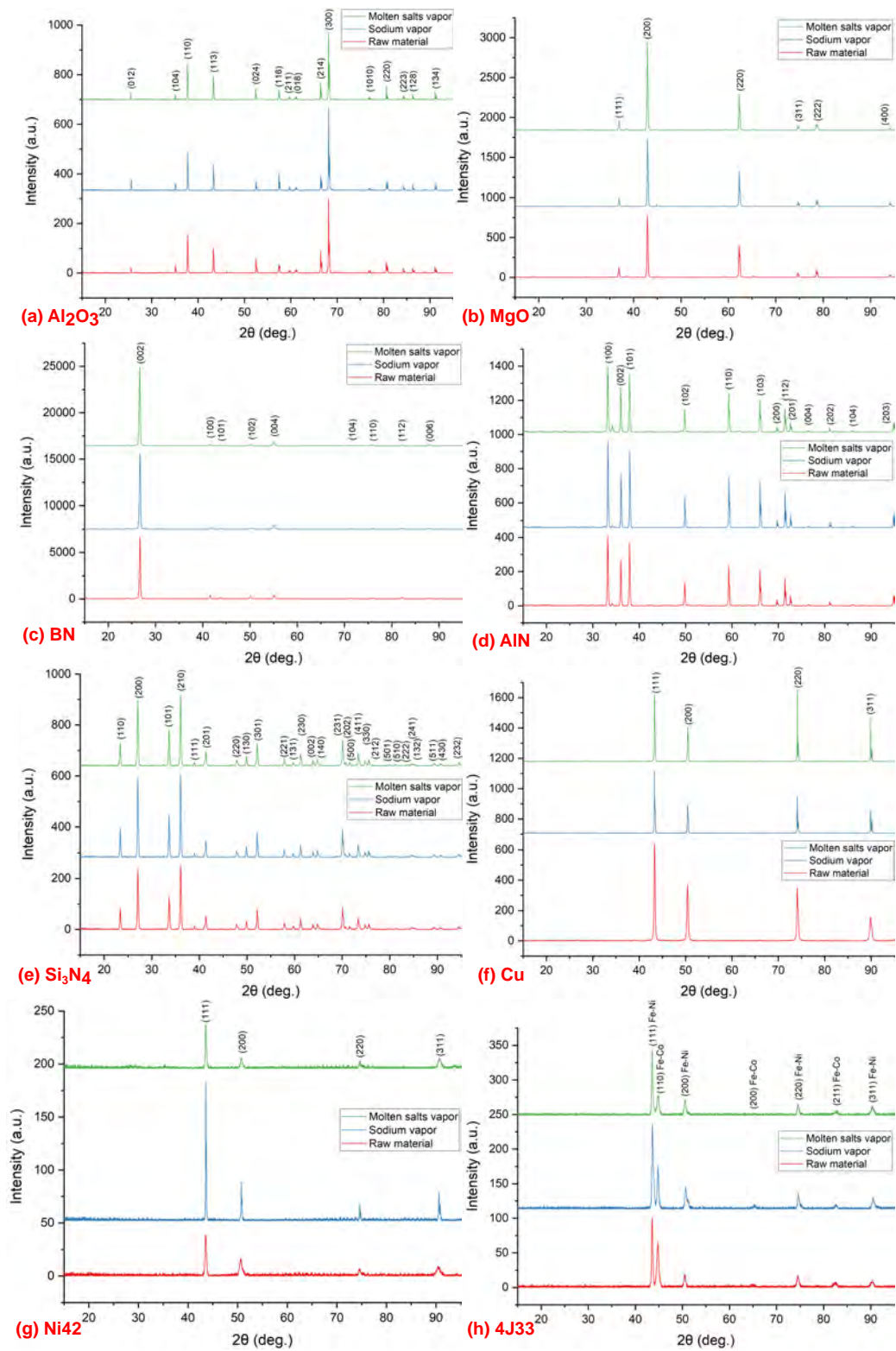


**Figure 4.2:** XRD results of (a)  $\text{Al}_2\text{O}_3$  specimen, (b) MgO specimen, (c) BN specimen, (d) AlN specimen, (e)  $\text{Si}_3\text{N}_4$ , (f) Cu specimen, (g) Ni42 Invar alloy specimen and (h) 4J33 Kovar alloy specimen before exposure, after 750 h exposure in sodium vapor at 450 °C and after 750 h exposure in molten salts vapor at 450 °C.

It can be seen from all images in Figure 4.2 that for all specimens before exposure, after exposure in sodium vapor and after exposure in molten salts vapor, their XRD patterns remain the same in a conventional  $\theta/2\theta$  analysis. This verifies that the bulk crystal structure of all specimens remained the same before and after exposure and that any potential reactions with the vapors occurred to an extent below the detection limit.

After investigating the potential changes of the structure by high-resolution XRD, high-resolution scanning electron microscope (SEM) with EDS was performed on the surface and cross-sections of those test specimens.

### SEM analysis with EDS

SEM images of surface morphology and cross-sections of test specimens before and after exposure are illustrated and analysed in three groups: oxide ceramics, nitride ceramics and metallic specimens.

Figure 4.3, 4.4 and 4.5 show the surface morphology of oxide ceramic, nitride ceramic and metallic specimens for NCC materials before exposure, after exposure in sodium vapor and after exposure in molten salts vapor, respectively.

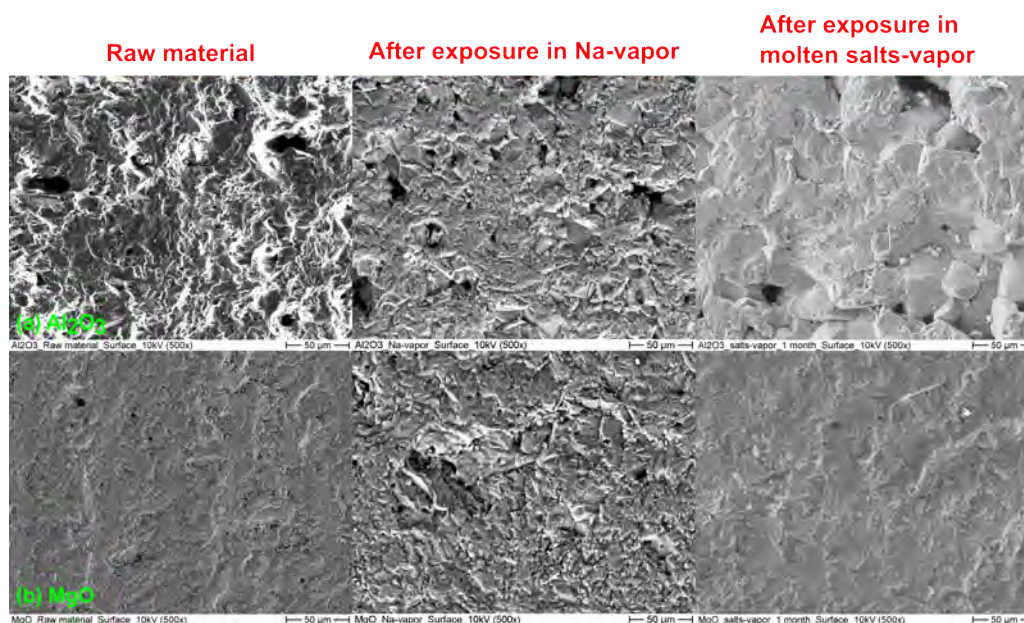


**Figure 4.3:** SE images of surface morphology of oxide ceramic specimens: (a) Al<sub>2</sub>O<sub>3</sub> and (b) MgO before exposure, after 750 h exposure in sodium vapor and after 750 h exposure in molten salts vapor.

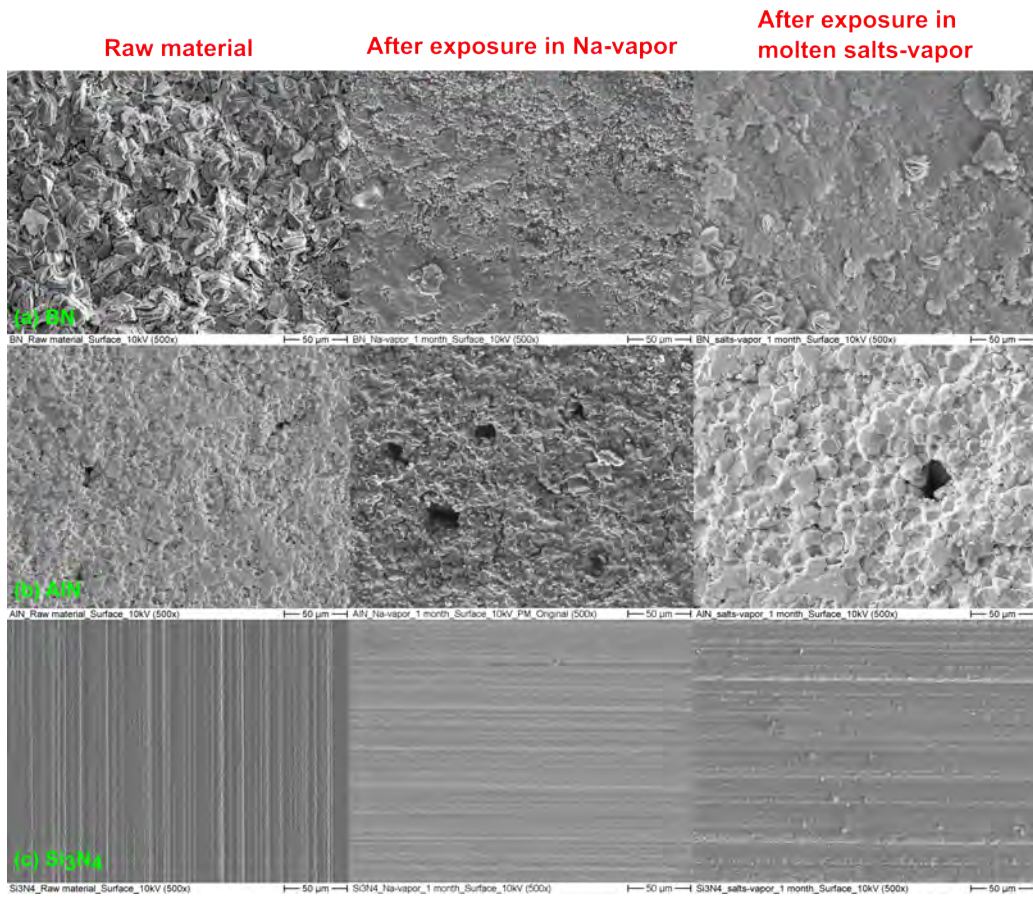


**Figure 4.4:** SE images of surface morphology of nitride ceramic specimens: (a) BN specimen, (b) AlN and (c) Si<sub>3</sub>N<sub>4</sub> after 750 h exposure in sodium vapor and after 750 h exposure in molten salts vapor.

According to Figure 4.3 and 4.4, it is easy to find out that the surface defects (e.g., pits and small holes) on the surface of ceramic specimens appear both before and after exposure, which indicates that they might be generated during ceramic fabrication or sample preparation, not due to the exposure in sodium vapor or in molten salts vapor.

It can be seen from Figure 4.5 that only some white particles appeared on Ni42 Invar alloy's surface after exposure in molten salts vapor. According to the point measurement, a extremely high amount of oxygen, the same amount of iron but almost no nickel can be detected on some of the white particles. Some other particles show a high amount of oxygen but less iron and less nickel. Therefore, those particles might be the impurities (oxides) generated during the exposure due to the existence of oxygen and moisture in salts mixture.

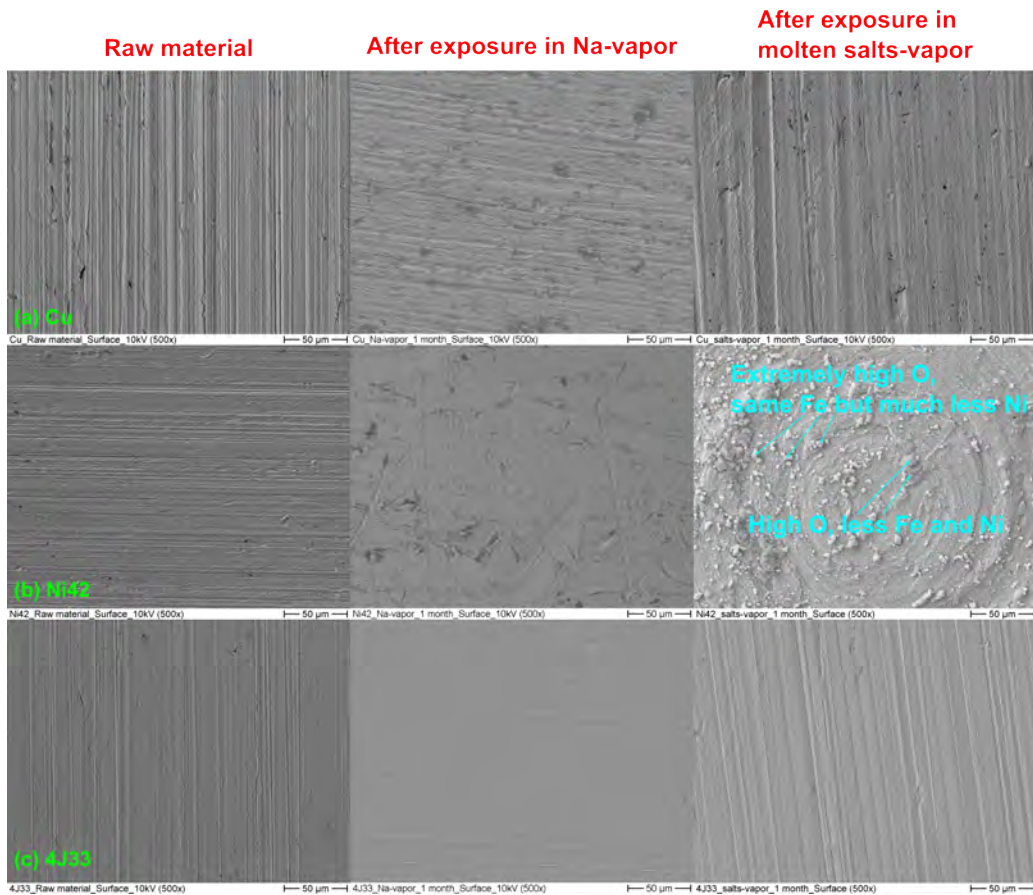


**Figure 4.5:** SE images of surface morphology of metallic specimens: (a) Cu, (b) Ni42 Invar alloy and (c) 4J33 Kovar alloy before exposure, after 750 h exposure in sodium vapor and after 750 h exposure in molten salts vapor.

Although the surface morphology of all specimens apparently remained the same before and after exposure in sodium vapor and in molten salts vapor, except for BN, which notably lost its laminated surface structure after exposure in sodium vapor and after exposure in molten salts vapor, corrosion attack can be found on the surface of Cu and 4J33 specimens at a much higher magnification (Figure 4.6).

As shown in Figure 4.6, compared with specimen before exposure, the Cu specimen after exposure in sodium vapor exhibited a large number of small particles which have a higher oxygen content while the Cu specimen after exposure in molten salts vapor presented much more small holes. As for 4J33 Kovar alloy, after exposure in sodium vapor, the surface almost remained intact. By contrast, after exposure in molten salts vapor, small holes were detected overall on 4J33 specimen's surface.

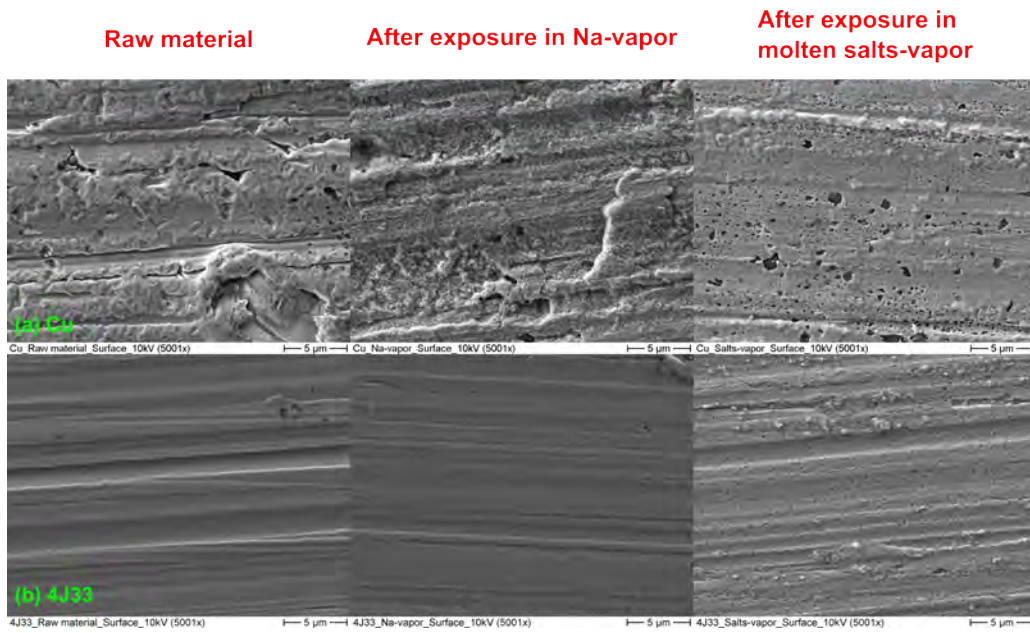


**Figure 4.6:** SE images of surface morphology of (a) Cu and (b) 4J33 Kovar alloy specimen before exposure, after after 750 h exposure in sodium vapor and after 750 h exposure in molten salts vapor.

The results in Figure 4.6 show that when compared with the specimens in sodium vapor, the metallic specimens in molten salts vapor suffered pitting corrosion. However, the pitting corrosion only occurred on near-surface region, the pitting depth was quite shallow and cannot be observed on the cross-sections.

Additionally, EDS point measurements were conducted on BN specimen for further information. SE images of BN raw material and of BN after exposure in molten salts vapor (selected as an example) are shown in Figure 4.7 and Figure 4.8, respectively, while the results are listed in Table 4.4 and Table 4.5, respectively.

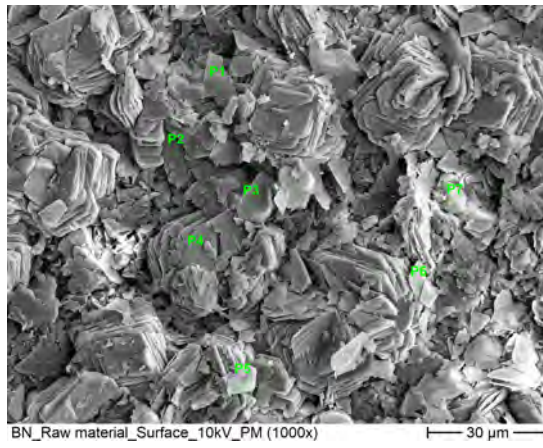


**Figure 4.7:** SE image of EDS point measurement of BN raw material before exposure.

**Table 4.4:** Results of EDS point measurement on BN raw material before exposure (in wt.%).

Point number	B	N	O	Ca
1	23.28	8.76	49.15	12.78
2	40.62	52.39	2.57	0.13
3	24.90	1.67	62.72	9.36
4	29.86	2.37	59.23	5.57
5	30.61	2.57	57.40	5.09
6	30.14	15.88	45.69	3.24
7	29.16	9.93	50.76	5.01

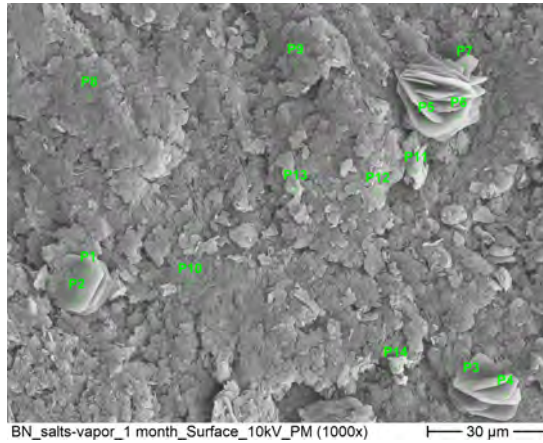


**Figure 4.8:** SE image of EDS point measurement of BN after 750 h exposure in molten salts vapor.

**Table 4.5:** Results of EDS point measurement on BN after exposure in molten salts vapor (in wt.%).

Point number	B	N	O	Ca
1	26.67	6.98	54.78	6.49
2	26.17	4.69	56.79	7.77
3	29.74	7.08	50.77	6.96
4	29.45	7.20	52.59	4.96
5	26.20	12.22	50.37	6.92
6	32.07	7.63	51.12	4.23
7	30.07	18.62	43.20	4.01
8	39.43	50.99	2.38	0.17
9	39.86	48.81	2.57	0.27
10	38.95	49.04	2.65	0.16
11	38.42	51.85	3.35	0.16
12	39.53	50.82	3.15	0.11
13	39.51	51.96	2.28	0.20
14	16.69	35.08	8.89	0.20

The results of EDS point measurement manifest that the laminated layers on BN raw material surface contains a high oxygen content but much less boron and nitrogen, which indicates that the BN surface was already oxidized before exposure. After exposure in molten salts vapor at high temperature, most of the laminated layers disappeared, which indicates that those oxide impurities are reduced during the exposure, which is most likely because that the sodium vapor captures the oxygen and just reduces the oxide layers on the BN, so the real substrate of BN was finally uncovered after exposure.

Figure 4.9 and 4.10 present the BSE images of cross-sections of dielectric ceramic materials with higher magnifications with the aim of clearly elucidating the details at specimens' interface.

Obviously, it can be seen from Figure 4.9 and 4.10 that the interface between ceramic specimens and epoxy resin is not straight and linear, which is due to the fact that ceramics are hard and fragile, after embedded in epoxy resin, ground and polished, it is quite normal and unavoidable that the interface between those ceramic specimens and epoxy resin is not flawless.

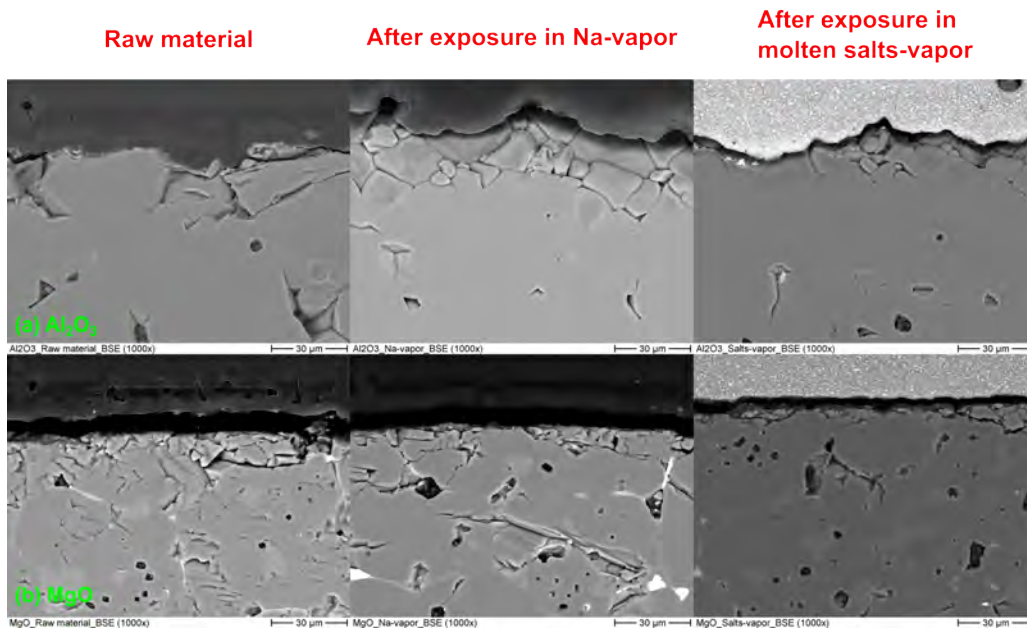


**Figure 4.9:** BSE images of cross-sections of oxide ceramic specimens: (a)  $\text{Al}_2\text{O}_3$  and (b)  $\text{MgO}$  before exposure, after 750 h exposure in sodium vapor and after 750 h exposure in molten salts vapor.

Besides, the white spots exist in AlN before and after both exposure in sodium vapor and in molten salts vapor. According to the point measurement, those white spots barely consists of yttrium and oxygen. Therefore, they might be the additive (sintering agent) during the AlN ceramic fabrication.

Moreover, the BSE images in Figure 4.9 and 4.10 exhibit that the material defects (e.g., cracks, rips and small holes) in ceramic specimens exist both before exposure and after exposure in sodium vapor or in molten salts vapor, which are probably generated during ceramic fabrication or sample preparation. The existence of those material defects in ceramic specimens is totally random and not triggered by exposure in sodium vapor or in molten salts vapor at high temperature.

Additionally, Figure 4.9 and 4.10 also exhibits that despite of those defects, the surface of those ceramic specimens maintains intact and unimpaired both after 750 h exposure in sodium vapor and after 750 h exposure in molten salts vapor. Neither penetration of sodium vapor or molten salts vapor into ceramic specimens nor obvious formation of corrosion products can be observed after exposure in sodium vapor and in molten salts vapor. All ceramic specimens exhibit promising corrosion resistance against sodium vapor

and molten salts vapor at the temperature of 450 °C. Thus, they all possess great potential to be applied as electrical insulator in Na-based LMBs.

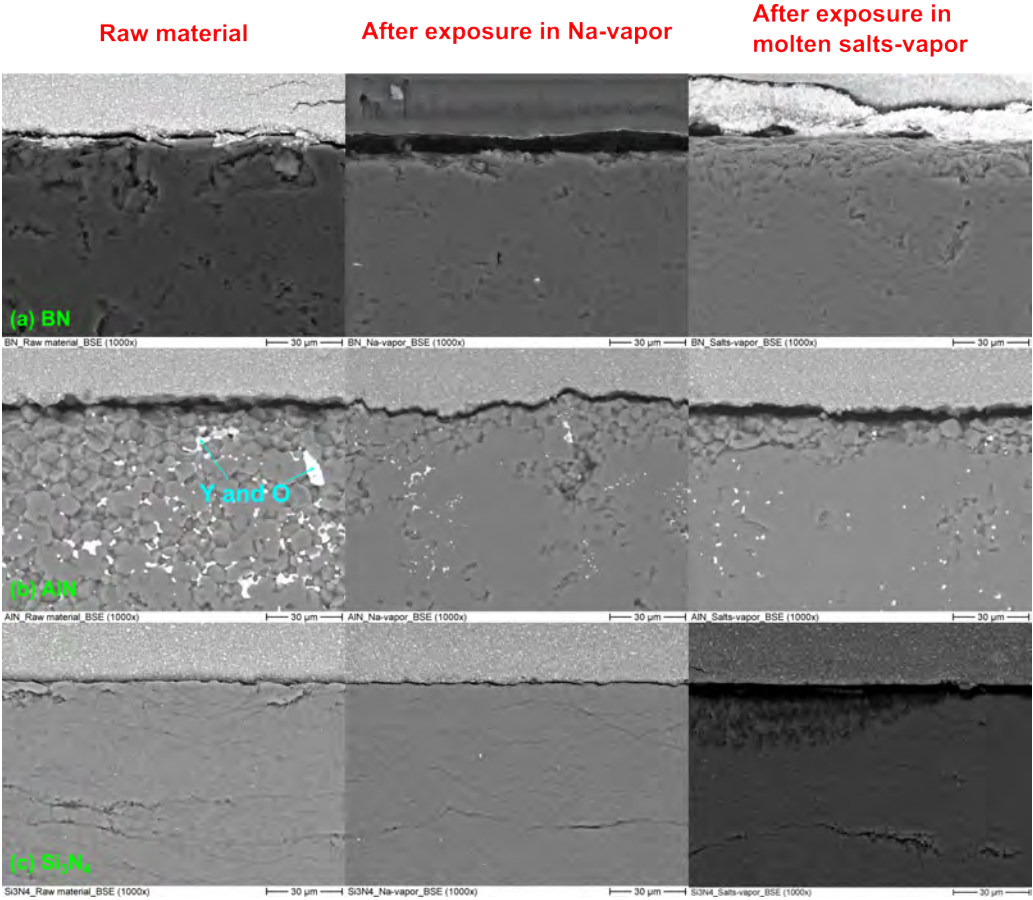


**Figure 4.10:** BSE images of cross-sections of nitride ceramic specimens: (a) BN, (b) AlN and (c) Si<sub>3</sub>N<sub>4</sub> before exposure, after 750 h exposure in sodium vapor and after 750 h exposure in molten salts vapor.

The line scans across the interface of ceramic specimens after exposure in sodium vapor and after exposure in molten salts vapor were performed as complement to those BSE images. MgO and of BN are taken as an example for oxide ceramics and nitride ceramics, respectively.

Figure 4.11 and Figure 4.12 present the BSE images and results of the line scan across the interface of MgO and BN specimens after exposure in sodium vapor and in molten salts vapor, respectively.

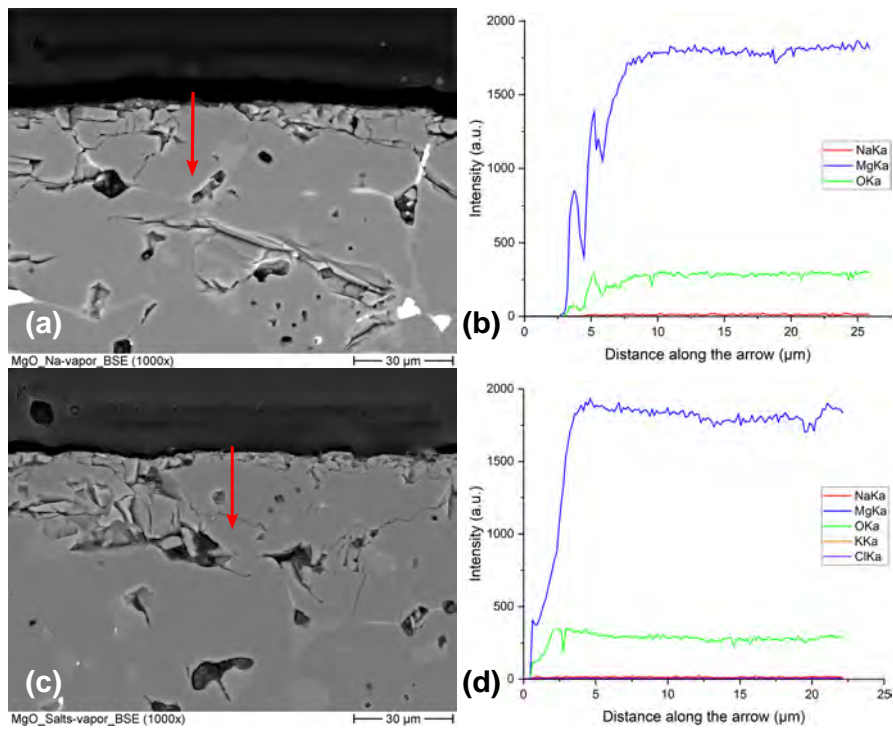


**Figure 4.11:** (a) Line scan across the interface of MgO specimen after 750 h exposure in sodium vapor with (b) results, (c) line scan of MgO specimen after 750 h exposure in molten salts vapor with (d) results.

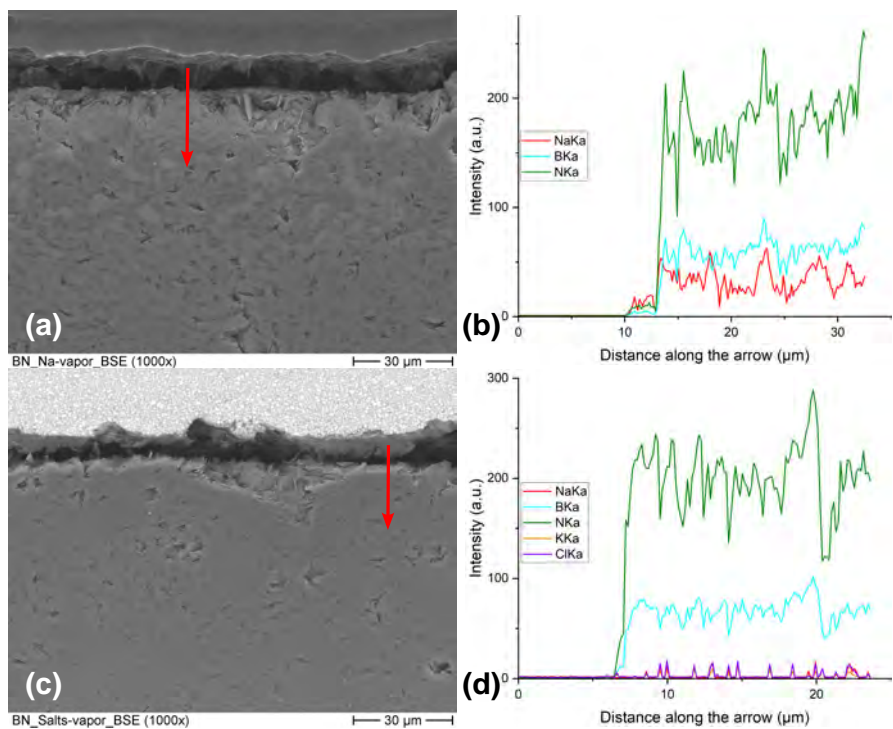


**Figure 4.12:** (a) Line scan across the interface of BN specimen after 750 h exposure in sodium vapor with (b) results, (c) line scan of BN specimen after 750 h exposure in molten salts vapor with (d) results.

It can be seen from Figure 4.11 and Figure 4.12 that for both MgO and BN, the constituents at interface and the constituents in bulk material remain unchanged and stable both after exposure in sodium vapor and after exposure in molten salts vapor. Neither penetration of sodium or molten salts vapor nor the formation of corrosion products can be observed at MgO, which further manifests its good corrosion resistance against sodium vapor and molten salts vapor at 450 °C. In contrast to MgO, an increased amount of Na can be found in BN after exposure while no penetration of molten salts vapor can be detected in BN after exposure in molten salts vapor. The results show that BN has better corrosion resistance against molten salts vapor.

The fluctuation of elemental compositions of those two ceramics at the interface is probably owing to the edge effect, which indicates the surface of these two ceramics is not totally upright and vertical, but a little bit aslant to the cross-section.

The other oxide ceramic ( $\text{Al}_2\text{O}_3$ ) and the other two nitride ceramic specimens ( $\text{AlN}$  and  $\text{Si}_3\text{N}_4$ ) present similar line scan results as MgO specimen, which reveals that all tested dielectric ceramic specimens ( $\text{Al}_2\text{O}_3$ , MgO, BN,  $\text{AlN}$  and  $\text{Si}_3\text{N}_4$ ) exhibit good corrosion resistance against against molten salts vapor at the operating temperature of Na-based LMBs (450 °C) while BN is the only one which has relatively worse corrosion resistance against sodium vapor at that temperature. Thus, their potential to be applied as electrical insulator for Na-based LMBs under certain circumstances was proven as well.

It can be seen from the BSE images of cross-sections of three conductive metallic joining materials at a lower magnification (Figure 4.13) that compared with the specimens exposed in sodium vapor, after 750 h exposure in molten salts vapor, the surface of Cu and Ni42 specimens became a little rough, which indicates the slight corrosion attack on the surface.

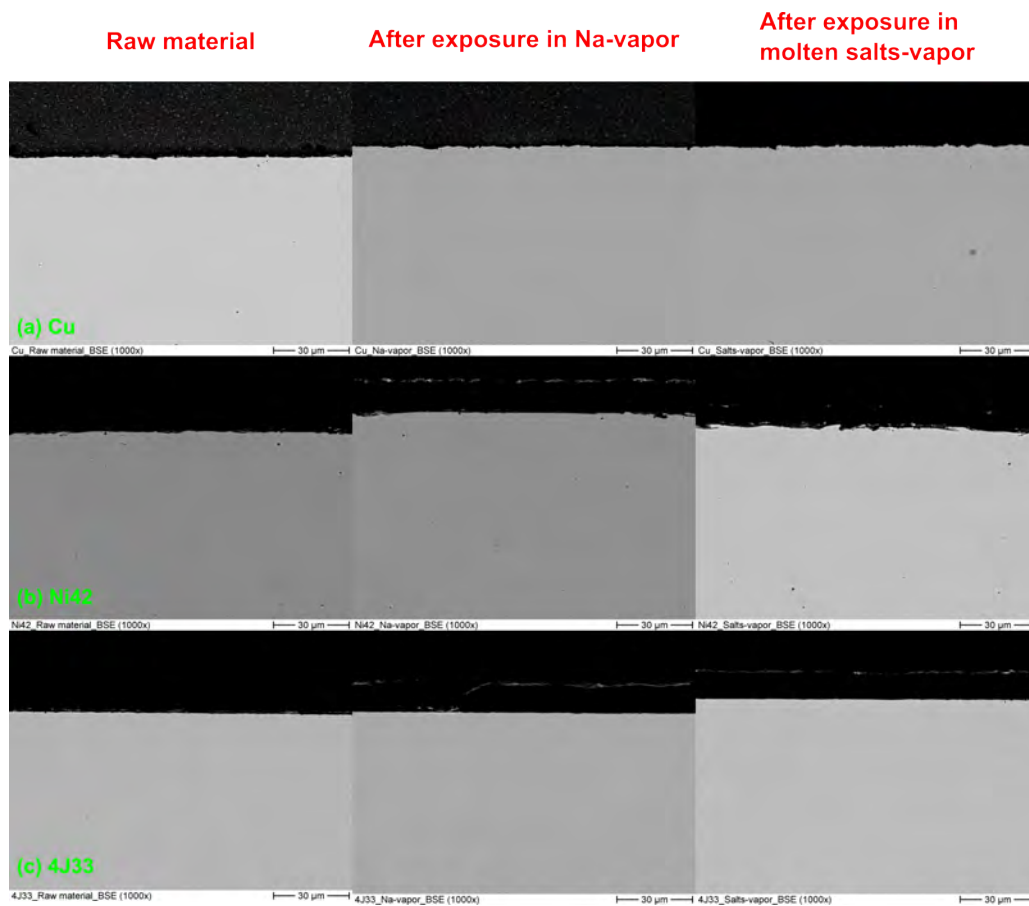


**Figure 4.13:** BSE images of cross-sections of (a) Cu and (b) 4J33 Kovar alloy specimen before exposure, after after 750 h exposure in sodium vapor and after 750 h exposure in molten salts vapor.

Line scans across the interface of conductive metallic specimens after exposure in sodium vapor and after exposure in molten salts vapor were implemented at a much higher magnification for further information as well. Cu and 4J33 Kovar alloy are selected as examples for potential conductive NCC materials. Line scan and its results across the interface of Cu specimen and 4J33 specimen after exposure in sodium vapor and in molten salts vapor are shown in Figure 4.14 and Figure 4.15.

It can be observed that both the surface of Cu and 4J33 specimens became a little bit rough, especially after exposure in molten salts vapor, which is probably due to the pitting corrosion. Compared with 4J33 specimen, the slope of Cu in Figure 4.14 (d) indicates that the phenomenon is more significant on Cu specimen. The elemental compositions of those two metallic specimens at the interface also fluctuate, which is probably because of the edge effect as well.

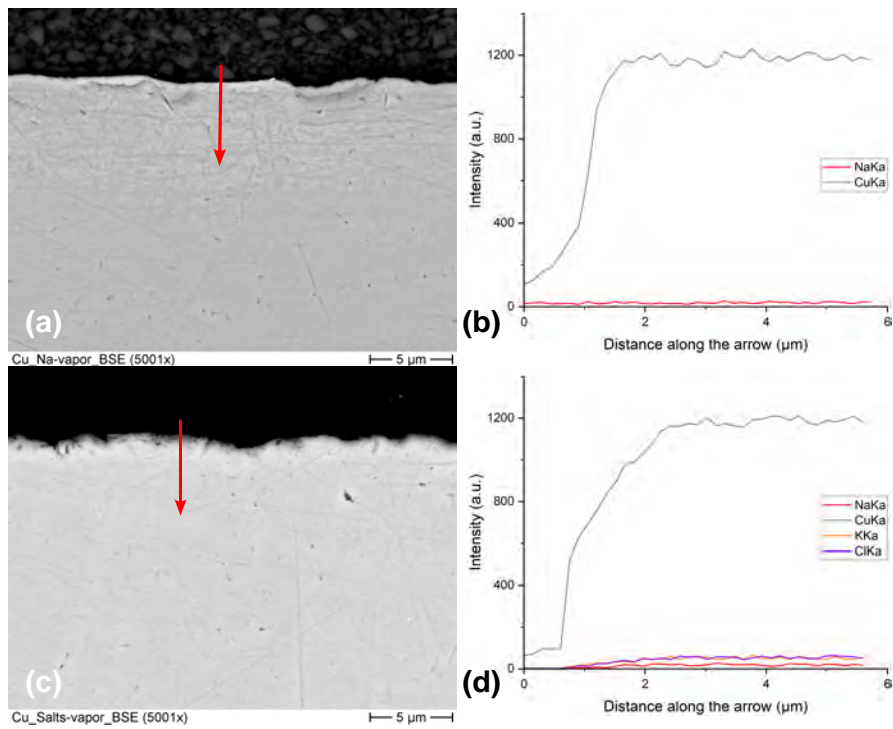


**Figure 4.14:** (a) Line scan across the interface of Cu specimen after 750 h exposure in sodium vapor with (b) results, (c) line scan of Cu specimen after 750 h exposure in molten salts vapor with (d) results.

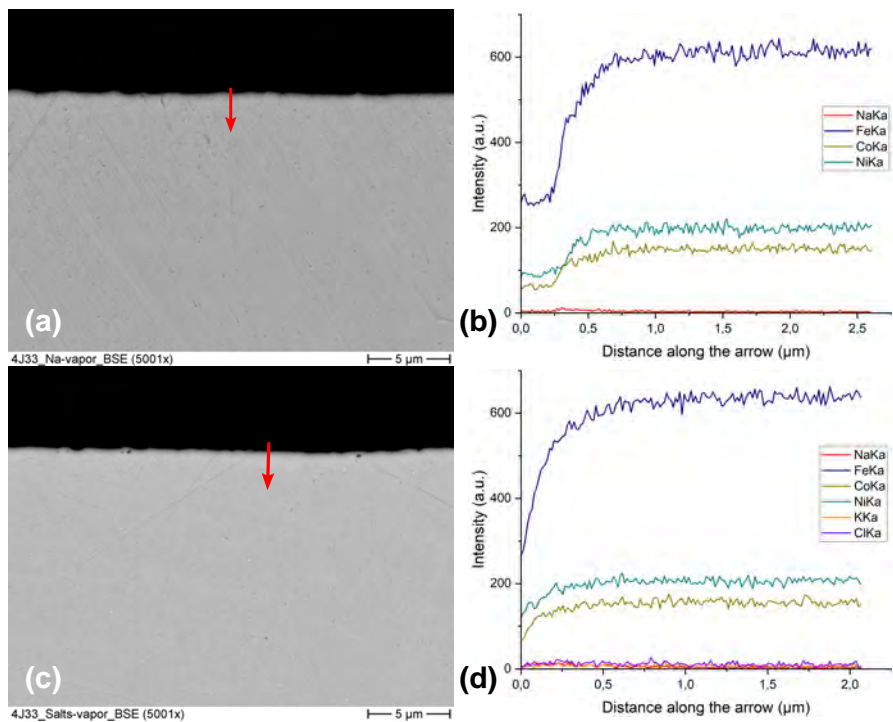


**Figure 4.15:** (a) Line scan across the interface of 4J33 specimen after 750 h exposure in sodium vapor with (b) results, (c) line scan of 4J33 specimen after 750 h exposure in molten salts vapor with (d) results.

Despite the pitting corrosion, Cu and the constituents (Fe, Ni and Co) of 4J33 Kovar alloy remain unchanged and stable after exposure in sodium vapor and after exposure in molten salts vapor at 450 °C. Therefore, both of them show huge potential to be applied as NCC in Na-based LMBs.

Ni42 Invar alloy specimen presents the same results as Cu and 4J33 Kovar alloy. Despite the pitting corrosion, which mainly took place on the surface of all metallic specimens after exposure in molten salts vapor, all tested metallic specimens (Cu, Ni42 Invar alloy and 4J33 Kovar alloy) possess good corrosion resistance against sodium vapor and against molten salts vapor at the operating temperature of Na-based LMBs (450 °C) for short term. Therefore, their potential to be applied as NCC for Na-based LMBs was also confirmed.

#### 4.1.4 Discussion

In this part, five dielectric ceramics ( $\text{Al}_2\text{O}_3$ , MgO, BN, AlN and  $\text{Si}_3\text{N}_4$ ) and three conductive metallic joining materials (Cu, Ni42 Invar alloy and 4J33 Kovar alloy) were tested in Na vapor and in molten salts vapor, respectively, in order to investigate their potential to be applied as electrical insulator and NCC for Na-based LMBs.

Firstly, it can be seen from the results of metallic NCC materials that pitting corrosion can be found on both Cu and 4J33 Kovar alloy after exposure in molten salts vapor while both of them almost remain intact after exposure in Na vapor. The results point out that when compared with Na vapor, molten salts vapor is more aggressive on metallic specimens (Cu and 4J33 Kovar alloy). Despite the pitting corrosion after exposure in molten salts vapor, the pitting corrosion is relatively marginal, which only exists at the near-surface region of the test specimens for short term. Hence the cell design without foam (see Figure 3.2 (b)) might be advantageous to the cell design with foam (Figure 3.2 (a)): the NCC is only exposed to Na vapor in this design and the cell capacity is not limited by the Na amount absorbed in the foam.

Next, the results of electrical insulator materials and NCC materials after exposure in molten salts vapor show that all those oxide and nitride ceramics remain intact and uncorroded after 750 h exposure in molten salts vapor at 450 °C while the near-surface

region of metallic NCC materials (Cu and 4J33 Kovar alloy) suffer slight pitting corrosion, which illustrates that compared with the metallic NCC materials, those oxide and nitride ceramics possess better corrosion resistance against molten chloride salts vapor at 450 °C. Nevertheless, although the near-surface region of metallic materials are slightly corroded after exposure in molten salts vapor, no severe corrosion attack and roughness of particles can be detected on all five those dielectric ceramics and three conductive metallic materials, which indicates that all test materials possess good corrosion resistance against Na vapor and molten salts vapor at the operating temperature of Na-based LMBs (450 °C). Hence all five dielectric ceramics and three conductive metallic materials manifest great potential to be applied as electrical insulator and NCC respectively for low-temperature and low-cost Na-based LMBs with long service lifetime. Especially, our results on Al<sub>2</sub>O<sub>3</sub> ceramic after exposure in LiCl-NaCl-KCl molten salts vapor coincide with the results and conclusion from Nagaoka et al. [81], namely Al<sub>2</sub>O<sub>3</sub> ceramic exhibits good compatibility with molten salts and is expected to be a promising container material for molten salts.

Hence, the key factor for material selection for electrical insulator and NCC for Na-based LMBs in grid-scale energy storage application becomes the price. For electrical insulators, considering that the price of nitride ceramics is much higher than oxide ceramics, Al<sub>2</sub>O<sub>3</sub> and MgO are more affordable and might be more appropriate to be applied as electrical insulator for Na-based LMBs.

Regarding the NCC materials, take the rarity (0.00266 wt.% in Earth's crust) and the increasing cost of natural resources of Co [18, 22, 23, 28] into account, Cu and Invar alloy are more affordable than Kovar alloy, which contains a certain amount of cobalt ( $\geq 14$  wt.%).

#### 4.1.5 Short summary

In short, all tested specimens exhibit promising corrosion resistance against Na vapor and molten salts vapor. However, when taking the cost factor into consideration, the most promising candidates for electrical insulator and conductive NCC for Na-based LMBs are the combination of oxide ceramics (Al<sub>2</sub>O<sub>3</sub>/MgO) with Cu/Invar alloy. Additionally, to

accomplish Na-based LMBs with excellent battery performance and long service lifetime, LMB cell design, metal-metal/metal-ceramic joining and cell active components are still need to be further investigated and optimized.

## **4.2 Static corrosion tests for PCC materials in positive electrode at fully-charged state**

### **4.2.1 Material selection**

Both designs in Figure 3.2 (a) and (b) illustrate that PCC always has direct contact to positive electrode in a LMB cell. Combined with the high operating temperature of LMB cells, one of the biggest issues for LMB cells emerges: the compatibility of PCC materials with active cell components (positive electrode and electrolyte). Hence, PCC materials should fulfill these criteria: high electronic conductive, thermally/chemically stable, corrosion resistant to positive electrode and electrolyte. Moreover, for grid-scale application, the cost for PCC materials must also be moderate, or at least acceptable, which is the same as the criteria for electrical insulator materials and NCC materials mentioned in Section 4.1.1 [35].

According to previous studies, ferrous alloys (iron and steels) are corrosion resistant to liquid metals to a certain extent, thus they might be attractive candidates for PCC for LMB cells [35].

As mentioned in Section 4.1.1, 4J33 Kovar alloy is regarded as one of the appropriate candidates for NCC materials due to its similar thermal expansion properties as ceramic materials with the aim of reducing residual stresses between ceramic-metal joint and therefore avoiding joint reliability issues [120, 121], therefore, 4J33 Kovar alloy is also selected as candidate for PCC in LMB cells.

MAX-phases are nano-layered, hexagonal, ternary carbides and nitrides which have the general formular:  $M_{n+1}AX_n$  ( $n = 1$  to  $3$ ), where M is a transitional metal, A is an A-group element from IIIA or IVA group and X is either carbon (C) and/or nitrogen (N). Due to the fact that MAX-phases exhibit the combination of metallic and ceramic properties, including high electrical conductivity, high thermal conductivity, good machinability and

good corrosion resistance against chemical attack [133, 134], MAX-phase coatings are regarded as promising candidate for PCC in LMB cells as well.

Therefore, six different metallic bulk materials (Cr metal, Mo metal, T91 ferritic steel, 304 austenitic stainless steel (SS304) and 316L austenitic stainless steel (SS316L), 4J33 Kovar alloy) and three MAX-phase coatings ( $\text{Cr}_2\text{AlC}$ ,  $\text{Ti}_2\text{AlC}$  and  $\text{Ti}_3\text{AlC}_2$ ) on  $\text{Al}_2\text{O}_3$ -substrate) were chosen to first evaluate their corrosion resistance against liquid Sb-Sn and Sb-Bi alloys.

## 4.2.2 Experiments

### Materials and preparation of specimens

The test specimens in this work were chromium (Cr) metal (IHM/KIT), molybdenum (Mo) metal (Plansee SE), T91 ferritic steel (EUROTRANS-DEMETRA [135]), SS304 (Workshop/KIT), SS316L (EUROTRANS-DEMETRA [135]), 4J33 Kovar alloy (Dongguan Saijing Special Alloy Co. Ltd.) and three MAX-phase coatings ( $\text{Cr}_2\text{AlC}$ ,  $\text{Ti}_2\text{AlC}$  and  $\text{Ti}_3\text{AlC}_2$ ) on  $\text{Al}_2\text{O}_3$ -substrate (IAM-AWP/KIT).

The MAX-phase coatings were provided by Dr. Chongchong Tang (IAM-AWP/KIT), they were synthesized by a two-step method, deposition of nanoscale elemental M/C/Al multilayers by magnetron sputtering and the subsequent ex-situ thermal annealing in argon atmosphere. The coating thickness here were  $\sim 3 \mu\text{m}$  and more details on the coating synthesis can be found in previous publication [136].

The Cr metal used was produced by re-melting chromium flakes (HMW Hauner GmbH & Co. KG with 99.99 % purity) via arc-melting under argon atmosphere.

The compositions of steel and alloy specimens are listed in Table 4.6.

**Table 4.6:** Composition of steel and alloys specimens for static corrosion test in positive electrode at fully-charged state (in wt.%).

Material	C	Co	Cr	Ni	Mn	Mo	Fe
T91	0.08 – 0.12	/	8.00 – 9.50	/	0.30 – 0.60	0.85 – 1.05	Bal.
SS304	≤ 0.08	/	18.00 – 20.00	8.00 – 10.50	≤ 2.00	/	Bal.
SS316L	≤ 0.03	/	16.00 – 18.00	10.00 – 14.00	≤ 2.00	2.00 – 3.00	Bal.
4J33	≤ 0.05	14.00 – 15.20	/	32.10 – 33.60	≤ 0.50	/	Bal.

All specimens were cut into appropriate size to fit into the sample holder (Figure 4.16). Particularly, before exposure, except for those three MAX-phase coatings, all test materials were ground by sandpaper with a grid size of 800 and 1200, successively.

As shown in Figure 4.16, all specimens were fixed on an  $\text{Al}_2\text{O}_3$ -holder by Mo-wires to force them immerse or sub-immersed (depends on the shape and size of specimens) in liquid  $\text{Sb}_3\text{Sn}_7$  and in liquid  $\text{SbBi}_9$  in  $\text{Al}_2\text{O}_3$ -crucibles, respectively.



**Figure 4.16:** Cross-section of a sample holder ( $\text{Al}_2\text{O}_3$ -crucible with an  $\text{Al}_2\text{O}_3$ -holder on top) for corrosion tests for PCC materials at fully-charged state and a sample (fixed on  $\text{Al}_2\text{O}_3$ -holder by Mo-wires) inside.

### Test facility

The corrosion tests were performed in the COSTA facility (Figure 4.17) in the Institute for Pulsed Power and Microwave Technology/Karlsruhe Institute of Technology (IHM/KIT) laboratory [89]. It consists of a furnace, which is applied to regulate the isothermal condition for the exposure, with two half-open quartz tubes, in which the exposure occurred. Each quartz tube is connected with a gas control system and flow

meters to adjust the gas flow and to control the atmosphere inside the tubes.



**Figure 4.17:** Schematic of COSTA facility.

### **Preparation of Sb-Sn and Sb-Bi alloys**

The test compositions for Sb-Sn and Sb-Bi alloys are selected based on their phase diagrams [137, 138]. For Sb-Sn alloy, the test compositions for Sb-Sn alloy are  $\text{Sb}_3\text{Sn}_7$ ,  $\text{Sb}_4\text{Sn}_6$  and  $\text{SbSn}$ ; for Sb-Bi alloy, the test compositions are  $\text{SbBi}_9$ ,  $\text{Sb}_2\text{Bi}_8$  and  $\text{Sb}_3\text{Bi}_7$ .

Tin (Sn) was delivered by HMW Haunder GmbH & Co. KG with the granular size of 2 – 4 mm and 99.99 % purity. Antimony (Sb) and bismuth (Bi) were delivered by Haines & Maassen Metallhandels-gesellschaft GmbH. The Sb granular has a purity of 99.65 % and a granular size of 1 – 10 mm, the Bi possesses a purity of 99.99 % and a granular size of 1 – 3 mm.

The Sb-Sn alloys were gained by mixing the individual heavy metals Sb and Sn in their granular forms in  $\text{Al}_2\text{O}_3$ -crucibles.

The surface of Bi was slightly oxidized, so it has been first melted in a Mo-crucible and the slag layer on top was removed. Then, the desired amount of molten Bi was poured into  $\text{Al}_2\text{O}_3$ -crucibles and cooled down to room temperature. Afterwards, the desired amount of granular Sb was added.

## Test procedures

After the crucibles were filled with around 100 g heavy metals, they were put into the furnace at room temperature. Afterwards, the atmosphere inside the quartz tubes was pre-purged with 100 mL/min Ar+5%H<sub>2</sub> gas for 2 days, until the oxygen content inside the tubes reached 10<sup>-17</sup> ppm. Then, the temperature was raised to 700 °C to melt the heavy metals, especially Sb (melting point: 631 °C), which has the highest melting point among those three heavy metals. The high temperature was hold for 2 h, afterwards, the temperature was decreased to the test temperature, which was selected slightly above the melting point of the Sb-Sn and Sb-Bi alloys (see Table 4.7) [137, 138].

**Table 4.7:** Test temperature for different compositions of Sb-Sn and Sb-Bi alloys.

Composition	Sb <sub>3</sub> Sn <sub>7</sub>	SbBi <sub>9</sub>	Sb <sub>4</sub> Sn <sub>6</sub>	Sb <sub>2</sub> Bi <sub>8</sub>	SbSn	Sb <sub>3</sub> Bi <sub>7</sub>
Test temperature (°C)	450		420		450	470

However, due to the shortage of MAX-phases, only metallic specimens (T91, SS304, SS316L, 4J33 alloy and Mo metal) were later tested in Sb<sub>4</sub>Sn<sub>6</sub>, SbSn, Sb<sub>2</sub>Bi<sub>8</sub>, and Sb<sub>3</sub>Bi<sub>7</sub> alloys at set temperature.

To prevent the oxidation of Sb-Sn and Sb-Bi alloys, the quartz tubes were purged with 100 mL/min Ar+5%H<sub>2</sub> gas for the entire duration of the experiment.

For loading and unloading the specimens, a glovebox was connected to the quartz tubes. To maintain the atmosphere inside the furnace, the glovebox was also purged with Ar+5%H<sub>2</sub> gas until an oxygen content of  $2 \times 10^{-15}$  ppm was reached.

To start the exposure of specimens in liquid Sb-Sn alloy and in liquid Sb-Bi alloy, all specimens were first set into glovebox, then the Al<sub>2</sub>O<sub>3</sub>-crucibles with liquid Sb-Sn alloy and Sb-Bi alloy were pulled out of the quartz tubes and temporarily set in glovebox. Each specimen was immediately and separately full-immersed/sub-immersed (depends on the shape and size of specimens) in one Al<sub>2</sub>O<sub>3</sub>-crucible. After that, all Al<sub>2</sub>O<sub>3</sub>-crucibles were set back into the COSTA facility and held isothermally at 450 °C for 750 h.

## Post-test analysis

After 750 h exposure, all specimens were extracted from the COSTA facility and cooled

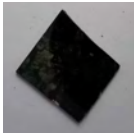
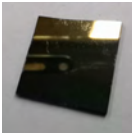
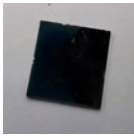
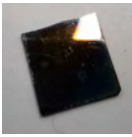
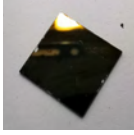
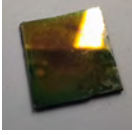
down in the glovebox to room temperature. Afterwards, scanning electron microscope (SEM) with energy-dispersive X-ray spectroscopy (EDS) was used for the examination of cross-sections of metallic specimens. Considering that no Sb-Sn alloy or Sb-Bi alloy stuck on those three MAX-phases' surface, only their surface was observed and examined.

### 4.2.3 Results

Table 4.8 shows the appearance of all specimens after exposure to liquid  $\text{Sb}_3\text{Sn}_7$  and  $\text{SbBi}_9$  at 450 °C for 750 h, respectively. For a better presentation of the results, those materials have been sorted into groups according to their chemical compositions.

As shown in 4.8, regardless of the two different liquid heavy metal systems (Sb-Sn system and Sb-Bi system), the immersed part of all metallic specimens is more or less covered by a layer of Sb-Sn or Sb-Bi alloy. In contrast, the attachment of liquid Sb-Sn alloy or Sb-Bi alloy on all three MAX-phases is invisible to the naked eyes, all of them retain their original appearance.

**Table 4.8:** Appearance of all specimens after exposure in liquid  $\text{Sb}_3\text{Sn}_7$  and  $\text{SbBi}_9$  at 450 °C for 750 h.

Group	Specimen	In liquid $\text{Sb}_3\text{Sn}_7$	In liquid $\text{SbBi}_9$
Fe-Cr steel	T91 ferritic steel		
Fe-Cr-Ni steel	304 stainless steel		
	316L stainless steel		
Fe-Co-Ni alloy	4J33 Kovar alloy		
Pure metals	Cr metal		
	Mo metal		
MAX-phases	$\text{Ti}_2\text{AlC}-\text{Al}_2\text{O}_3$		
	$\text{Ti}_3\text{AlC}_2-\text{Al}_2\text{O}_3$		
	$\text{Cr}_2\text{AlC}-\text{Al}_2\text{O}_3$		

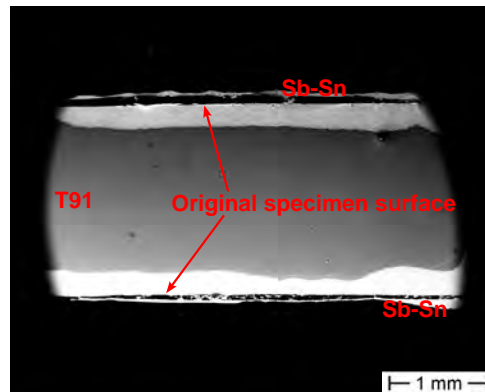
## Results in $\text{Sb}_3\text{Sn}_7$

### Fe-Cr steel (T91 ferritic steel)

T91 ferritic steel is a 9Cr steel that mainly consists of Fe and Cr. It serves as one example

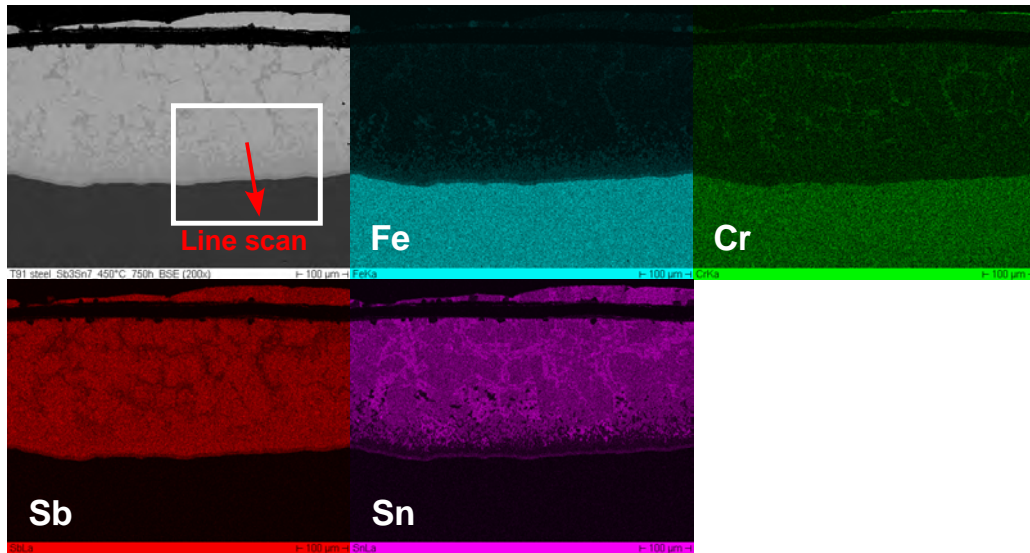
for steels without Ni.

Figure 4.18 shows the SE image of the cross-section of T91 ferritic steel after 750 h exposure in liquid  $\text{Sb}_3\text{Sn}_7$ . Sb-Sn alloy is attached at steel surface and reacted with the steel, which leads to the formation of corrosion regions throughout the surface of the remaining T91 ferritic steel. The corrosion depth of liquid  $\text{Sb}_3\text{Sn}_7$  into T91 steel ferritic steel is in the range of 200  $\mu\text{m}$  and 400  $\mu\text{m}$  which leads to a maximum calculated corrosion rate of 0.53  $\mu\text{m}/\text{h}$  for this material at the given conditions.



**Figure 4.18:** SE image of cross-section of T91 ferritic steel after 750 h exposure in liquid  $\text{Sb}_3\text{Sn}_7$  at 450 °C.

The BSE image and EDS element mapping images of cross-section of T91 ferritic steel after 750 h exposure in liquid  $\text{Sb}_3\text{Sn}_7$  with a higher magnification are shown in Figure 4.19. It can be seen from Figure 4.19 that both Fe and Cr in T91 ferritic steel are depleted in the corrosion region. Moreover, both Sb and Sn show apparent penetration into T91 ferritic steel.



**Figure 4.19:** BSE image and EDS element mapping images of cross-section of T91 ferritic steel after 750 h exposure in liquid  $\text{Sb}_3\text{Sn}_7$  at 450 °C.

For further investigation on the interaction mechanisms (dissolution, alloying, penetration) between solid test specimen and liquid Sb-Sn alloy, a line scan (Figure 4.20) across T91 ferritic steel after the exposure in liquid  $\text{Sb}_3\text{Sn}_7$  was implemented. The results exhibit that two Fe-Cr-Sb-Sn layers and an extended corrosion region with different elemental compositions are formed as corrosion products, the thinner one formed at the corrosion front (zone ② in Figure 4.20) consists of higher Fe and Sn contents but a lower Sb content while the other layer (zone ③ in Figure 4.20) has much lower Fe and Sn contents but a much higher Sb content. Besides, the composition of Sb and Sn in the layer formed at the corrosion front varies with the distance from the corrosion front, Sb increases with increasing distance while the amount of Sn decreases.

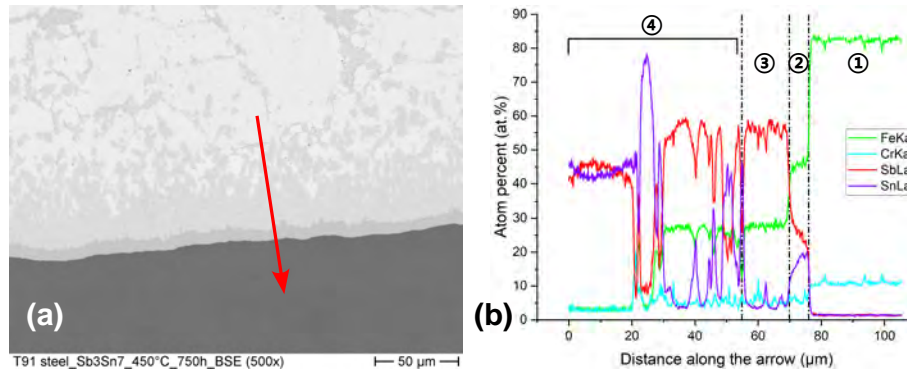


**Figure 4.20:** (a) Line scan across T91 ferritic steel after 750 h exposure in liquid  $\text{Sb}_3\text{Sn}_7$  at 450 °C with (b) results of composition analysis, where ① is the unmodified T91, ② is the corrosion layer at the corrosion front, ③ is the intermediate corrosion products and ④ is the extended corrosion region, which consists of patches of different compositions.

Phase diagrams of the main constituents in steel with Sb or Sn (Fe-Sb, Fe-Sn, Cr-Sb and Cr-Sn) can be used to predict the components in the corrosion products. It can be seen from Fe-Sb, Fe-Sn phase diagrams [139–143], both Sb and Sn could react with Fe and form FeSb, FeSb<sub>2</sub>, FeSn and FeSb<sub>2</sub> intermetallic compounds at 450 °C. According to Cr-Sb and Cr-Sn phase diagrams [144, 145], at 450 °C, Sn does not react with Cr and form new intermetallic phases, only Sb reacts with Cr and form CrSb and CrSb<sub>2</sub> intermetallic compounds.

Combined with the results of the line scan, the main composition of the corrosion layer formed in the middle (Fe:Sb = 1:2, molar ratio) is probably FeSb<sub>2</sub>, while the Fe-Cr-Sb-Sn layer formed at the corrosion front could be the mixture of FeSb, FeSn, FeSn<sub>2</sub>, CrSb and CrSb<sub>2</sub>. The different corrosion behavior of Sb and Sn can probably be contributed to the different Gibbs free energies of the reactions to form corresponding Fe-Sb, Fe-Sn, Cr-Sb and Cr-Sn intermetallic compounds.

### Fe-Cr-Ni steel (SS304 and SS316L)

As one of the most common and most widely applied commercial structural materials, 304 austenitic stainless steel (SS304), which mainly consists of Fe, Cr and Ni (composition see Table 4.6), is also taken as an example.

Figure 4.21 shows the SE image of the cross-section of SS304 after 750 h exposure in liquid  $\text{Sb}_3\text{Sn}_7$ . It can be seen from Figure 4.21 that Sb-Sn alloy attached on the surface of remaining SS304 and locally enormously penetrated into SS304. After 750 h exposure, the corrosion attack is not homogeneous, it occurs only locally, and the maximal corrosion depth of liquid  $\text{Sb}_3\text{Sn}_7$  into SS304 is around 1 mm, which leads to a maximum calculated corrosion rate of 1.33  $\mu\text{m}/\text{h}$

for this material.

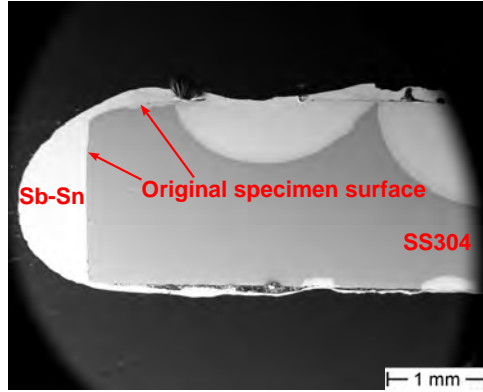


**Figure 4.21:** SE image of cross-section of SS304 after 750 h in liquid  $\text{Sb}_3\text{Sn}_7$  at 450 °C.

The BSE image and EDS element mapping images of cross-section of SS304 after 750 h exposure in liquid  $\text{Sb}_3\text{Sn}_7$  with a higher magnification shown in Figure 4.22 clarify that all main constituents (Fe, Cr and Ni) of SS304 are intensively depleted in corrosion region. However, in this case, a thin Cr-rich layer and a large amount of Cr-rich precipitations can be observed at and near the specimen surface. Moreover, both Sb and Sn present apparent penetration into SS304. Furthermore, the attached Sb-Sn alloy is enriched in Ni and Fe.

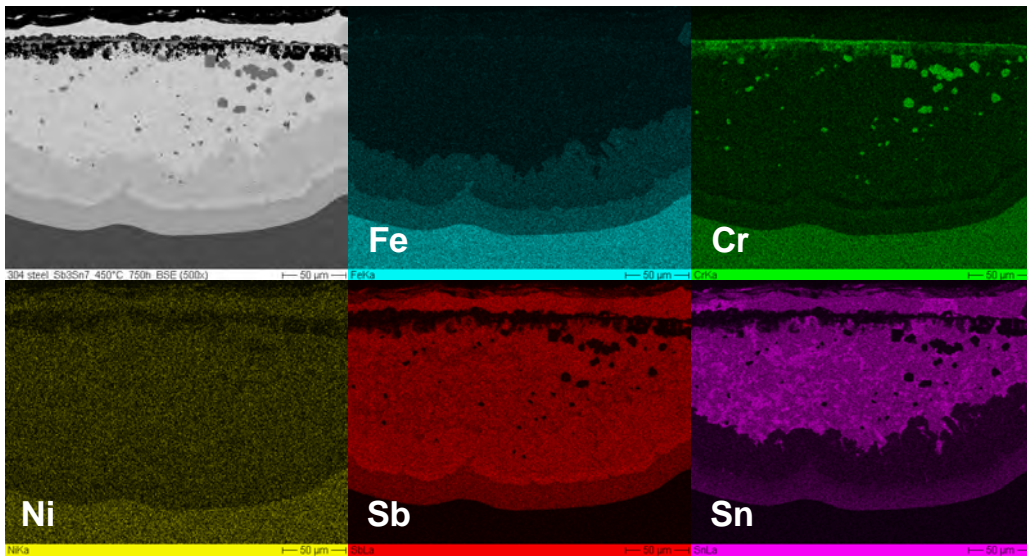


**Figure 4.22:** BSE image and EDS element mapping images of cross-section of SS304 after 750 h exposure in liquid  $\text{Sb}_3\text{Sn}_7$  at 450 °C.

The line scan (Figure 4.23) illustrates that two Fe-Cr-Ni-Sb-Sn layers and an extended corrosion region with different elemental compositions are formed as corrosion products. The layer formed at the corrosion front (zone ② in Figure 4.23) possesses higher Fe, Sn contents but a lower Sb content while the intermediate layer (zone ③ in Figure 4.23) presents lower Fe, Cr and Sn

contents but a much higher Sb content. Compared with those two corrosion layers, the extended corrosion region (zone ④ in Figure 4.23) exhibits even lower Fe and Cr contents, but much higher Sb, Sn contents with some Cr-rich precipitates (see Figure 4.22). Ni is heavily depleted in the entire corrosion attacked region. Besides, the composition of Sb and Sn in the Fe-Cr-Ni-Sb-Sn layer formed at the corrosion front varies with the distance from the corrosion front, the quantity of Sb increases with increasing distance, while the amount of Sn decreases, which corresponds to the results in T91 ferritic steel.

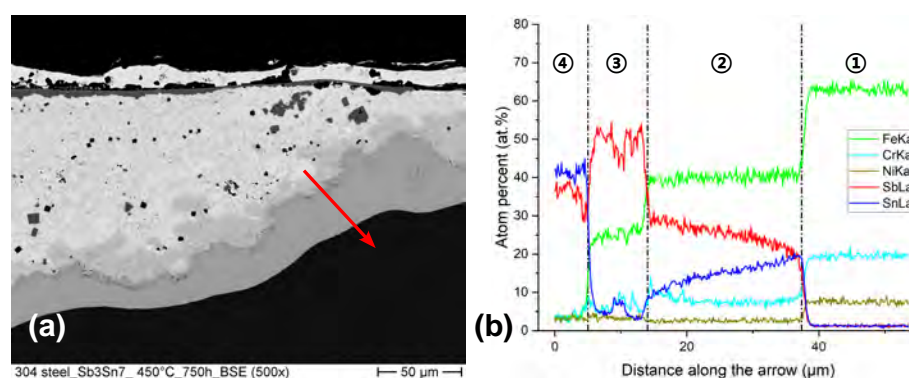


**Figure 4.23:** (a) Line scan across SS304 after 750 h exposure in liquid  $\text{Sb}_3\text{Sn}_7$  at 450 °C with (b) results of composition analysis, where ① is the unmodified SS304, ② is the corrosion layer at the corrosion front, ③ is the intermediate corrosion layer and ④ is the extended corrosion region.

According to Ni-Sb and Ni-Sn phase diagrams [146, 147], at the temperature of 450 °C, both Sb and Sn could react with Ni and form multiple intermetallic compounds including  $\text{Ni}_3\text{Sb}$ ,  $\text{Ni}_7\text{Sb}_3$ , NiSb,  $\text{NiSb}_2$ ,  $\text{Ni}_3\text{Sn}$ ,  $\text{Ni}_3\text{Sn}_2$  and  $\text{Ni}_3\text{Sn}_4$ . Besides, it can be seen from Figure 4.22 that when compared with Fe and Cr, which barely exist in the corroded steel, the Ni content in the corroded steel and in the attached Sb-Sn alloy are quite similar. The results indicates that those Ni-compounds not only exists in the corroded steel but also in Sb-Sn alloy.

The same as the line scan in T91 ferritic steel (Figure 4.20), the main composition of the intermediate corrosion layer (zone ③ in Figure 4.23, Fe:Sb = 1:2, molar ratio) formed on SS304 might be  $\text{FeSb}_2$  while the corrosion layer formed at the corrosion front (zone ② in Figure 4.23) could contain the mixture of all Fe-Sb, Fe-Sn, Cr-Sb, Cr-Sn, Ni-Sb and Ni-Sn compounds.

As for SS316L (displayed in Figure 4.24, 4.25 and 4.26), which also belongs to the group of Fe-Cr-Ni steel, it exhibits similar behavior as SS304 after exposure in liquid  $\text{Sb}_3\text{Sn}_7$ : the reaction between Sb-Sn alloy with steel, the partial penetration of Sb-Sn alloy into steel and the formation of Cr-rich precipitates at the interface.

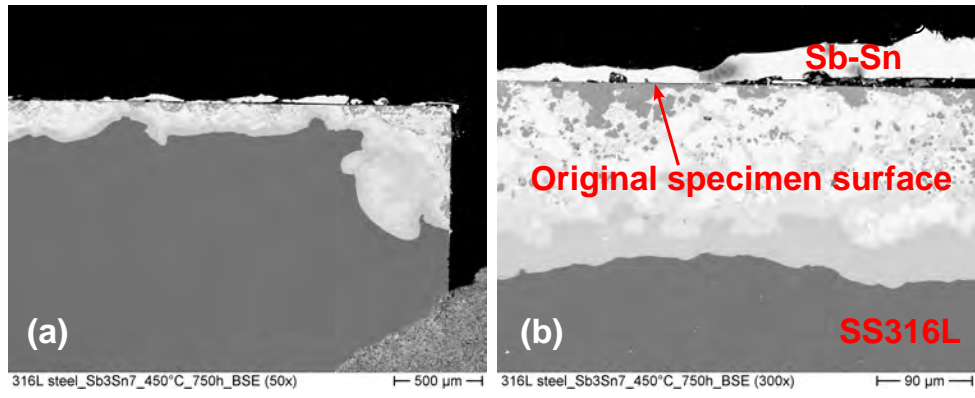


**Figure 4.24:** BSE images of cross-section of SS316L after 750 h in liquid  $\text{Sb}_3\text{Sn}_7$  at 450 °C.

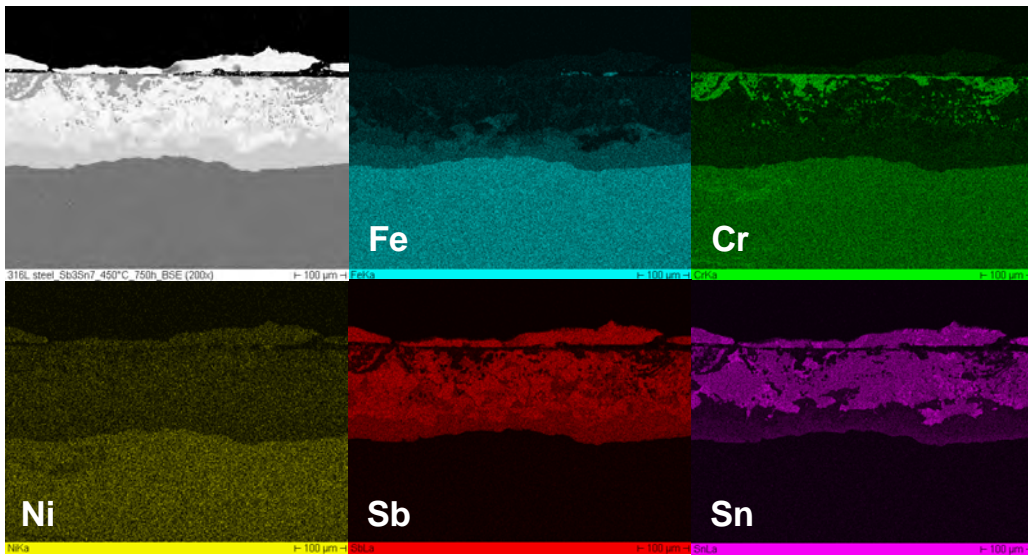


**Figure 4.25:** BSE image and EDS element mapping images of cross-section of SS316L after 750 h exposure in liquid  $\text{Sb}_3\text{Sn}_7$  at 450 °C.

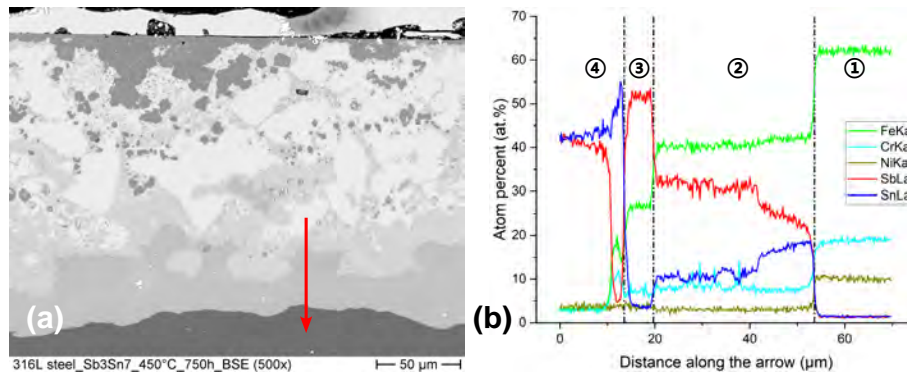


**Figure 4.26:** (a) Line scan across SS316L after 750 h exposure in liquid  $\text{Sb}_3\text{Sn}_7$  at 450 °C with (b) results of composition analysis, where ① is the unmodified SS316L, ② is the corrosion layer at the corrosion front, ③ is the intermediate corrosion layer and ④ is the extended corrosion region.

Compared with T91 ferritic steel, SS304 and SS316L present locally a much larger corrosion rate after exposure in liquid  $\text{Sb}_3\text{Sn}_7$ . Since the Cr-rich layer could act as a protective layer [69] to inhibit the corrosion of steels in heavy metal alloy, the accelerated corrosion rate of SS304 and SS316L can probably be attributed to the presence of Ni content. Therefore, Ni might be a detrimental element for PCC materials in LMBs.

### Fe-Co-Ni alloy (4J33 Kovar alloy)

After 750 h exposure, 4J33 Kovar alloy specimen lost its original shape and was strongly corroded. The BSE image and EDS element mapping images of cross-section of 4J33 Kovar alloy after 750 h exposure in liquid  $\text{Sb}_3\text{Sn}_7$  are shown in Figure 4.27. It can be observed that both Sb and Sn reacted with 4J33 Kovar alloy, formed a combination of Sb-Sn alloy (brighter parts in this image) and corrosion products (grey parts in this image), which totally attached and covered the whole surface of remaining 4J33 Kovar alloy. It can be seen from EDS element mapping images that all main constituents (Fe, Co and Ni) of 4J33 Kovar alloy are intensively depleted in corrosion products. The corrosion depth of liquid  $\text{Sb}_3\text{Sn}_7$  into 4J33 Kovar alloy is in the range of 300 μm and 400 μm, which leads to a maximum calculated corrosion rate of 0.53 μm/h for this material. However, compared with SS304, where the maximum corrosion depth was only confined to some spots, the corrosion depth of 4J33 alloy is nearly constant over the entire specimen.

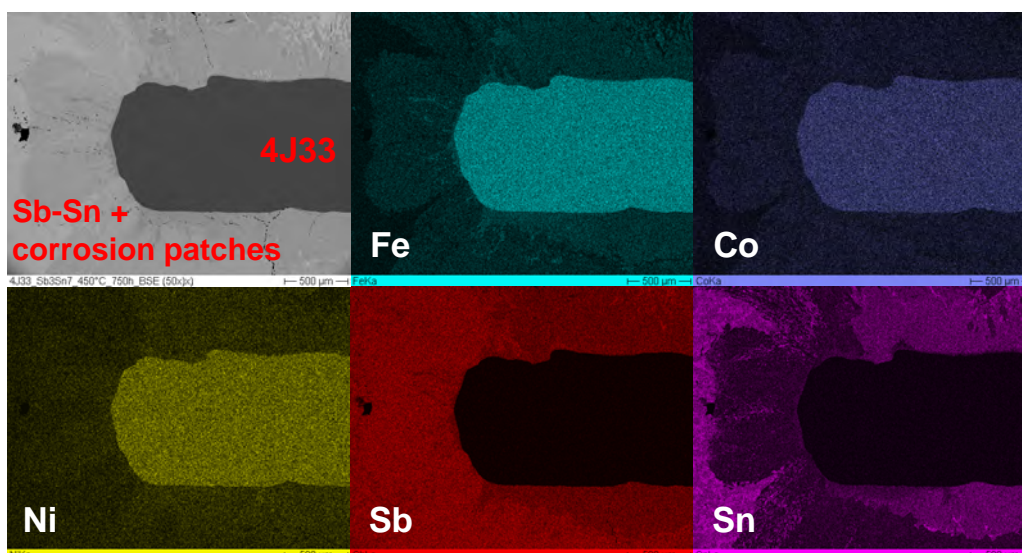


**Figure 4.27:** BSE image and EDS element mapping images of cross-section of 4J33 Kovar alloy after 750 h exposure in liquid  $\text{Sb}_3\text{Sn}_7$  at 450 °C.

Line scan across 4J33 Kovar alloy after 750 h exposure in liquid  $\text{Sb}_3\text{Sn}_7$  at 450 °C was also performed. The results (in Figure 4.28) illustrate that several Fe-Co-Ni-Sb-Sn patches with different elemental compositions are formed as corrosion products. Compared with the brighter patch(zone ③ in Figure 4.28) formed between the dark patch at the corrosion front and the attached Sb-Sn alloy, the dark patch formed at the corrosion front (zone ② in Figure 4.28) possesses relatively higher Fe, Ni and Sn contents but relatively lower Co and Sb contents.

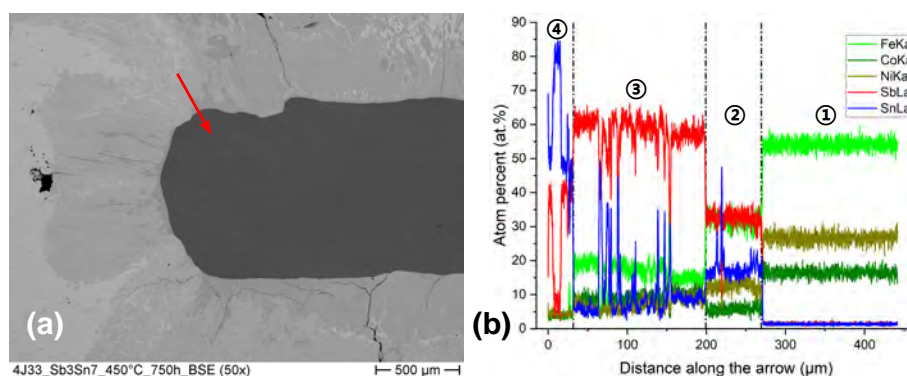


**Figure 4.28:** (a) Line scan across 4J33 Kovar alloy after 750 h exposure in liquid  $\text{Sb}_3\text{Sn}_7$  at 450 °C with (b) results of composition analysis, where ① is the unmodified 4J33 alloy, ② is the dark patch formed at the corrosion front, ③ is the intermediate corrosion product with a brighter color and ④ is the attached Sb-Sn alloy.

It can be seen from Co-Sb and Co-Sn phase diagrams [148, 149], at the temperature of 450 °C, both Sb and Sn could react with Co, form multiple intermetallic compounds including  $\text{CoSb}$ ,

CoSb<sub>2</sub>, CoSb<sub>3</sub>, Co<sub>3</sub>Sn<sub>2</sub>, CoSn and CoSn<sub>2</sub>. Compared with steels mentioned before, 4J33 alloy suffered much severer corrosion attack after exposure in liquid Sb<sub>3</sub>Sn<sub>7</sub>, which might be explained by the higher amounts of Ni and Co with the absence of Cr.

### Pure metal (Mo and Cr)

The BSE image and EDS element mapping images of cross-section of Mo metal after 750 h exposure in liquid Sb<sub>3</sub>Sn<sub>7</sub> are shown in Figure 4.29. Obviously, a layer of Sb-Sn alloy was attached on the surface of Mo metal, which is the same as the case of all other metallic specimens. However, Mo metal still preserved its original shape. Arsenic (As) was found at the interface between Mo metal and Sb-Sn alloy (Figure 4.29), which is probably a result of contaminated Sb metal. As a result, after 750 h exposure in liquid Sb<sub>3</sub>Sn<sub>7</sub>, many tiny corrosion pits can be seen, the Mo was slightly attacked. However, neither notable penetration of Sb-Sn alloy into Mo metal nor distinct depletion/destruction of Mo metal can be observed in this case.

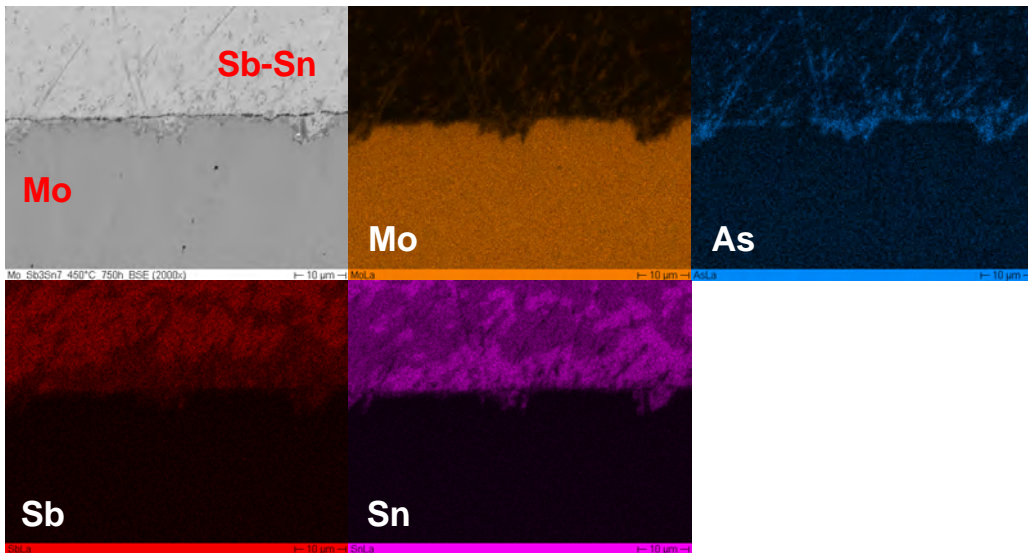


**Figure 4.29:** BSE image and EDS element mapping images of cross-section of Mo metal after 750 h exposure in liquid Sb<sub>3</sub>Sn<sub>7</sub> at 450 °C.

The line scan in Figure 4.30 reveals that the Sb-Sn alloy (zone ② in Figure 4.30) attached on the surface of Mo metal (zone ① in Figure 4.30) also contains a small quantity of Mo with As, which might be the reason for the corrosion attack during the exposure in liquid Sb<sub>3</sub>Sn<sub>7</sub>.

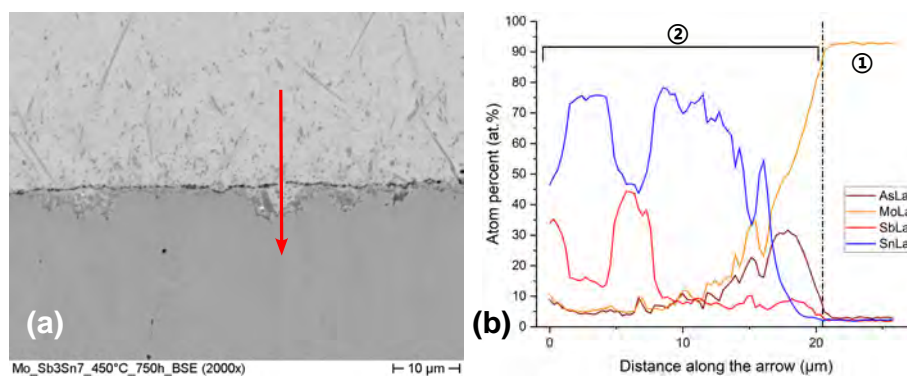


**Figure 4.30:** (a) Line scan across Mo metal after 750 h exposure in liquid  $\text{Sb}_3\text{Sn}_7$  at 450 °C with (b) results of composition analysis, where ① is the unmodified Mo and ② is the Sb-Sn alloy + corroded Mo.

Compared with Sb and Sn, As seems to be more aggressive, and according to As-Mo phase diagram [150], at the temperature of 450 °C, As reacts with Mo and forms  $\text{As}_5\text{Mo}$ . Besides, both Sb and Sn could react with Mo and form several different intermetallic compounds according to Mo-Sb and Mo-Sn phase diagrams [151, 152]. Therefore, the corrosion occurred on Mo metal could be triggered by the arsenic contamination in Sb-Sn accompanied by the reaction with Sb-Sn alloy. Nevertheless, the corrosion rate of Mo in liquid  $\text{Sb}_3\text{Sn}_7$  is quite insignificant, the maximal corrosion depth is barely 10  $\mu\text{m}$ , which results in a maximum calculated corrosion rate of 0.01  $\mu\text{m}/\text{h}$ .

After exposure in liquid  $\text{Sb}_3\text{Sn}_7$ , Cr partially forms a corrosion product at the interface between test specimen and Sb-Sn alloy (seen in Figure 4.31 and 4.32). Like in the Mo case, an enrichment of As can be observed in the corroded area of Cr as well, which might be brought by contaminated Sb as well. After 750 h exposure, the maximal corrosion depth of liquid  $\text{Sb}_3\text{Sn}_7$  into Cr is around 400  $\mu\text{m}$ , which leads to a maximum calculated corrosion rate of 0.53  $\mu\text{m}/\text{h}$  for Cr. In other words, Cr also suffer corrosion attack in liquid  $\text{Sb}_3\text{Sn}_7$  with a small amount of As.

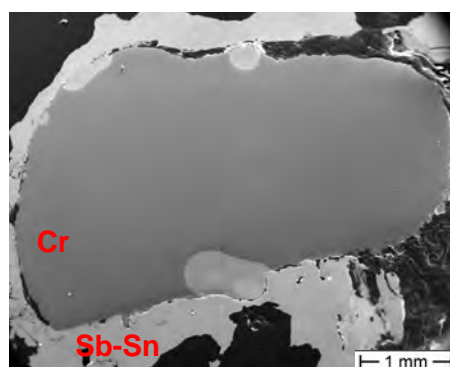


**Figure 4.31:** SE image of cross-section of Cr metal after 750 h in liquid  $\text{Sb}_3\text{Sn}_7$  at 450 °C.

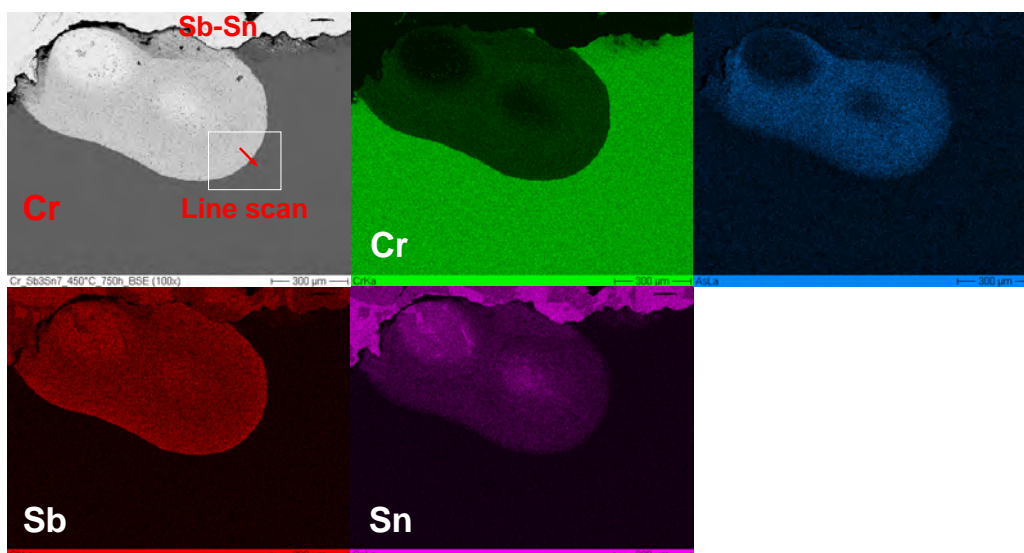


**Figure 4.32:** BSE image and EDS element mapping images of cross-section of Cr metal after 750 h exposure in liquid  $\text{Sb}_3\text{Sn}_7$  at 450 °C.

According to the Cr-Sb and Cr-Sn phase diagrams [144, 145], Cr only react with Sb, form CrSb and CrSb<sub>2</sub> intermetallic compounds. Combined with the results of the line scan (seen in Figure 4.33), the main composition of the corrosion product (Cr:Sb = 1:1, molar ratio) formed at the interface is probably CrSb. The black spots are the chromium oxide precipitates formed at the grain boundary during the production process.

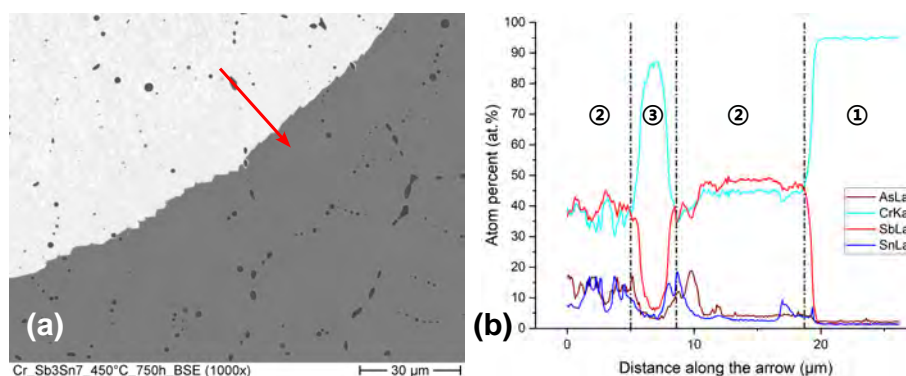


**Figure 4.33:** (a) Line scan across Cr metal after 750 h exposure in liquid  $\text{Sb}_3\text{Sn}_7$  at 450 °C with (b) results of composition analysis, where ① is the unmodified Cr, ② is the corrosion product formed at interface and ③ is the chromium oxides at the grain boundary.

### MAX-phase on $\text{Al}_2\text{O}_3$ -substrate

The SE image of surface morphology of  $\text{Ti}_2\text{AlC}$  on  $\text{Al}_2\text{O}_3$ -substrate after 750 h exposure in liquid  $\text{Sb}_3\text{Sn}_7$  (Figure 4.34) shows that the surface of  $\text{Ti}_2\text{AlC}$ - $\text{Al}_2\text{O}_3$  specimen is attached by some small

bright particles after the exposure. Nevertheless, the surface of  $Ti_2AlC-Al_2O_3$  specimen remains smooth and perfect after exposure in liquid  $Sb_3Sn_7$ , no depletion or destruction of  $Ti_2AlC-Al_2O_3$  specimen can be observed in this case.

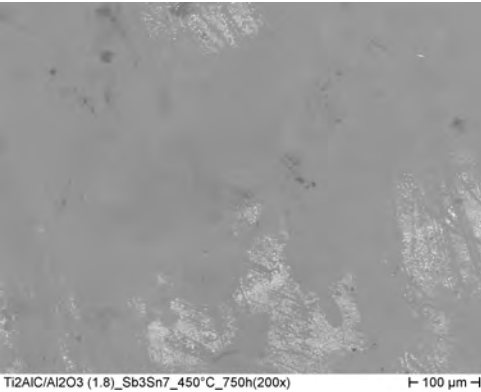


**Figure 4.34:** SE image of surface morphology of  $Ti_2AlC$  on  $Al_2O_3$ -substrate after 750 h exposure in liquid  $Sb_3Sn_7$  at 450 °C.

The results of EDS analysis (Figure 4.35) illustrate that the small bright particles attached on the surface of  $Ti_2AlC-Al_2O_3$  specimen are Sb and Sn drops. The results also indicate that the surface of  $Ti_2AlC$  specimen on  $Al_2O_3$ -substrate suffers no attack in liquid  $Sb_3Sn_7$  and remains uncorroded after 750 h exposure.

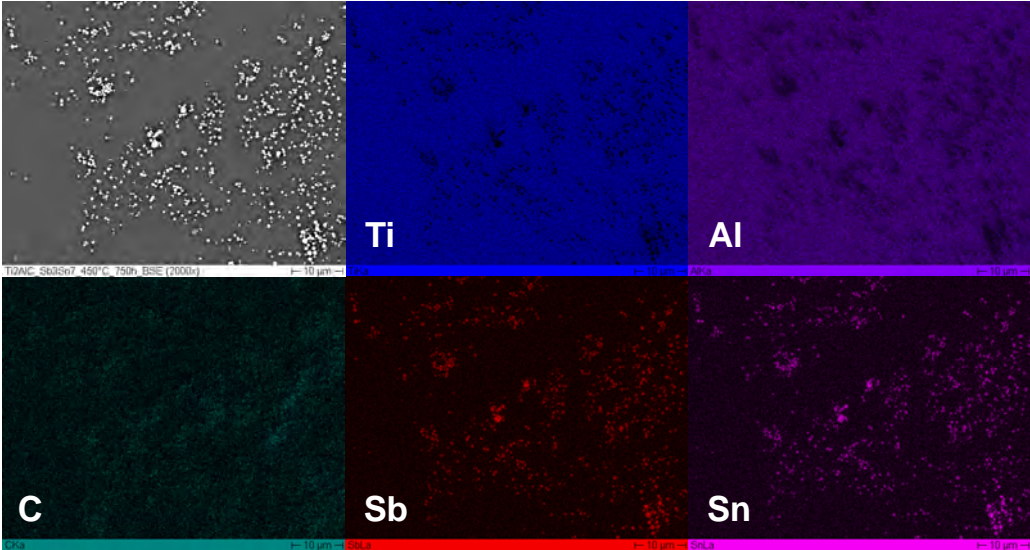


**Figure 4.35:** BSE image and EDS element mapping images of surface morphology of  $Ti_2AlC$  on  $Al_2O_3$ -substrate after 750 h exposure in liquid  $Sb_3Sn_7$  at 450 °C.

The other two MAX-phases ( $Ti_3AlC_2$  and  $Cr_2AlC$ ) (seen in Figure 4.36 and 4.37) show much similar corrosion performance to  $Ti_2AlC$  on  $Al_2O_3$ -substrate after exposure in liquid  $Sb_3Sn_7$ .

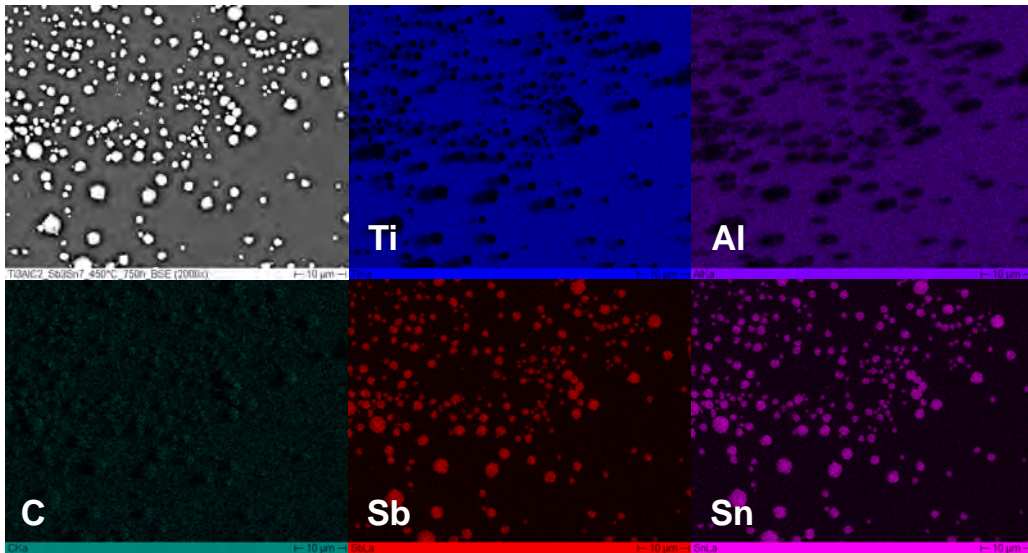


**Figure 4.36:** BSE image and EDS element mapping images of surface morphology of  $Ti_3AlC_2$  on  $Al_2O_3$ -substrate after 750 h exposure in liquid  $Sb_3Sn_7$  at 450 °C.

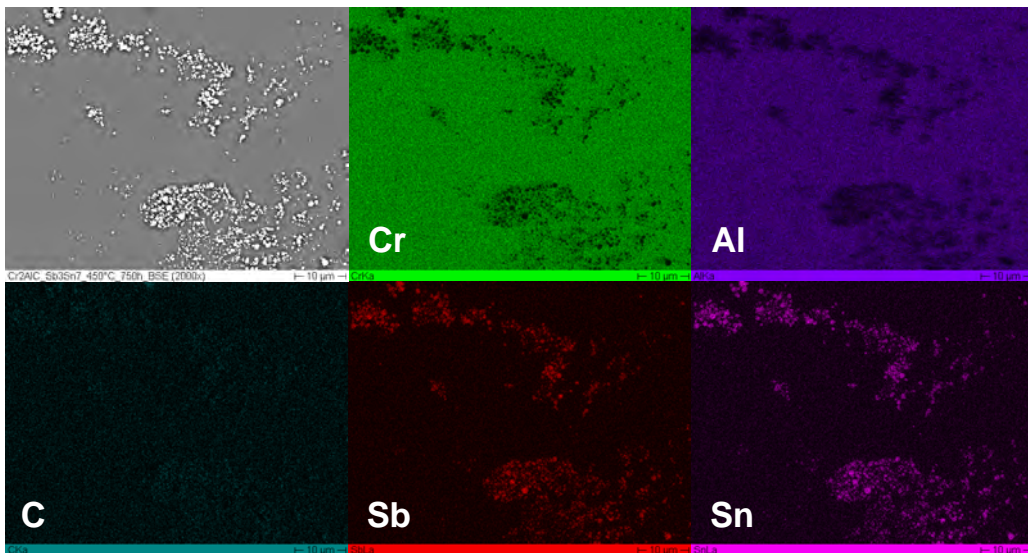


**Figure 4.37:** BSE image and EDS element mapping images of surface morphology of  $Cr_2AlC$  on  $Al_2O_3$ -substrate after 750 h exposure in liquid  $Sb_3Sn_7$  at 450 °C.

## Results in $SbBi_9$

### Fe-Cr steel (T91 ferritic steel)

As shown in Figure 4.38, after 750 h exposure in liquid  $SbBi_9$ , both Sb and Bi reacted with T91 ferritic steel, which resulted in a corrosion layer at the specimen surface (gray parts in the image) and a layer of Sb-Bi (bright parts in this image) attached on the surface of remaining T91

ferritic steel. In this case, no local deeper attack can be observed, the corrosion depth of liquid  $\text{SbBi}_9$  into T91 steel ferritic steel is only around  $30\ \mu\text{m}$ , which means the maximum calculated corrosion rate for this material in liquid  $\text{SbBi}_9$  is only  $0.04\ \mu\text{m}/\text{h}$ . Therefore, compared with T91 ferritic steel in liquid  $\text{Sb}_3\text{Sn}_7$ , the corrosion caused by liquid  $\text{SbBi}_9$  is much milder.

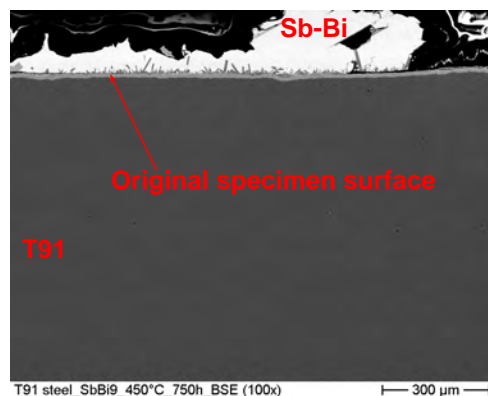


**Figure 4.38:** BSE image of cross-section of T91 ferritic steel after 750 h exposure in liquid  $\text{SbBi}_9$  at  $450\ ^\circ\text{C}$ .

The BSE image and EDS element mapping images of cross-section of T91 ferritic steel after 750 h exposure in liquid  $\text{SbBi}_9$  (Figure 4.39) illustrate that in this case, both Fe and Cr in T91 ferritic steel are depleted in the corrosion products formed at the corrosion front, which exhibits an enrichment of Sb. Besides, Figure 4.39 also manifests that after exposure in liquid  $\text{SbBi}_9$ , a thin Cr-rich layer and a dendrite-like Fe-rich layer can be observed at the interface between test specimen and liquid Sb-Bi alloy ( $\text{SbBi}_9$ ).

Moreover, the penetration of Bi into the T91 ferritic steel is significantly reduced or almost even missing compared with the Sb penetration.

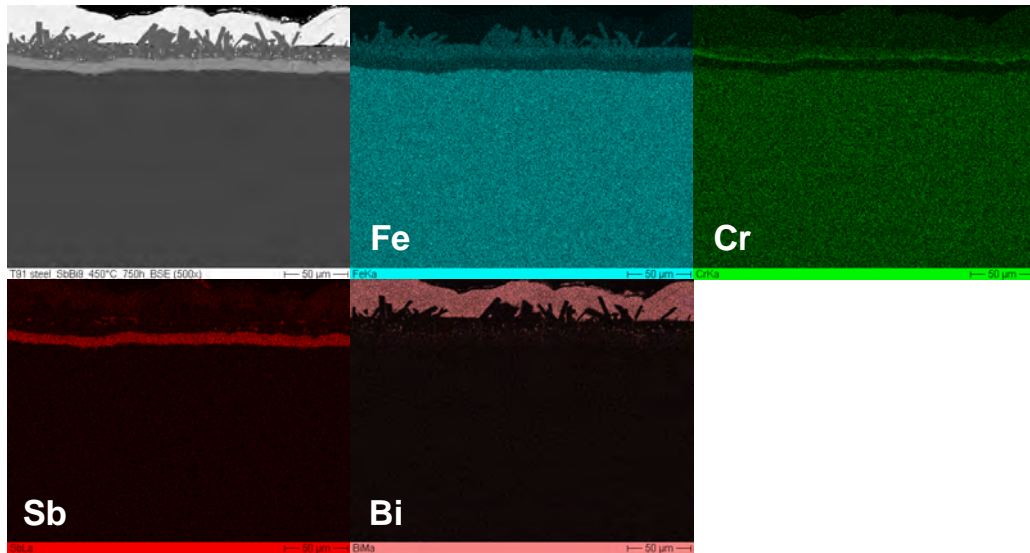


**Figure 4.39:** BSE image and EDS element mapping images of cross-section of T91 ferritic steel after 750 h exposure in liquid  $\text{SbBi}_9$  at 450 °C.

The line scan across T91 ferritic steel after 750 h exposure in liquid  $\text{SbBi}_9$  at 450 °C (Figure 4.40) confirms the results of the EDS mapping in Figure 4.39. Three Fe-Cr-Sb layers with different elemental compositions are formed as corrosion products. The Fe-Cr-Sb layer formed at the corrosion front (zone ② in Figure 4.40) presents low Fe and Cr contents but a much higher Sb content. Compared with this Fe-Cr-Sb layer, the thinnest Fe-Cr-Sb corrosion layer formed in the middle (zone ③ in Figure 4.40) is a Cr-rich layer, which also exhibits a higher Fe content. The outer Fe-Cr-Sb corrosion layer with dendrites (zone ④ in Figure 4.40) possesses an extremely high Fe content but a much lower Sb content. Additionally, the reduced penetration of Bi when compared with Sb is as well confirmed by this line scan.

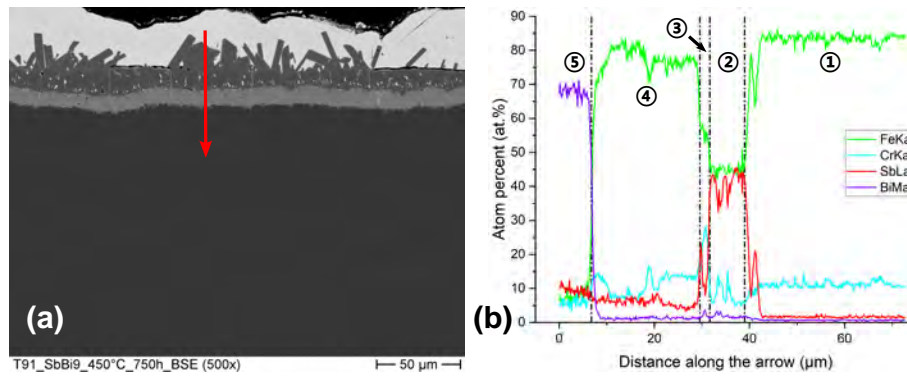


**Figure 4.40:** (a) Line scan across T91 ferritic steel after 750 h exposure in liquid  $\text{SbBi}_9$  at 450 °C with (b) results of composition analysis, where ① is the unmodified T91, ② is the corrosion layer at the corrosion front, ③ is the intermediate Cr-rich layer, ④ is the outer corrosion layer with dendrites and ⑤ is the attached Sb-Bi alloy.

The components in the corrosion products can also be predicted with the help from phase diagrams of the main constituents in steel (Fe, Cr) with Sb or Bi. According to the previous studies [153–155], Fe and Cr do not form stable phases with Bi and the solubility of Fe and Cr is very small (only 0.005 at.% Fe dissolves in Bi) at the test conditions. Therefore, Fe and Cr in T91 ferritic steel only react with Sb in liquid  $\text{SbBi}_9$  and form Fe-Sb and Cr-Sb intermetallic compounds. Combined with the results of the line scan, the main composition of the corrosion layer formed at the corrosion front (Fe:Sb = 1:1, molar ratio) could be FeSb.

### Fe-Cr-Ni steel (SS304 and SS316L)

As shown in Figure 4.41, after 750 h exposure in liquid  $\text{SbBi}_9$ , Sb-Bi alloy reacted with the steel, resulted in a corrosion attack (grey parts in this image) and an attached layer of Sb-Bi alloy (brighter parts in this image) throughout the surface of remaining SS304. The corrosion depth into SS304 is only around 20  $\mu\text{m}$  without any local deep attack, which leads to a maximum calculated corrosion rate of 0.03  $\mu\text{m}/\text{h}$  for this material. Compared with SS304 in liquid  $\text{Sb}_3\text{Sn}_7$ , the corrosion attack from liquid  $\text{SbBi}_9$  is much milder, which corresponds the results on T91 ferritic steel.

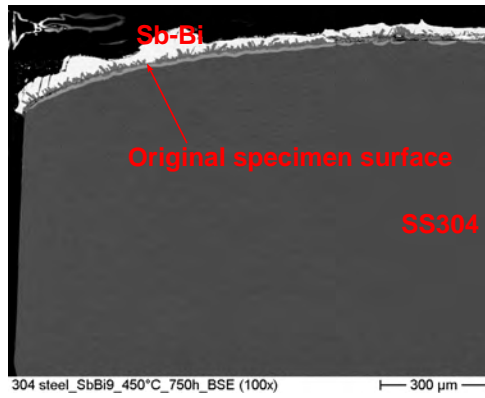


**Figure 4.41:** BSE image of cross-section of SS304 after 750 h exposure in liquid SbBi<sub>9</sub> at 450 °C.

The BSE image and EDS element mapping images of cross-section of SS304 after 750 h exposure in liquid SbBi<sub>9</sub> (Figure 4.42) reveal that all main constituents (Fe, Cr and Ni) of SS304 are depleted in the corrosion front. Besides, EDS element mapping images also manifest that after exposure in liquid SbBi<sub>9</sub>, a remarkable Cr-rich layer and a dendrite-like Fe- and Cr-rich layer can be observed at the interface between the SS304 steel specimen and liquid SbBi<sub>9</sub>, respectively. Moreover, Ni is found in the Bi-rich layer attached on top. Additionally, compared with Sb, the penetration of Bi into SS304 is as well significantly reduced or almost even missing.

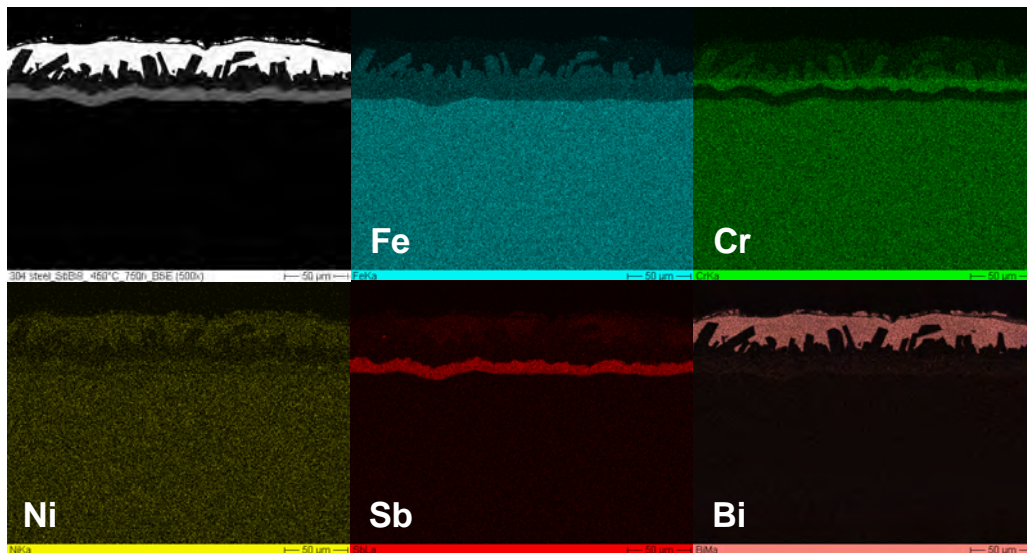


**Figure 4.42:** BSE image and EDS element mapping images of cross-section of SS304 after 750 h exposure in liquid SbBi<sub>9</sub> at 450 °C.

The line scan (Figure 4.43) confirms three Fe-Cr-Ni-Sb-Bi layers with different elemental compositions as corrosion products. All Fe, Cr and Ni in SS304 are depleted at the corrosion front (zone ② in Figure 4.43) while Sb is enriched. A layer with dendrites (zone ④ in

Figure 4.43), which presents the highest Fe content a medium Cr content is formed at the outer corrosion region. Besides, the generation of an intermediate Cr-rich layer (zone ③ in Figure 4.43), which also exhibits a higher Fe but a much lower Sb content can also be observed in between those two layers. Additionally, Ni can not only be detected in those corrosion products but also be found in the attached Bi-rich layer on top (zone ⑤ in Figure 4.43).

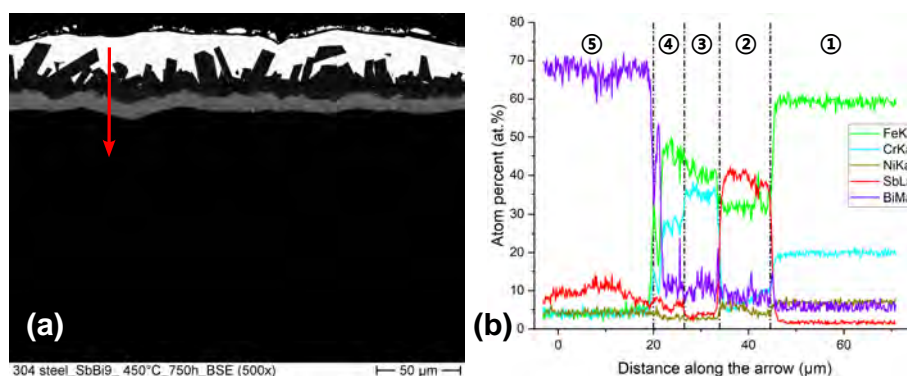


**Figure 4.43:** (a) Line scan across SS304 after 750 h exposure in liquid  $\text{SbBi}_9$  at 450 °C with (b) results of composition analysis, where ① is the unmodified SS304, ② is the corrosion layer at the corrosion front, ③ is the intermediate Cr-rich layer, ④ is the outer corrosion layer with dendrites and ⑤ is the attached Sb-Bi alloy.

According to Ni-Sb and Ni-Bi phase diagrams [146, 156, 157], at the temperature of 450 °C, both Sb and Bi could react with Ni and form multiple intermetallic compounds including  $\text{Ni}_3\text{Sb}$ ,  $\text{Ni}_7\text{Sb}_3$ ,  $\text{NiSb}$ ,  $\text{NiSb}_2$ ,  $\text{NiBi}$  and  $\text{NiBi}_3$ . From the experimental results, no dedicated phases are explicitly detected.

The corrosion behavior of SS316L (displayed in Figure 4.44, 4.45 and 4.46) shows great similarity to that of SS304: slightly corroded and penetrated by Sb-Bi alloy, the formation of a Cr-rich intermediate layer and the formation of a corrosion layer with dendrites in outer corrosion region. Besides, the corrosion depth and maximum calculated corrosion rate of SS316L is almost the same for SS304 (20  $\mu\text{m}$  and 0.03  $\mu\text{m}/\text{h}$ , respectively).

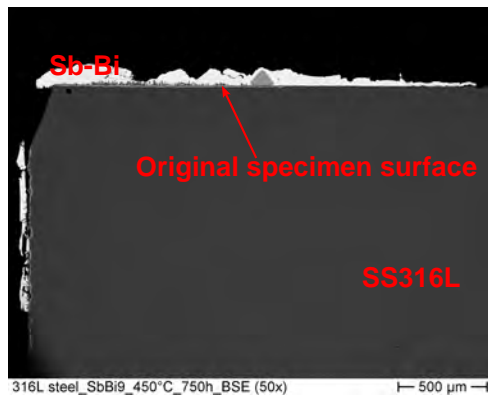


**Figure 4.44:** BSE image of cross-section of SS316L after 750 h exposure in liquid SbBi<sub>9</sub> at 450 °C.

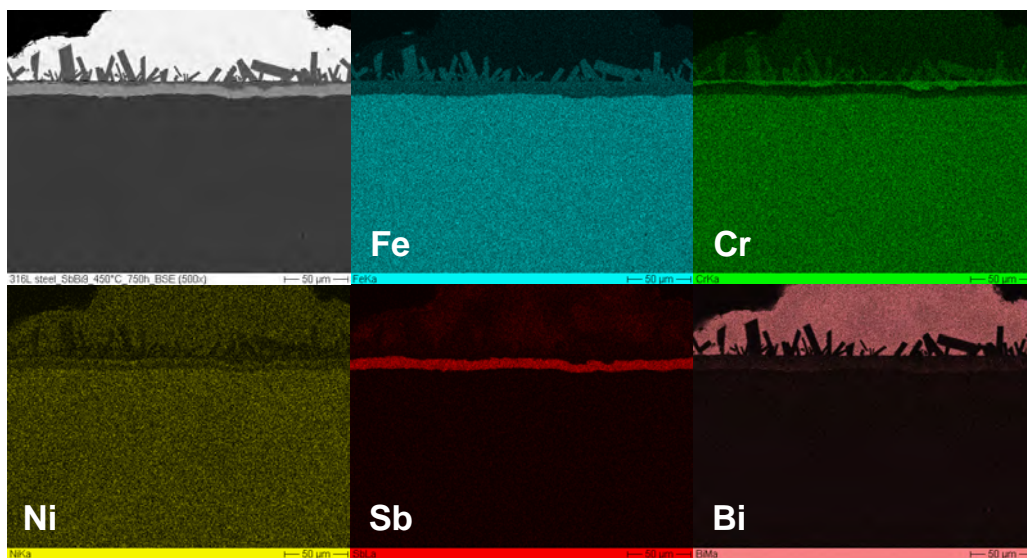


**Figure 4.45:** BSE image and EDS element mapping images of cross-section of SS316L after 750 h exposure in liquid SbBi<sub>9</sub> at 450 °C.

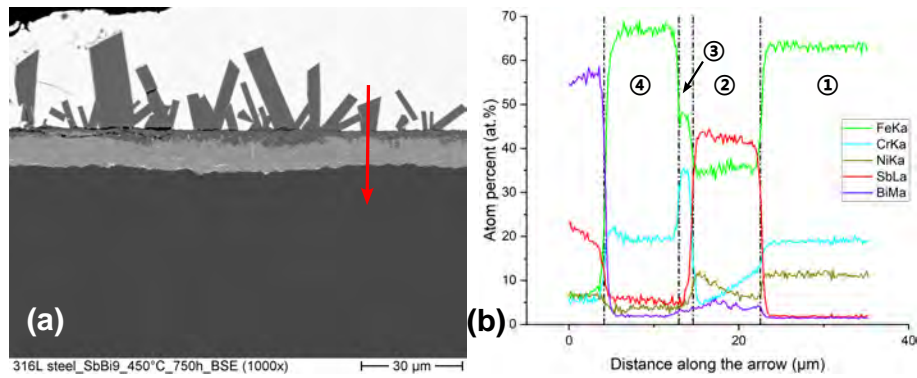


**Figure 4.46:** (a) Line scan across SS316L after 750 h exposure in liquid  $\text{SbBi}_9$  at 450 °C with (b) results of composition analysis, where ① is the unmodified SS316L, ② is the corrosion layer at the corrosion front, ③ is the intermediate Cr-rich layer, ④ is the outer corrosion layer with dendrites and ⑤ is the attached Sb-Bi alloy.

The results also reveal that the behavior of Fe-Cr-Ni steels (SS304 and SS316L) and Fe-Cr steel (T91 ferritic steel) is quite similar, for all steels, the structure of corrosion layers with a Sb-rich layer at front, followed by a Cr-rich layer and a layer with dendrites can be observed. Besides, the same as T91 ferritic steel, the main composition of the corrosion layer formed at the corrosion front (Fe:Sb = 1:1, molar ratio) on Fe-Cr-Ni steels (SS304 and SS316L) is probably FeSb.

### Fe-Co-Ni alloy (4J33 Kovar alloy)

The BSE image and EDS element mapping images of cross-section of 4J33 Kovar alloy after 750 h exposure in liquid  $\text{SbBi}_9$  (Figure 4.47) illustrate that 4J33 Kovar alloy is fully covered by Sb-Bi alloy. Compared with 4J33 Kovar alloy in liquid  $\text{Sb}_3\text{Sn}_7$ , after 750 h exposure in liquid  $\text{SbBi}_9$ , the original shape of 4J33 Kovar alloy is still maintained. However, 4J33 Kovar alloy undergoes different corrosion mechanisms in liquid  $\text{SbBi}_9$ . As shown in Figure 4.47, only Ni is distinctly depleted and reacts with Sb in liquid  $\text{SbBi}_9$  to form a Ni-Sb layer as corrosion product. Besides, penetration of Sb and Bi can be observed. It can be seen from the EDS images in Figure 4.47 that almost the entire 4J33 Kovar alloy is penetrated by Bi, which is a direct contradiction to the results on steel specimens (T91, SS304 and SS316L) exposed in liquid  $\text{SbBi}_9$ . The corrosion depth of 4J33 Kovar alloy is approximately 800  $\mu\text{m}$ , which leads to a maximum calculated corrosion rate of 1.07  $\mu\text{m}/\text{h}$  for this material.

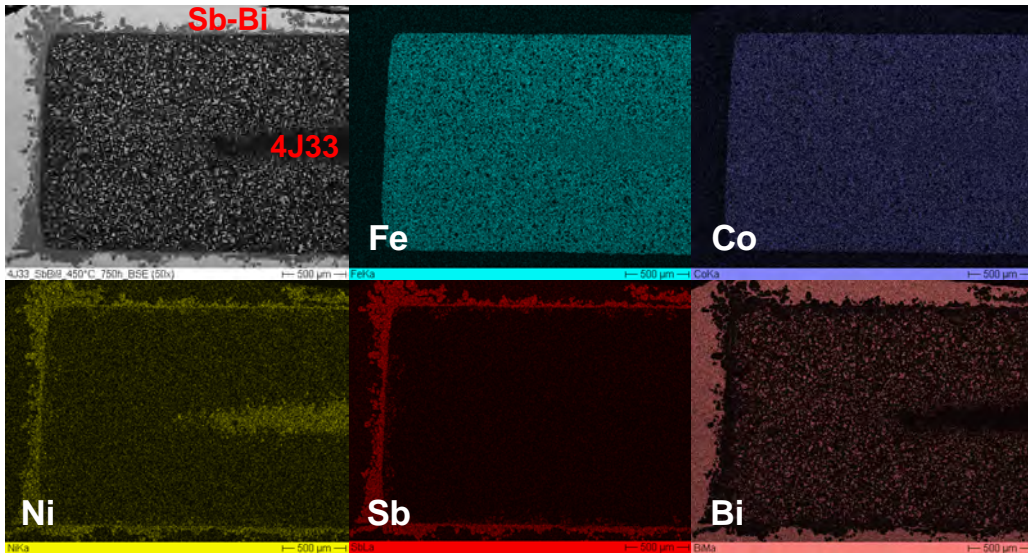


**Figure 4.47:** BSE image and EDS element mapping images of cross-section of 4J33 Kovar alloy after 750 h exposure in liquid  $\text{SbBi}_9$  at 450 °C.

The results of the line scan (Figure 4.48) manifest the formation of Ni-Sb layer (zone ③ in Figure 4.48) as corrosion product due to the prominent solubility and diffusion of Ni in 4J33 Kovar alloy. Besides, a remarkable penetration of Bi (zone ① in Figure 4.48) is also observed in 4J33 Kovar alloy, which can be probably attributed to the high selective solubility of Ni in 4J33 Kovar alloy and the reaction of Ni with Sb in liquid  $\text{SbBi}_9$ .

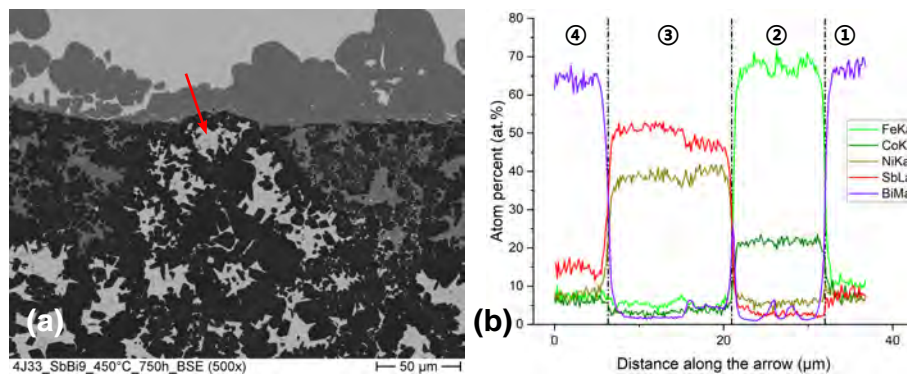


**Figure 4.48:** (a) Line scan across 4J33 Kovar alloy after 750 h exposure in liquid  $\text{SbBi}_9$  at 450 °C with (b) results of composition analysis, where ① is the penetrated Bi, ② is the destroyed 4J33 alloy, ③ is the corrosion products attached on specimen's surface and ④ is the attached Sb-Bi alloy + corrosion products.

### Pure metal (Mo and Cr)

The BSE image and EDS element mapping images of the cross-section of Mo metal after 750 h

exposure in liquid  $\text{SbBi}_9$  (Figure 4.49) illustrate that after the exposure, although the surface of Mo metal was attacked by Sb-Bi alloy, there is still a clear interface. Figure 4.49 also illustrates the enrichment of arsenic (As) at the interface between Mo and Sb-Bi alloy, which comes from the contamination in Sb metal. Moreover, according to Figure 4.49, after 750 h exposure in liquid  $\text{SbBi}_9$ , Sb-Bi alloy is not able to penetrate Mo metal and no distinct depletion or destruction of Mo metal can be observed. Compared with Mo metal after exposure in liquid  $\text{Sb}_3\text{Sn}_7$ , the original surface of Mo metal still remains in good condition in this case.

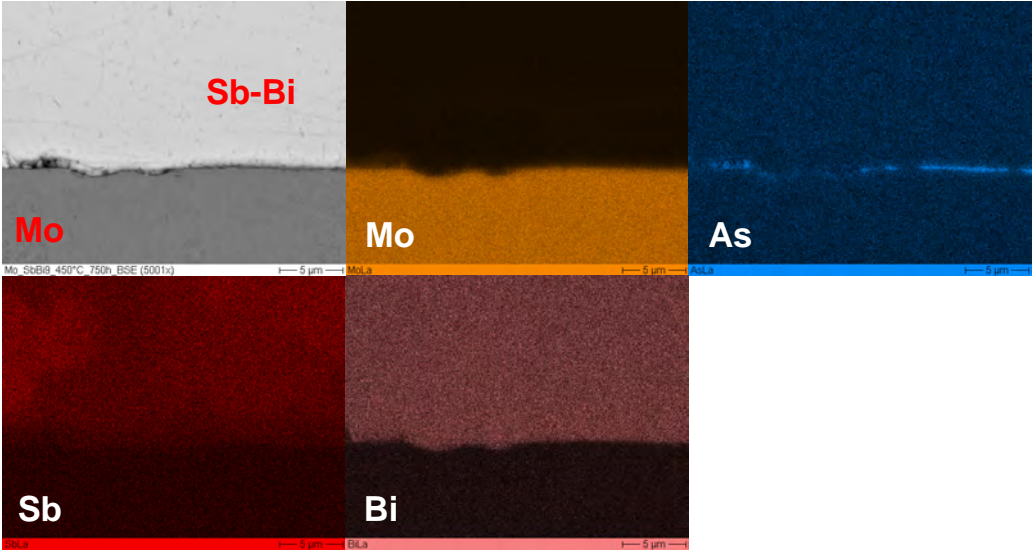


**Figure 4.49:** BSE image and EDS element mapping images of cross-section of Mo metal after 750 h exposure in liquid  $\text{SbBi}_9$  at 450 °C.

The results of the line scan (Figure 4.50) manifest the enrichment of As at the surface of Mo metal. Nevertheless, no penetration of heavy metal (Sb and Bi) into Mo metal specimen can be found and no enrichment of Mo in the Sb-Bi alloy is observed.

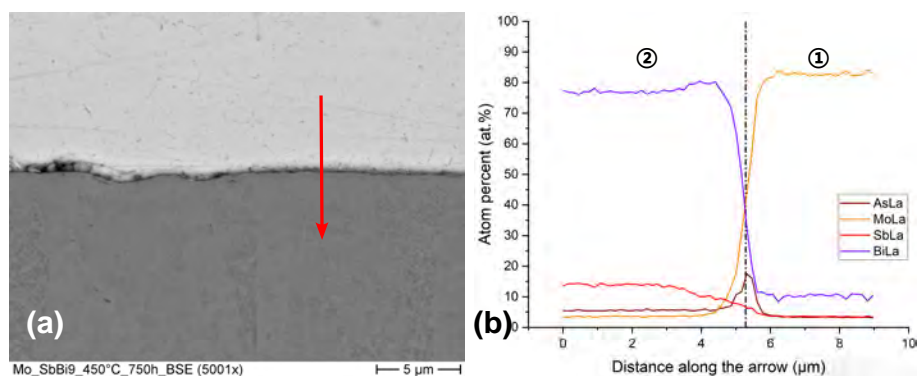


**Figure 4.50:** (a) Line scan across Mo metal after 750 h exposure in liquid  $\text{SbBi}_9$  at 450 °C with (b) results of composition analysis, where ① is the unmodified Mo and ② is the Sb-Bi alloy.

Compared to line scans in Figure 4.30, the quantity of Mo in the Sb-Bi alloy (Figure 4.50) attached on the surface of Mo metal is much lower. In addition, no visible corrosion attack can be observed on Mo metal after exposure in liquid  $\text{SbBi}_9$ , while Mo suffers visible corrosion attack in liquid  $\text{Sb}_3\text{Sn}_7$ . This is probably due to the relative amount of Sb in  $\text{Sb}_3\text{Sn}_7$  is much higher than that in  $\text{SbBi}_9$ , hence the amount of As is higher in  $\text{Sb}_3\text{Sn}_7$  as well and might have a higher activity.

For another pure Metal, Cr (displayed in Figure 4.51 and 4.52), a corrosion layer depleted in Cr can be locally observed at the interface between test specimen and Sb-Bi alloy. However, in this case, no obvious enrichment of As can be observed in the corroded Cr. After 750 h exposure, the maximal corrosion depth of liquid  $\text{SbBi}_9$  into Cr is only around 15  $\mu\text{m}$ , which leads to a maximum calculated corrosion rate of 0.02  $\mu\text{m}/\text{h}$  for Cr. Hence, Cr is slightly corroded in liquid  $\text{SbBi}_9$ .

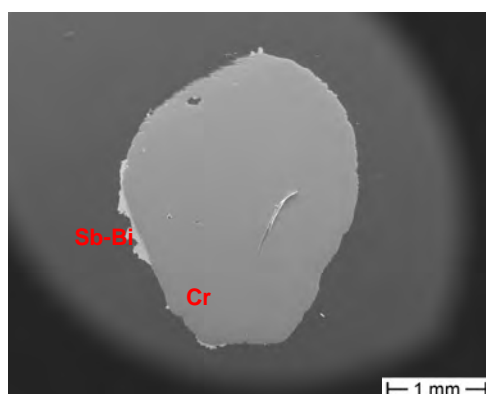


**Figure 4.51:** SE image and EDS element mapping images of cross-section of Cr metal after 750 h exposure in liquid  $\text{SbBi}_9$  at 450 °C.

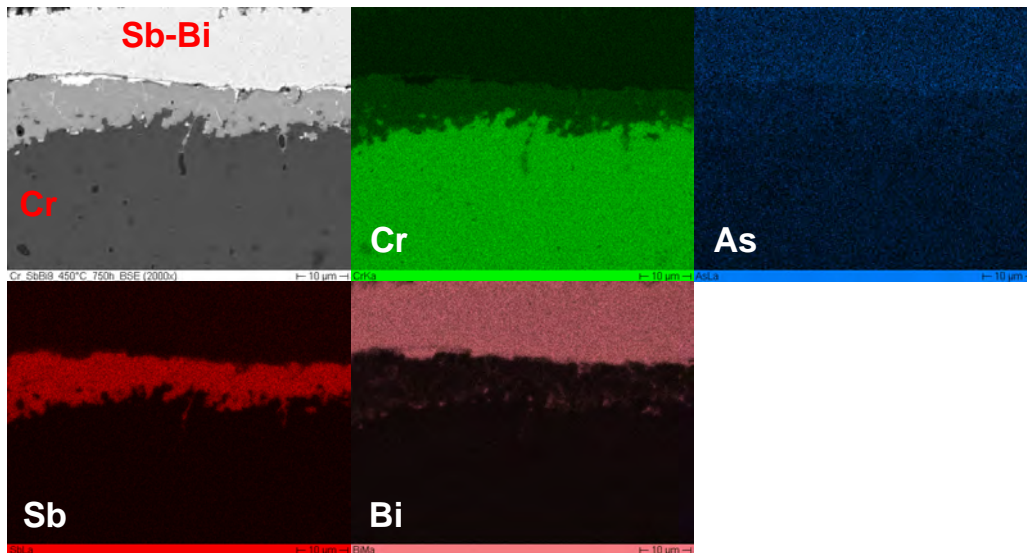


**Figure 4.52:** BSE image and EDS element mapping images of cross-section of Cr metal after 750 h exposure in liquid  $\text{SbBi}_9$  at 450 °C.

It can be seen from Cr-Sb and Cr-Bi phase diagrams [144, 155] that at the temperature of 450 °C, no intermetallic Cr-Bi phases occurred, Cr only react with Sb, form  $\text{CrSb}$  and  $\text{CrSb}_2$  intermetallic compounds. According to the line scan results (displayed in Figure 4.53), the main composition of the corrosion layer ( $1:1 < \text{Cr:Sb} < 1:2$ , molar ratio) formed at the interface might be a mixture of  $\text{CrSb}$  and  $\text{CrSb}_2$ .

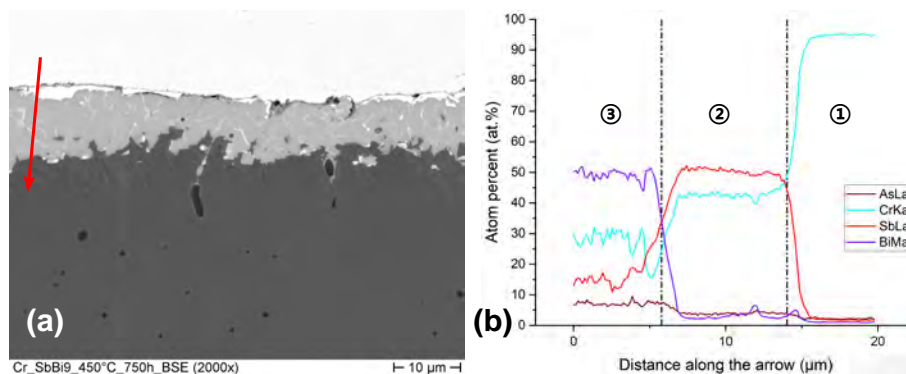


**Figure 4.53:** (a) Line scan across Cr metal after 750 h exposure in liquid  $\text{Sb}_3\text{Sn}_7$  at 450 °C with (b) results of composition analysis, where ① is the unmodified Cr, ② is the corrosion product formed at interface and ③ is the chromium oxides at the grain boundary.

### MAX-phase on $\text{Al}_2\text{O}_3$ -substrate

The SE image of surface morphology of  $\text{Ti}_2\text{AlC}$  on  $\text{Al}_2\text{O}_3$ -substrate after 750 h exposure in liquid  $\text{SbBi}_9$  are shown in Figure 4.54. Apparently, after 750 h exposure in liquid  $\text{SbBi}_9$ , small bright

particles adhere to the surface of  $Ti_2AlC-Al_2O_3$  specimen. However, compared with  $Ti_2AlC-Al_2O_3$  specimen in liquid  $Sb_3Sn_7$ , in this case, the number of the small particles attached on the surface of  $Ti_2AlC-Al_2O_3$  specimen is much lower.

Nevertheless, after exposure in liquid  $SbBi_9$ , the surface of  $Ti_2AlC-Al_2O_3$  specimen also remains smooth and intact, no depletion or destruction of  $Ti_2AlC-Al_2O_3$  specimen can be found.



**Figure 4.54:** SE image of surface morphology of  $Ti_2AlC$  on  $Al_2O_3$ -substrate after 750 h exposure in liquid  $SbBi_9$  at 450 °C.

It can be seen from Figure 4.55 that the small bright particles attached on specimen’s surface are remained drops from  $Sb-Bi$  alloy, the results also manifest that the surface of  $Ti_2AlC$  specimen on  $Al_2O_3$ -substrate suffer no attack and remains unattacked after 750 h exposure in liquid  $SbBi_9$ .

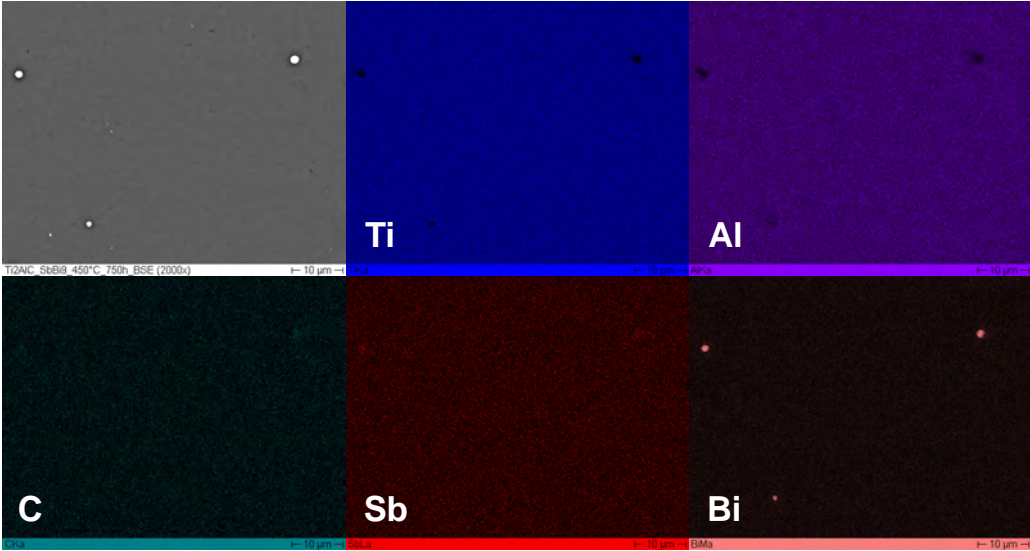


**Figure 4.55:** BSE image and EDS element mapping images of surface morphology of  $Ti_2AlC$  on  $Al_2O_3$ -substrate after 750 h exposure in liquid  $SbBi_9$  at 450 °C.

The other two MAX-phases ( $Ti_3AlC_2$  and  $Cr_2AlC$ ) (seen in Figure 4.56 and 4.57) show a very

similar corrosion performance like the  $Ti_2AlC$  on  $Al_2O_3$ -substrate after exposure in liquid  $SbBi_9$ .

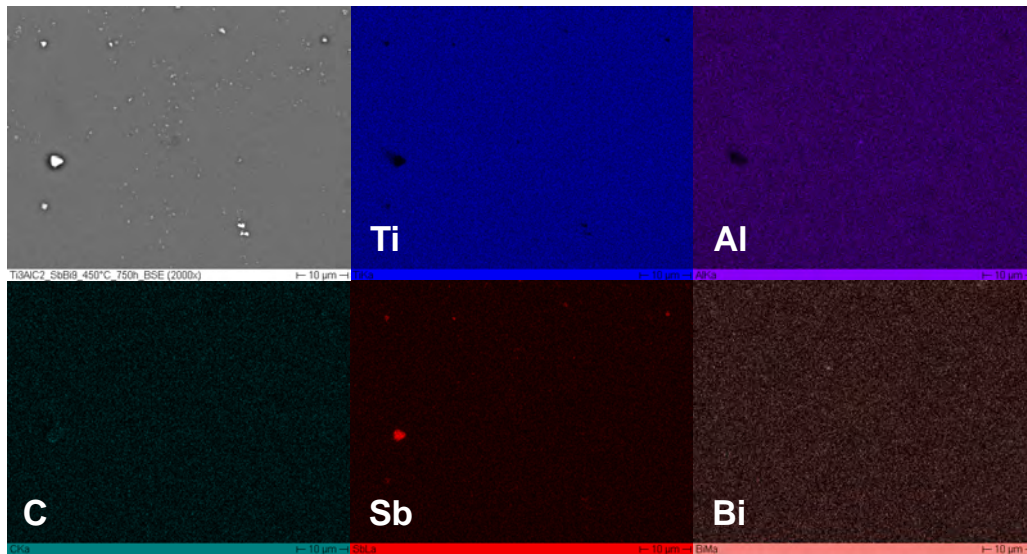


**Figure 4.56:** BSE image and EDS element mapping images of surface morphology of  $Ti_3AlC_2$  on  $Al_2O_3$ -substrate after 750 h exposure in liquid  $SbBi_9$  at 450 °C.

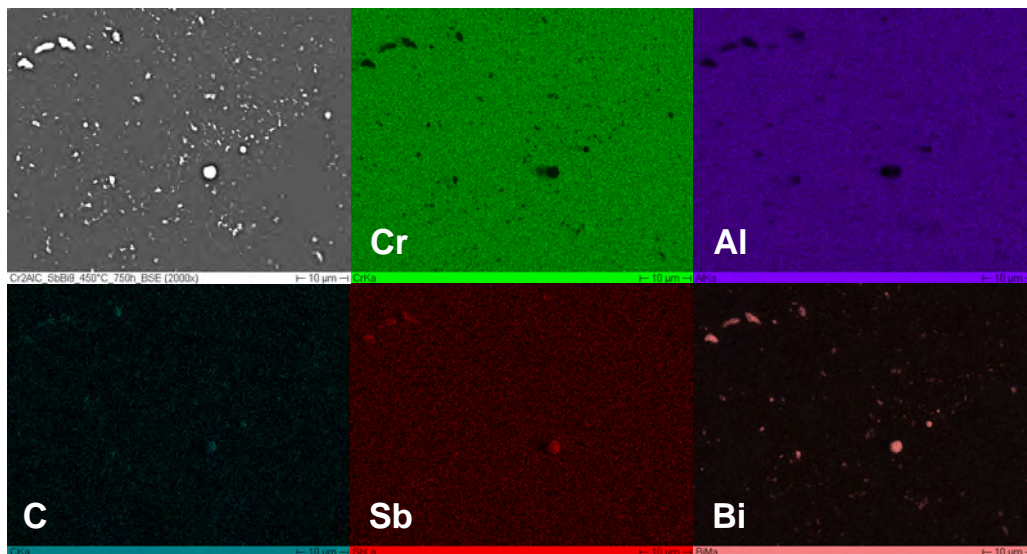


**Figure 4.57:** BSE image and EDS element mapping images of surface morphology of  $Cr_2AlC$  on  $Al_2O_3$ -substrate after 750 h exposure in liquid  $SbBi_9$  at 450 °C.

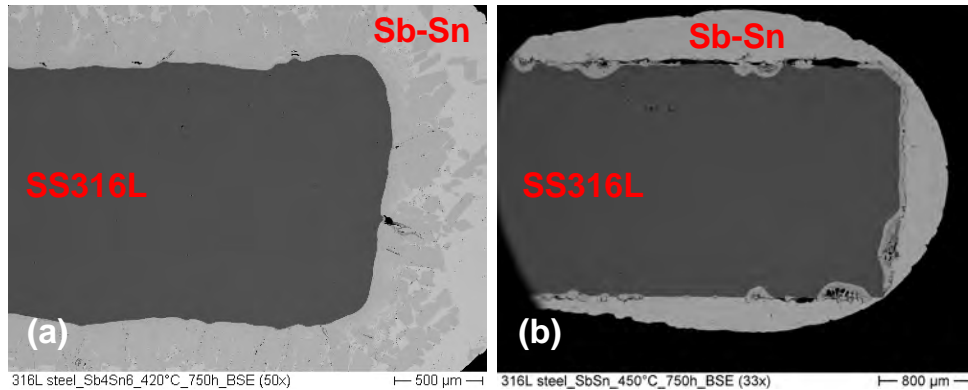
### Results in $Sb_4Sn_6$ , $SbSn$ , $Sb_2Bi_8$ and $Sb_3Bi_7$

The results in other compositions of Sb-Sn and Sb-Bi alloys showed great similarity to the results in  $Sb_3Sn_7$  and  $SbBi_9$ , respectively.

### Fe-Cr-Ni steel (SS316L)

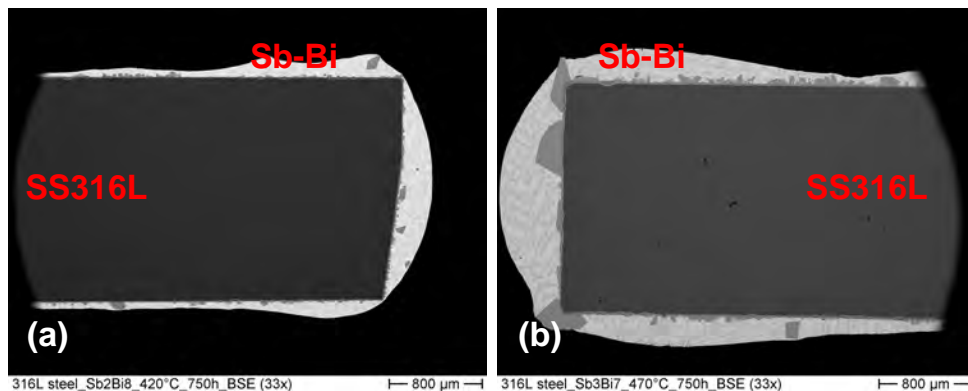
Since all steel specimens exhibit similar corrosion performance in different compositions of Sb-Sn and Sb-Bi alloy, only SS316L is cited here as an example for all steel specimens.

Figure 4.58 shows the BSE images of cross-section of SS316L after 750 h exposure in liquid  $\text{Sb}_4\text{Sn}_6$  at 420 °C and in liquid SbSn at 450 °C, respectively.



**Figure 4.58:** BSE image of cross-section of SS316L after 750 h exposure in (a) liquid  $\text{Sb}_4\text{Sn}_6$  at 420 °C and in (b) liquid SbSn at 450 °C.

The BSE images of cross-section of SS316L after 750 h exposure in liquid  $\text{Sb}_2\text{Bi}_8$  at 420 °C and in liquid  $\text{Sb}_3\text{Bi}_7$  at 470 °C are shown in Figure 4.59. Obviously, steels suffer severe attack in Sb-Sn alloys than in Sb-Bi alloys. Additionally, the corrosion rate ( $\sim 0.04 \mu\text{m}/\text{h}$ ) of steels in Sb-Bi alloys is acceptable for short-term application as PCC.



**Figure 4.59:** BSE image of cross-section of SS316L after 750 h exposure in (a) liquid  $\text{Sb}_2\text{Bi}_8$  at 420 °C and in (b) liquid  $\text{Sb}_3\text{Bi}_7$  at 470 °C.

### Fe-Cr-Ni alloy (4J33 Kovar alloy)

It can be seen from Figure 4.60 and 4.61 that similar to the results obtained from exposure in  $\text{Sb}_3\text{Sn}_7$  at in  $\text{SbBi}_9$ , 4J33 Kovar alloy exhibits the worst corrosion resistance among all metallic

specimens, regardless of the compositions of Sb-Sn or Sb-Bi alloys. Particularly, 4J33 Kovar alloy was surprisingly but completely dissolved after 750 h exposure in  $\text{Sb}_4\text{Sn}_6$  (see Figure 4.60 (a)), which totally excludes its application as PCC materials for LMBs.

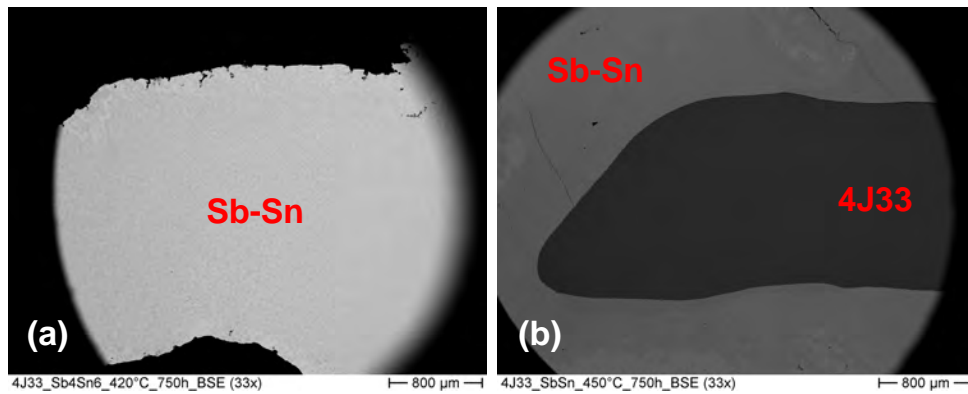


**Figure 4.60:** BSE image of cross-section of 4J33 Kovar alloy after 750 h exposure in (a) liquid  $\text{Sb}_4\text{Sn}_6$  at 420 °C and in (b) liquid SbSn at 450 °C.

Additionally, Figure 4.61 exhibits that after 750 h exposure in  $\text{Sb}_2\text{Bi}_8$  and  $\text{Sb}_3\text{Bi}_7$  alloys, the corrosion mechanism is apparently different from our observation in  $\text{SbBi}_9$  alloy: distinct dissolution of 4J33 Kovar alloy instead of the distinct penetration of Sb and Bi.

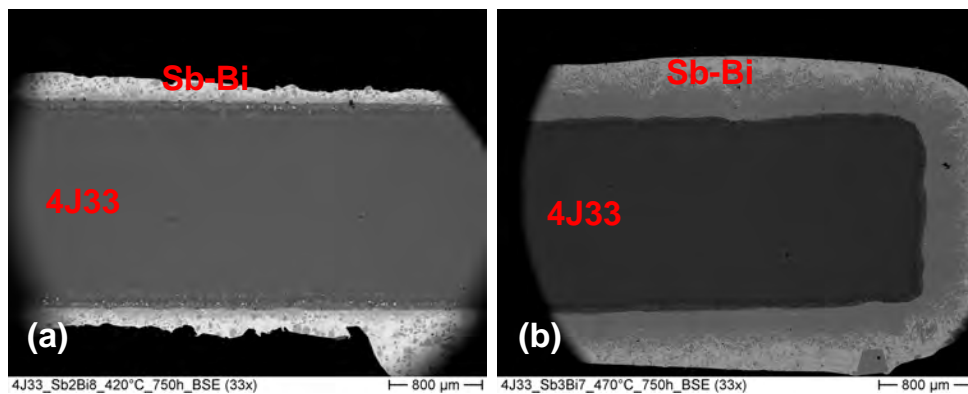


**Figure 4.61:** BSE image of cross-section of 4J33 Kovar alloy after 750 h exposure in (a) liquid  $\text{Sb}_2\text{Bi}_8$  at 420 °C and in (b) liquid  $\text{Sb}_3\text{Bi}_7$  at 470 °C.

## Mo metal

By contrast, among those metallic specimens, Mo is the one which presents the best corrosion resistance against both Sb-Sn and Sb-Bi alloys. The BSE and EDS mapping images of cross-sections of Mo metal after exposure in  $\text{Sb}_4\text{Sn}_6$ ,  $\text{Sb}_2\text{Bi}_8$ , SbSn and  $\text{Sb}_3\text{Bi}_7$  are shown in Figure 4.62, 4.63, 4.64, and 4.65, respectively. Nevertheless, As, as contamination, was

detected at the interface between Mo and Sb-Sn or Sb-Bi alloys as well, which coincides with our previous results in  $Sb_3Sn_7$  and  $SbBi_9$  alloys. Hence As might be the reason for the tiny corrosion attack on Mo.

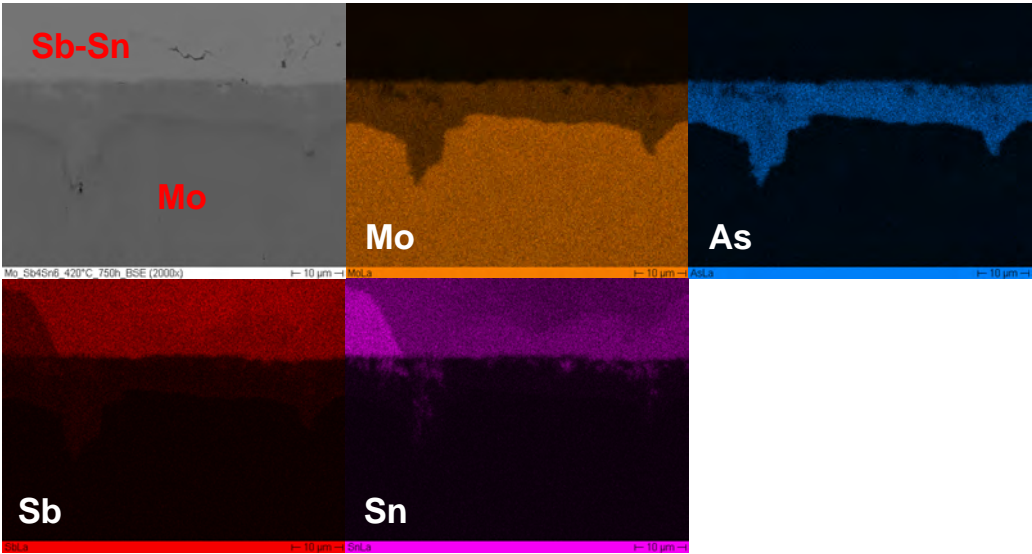


**Figure 4.62:** BSE image and EDS element mapping images of cross-section of Mo metal after 750 h exposure in liquid  $Sb_4Sn_6$  at 420 °C.

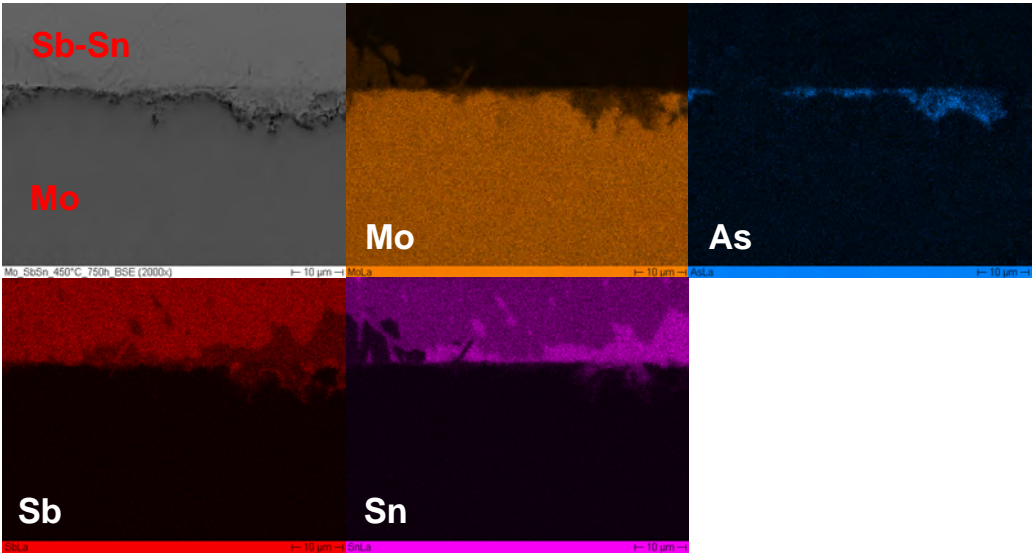


**Figure 4.63:** BSE image and EDS element mapping images of cross-section of Mo metal after 750 h exposure in liquid  $SbSn$  at 450 °C.

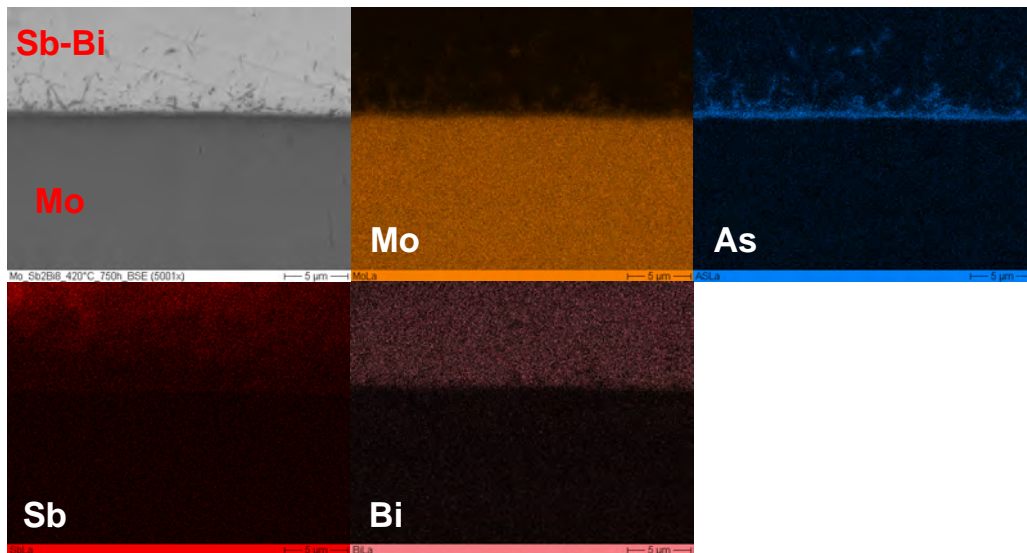


**Figure 4.64:** BSE image and EDS element mapping images of cross-section of Mo metal after 750 h exposure in liquid  $\text{Sb}_2\text{Bi}_8$  at 420 °C.

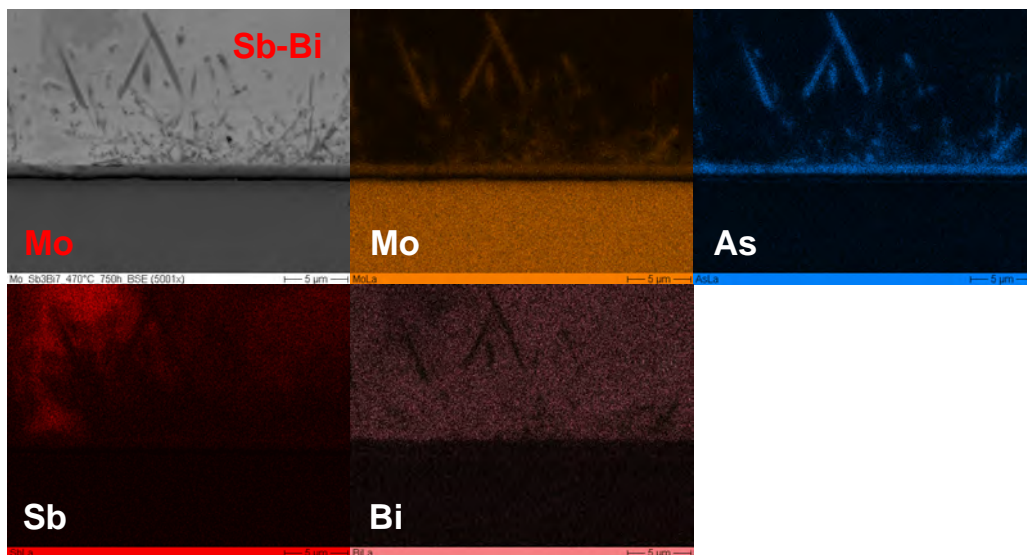


**Figure 4.65:** BSE image and EDS element mapping images of cross-section of Mo metal after 750 h exposure in liquid  $\text{Sb}_3\text{Bi}_7$  at 470 °C.

#### 4.2.4 Discussion

In this part, the corrosion behavior of nine different materials (Cr metal, Mo metal, T91 ferritic steel, SS304 and SS316L austenitic stainless steel, 4J33 Kovar alloy and three MAX-phase coatings  $\text{Cr}_2\text{AlC}$ ,  $\text{Ti}_2\text{AlC}$  and  $\text{Ti}_3\text{AlC}_2$  on  $\text{Al}_2\text{O}_3$ -substrate) against liquid Sb-Sn and Sb-Bi alloys with the duration of 750 h were systematically investigated, with the aim of evaluating

their potential to be applied as PCC in LMB cells. The results of exposure in  $\text{Sb}_3\text{Sn}_7$  and  $\text{SbBi}_9$  at 450 °C are mainly discussed in the following paragraphs as examples.

Firstly, for Fe-Cr and Fe-Cr-Ni steels, the same as the results and conclusions gained by the other investigators [69, 70, 92], Fe, Cr and Ni in steels all deplete distinctly not only in liquid  $\text{Sb}_3\text{Sn}_7$  but also in liquid  $\text{SbBi}_9$ , but the corrosion products vary with the elemental composition of steels and diffusion distance in steels. Besides, the formation of a Cr-rich layer near the interface can be observed in all steels except for the exposure of T91 ferritic steel in liquid  $\text{Sb}_3\text{Sn}_7$ , which is probably due to the lower Cr content in T91 ferritic steel and the higher solubility of Cr in liquid  $\text{Sb}_3\text{Sn}_7$ . Moreover, the comparison of line scans of T91 with SS304 in  $\text{SbBi}_9$  also manifests that the existence of Ni in steels promotes the penetration of Bi, which verified the detrimental effect of Ni for PCC materials in LMBs. Therefore, Ni should be expelled at material selection for PCC.

Fe-Co-Ni alloys such as 4J33 Kovar alloy, compared with Fe-Cr and Fe-Cr-Ni steels, suffers severer corrosion attack in both liquid  $\text{Sb}_3\text{Sn}_7$  and  $\text{SbBi}_9$  alloys, which excludes their application as PCC in LMBs. Nevertheless, the application of those special alloys as NCC will not be adversely affected owing to the position of NCC, which has no direct contact to the positive electrode. The severer corrosion attack of Sb-Sn and Sb-Bi on Kovar alloy can be probably attributed to its relatively higher Ni and Co content and the absence of Cr, which coincides with our results from Fe-Cr-Ni steels and manifests the harmful impact of Ni.

The results show that among all test specimens, most metallic bulk specimens (Cr metal, T91 ferritic steel, SS304, SS316L and 4J33 Kovar alloy) could not meet the corrosion resistance requirements in both  $\text{SbBi}_9$  and  $\text{Sb}_3\text{Sn}_7$  systems. The only exception is Mo metal, the only tested metallic bulk material which possesses an outstanding corrosion-resistant performance during the exposure in both  $\text{Sb}_3\text{Sn}_7$  and  $\text{SbBi}_9$  alloys. Based on the previous studies [75, 86, 91], Mo is regarded as corrosion-resistant against liquid Bi (up to 1010 °C) and Sn, hence the tiny corrosion issues occurred on the surface of Mo metals after our tests might be contributed to the presence of As in Sb-Sn and Sb-Bi, which exacerbates the corrosion of Mo. Nevertheless, for the application of Mo, its extremely high price (From London Metal Exchange in 2022: \$ 45000/ton) must be taken into consideration, which makes the coating of Mo on a conductive metallic substrate the appropriate method.

With regards to MAX-phases, after exposure in both liquid  $\text{Sb}_3\text{Sn}_7$  and  $\text{SbBi}_9$  alloy at 450 °C, neither destruction of any MAX-phases nor penetration of Sb-Sn or Sb-Bi alloy can be observed in all of those three MAX-phases ( $\text{Cr}_2\text{AlC}$ ,  $\text{Ti}_2\text{AlC}$  and  $\text{Ti}_3\text{AlC}_2$ ) on  $\text{Al}_2\text{O}_3$ -substrate. The

surface of all MAX-phases maintains smooth and intact after exposure, regardless whether in liquid  $\text{Sb}_3\text{Sn}_7$  or in liquid  $\text{SbBi}_9$ . Therefore, they also exhibit promising corrosion resistance in both  $\text{SbBi}_9$  and  $\text{Sb}_3\text{Sn}_7$  systems. Hence, the coating of those MAX-phases on a conductive metallic substrate is feasible as PCC materials in LMBs. However, this coating must be defect-free, which is quite difficult to achieve. Additionally, for the application of MAX-phases, the electrical conductivity, thermal conductivity and other mechanical properties, especially their compatibility with steel and alloy substrate at higher temperature must be under consideration.

Moreover, the results of all test specimens after 750 h exposure in liquid  $\text{Sb}_3\text{Sn}_7$  and  $\text{SbBi}_9$  at 450 °C illustrate that  $\text{SbBi}_9$  and  $\text{Sb}_3\text{Sn}_7$  exhibit dramatically different corrosion effect on PCC materials. In comparison with  $\text{SbBi}_9$ ,  $\text{Sb}_3\text{Sn}_7$  attacks steels more heavily, for T91 steel, the corrosion rate in liquid  $\text{Sb}_3\text{Sn}_7$  is 0.53  $\mu\text{m}/\text{h}$  versus 0.04  $\mu\text{m}/\text{h}$  in  $\text{SbBi}_9$ . For SS304, the value in liquid  $\text{Sb}_3\text{Sn}_7$  is 1.33  $\mu\text{m}/\text{h}$  while is only 0.03  $\mu\text{m}/\text{h}$  in  $\text{SbBi}_9$ . For SS316L, the value in liquid  $\text{Sb}_3\text{Sn}_7$  is 0.80  $\mu\text{m}/\text{h}$  but only 0.03  $\mu\text{m}/\text{h}$  in  $\text{SbBi}_9$ . In other words, when compared with  $\text{SbBi}_9$ ,  $\text{Sb}_3\text{Sn}_7$  is much more aggressive and corrosive probably due to the extremely aggressive corrosivity of Sn or due to a higher concentration of Sb, which indicates that compared with Sb-Bi system, Sb-Sn system triggers much severer corrosion issues on PCC materials.

In addition, the comparison between the results of SS316L in liquid  $\text{Sb}_3\text{Sn}_7$  at 450 °C (max. corrosion rate = 0.80  $\mu\text{m}/\text{h}$ ) with the results of SS316L in liquid Sn at 450 °C [89], where the max. corrosion rate was more than 2.00  $\mu\text{m}/\text{h}$  indicates that in comparison to Sb, Sn is more aggressive on steels, when alloying Sn with Sb, the corrosion issues on steels will be reduced.

Furthermore, according to previous studies, both ferrous metals and Cr exhibit good corrosion resistance to attack by liquid Bi up to around 700 °C [75, 86]. However, our results show that when Bi was alloyed with a small amount of Sb (only 10 mol.%), corrosion attack can be clearly observed both on steels and chromium when the temperature is barely 450 °C, which points out that the corrosion caused by liquid  $\text{SbBi}_9$  is mainly triggered by the added Sb. Besides, those previous studies also present that ferrous metals exhibit poor corrosion resistance in liquid Sb at temperatures above 630 °C (melting point of Sb) while in liquid Sn already at 300 °C [75, 86, 87], which coincides with our results that in comparison with Sb, Sn is more aggressive on steels. Combined those two points mentioned before, we could conclude that compared with Sb and Sn, Bi is the mildest liquid metal. Additionally, previous studies reveal that Ni presents poor corrosion resistance against attack by liquid Sb, liquid Sn and liquid Bi at low temperatures [75, 86, 88–90], in comparison to the corrosion resistance of Fe and Cr in liquid Sb, liquid Sn and liquid Bi, obviously, Ni is the easiest metal to be corroded by liquid metals (Sb, Sn and Bi) ,

which corresponds to the conclusion of our results that Ni is detrimental for PCC materials.

Finally, the corrosion caused by liquid Sb-Sn or Sb-Bi alloys on PCC materials not only bring safety concerns on long service lifetime of LMBs, the diffusion of dissolved constituents of PCC materials into liquid positive electrode and alloying with the active components in liquid positive electrode could also have adverse effects on cell performance, including undesirable side-reactions, increased cell internal resistance and reduced cell capacity [35, 69, 70], which should be further investigated in assembled cells.

#### **4.2.5 Short summary**

To sum up, the corrosion rate of steels in Sb-Bi alloys is acceptable for its applications as PCC for short term while Fe-Co-Ni alloys (4J33 Kovar alloy) are definitely unsuitable to be applied as PCC for LMB cells with either Sb-Sn or Sb-Bi alloy as positive electrode. Among all test specimens, only pure Mo metal and those three MAX-phase coatings ( $\text{Cr}_2\text{AlC}$ ,  $\text{Ti}_2\text{AlC}$  and  $\text{Ti}_3\text{AlC}_2$ ) present outstanding corrosion resistance against both liquid Sb-Sn and Sb-Bi alloys, hence they are regarded as the most promising candidates to be applied as PCC materials for LMBs for long term. However, considering about the higher price and manufacture of battery cells, coating of those promising materials (conductive and corrosion-resistant) on a suitable substrate (conductive metallic materials, e.g., steels or alloys) might be the most economically reasonable and feasible method.

Moreover, due to the fact that the material performance in different compositions of Sb-Bi alloy exhibits no significant difference, combined with the melting point of different Sb-Bi alloy compositions,  $\text{SbBi}_9$  alloy, which possesses the lowest melting point ( $\sim 300^\circ\text{C}$ ) [138], was selected for the corrosion tests (Section 4.3) and cell assembly (Section 5.2) hereinafter referred to.

### **4.3 Static corrosion tests for PCC materials in positive electrode at fully-discharged state**

#### **4.3.1 Material selection**

According to the results in Section 4.2.3, when compared with Sb-Bi alloy, Sb-Sn alloy is much more aggressive and corrosive, hence, in this case, only  $\text{SbBi}_9$  was selected as positive electrode to prepare the Na-Sb-Bi alloy. Besides, the results in Section 4.2.3 also reveal that the first

batch of Sb used to prepare the Sb-Sn and Sb-Bi alloys were contaminated by arsenic (As), which might exacerbate the corrosion attack in heavy metals and probably be the reason for the slight corrosion on Mo metal. Therefore, antimony and bismuth both with the purity of 99 %, were applied to prepare the Na-Sb-Bi alloy in this section in order to eliminate the negative influence of arsenic and to get the precise and reliable results.

During discharging, liquid sodium (Na) alloys with the Sb-Sn or Sb-Bi alloy at bottom and forms a new Na-containing Sb-Sn or Sb-Bi alloy. Combined with the fact that no corrosion experiments in the ternary Na-containing alloys were performed, the main objective of this test is to further investigate the corrosion performance of PCC materials, especially those promising candidates obtained from the static exposure test in liquid Sb-Sn and Sb-Bi alloys in Section 4.2 (Mo metal and MAX-phases) in positive electrode at fully-discharged state (ternary Na-containing alloys).

### 4.3.2 Experiments

#### Materials and preparation of specimens

The test specimens in this work were molybdenum (Mo) metal (Plansee SE), T91 ferritic steel (EUROTRANS-DEMETRA [135]), SS304 (Workshop/KIT), SS316L (EUROTRANS-DEMETRA [135]), SS316Ti (Workshop/KIT) and two MAX-phase coatings ( $\text{Cr}_2\text{AlC}$  and  $\text{Ti}_2\text{AlC}$ ) on T91 steel (IAM-AWP/KIT).

316Ti austenitic stainless steel (SS316Ti) was added because it will later be applied as PCC for our Na-based LMB cells.

The MAX-phase coatings on T91 steel substrate were synthesized in the same way as above-mentioned in Section 4.2.2 [136]. However, the coating thickness here on steel substrates were a little thicker,  $\sim 4 \mu\text{m}$ .

The composition of SS316Ti is listed in Table 4.9.

**Table 4.9:** Composition of SS316Ti (in wt.%).

Material	C	Cr	Ni	Mn	Mo	Ti	Fe
SS316Ti	$\leq 0.08$	16.00 – 18.00	10.00 – 14.00	$\leq 0.50$	2.00 – 3.00	$5 \times \text{C}\% - 0.70$	Bal.

All specimens were cut into appropriate size to fit into the Mo-crucible (Figure 4.66). Additionally, before exposure, all test materials were ground by sandpaper with a grid size of 800 and 1200, successively. Then the test materials were polished to a grain size of  $1 \mu\text{m}$ .

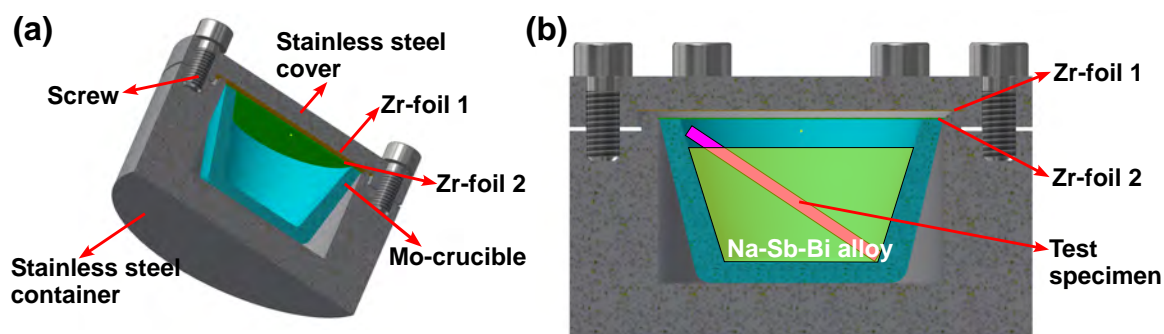


**Figure 4.66:** Cross-section of (a) a test container for corrosion test for PCC materials at fully discharged state and (b) the test container with test specimen inside.

### Test facility

The corrosion tests were performed in a special COSTA facility. Compared with common COSTA facilities, this special COSTA is particularly equipped with a stainless steel tube, instead of half-open quartz tubes, in which the exposure occurred, since sodium could react with silicon dioxide in glass and quartz glass and hence is able to etch them. Moreover, the stainless steel tube is welded to a glovebox for loading and unloading the specimens. The stainless steel tube is also connected with a gas control system and flow meters to adjust the gas flow and to control the atmosphere inside the tube.

### Preparation of Na-Sb-Bi alloy

The desired Na-Sb-Bi alloy was gained by adding liquid sodium into molten  $\text{SbBi}_9$  alloy, and the  $\text{SbBi}_9$  alloy was gained by mixing the individual heavy metals Sb and Bi in their granular forms in  $\text{Al}_2\text{O}_3$ -crucibles.

Both antimony (Sb) and bismuth (Bi) were delivered by HHW Haunder GmbH & Co. KG. The Sb granular has a purity of 99.99 % and a granular size of 1 - 6 mm, the Bi possesses a purity of 99.99 % and a granular size of < 5 mm. Sodium (99.8 % purity) was delivered by Haines & Maassen Metallhandels-gesellschaft GmbH in its block form.

To avoid the impact brought by the oxides of Bi, the used Bi was first melted in a stainless steel-crucible and the slag layer on top was removed. Next, the molten Bi was poured into another stainless steel-crucible and broken into small granules after it cooled down to room temperature. Afterwards, the desired amount of granular Sb was added.

The used sodium was purified in this same way as mentioned in Section 4.1.2 in the glovebox

( $O_2 < 0.1$  ppm,  $H_2O < 0.1$  ppm). According to the phase diagrams of Na-Sb and Na-Bi (seen Figure 4.67) [158, 159], at the molar ratio of 1:1, Na reacts with both Sb and Bi and forms solid intermetallic compounds NaSb and NaBi, both NaSb and NaBi possess a melting point of around 440 °C. At increasing molar ratio of Na (3:1), Na forms the solid intermetallic compounds  $Na_3Sb$  and  $Na_3Bi$ , both possess a relatively melting point (more than 800 °C) and may probably impede the diffusion of Na-ions in LMB cells. Therefore, a higher molar ratio of Na (75 mol.%) in Sb-Bi alloy should be avoided. As a result, the Na ratio in the Na-Sb-Bi alloy was to be about 30 mol.%.

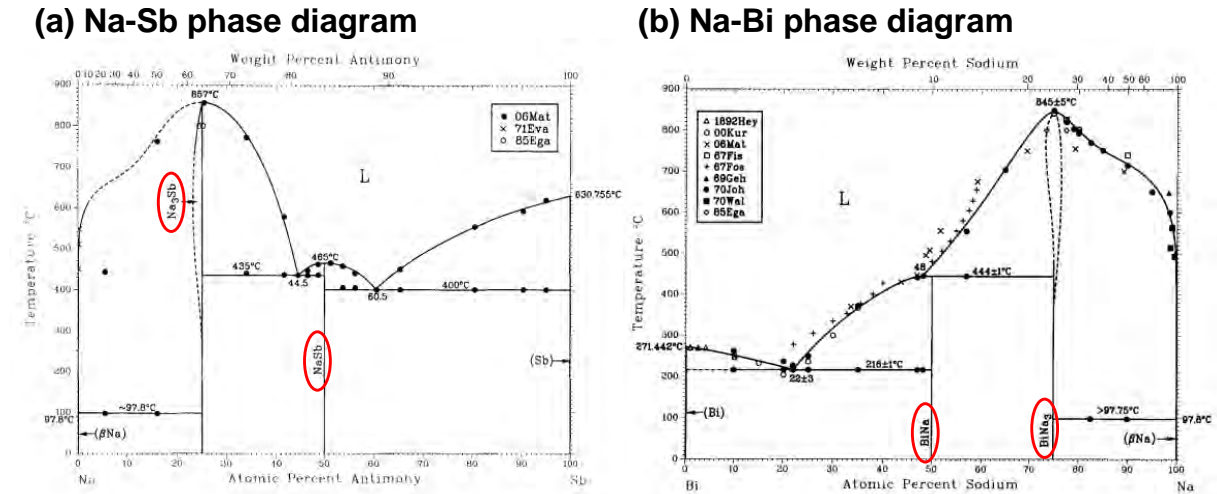


**Figure 4.67:** Phase diagrams of (a) Na-Sb [158] and (b) Na-Bi [159].

## Test procedures

First of all, the  $Al_2O_3$ -crucibles were filled with 120 g  $SbBi_9$ , then they were set into the furnace of a common COSTA at room temperature and the atmosphere inside the quartz tube was purged with 100 mL/min  $Ar+5\%H_2$  gas until the oxygen content inside the tube reached  $10^{-17}$  ppm.

Next, the temperature was raised to 700 °C to melt and alloy the heavy metals. The high temperature was hold for 2 h, then the furnace was cooled down to room temperature. To prevent the oxidation of  $SbBi_9$ , the quartz tube was purged with 100 mL/min  $Ar+5\%H_2$  gas for the entire duration of melting. After that, the  $Al_2O_3$ -crucibles were taken out and transported into the glovebox immediately, in which the sodium purification equipment (sodium sink) used in Section 4.1.2 is located.

Those  $Al_2O_3$ -crucibles were set on the heating plate inside the glovebox. The setting temperature of this heating plate was 530 °C, in order to melt the  $SbBi_9$  alloy and to pre-heat a bigger stainless steel crucible, which is used as the container to mix liquid sodium and molten  $SbBi_9$

alloy. After the  $\text{SbBi}_9$  alloy in the  $\text{Al}_2\text{O}_3$ -crucibles melted, it was poured into the bigger stainless steel crucible and the heating temperature of the heating plate was re-set to 390 °C. Then the required amount of sodium was added to the heated  $\text{SbBi}_9$  alloy.

As next step, the molten Na-Sb-Bi alloy was evenly distributed into six Mo-crucibles to almost completely fill their volume. Then the six Mo-crucibles with Na-Sb-Bi alloy inside were put on the heating plate with the heating temperature of 390 °C. After the Na-Sb-Bi alloy melted, all test specimens were set into the six Mo-crucibles and almost fully-immersed into the Na-Sb-Bi alloy. After that, the Mo-crucibles containing the test specimens and the Na-Sb-Bi alloy were cooled down to room temperature. Each cooled down Mo-crucible was set into one stainless steel container and one Zr-foil was added on top of each Mo-crucible. Then another Zr-foil was added between the stainless steel container and its lid, after that each container was screwed to its lid to achieve a tight sealing.

To start the exposure of specimens in Na-Sb-Bi alloy, those sealed containers were transported into the stainless steel tube of the special COSTA facility that was held isothermally at 450 °C for 750 h.

### **Post-test analysis**

After 750 h exposure in Na-Sb-Bi alloy, all containers were taken out of the specialized COSTA facility and cooled down in the glovebox to room temperature. Then the containers were opened, the Mo-crucibles with solidified Na-Sb-Bi alloy and specimens inside were taken out of the containers and heated at 390 °C on the heating plate in the glovebox. When the Na-Sb-Bi alloy in Mo-crucibles remelted, the specimens were extracted from the Mo-crucibles, cooled down in the glovebox to room temperature. Afterwards, the cross-sections of specimens were analysed by scanning electron microscope (SEM) with energy-dispersive X-ray spectroscopy (EDS).

### **4.3.3 Results**

Table 4.10 shows the appearance of all specimens after exposure to Na-Sb-Bi alloy at 450 °C for 750 h. After exposure in Na-Sb-Bi alloy, the immersed part of all metallic specimens is more or less covered by a layer of Na-Sb-Bi alloy. In contrast, only a few drops of Na-Sb-Bi alloy can be observed on the MAX-phases' surface.

**Table 4.10:** Appearance of all specimens after exposure in Na-Sb-Bi alloy at 450 °C for 750 h.

Group	Specimen	After exposure in Na-Sb-Bi alloy
Fe-Cr steel	T91 ferritic steel	
Fe-Cr-Ni steel	304 stainless steel	
	316L stainless steel	
	316Ti stainless steel	
	Pure metal	Mo
MAX-phases	Ti <sub>2</sub> AlC on T91 steel	
	Cr <sub>2</sub> AlC on T91 steel	

For a better presentation of the results, the materials have been sorted into the same groups as in Section 4.2.3.

### Fe-Cr steel (T91 ferritic steel)

As shown in Figure 4.68, taken after 750 h exposure, Na-Sb-Bi was partially attached on the surface of the T91 steel specimen. However, no massive corrosion attack is visible at this magnification at least.

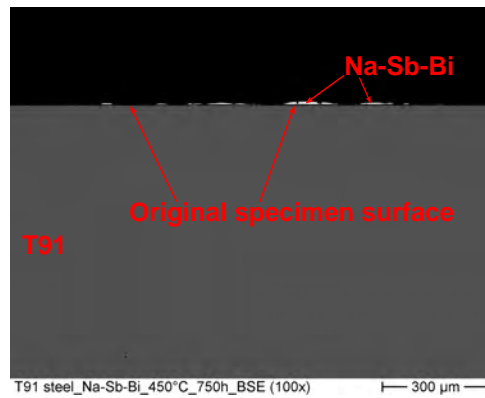


**Figure 4.68:** BSE image of cross-section of T91 after 750 h exposure in Na-Sb-Bi alloy at 450 °C.

Even at higher magnification (Figure 4.69), no visible corrosion attack can be observed on T91 steel. A thin Fe- and Cr-rich layer can be found in the Na-Sb-Bi alloy attached to specimen's surface.

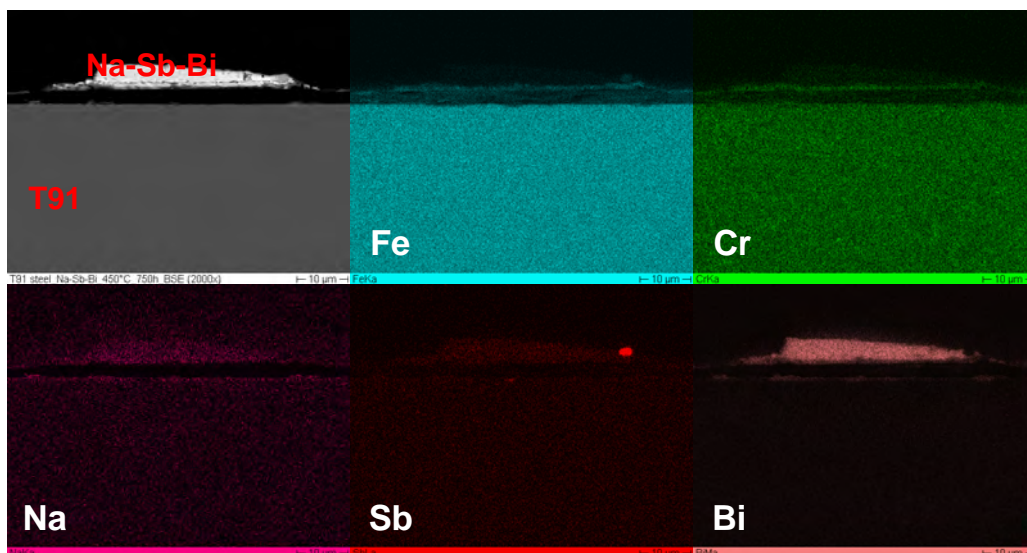


**Figure 4.69:** BSE image and EDS element mapping images of cross-section of T91 after 750 h exposure in Na-Sb-Bi alloy at 450 °C.

The results of the line scan (Figure 4.70) exhibit that neither distinct penetration of Na-Sb-Bi alloy nor clear depletion/destruction of T91 steel can be found after 750 h exposure, the corrosion attack on T91 steel is negligible.

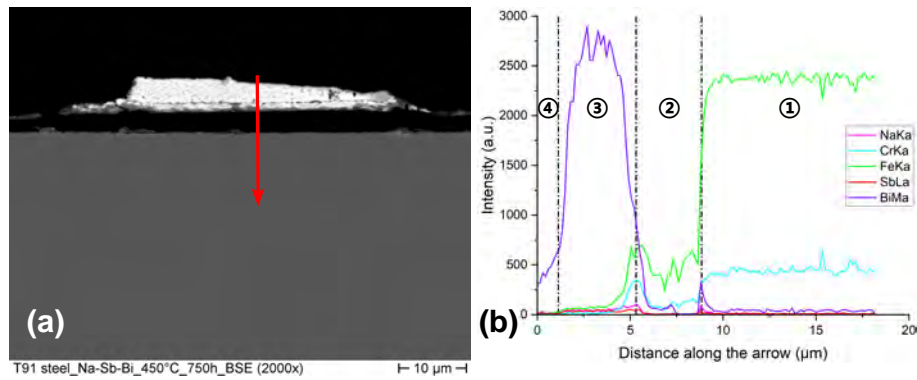


**Figure 4.70:** (a) Line scan across T91 after 750 h exposure in Na-Sb-Bi alloy at 450 °C with (b) results of composition analysis, where ① is the unmodified T91, ② is the gap generated during embedding due to different shrinkage coefficients, ③ is the attached Na-Sb-Bi alloy and ④ is the embedding material.

### Fe-Cr-Ni steel (SS304, SS316L and SS316Ti)

As in Section 4.2.3, SS304 serves as an example for the group of Fe-Cr-Ni steels.

The overview BSE image of the cross-section of SS304 after 750 h exposure in Na-Sb-Bi alloy illustrated in Figure 4.71 is quite similar to that of the T91 ferritic steel specimen: the surface of SS304 is partially covered by Na-Sb-Bi alloy but no significant attack can be observed as well.

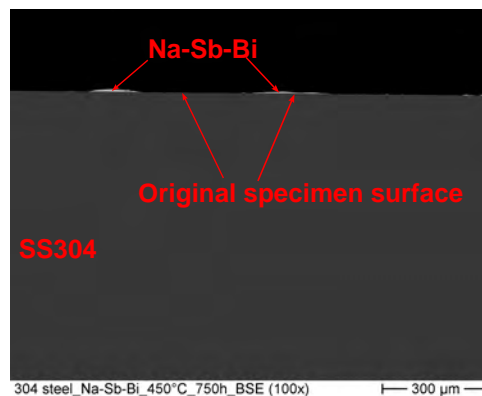


**Figure 4.71:** BSE image of cross-section of SS304 after 750 h exposure in Na-Sb-Bi alloy at 450 °C.

It can be seen from the EDS mapping (Figure 4.72) of the cross-section of SS304 after 750 h exposure in Na-Sb-Bi alloy that although the surface of SS304 was covered by a layer of Na-Sb-Bi alloy, no penetration of Na-Sb-Bi alloy, no distinct destruction or depletion of SS304 and no formation of corrosion products can be observed at the interface. However, a certain amount of Ni can be found in the attached Na-Sb-Bi alloy.

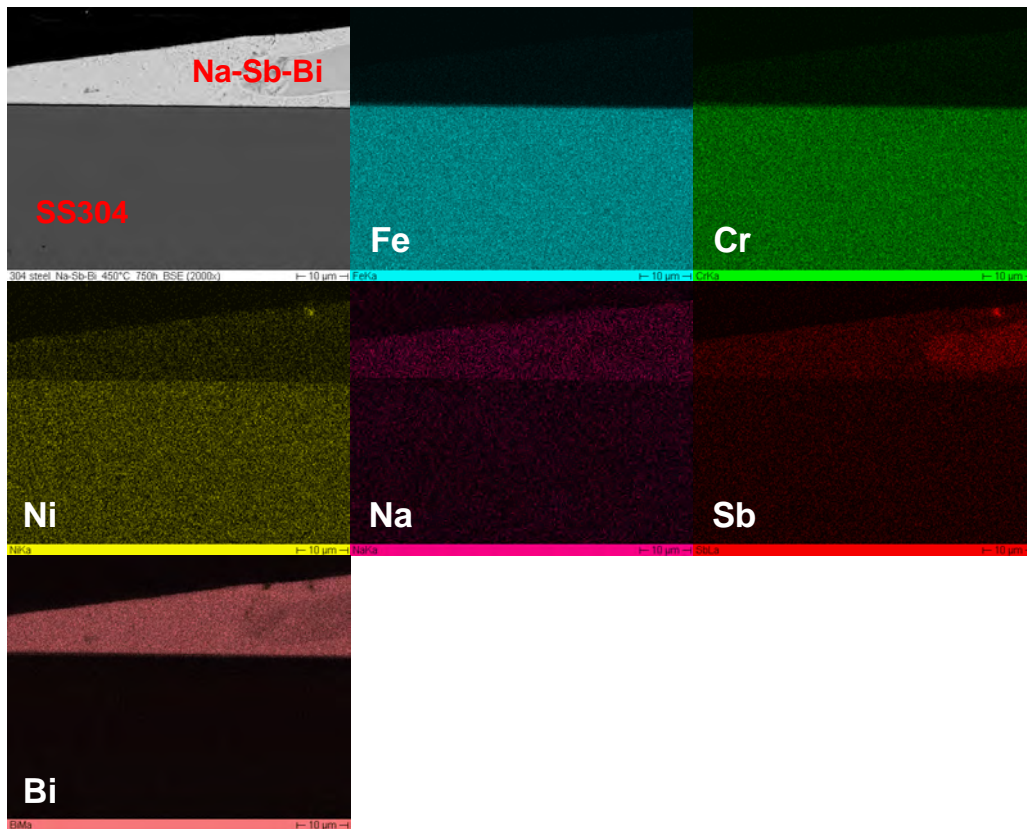


**Figure 4.72:** BSE image and EDS element mapping images of cross-section of SS304 after 750 h exposure in Na-Sb-Bi alloy at 450 °C.

Despite Ni mapping image, the line scan at a higher magnification (Figure 4.73) not only reveals that no Na-Sb-Bi alloy penetrates into SS304, but also manifests that no constituents of SS304 (Fe, Cr and Ni) exists in the Na-Sb-Bi alloy. The line scan confirms the good performance of SS304 against the corrosion attack from the Na-Sb-Bi alloy at 450 °C after at least 750 h.

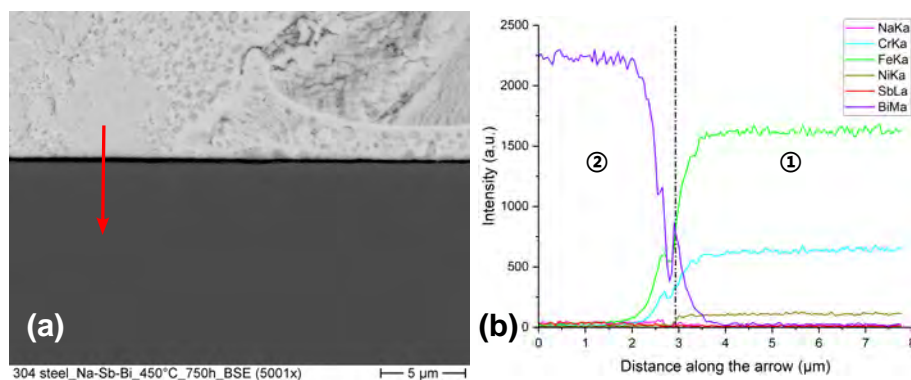


**Figure 4.73:** (a) Line scan across SS304 after 750 h exposure in Na-Sb-Bi alloy at 450 °C with (b) results of composition analysis, where ① is the unmodified SS304 and ② is the attached Na-Sb-Bi alloy.

The SS316L (see Figure 4.74) and SS316Ti (Figure 4.75) exhibit similar behavior as the SS304 after 750 h exposure in Na-Sb-Bi alloy: despite the fact that a thin layer of Na-Sb-Bi alloy partially covered their surface, no massive corrosion attack can be observed on SS316L and SS316Ti.

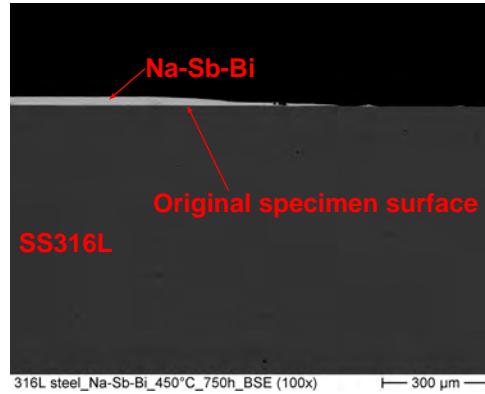


**Figure 4.74:** BSE image of cross-section of SS316L after 750 h exposure in Na-Sb-Bi alloy at 450 °C.

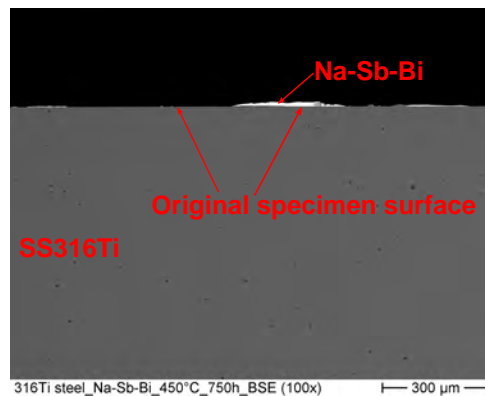


**Figure 4.75:** BSE image of cross-section of SS316Ti after 750 h exposure in Na-Sb-Bi alloy at 450 °C.

The corrosion performance of SS316L and SS316Ti is further verified by the EDS mappings (Figure 4.76 and 4.78) and line scans (Figure 4.77 and 4.79) of their cross-sections at higher magnifications: no penetration of Na-Sb-Bi alloy, neither interdiffusion nor depletion of steel constituents (Fe, Cr and Ni) can be observed. The results as well confirm the good compatibility of SS316L and SS316Ti with Na-Sb-Bi alloy at 450 °C for at least 750 h.

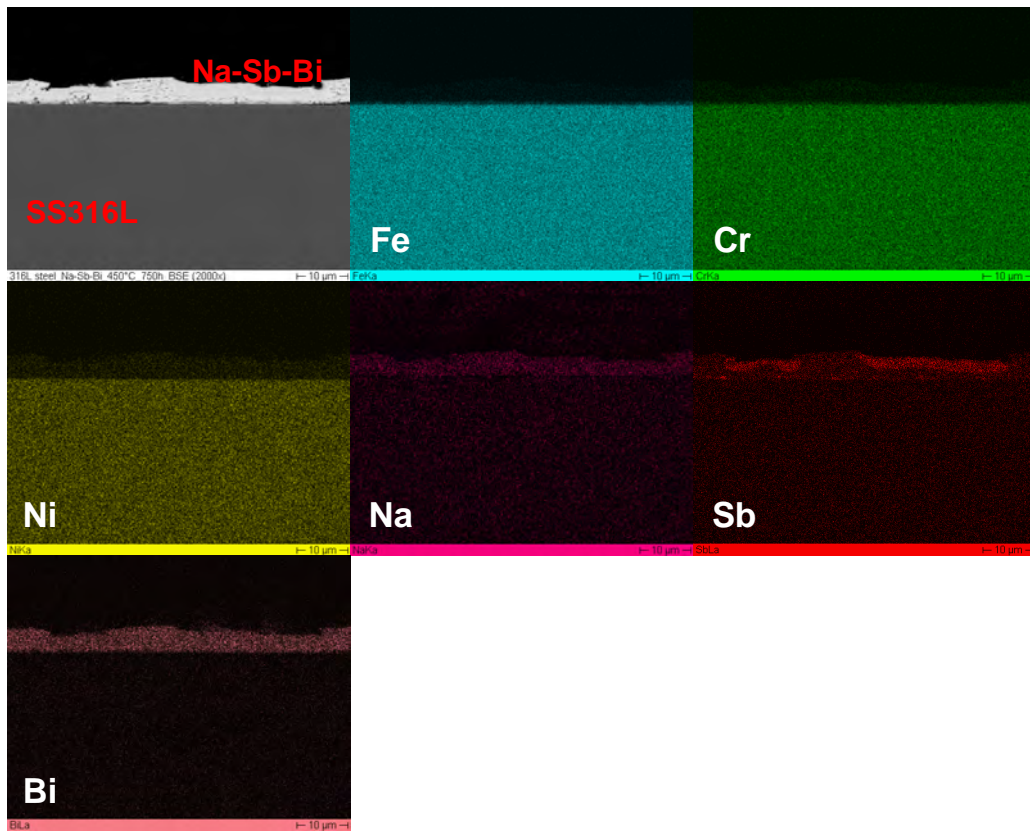


**Figure 4.76:** BSE image and EDS element mapping images of cross-section of SS316L after 750 h exposure in Na-Sb-Bi alloy at 450 °C.

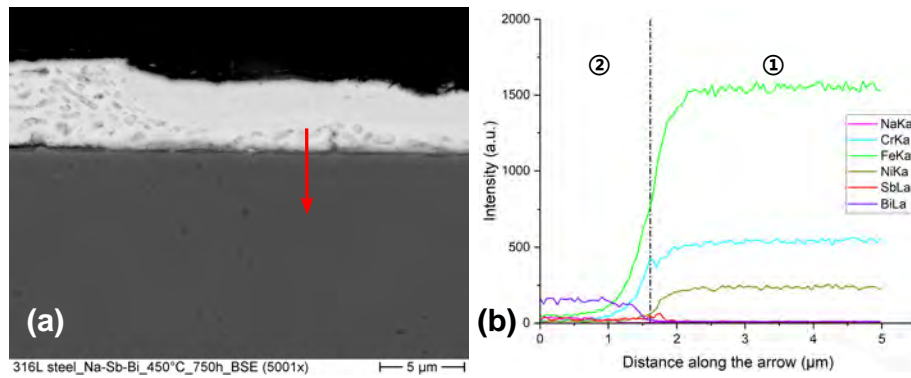


**Figure 4.77:** (a) Line scan across SS316L after 750 h exposure in Na-Sb-Bi alloy at 450 °C with (b) results of composition analysis, where ① is the unmodified SS316L and ② is the attached Na-Sb-Bi alloy.

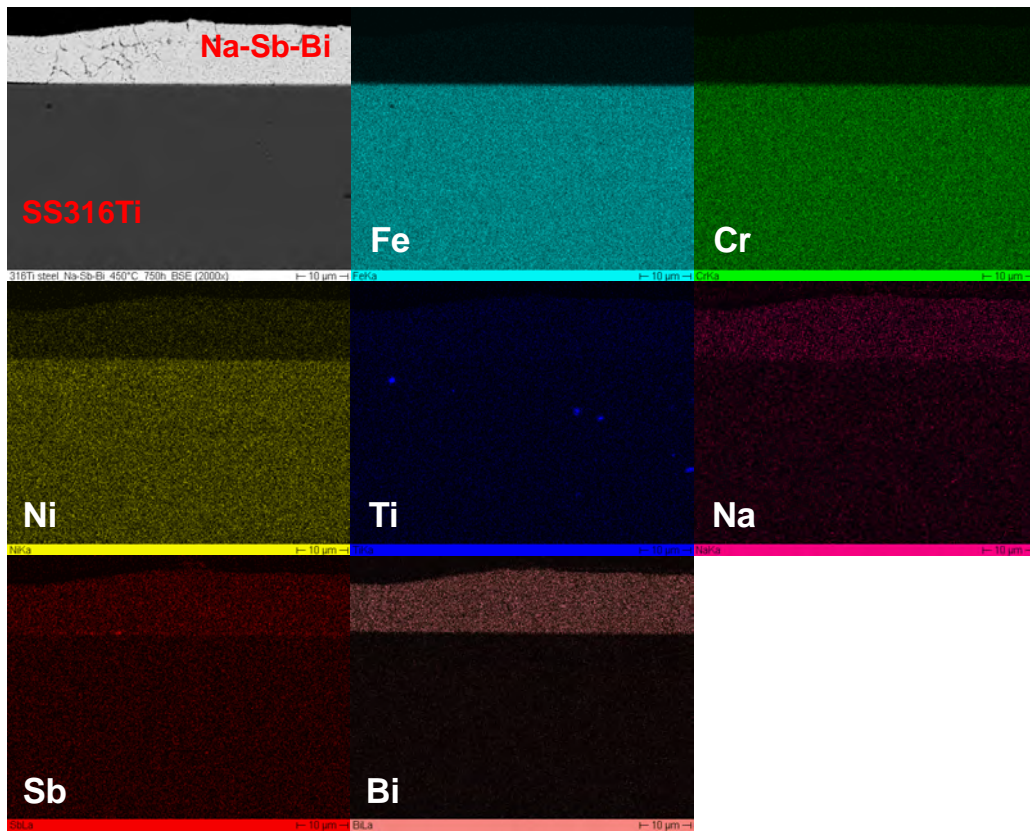


**Figure 4.78:** BSE image and EDS element mapping images of cross-section of SS316Ti after 750 h exposure in Na-Sb-Bi alloy at 450 °C.

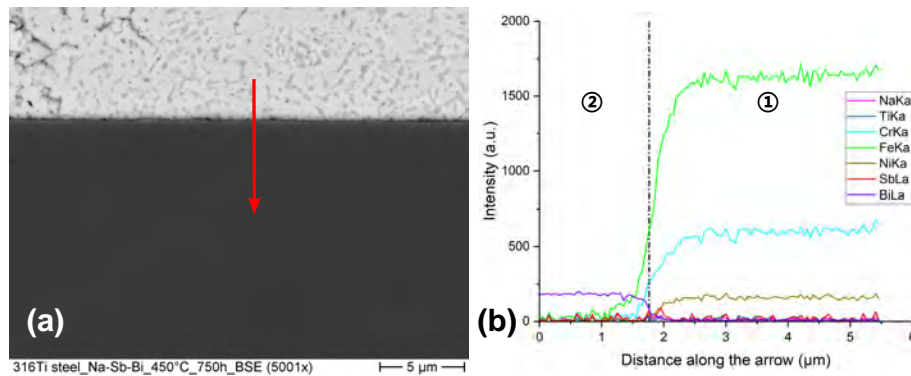
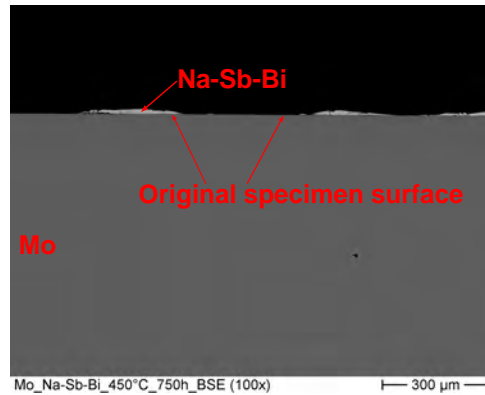


**Figure 4.79:** (a) Line scan across SS316Ti after 750 h exposure in Na-Sb-Bi alloy at 450 °C with (b) results of composition analysis, where ① is the unmodified SS316L and ② is the attached Na-Sb-Bi alloy.

The results of steels show that after 750 h exposure in Na-Sb-Bi alloy at 450 °C, the behavior of Fe-Cr steel (T91 ferritic steel) and Fe-Cr-Ni steels (SS304, SS316L and SS316Ti austenitic steels) is very similar, the corrosion attack on all steels are neglectable.

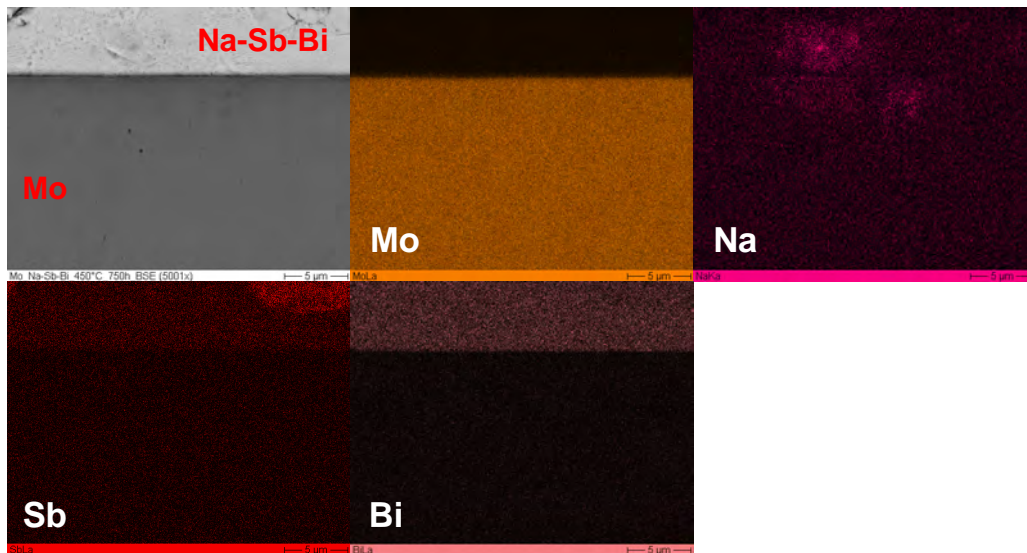
## Pure metal (Mo)

Figure 4.80 shows that after 750 h exposure, the surface of Mo metal was partially covered with a thin layer of Na-Sb-Bi alloy but no corrosion attack is visible.



**Figure 4.80:** BSE image of cross-section of Mo metal after 750 h exposure in Na-Sb-Bi alloy at 450 °C.

The EDS mapping images of cross-section of Mo metal after 750 h exposure in Na-Sb-Bi alloy (Figure 4.81) illustrate that although the surface of Mo metal was also partially attached by Na-Sb-Bi alloy, Mo metal still presents a clear and distinct interface and neither interdiffusion or depletion of Mo can be observed. Moreover, compared with the results in Section 4.2, no arsenic (As) can be found in this case, as a result, no tiny corrosion pits can be found at the interface, which indicates that the corrosion attack on Mo metal described in Section 4.2 can be mainly attributed to the presence of As.



**Figure 4.81:** BSE image and EDS element mapping images of cross-section of Mo metal after 750 h exposure in Na-Sb-Bi alloy at 450 °C.

The results of the line scan (Figure 4.82) confirm that neither notable penetration of Na-Sb-Bi alloy into Mo metal nor distinct depletion/destruction of Mo or enrichment of Mo into Na-Sb-Bi alloy can be observed after exposure in Na-Sb-Bi alloy. This reveals that Mo possesses excellent corrosion resistance against the attack from Na-Sb-Bi alloy at 450 °C.

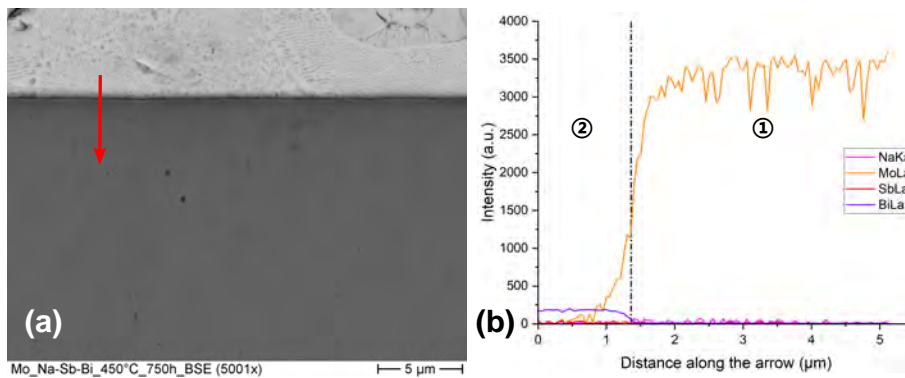
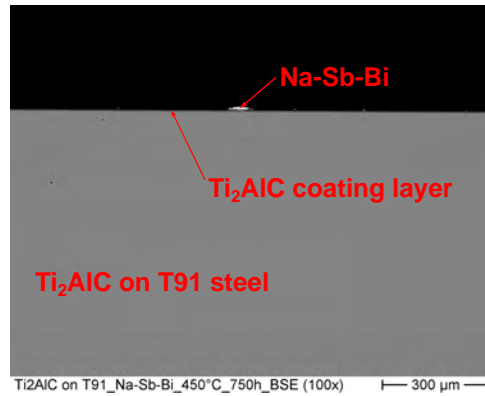


**Figure 4.82:** (a) Line scan across Mo metal after 750 h exposure in Na-Sb-Bi alloy at 450 °C with (b) results of composition analysis, where ① is the unmodified Mo metal and ② is the attached Na-Sb-Bi alloy.

### MAX-phase on T91-substrate

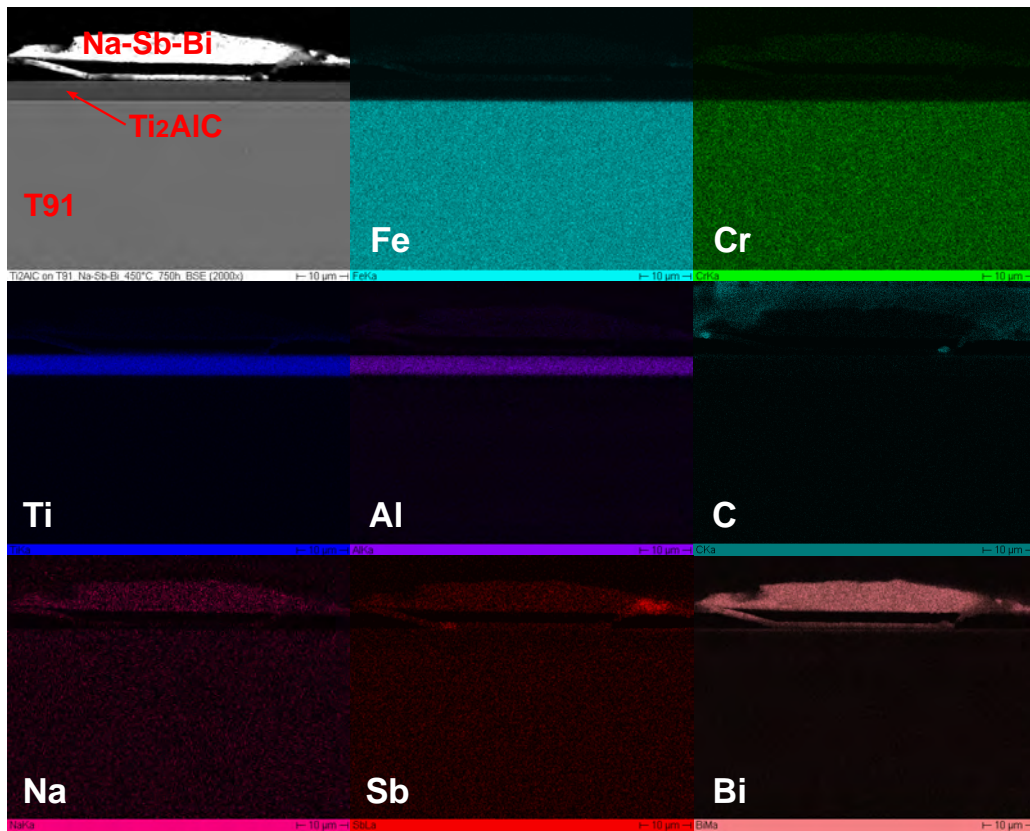
As another promising candidate to be applied as PCC materials in Section 4.2, two MAX-phases ( $Ti_2AlC$  and  $Cr_2AlC$ ) were coated on T91 steel substrate to describe the corrosion performance of those two MAX-phases in Na-Sb-Bi alloy.

Figure 4.83 shows the BSE image of cross-section of  $Ti_2AlC$  on T91 steel substrate after 750 h exposure in Na-Sb-Bi alloy. It can be seen from Figure 4.83 that the specimen surface was only attached by very little Na-Sb-Bi alloy, and no corrosion attack can be observed on  $Ti_2AlC$  on T91 steel substrate.



**Figure 4.83:** BSE image of cross-section of  $Ti_2AlC$  on T91 steel substrate after 750 h exposure in Na-Sb-Bi alloy at 450 °C.

The EDS mapping images (Figure 4.84) and line scan (Figure 4.85) illustrate that the cross-section of  $Ti_2AlC$  coating layer with the T91 substrate underneath remains perfect and intact after exposure, which indicates that  $Ti_2AlC$  coating layer suffers no attack and remains unattacked after 750 h exposure in Na-Sb-Bi alloy.



**Figure 4.84:** BSE image and EDS element mapping images of cross-section of  $Ti_2AlC$  on T91 steel substrate after 750 h exposure in Na-Sb-Bi alloy at 450 °C.

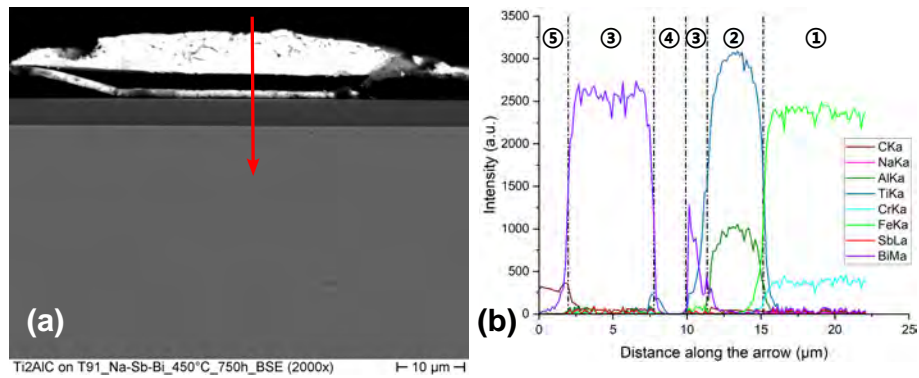


**Figure 4.85:** (a) Line scan across  $Ti_2AlC$  on T91 steel substrate after 750 h exposure in Na-Sb-Bi alloy at 450 °C with (b) results of composition analysis, where ① is the unmodified T91 substrate, ② is the  $Ti_2AlC$  coating layer, ③ is the attached Na-Sb-Bi alloy, ④ is the gap generated during embedding because of the different shrinkage coefficient and ⑤ is the embedding material.

The other MAX-phase ( $Cr_2AlC$ ) (seen in Figure 4.86, 4.87 and 4.88) show a quite similar or even the same corrosion performance as the  $Ti_2AlC$  on T91 steel substrate after exposure in

Na-Sb-Bi alloy.

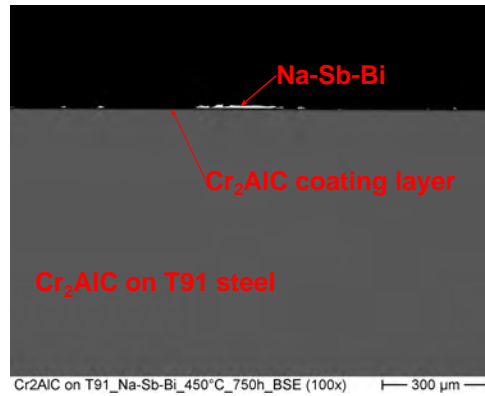


**Figure 4.86:** BSE image and EDS element mapping images of cross-section of Cr<sub>2</sub>AlC on T91 steel substrate after 750 h exposure in Na-Sb-Bi alloy at 450 °C.

Neither penetration of Na-Sb-Bi alloy nor the destruction/depletion of the Cr<sub>2</sub>AlC coating layer on the T91 substrate can be observed on the EDS mapping (Figure 4.87) and line scan (Figure 4.88). This confirms the good corrosion resistance of Cr<sub>2</sub>AlC coating layer against Na-Sb-Bi alloy at 450 °C.

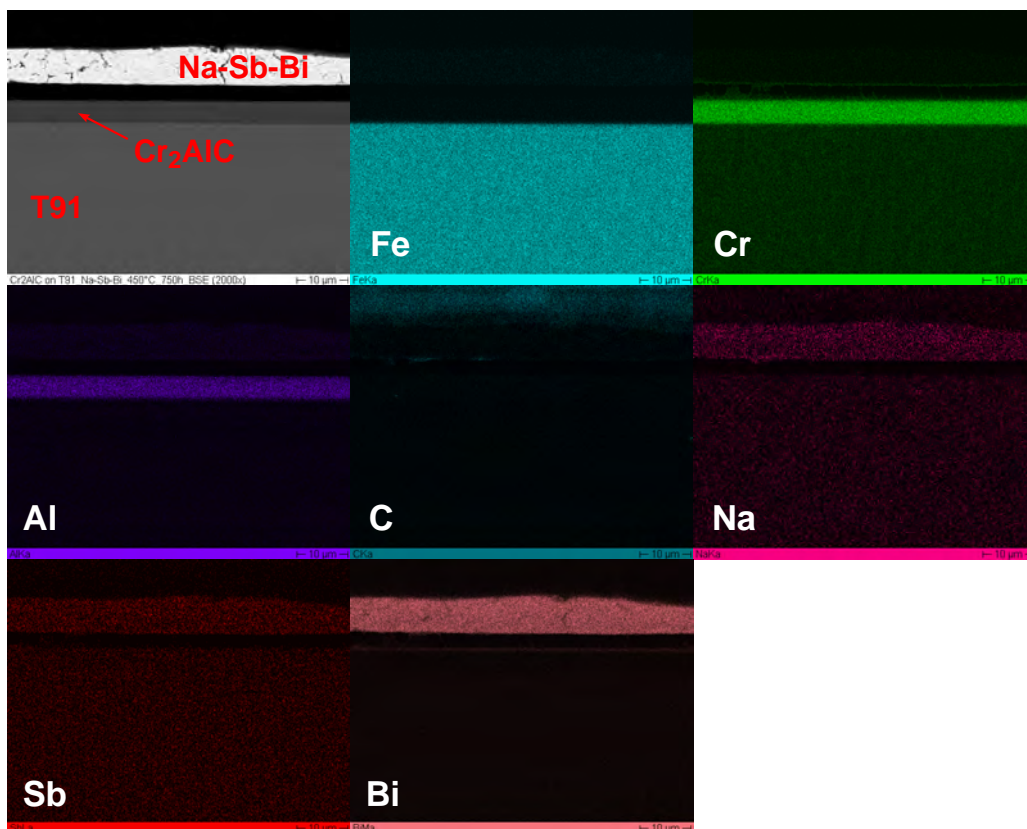


**Figure 4.87:** BSE image and EDS element mapping images of cross-section of Cr<sub>2</sub>AlC on T91 steel substrate after 750 h exposure in Na-Sb-Bi alloy at 450 °C.

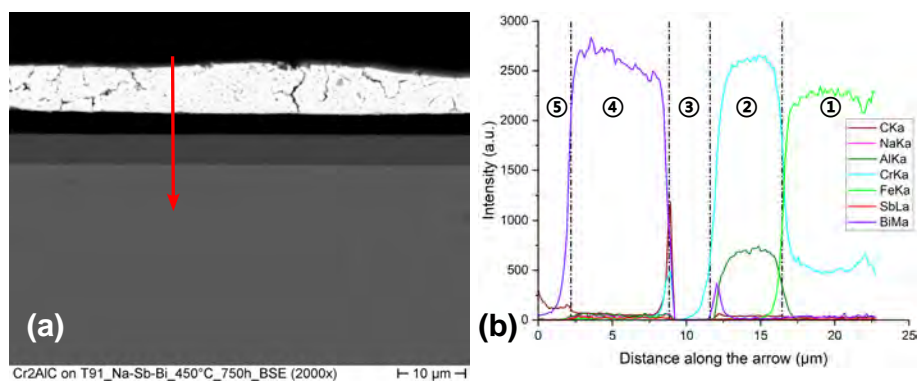


**Figure 4.88:** (a) Line scan across  $\text{Cr}_2\text{AlC}$  on T91 steel substrate after 750 h exposure in Na-Sb-Bi alloy at 450 °C with (b) results of composition analysis, where ① is the unmodified T91 substrate, ② is the  $\text{Cr}_2\text{AlC}$  coating layer, ③ is the attached Na-Sb-Bi alloy, ④ is the gap generated during embedding because of the different shrinkage coefficient and ⑤ is the embedding material.

#### 4.3.4 Discussion

The Na-Sb-Bi alloy of this test represents the positive electrode of our Na-based LMB cells at fully-discharged state. The corrosion performance of seven materials (T91 ferritic steel, SS304, SS316L and SS316Ti austenitic stainless steel, Mo metal and two MAX-phase coatings  $\text{Cr}_2\text{AlC}$  and  $\text{Ti}_2\text{AlC}$  on T91-substrate) in liquid Na-Sb-Bi alloy at 450 °C with the duration of 750 h was investigated in order to ensure the long-term application of promising PCC candidates in LMB cells.

Firstly, the clear difference on the amount of attached Sb-Bi alloy and Na-Sb-Bi alloy on metallic specimens indicates the obvious change on the physical properties such as melting point, viscosity or the wettability to metallic substrate by the adding a large amount of Na.

Moreover, when compared with the results of static corrosion test for PCC materials in positive electrode at fully-charged state (SbBi<sub>9</sub> alloy in Section 4.2), surprisingly, all Fe-Cr and Fe-Cr-Ni steels exhibit good corrosion resistance against Na-Sb-Bi alloy at 450 °C for at least 750 h, which indicates that the presence of aggressive As impurity in Sb-Bi alloys might be the reason for the occurrence of the relatively severe corrosion attack [160].

Furthermore, as for Mo metal, the only promising metallic candidate for PCC in Section 4.2, also exhibits outstanding corrosion-resistant performance after 750 h exposure in Na-Sb-Bi alloy. Therefore, the corrosion attack (tiny cuts at the interface) on Mo metal during the exposure in Sb-Sn and Sb-Bi alloys (seen in Section 4.2) may be most probably attributed to the presence

of aggressive As contamination.

With regards to MAX-phase, the only auspicious PCC candidate in Section 4.2 except for Mo metal, after 750 h exposure in Na-Sb-Bi alloy at 450 °C, both two MAX-phase coatings ( $\text{Cr}_2\text{AlC}$  and  $\text{Ti}_2\text{AlC}$ ) on T91-substrate maintain intact and uninjured, which indicates that both of them also possess excellent corrosion resistance in Na-Sb-Bi alloy. Moreover, in this case, the MAX-phases were coated on a steel (T91 ferritic steel) substrate instead of on a ceramic substrate, after 750 h exposure at 450 °C, MAX-phase coatings are still adhesive to the ferritic steel substrate, which proves the good compatibility of those MAX-phases with ferritic steel substrate at higher temperature (up to 450 °C).

#### **4.3.5 Short summary**

In brief, the results show that when As impurity is excluded from the heavy metals and extra Na is added into the Sb-Bi alloy, after 750 h exposure in pure Na-Sb-Bi alloy, the corrosion attack on all test materials becomes negligible, all test specimens (T91 ferritic steel, SS304, SS316L, SS316Ti, Mo metal and two MAX-phases on steel substrate) show good corrosion resistance and could meet the requirements for long-term application, which indicates the severe corrosion attack from Sb-Bi alloys (see Section 4.2) may be contributed to the presence of As.

Combined with the conclusion from tests in positive electrode at fully-charged state (Section 4.2), SS316Ti was later applied as PCC (cell case) for our Na-based LMB cells in Section 5,.

## **4.4 Static corrosion tests for PCC materials in electrolyte**

### **4.4.1 Material selection**

All above-mentioned studies in Section 2.5.3 used binary molten chloride salts and were performed under the presence of air. It is well known that the oxygen, moisture in air will exacerbate the corrosion issues caused by molten salts, therefore, the compatibility of PCC materials with multic-cation ternary chloride molten salts ( $\text{LiCl-NaCl-KCl}$ ) under inert argon atmosphere (to simulate the real working conditions in LMB cells) are worthy to be studied as well, especially the promising candidates obtained from aforementioned tests (Mo metal and NAX-phases).

## 4.4.2 Experiments

### Materials and preparation of specimens

As shown in Figure 3.2 (a), in LMB cells with foam, the cell case or the PCC has direct contact to the molten salts electrolyte, hence, the aim of this section is to find out the compatibility of PCC materials with molten salts electrolyte under inert atmosphere, especially the promising PCC candidates mentioned in the previous sections. However, due to the shortage of MAX-phases, they were not investigated in this section.

The test specimens in this work were molybdenum (Mo) metal (Plansee SE), T91 ferritic steel (EUROTRANS-DEMETRA [135]), SS304 and SS316L (EUROTRANS-DEMETRA [135]).

All specimens were cut into appropriate size. Additionally, before exposure, all test specimens were ground by sandpaper with a grid size of 800 and 1200, successively.

### Test facility

The exposure test was implemented by the Deutsches Zentrum für Luft- und Raumfahrt (DLR) in Stuttgart. The schematic of the experimental set-up for corrosion tests for PCC materials in molten salts mixture is shown in Figure 4.89. The exposure test was carried out in an autoclave with flange.

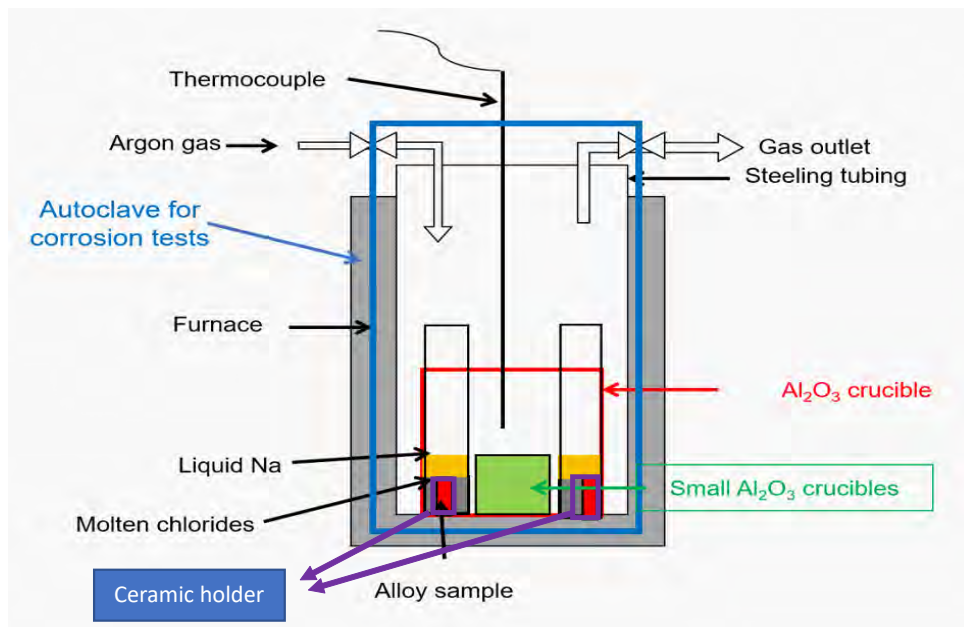


**Figure 4.89:** Schematic of experimental set-up for static corrosion tests for PCC materials in molten salts mixture.

## Preparation of molten salts electrolyte

The ternary salts mixture of LiCl-NaCl-KCl (56-5-39 mol.%) was synthesized by mixing of LiCl (Alfa Aesar, purity: > 99 %), NaCl (VWR Chemical, purity: > 99 %) and KCl (Acros Organics, purity: > 99 %) in a glovebox ( $O_2 < 0.5$  ppm,  $H_2O < 1$  ppm).

## Test procedures

After the test samples were separately fixed in the small alumina crucibles, each small alumina crucible was loaded by 6 g of salts mixture, afterwards, 1 g Na was set on the top of the salts mixture. Then the bigger alumina crucibles were sealed and heated under argon atmosphere (purity:  $\geq 99.9999$  %,  $H_2O \leq 0.05$  ppm) with a gas flow of 20 L/h to 500 °C with a heating rate of 5 °C/min, which is controlled by the programmable furnace and a thermocouple close to the alumina holders (see Figure 4.89). After that, the temperature was isothermally hold at this temperature for 500 h.

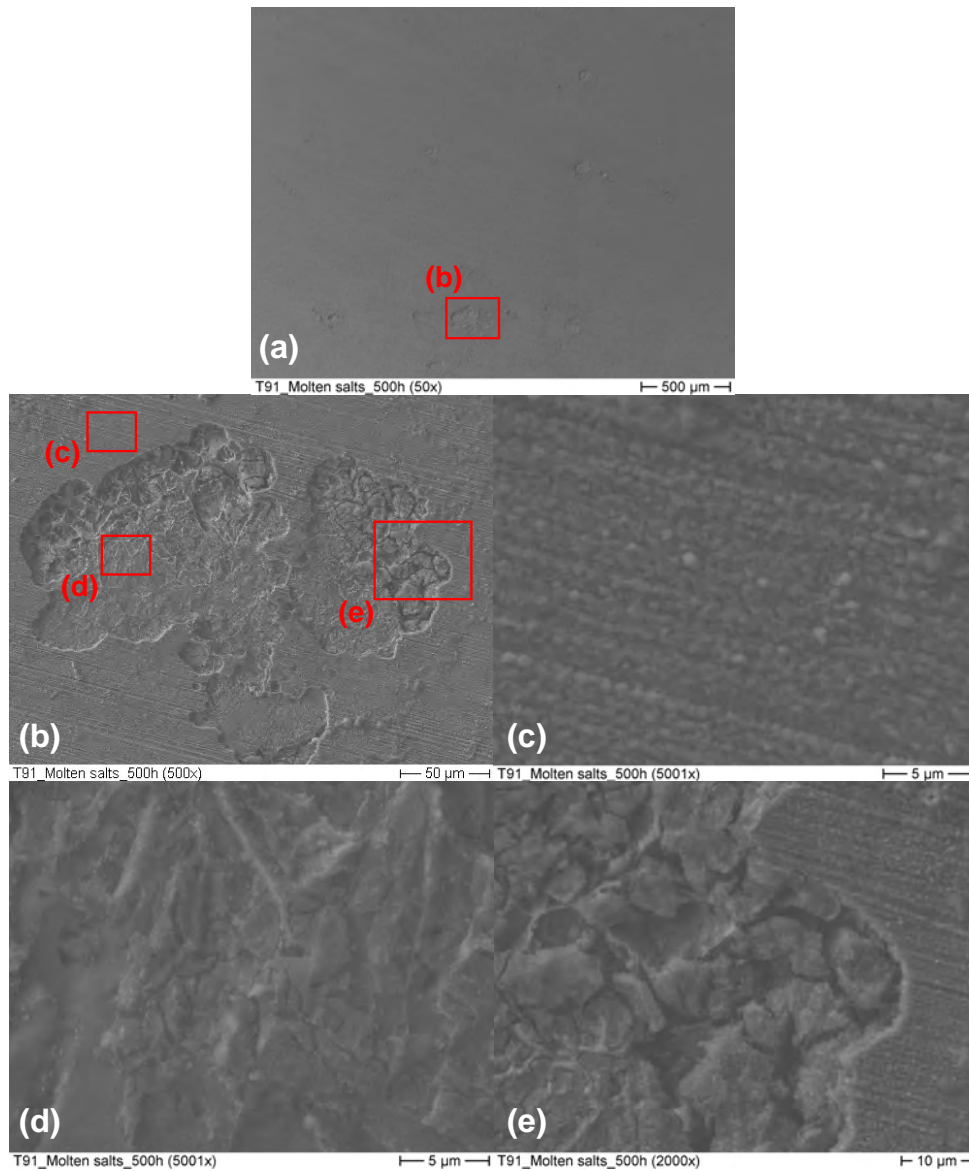
## Post-test analysis

After the immersion tests of 500 h, the furnace was cooled to room temperature under argon atmosphere. Then, all specimens were extracted from the stainless steel crucible, cleaned by distilled water and ethanol, then dried by compressed air. Afterwards, the surface morphology and cross-sections of specimens were analysed by scanning electron microscope (SEM) with energy-dispersive X-ray spectroscopy (EDS) at KIT.

### 4.4.3 Results

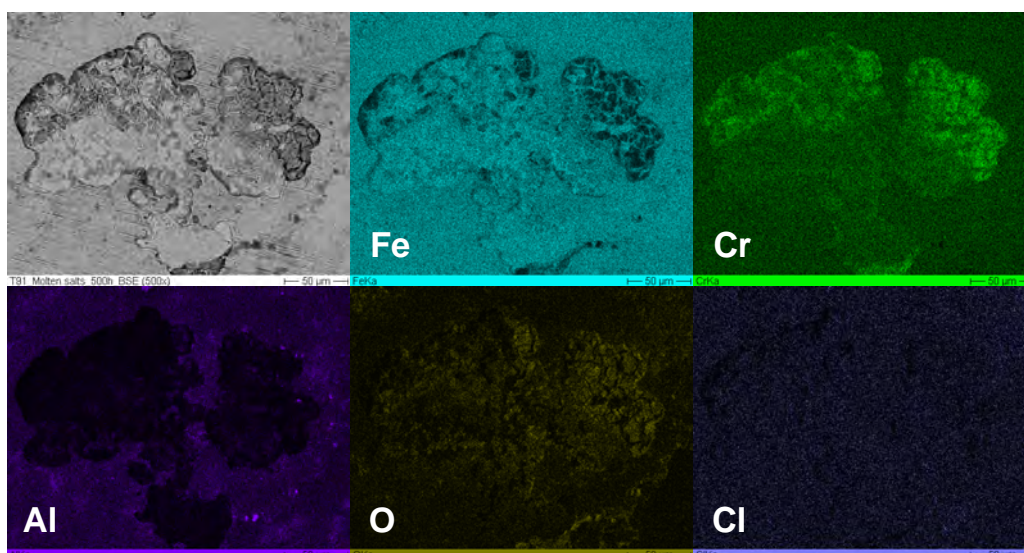
#### Fe-Cr steel (T91 ferritic steel)

Figure 4.90 shows the surface morphology of T91 ferritic steel after 500 h exposure in molten LiCl-NaCl-KCl salts mixture at different magnifications. Obviously, Figure 4.90 reveals that T91 ferritic steel was exposed to a localized corrosion attack after 500 h exposure in molten LiCl-NaCl-KCl salts mixture. Many pits of several 100  $\mu$ m area with localized loss of materials can be seen at the surface of T91 steel.



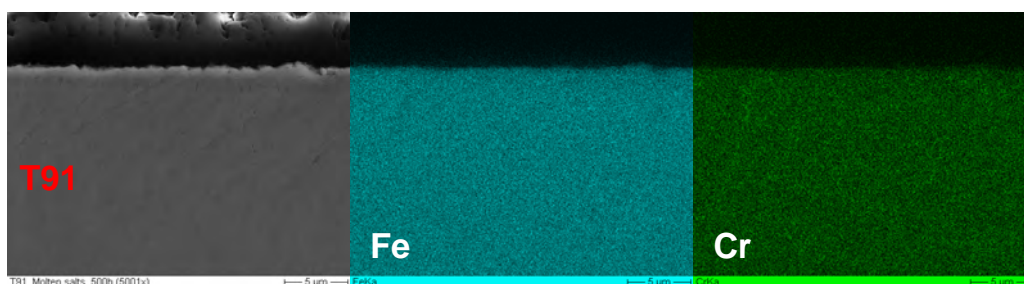
**Figure 4.90:** SE image of surface morphology of T91 ferritic steel after 500 h exposure in molten LiCl-NaCl-KCl salts mixture at 500 °C (a) at lower magnification, (b) at higher magnification with Zoom-in images (c), (d) and (e) show details at different regions.

At the BSE and EDS mapping image (Figure 4.91) is clearly depicted that some of the material loss areas on T91 steel exhibit higher Cr and O contents but a depletion on Fe. Therefore, those areas indicate the formation and the subsequent loss of chromium oxide and iron-chromium oxide. Moreover, aluminium was measured on the surface of T91 steel as well, which is probably due to an unexpected reaction of molten salts mixture with the alumina sample holder used during the exposure. This will be evidenced in the next part in this dissertation.



**Figure 4.91:** BSE image and EDS element mapping images of surface morphology of T91 ferritic steel after 500 h exposure in molten LiCl-NaCl-KCl salts mixture at 500 °C.

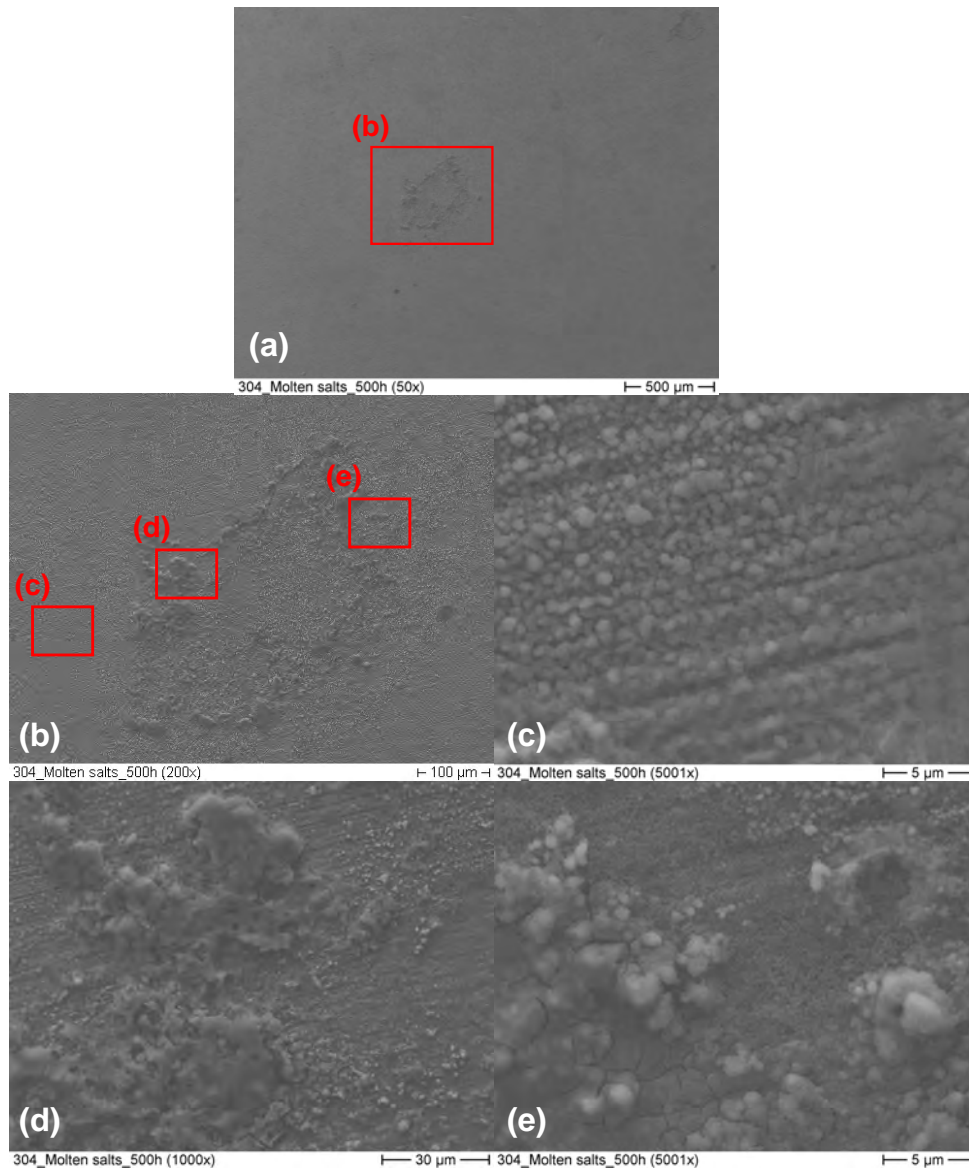
The BSE and EDS mapping images (Figure 4.92) of the cross-section of T91 steel specimen illustrate that the corrosion on T91 steel is quite marginal with a corrosion depth of < 1 µm.



**Figure 4.92:** BSE image and EDS element mapping images of cross-section of T91 ferritic steel after 500 h exposure in LiCl-NaCl-KCl at 500 °C.

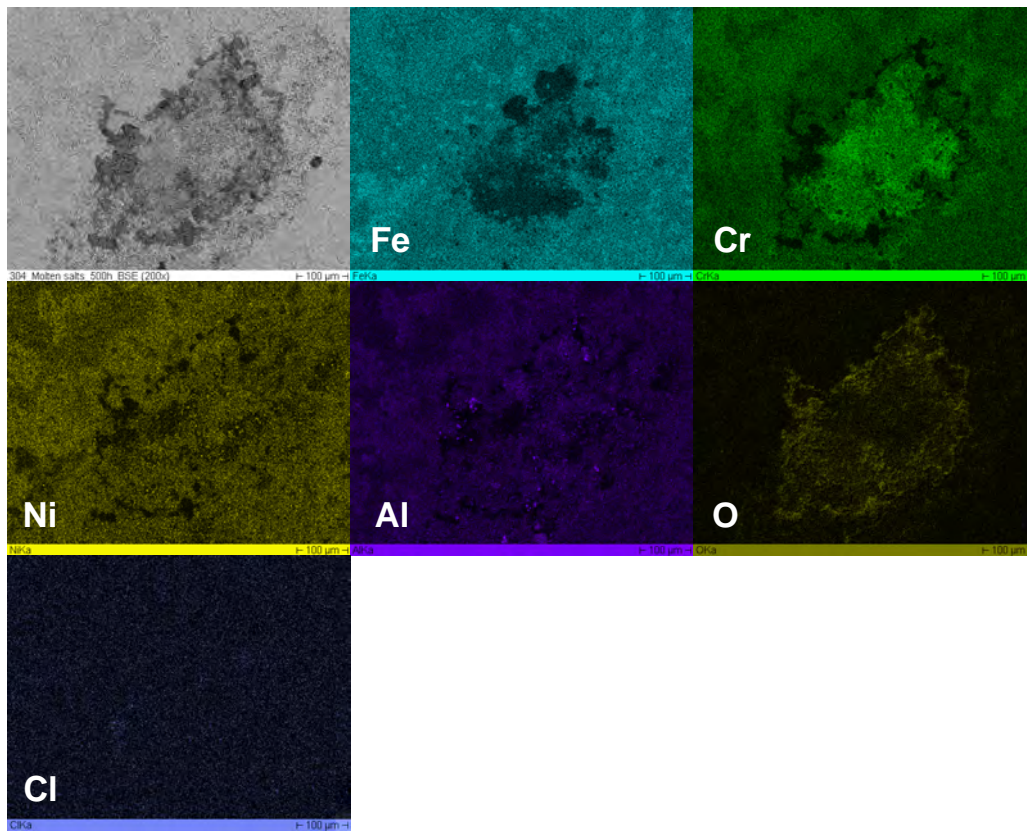
### Fe-Cr-Ni steel (SS304 and SS316L)

Figure 4.93 show the surface morphology of 304 austenitic stainless steel after 500 h exposure in molten LiCl-NaCl-KCl salts mixture at different magnifications. The Zoom-in images (Figure 4.93 (c), (d) and (e)) show that after the exposure, some particles can be seen attached on SS304's surface, which cannot be removed by the distilled water and ethanol after the exposure test. When compared with T91 steel, neither pitting corrosion nor localized material loss can be observed on the surface of SS304.



**Figure 4.93:** SE image of surface morphology of SS304 after 500 h exposure in molten LiCl-NaCl-KCl salts mixture at 500 °C (a) at lower magnification, (b) at higher magnification with Zoom-in images (c), (d) and (e) show details at different regions.

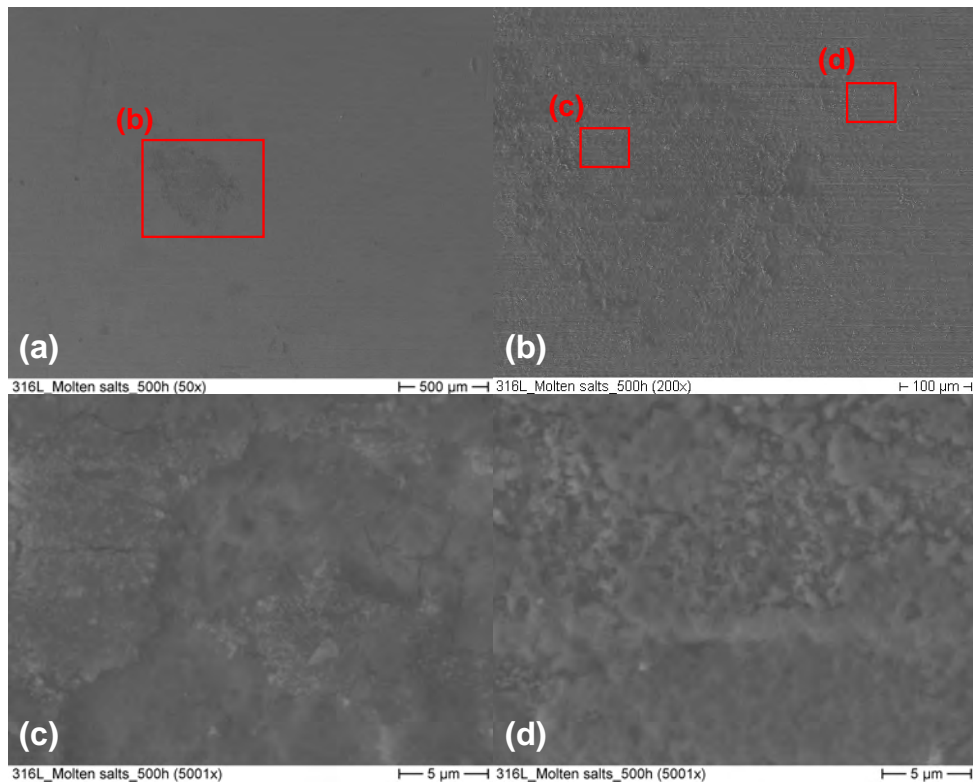
The BSE and EDS mapping images (Figure 4.94) illustrate that all the attached particles on SS304 exhibit an increased O content. Fe content is increased in some of the particles, while some show an increased Cr content and others show an increase in both Fe and Cr. Therefore, the particles might consist of iron-nickel oxide, chromium-nickel oxide and iron-chromium-nickel oxide. Moreover, the same as T91 steel, aluminium can be detected on the surface of SS304 as well.



**Figure 4.94:** BSE image and EDS element mapping images of surface morphology of SS304 after 500 h exposure in molten LiCl-NaCl-KCl salts mixture at 500 °C.

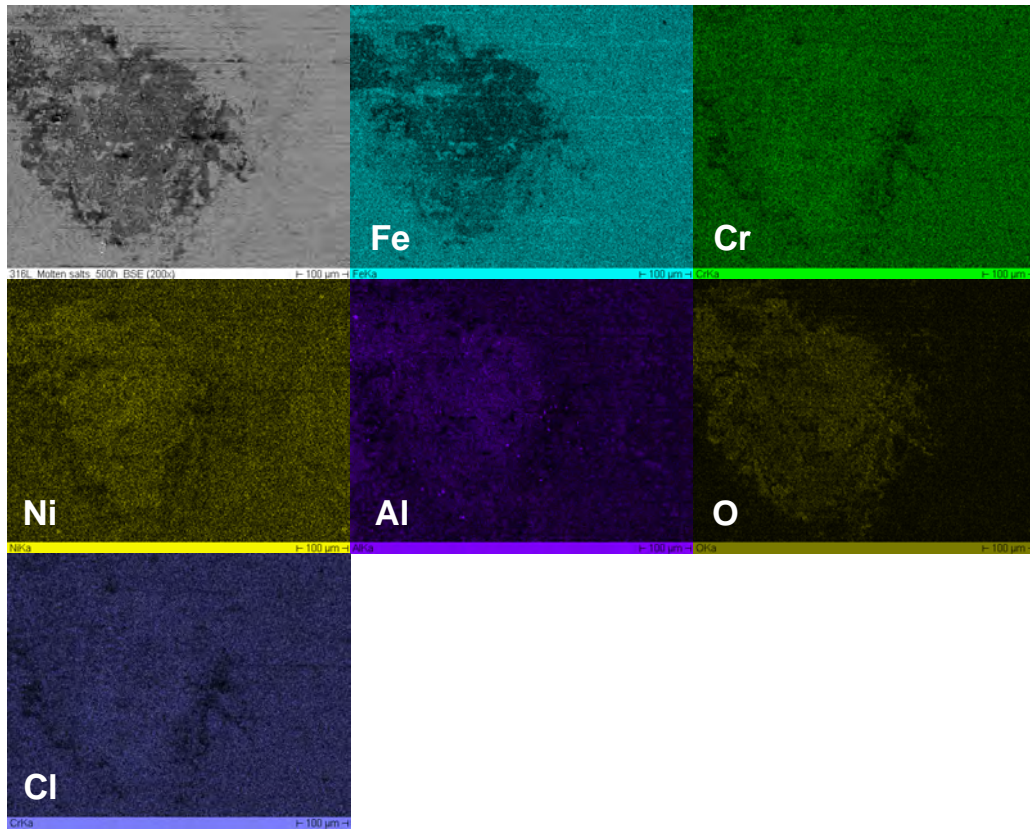
It can be seen from Figure 4.95 that SS304 suffered localized corrosion at the metal-salt interface slightly, however, neither obvious depletion of Fe, Cr and Ni nor enrichment of O can be observed at the interface region. The corrosion on SS304 is still minor with a corrosion depth of  $\sim 2 \mu\text{m}$ .





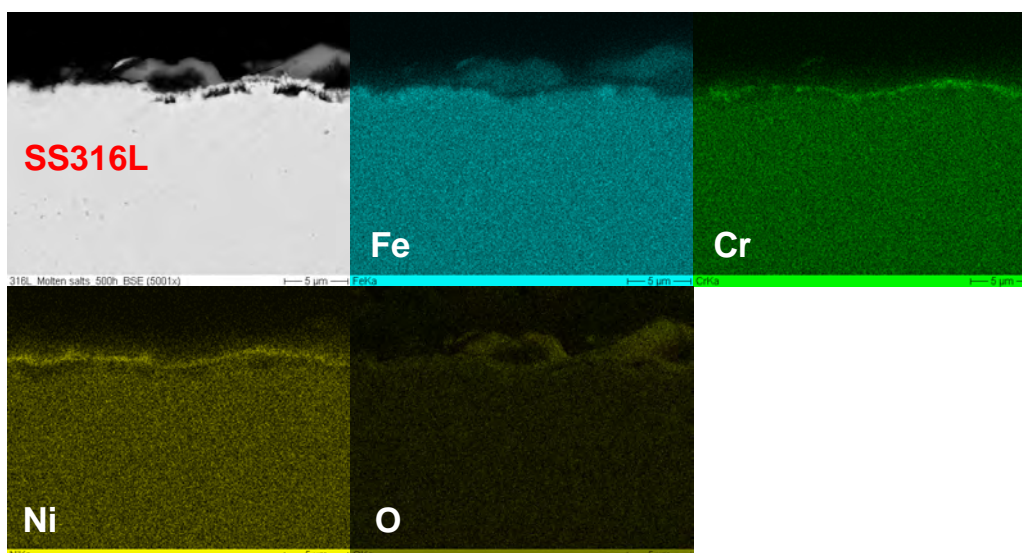
**Figure 4.96:** SE image of surface morphology of SS316L after 500 h exposure in molten LiCl-NaCl-KCl salts mixture at 500 °C at lower magnification, (b) at higher magnification with Zoom-in images (c) and (d) show details at different regions.

The BSE image and EDS element mapping images of surface morphology of SS316L after 500 h exposure in molten LiCl-NaCl-KCl salts mixture (Figure 4.97) show that some of the attached particles on SS316L exhibit an enrichment on Fe, Al and O but low Cr and Ni contents, while some show higher Al and O contents with the presence of Cr and Ni but a distinct depletion on Fe. Therefore, the particles are probably the iron-aluminium oxide and aluminium-chromium-nickel oxide. Moreover, when compared with SS304, no distinct depletion of Fe, Cr and Ni can be observed at the surface of SS316L.



**Figure 4.97:** BSE image and EDS element mapping images of surface morphology of SS316L after 500 h exposure in molten LiCl-NaCl-KCl salts mixture at 500 °C.

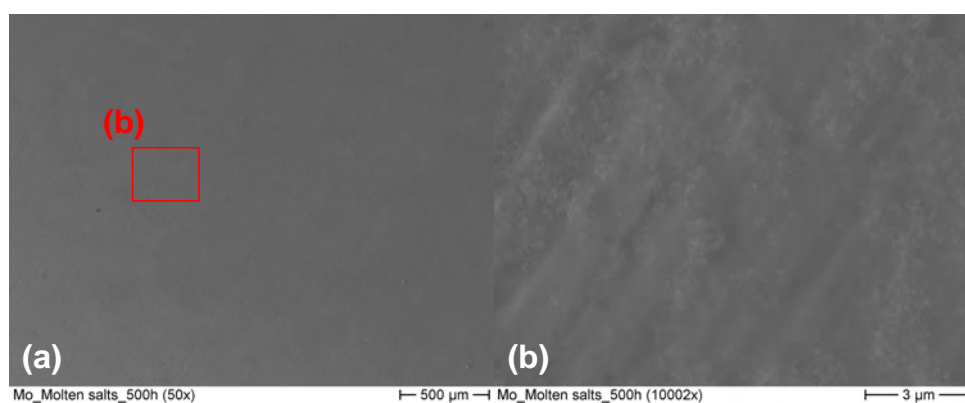
The BSE image and EDS element mapping on the cross-section of SS316L after exposure (Figure 4.98) illustrate that SS316L suffered marginal localized corrosion at the metal-salt interface with a corrosion depth of around 2  $\mu\text{m}$ . However, unlike SS304, an outer layer with an enrichment in Fe and Ni contents can be observed at the metal-salt interface, the layer underneath of this Cr- and Ni-rich layer is slightly enriched in Fe but clearly depleted in Ni.



**Figure 4.98:** BSE image and EDS element mapping images of cross-section of SS316L after 500 h exposure in LiCl-NaCl-KCl at 500 °C.

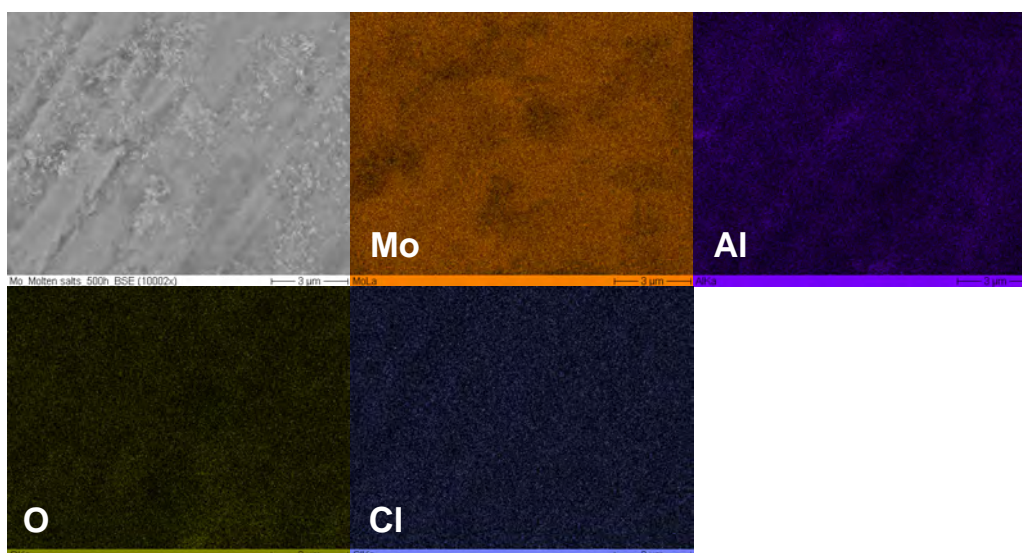
### Pure metal (Mo)

Figure 4.99 shows the surface morphology of Mo metal after 500 h exposure in molten LiCl-NaCl-KCl salts mixture at different magnifications. Although Figure 4.99 (a) shows no signal for corrosion attack, it can be seen from Figure 4.99 (b) that some bright particles were unevenly attached on the surface of Mo metal after 500 h exposure in molten LiCl-NaCl-KCl salts mixture.



**Figure 4.99:** SE image of surface morphology of Mo metal after 500 h exposure in molten LiCl-NaCl-KCl salts mixture at 500 °C (a) at low magnification and (b) at high magnification.

The BSE image and EDS element mapping images of surface morphology of T91 ferritic steel after 500 h exposure in molten LiCl-NaCl-KCl salts mixture (seen in Figure 4.100) present no depletion of Mo, however, a small amount of Al and O were detected on the bright particles on Mo metal's surface.



**Figure 4.100:** BSE image and EDS element mapping images of surface morphology of Mo metal after 500 h exposure in molten LiCl-NaCl-KCl salts mixture at 500 °C.

The BSE image and EDS element mapping on the cross-section of Mo metal after exposure (Figure 4.101) illustrate that Mo metal suffered no localized corrosion on the metal-salt interface, neither depletion of Mo nor the formation of new phases can be observed at the interface. The corrosion on Mo metal after 500 h exposure is almost invisible and therefore can be negligible.

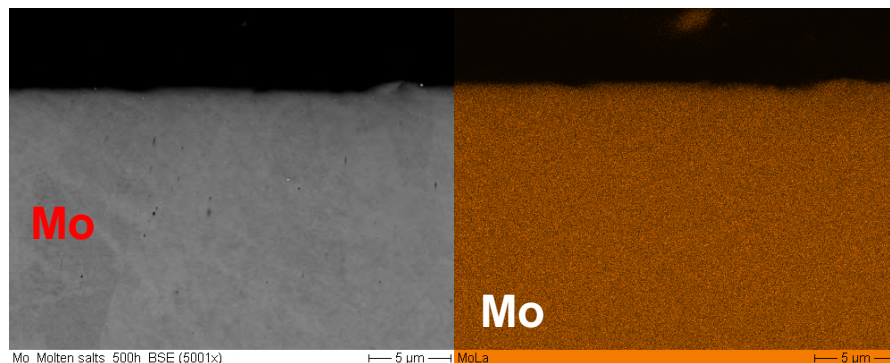


**Figure 4.101:** BSE image and EDS element mapping images of cross-section of Mo metal after 500 h exposure in LiCl-NaCl-KCl at 500 °C.

#### 4.4.4 Discussion

The compatibility of four materials (T91 ferritic steel, SS304 and SS316 austenitic stainless steel and Mo metal) with molten chloride salts mixture (LiCl-NaCl-KCl) under inert argon atmosphere at 500 °C with the duration of 500 h was investigated.

Firstly, a certain amount of Al can be measured on all specimens' surface, which is probably due to the occurrence of side reactions in electrolyte (exchange reaction between Li-ions and Na and the exchange reaction between the reduced Li from lithium chloride and alumina-ceramic), which will be detailed discussed in Section 5.4.1. Hence, the application of alumina-ceramic as sample holder seems to be inappropriate in this work.

Next, except for Al, a certain amount of O can be detected on the surface of all test specimens, which indicates the presence of elemental oxygen or O-containing compounds during the exposure. This might be owing to synergistic effect of the side reaction of the reduced Li from lithium chloride with alumina sample holder and the inappropriate pre-treatment on chloride salts mixture and the added Na on top. Considering that the presence of oxygen may not only accelerate the corrosion rate in molten salts, but also exert an adverse influence on the performance of LMB cells, therefore, in contrast to the salts mixture used in CSP, an appropriate pre-treatment on chloride salts electrolyte and on the used Na negative electrode in LMB cells is required.

Then, Fe-Cr and Fe-Cr-Ni steels all suffer pitting corrosion after 500 h exposure in molten chloride salts mixture under inert argon atmosphere at 500 °C. Besides, the formation of metal oxides with different compositions can be observed on the surface of all steel specimens. Additionally, the most pronounced pits with localized material loss are observed on Fe-Cr steel (T91 ferritic steel) while both Fe-Cr-Ni steels (SS304 and SS316L) show only very weak corrosion pits. Nevertheless, the corrosion attack on steels is relatively marginal and negligible, which is a direct contradiction to previous studies of corrosion in molten salts in air [79]. This indicates that the oxygen or moisture in air may play an important roll in corrosion in molten salts [77].

In addition, as for Mo metal, which exhibits outstanding corrosion resistance in both Sb-Bi and Na-Sb-Bi alloys, after 500 h exposure in molten salts electrolyte with Na on top, although a small amount of Al and O can be measured on the surface of Mo metal, Mo metal still presents an excellent corrosion-resistant performance in molten salts electrolyte, which is contrary to Shankar's conclusion that Mo is not beneficial for molten salts environment in air [76].

Furthermore, obviously, it is easy to find out that when compared with the results of corrosion tests in positive electrode (Section 4.2 and 4.3), the corrosion attack by molten salts electrolyte is much milder and almost negligible. Therefore, the key factor which may adversely influence the performance of LMB cells is the corrosion attack induced by positive electrode.

Finally, due to the lack of MAX-phases, the compatibility of MAX-phase coatings on steel substrate with molten chloride salts mixture under inert argon atmosphere has not been studied yet and should be further tested to investigate the feasibility of applying MAX-phases in Na-based LMB cells.

#### **4.4.5 Short summary**

In conclusion, compared with the corrosion attack from positive electrode, the corrosion attack by molten salts electrolyte is almost negligible, hence the corrosion by molten salts on PCC is not the key factor in Na-based LMB cells, all test specimens (steels and Mo metal) exhibit good corrosion resistance.

Additionally, the combination of molten salts electrolyte and liquid Na results in side reactions, which decompose the used alumina sample holder. Thereby the application of alumina ceramic as insulating sheath for Na-based LMB cells without foam is in doubt and need to be further investigated.

## 5 Cell performance

### 5.1 Preparation of cell active components

#### 5.1.1 Preparation of negative electrode

Regardless of cells with Ni-foam or cells without Ni-foam, the used Na was purified in the same way as mentioned in Section 4.1.2 and 4.3.2. The sodium sink inside the glovebox was set to 130 °C to melt solid Na and to minimize the oxygen content in Na as well.

For cells with Ni-foam, the Ni-foams with Mo-wires were first together weighed on a balance inside the glovebox. After the Na in the sink melted, the liquid Na was filled into a glass beaker with a deepness of approximately 2 cm through the spout of the sink. Then a stainless steel rod was used to immerse the Ni-foam with Mo-wires in liquid Na in the glass beaker and the glass beaker was heated on the heating plate at 350 °C for 30 min. As next step, the glass beaker with liquid Na and Ni-foam inside was set into the vacuum chamber of glovebox, evacuated and held for 3 min. After that, the glass beaker was taken out from the chamber and re-set on the heating plate. After the Na drops attached on the surface of Ni-foam were removed, the Ni-foam with Mo-wires was taken out from the liquid Na, cooled down to room temperature and weighed again, so the weight difference is the weight of Na absorbed in the Ni-foam.

For cells without Ni-foams, the desired liquid Na was filled into the glass beaker from the sodium sink, after that, it was directly poured into cell case when needed.

#### 5.1.2 Preparation of electrolyte

The salts used and the preparation of the molten salts electrolyte is exactly the same as the procedures described in Section 4.1.2.

#### 5.1.3 Preparation of positive electrode

According to the previous results from the corrosion tests on PCC materials, only  $\text{SbBi}_9$  was selected as positive electrode for Na-based LMB cells, which was gained by mixing the individual heavy metals Sb and Bi in their granular forms in  $\text{Al}_2\text{O}_3$ -crucibles.

The used Sb and Bi are the same as the heavy metals used in Section 4.2.2 and the preparation of positive electrode is the same as the preparation of  $\text{SbBi}_9$  alloy in Section 4.3.2.

## 5.2 Cell assembly

As aforementioned designs in Section 3.2, the Na-based LMB cells can also be classified into two types, namely cells with Ni-foam and cells without foam.

Before assembly, the connecting pieces, fastening discs and the inner surface of cell cases (SS316Ti) were cleaned in ethanol in an ultrasonic bath for 15 min. Then they were dried by compressed air and transported into a glovebox ( $\text{O}_2 < 0.1$  ppm,  $\text{H}_2\text{O} < 0.1$  ppm), in which the whole process of cell assembly was preformed.

### 5.2.1 Cell with a Ni-foam

The schematic cross-section of a LMB cell with a Ni-foam is shown in Figure 5.1.

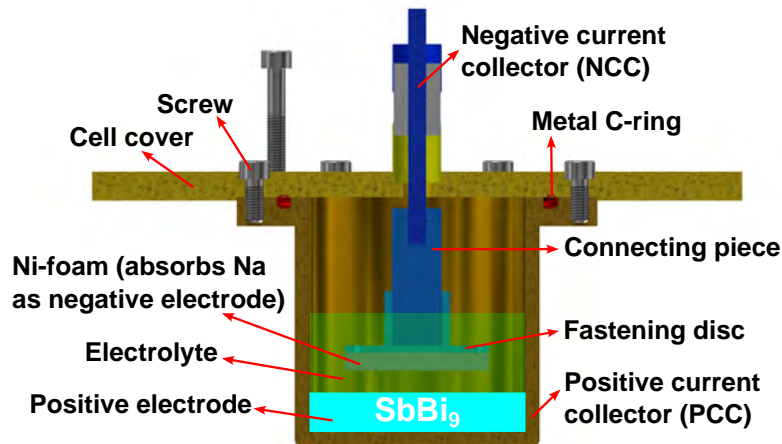


**Figure 5.1:** Schematic cross-section of a LMB cell with a Ni-foam.

For cells with Ni-foam (porosity: 50 PPI, diameter:  $50 \pm 0.2$  and  $40 \pm 0.2$  mm, thickness:  $5 \pm 0.2$  mm, RECEMAT BV), 4 small holes (diameter: 1.2 mm) were first drilled on the Ni-foam and threaded by Mo-wires (diameter: 0.4 mm). Then those Ni-foams with Mo-wires were set into the furnace common COSTA (used in Section 4.2.2) at room temperature and the atmosphere inside the quartz tube was pre-purged by 100 mL/min  $\text{Ar}+5\%\text{H}_2$  gas until the oxygen content inside the tube reached  $10^{-17}$  ppm.

Next, the temperature was raised to 700 °C and hold for 1 h in order to reduce the oxides generated at Ni-foams' surface, then the furnace was cooled down to room temperature. To prevent the further oxidation of Ni-foams, the quartz tube was hold under 100 mL/min Ar+5%H<sub>2</sub> gas flow for the entire time. After that, those Ni-foams with Mo-wires were taken out and transported into the glovebox immediately.

Then the Ni-foam was fastened to the fastening disc by Mo-wires. The fastening disc was then connected with connecting piece through threaded connection, which was later connected to the NCC on the cell cover in order to adjust the distance between the upper surface of positive electrode and the lower surface of the Ni-foam as 11 mm.

After the Ni-foam is imported into the glovebox, the heating plate was set to 500 °C to melt the 130 g solidified SbBi<sub>9</sub> in the Al<sub>2</sub>O<sub>3</sub>-crucible. When the SbBi<sub>9</sub> melted, it was poured into the cell case (SS316Ti, inner diameter: 60 mm, outer diameter: 68 mm, bottom thickness: 4 mm, height: 69 mm, KIT-IHM workshop) at room temperature. Next, the sealing ring was added to the cell case. Then, three bracket supports were added to the cell case through the screw holes and the molten salt electrolyte (LiCl-NaCl-KCl: 61-3-36 mol.%) was poured into the cell case. After that, the cell cover (with connecting pieces, fastening disc and the Ni-foam) was immediately but slightly screwed to the cell case by the remaining three screws. The bracket supports were removed and all screws were tighten after the cell was cooled down to room temperature.

Figure 5.2 illustrates the improvement on a LMB cell with a Ni-foam, in which a Mo-crucible (inner  $\varnothing$ : 56 mm, outer  $\varnothing$ : 58 mm, bottom thickness: 2 mm, height: 40 mm, BeamTec GmbH) is inserted as corrosion protection layer for PCC.

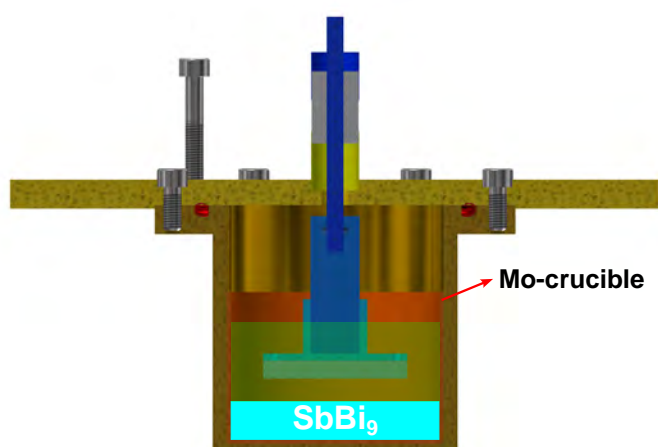


**Figure 5.2:** Schematic cross-section of a LMB cell with a Ni-foam equipped with a Mo-crucible.

At beginning, 130 g solidified  $\text{SbBi}_9$  in the  $\text{Al}_2\text{O}_3$ -crucible was poured into the Mo-crucible instead of the cell case and a few drops of  $\text{SbBi}_9$  were poured into the cell case before the Mo-crucible was inserted in order to ensure the conductivity between the PCC and the Mo-crucible. Then the cell case with the Mo-crucible and  $\text{SbBi}_9$  inside was set on the heating plate ( $500\text{ }^\circ\text{C}$ ) to melt the  $\text{SbBi}_9$  and the Mo-crucible was pressed to the bottom of cell case. After that, the assembly procedures of a LMB with Ni-foam and Mo-crucible are exactly the same as the normal LMB cells only equipped with a Ni-foam.

### 5.2.2 Cell without foam

The schematic cross-section of a LMB cell without foam is shown in Figure 5.3.

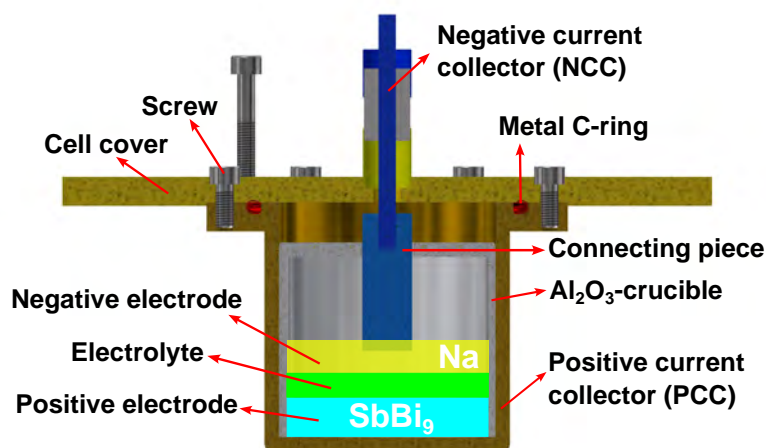


**Figure 5.3:** Schematic cross-section of a LMB cell without foam but with a  $\text{Al}_2\text{O}_3$ -crucible.

For cells without foam, the heating plate was set to  $500\text{ }^\circ\text{C}$  to melt the 130 g solidified  $\text{SbBi}_9$  in an  $\text{Al}_2\text{O}_3$ -crucible (99.7 %  $\text{Al}_2\text{O}_3$ , inner  $\varnothing$ : 52 mm, outer  $\varnothing$ : 58 mm, bottom thickness: 3 mm, height: 62 mm, Gieß-Technische-Sonderkeramik GmbH & Co. KG) or an spinel-ceramic ( $\text{MgAl}_2\text{O}_4$ , 70 %  $\text{Al}_2\text{O}_3$  + 30 %  $\text{MgO}$ , inner  $\varnothing$ : 56 mm, outer  $\varnothing$ : 58 mm, bottom thickness: 2 mm, height: 40 mm, Gieß-Technische-Sonderkeramik GmbH & Co. KG). When the  $\text{SbBi}_9$  melted, it was poured into the cell case at room temperature. Next, the sealing ring was added to the cell case and the desired amount of molten salt electrolyte ( $\text{LiCl-NaCl-KCl}$ : 61-3-36 mol.%) was poured into the cell case to ensure the distance between the positive electrode and negative electrode. Then the ceramic insulation was set into the cell case and the cell case was cooled down to room temperature. As next step, the three bracket supports was added to cell case through the screw holes and the desired amount of Na was directly poured into the cell case

from the glass beaker. After that, the cell cover (with connecting piece) was screwed to the cell case immediately but slightly by the rest three screws. As last step, the brackets supports were removed and all screws were tighten after the cell was cooled down to room temperature.

### 5.3 Cell testing

After cell assembly, the cells were set into the heating sleeve, an alumina cover was used for heat isolation (see Figure 5.4).



**Figure 5.4:** Heating sleeve and temperature regulator with alumina covers for cell testing.

At beginning, the temperature in different areas (in positive electrode, in molten salts electrolyte and in the vapor phase at top) inside the cell during cell operation was measured by thermocouples (Figure 5.5) and a temperature gradient between the set temperature at the heating sleeve and the real temperature inside the cell was found. When the set temperature of temperature regulator is 500 °C, the real temperature at cell bottom is around 450 °C. Additionally, the temperature at the outer surface on cell cover was measured as well: the temperature in the middle is more than 180 °C while it is only around 130 °C at the edge.

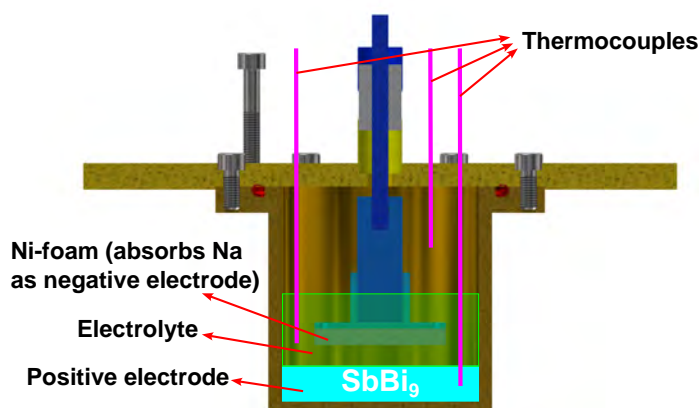


**Figure 5.5:** Temperature measurement on cell.

Therefore, to start cell tests, all cells were first pre-heated at 500 °C for 5 h. Then, for the entire duration of cell tests, the temperature in the heating sleeve was maintained at 500 °C.

The Galvanostatic Intermittent Titration Technique (GITT) and Galvanostatic Cycling with Potential Limitation (GCPL) tests were performed by a high-current Arbin electrochemical station (LBT21084HC). The specific current density was calculated based on the contact area between electrolyte and positive electrode.

The Electrochemical Impedance Spectroscopy (EIS) tests were carried out on a Gamry 5000E Potentiostat/Galvanostat.

## 5.4 Unexpected problems

### 5.4.1 Side reactions in electrolyte

For cells without foam but with an Al<sub>2</sub>O<sub>3</sub>-ceramic insulating sheath (Figure 5.3), after cell testing, the cell was disassembled and an obvious darkening on the Al<sub>2</sub>O<sub>3</sub>-ceramic insulating sheath was witnessed exactly on the position where directly contacts the electrolyte (seen in Figure 5.6). Considering that alumina possesses good compatibility with heavy metals, molten salts and liquid Na, the unusual phenomenon on alumina-ceramic indicates the presence of some side reactions in electrolyte. Hence, inductively coupled plasma optical emission spectroscopy (ICP-OES) was implemented to measure the electrolyte composition before and after testing of cells with Ni-foam, whose results are listed in Table 5.1.

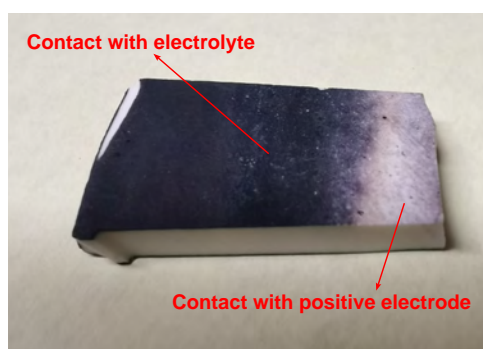


**Figure 5.6:** A piece of Al<sub>2</sub>O<sub>3</sub>-ceramic insulating sheath in Na || SbBi<sub>9</sub> cell without foam.

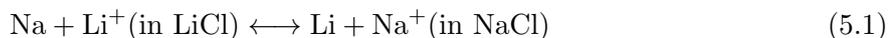
**Table 5.1:** Results of ICP-OES on cells with Ni-foam.

		Electrolyte before cell testing		Electrolyte after cell testing	
Elements	Atomic mass	Weight percent (%)	Mole percent (%)	Weight percent (%)	Mole percent (%)
Li	6.94	7.63	61.35	6.61	54.70
Na	22.99	1.34	3.25	3.43	8.57
K	39.09	24.80	35.40	25.00	36.73
Sum		33.77	100.00	35.04	100.00

According to Table 5.1, obviously, the electrolyte composition before cell testing corresponds to the mole fraction during the preparation of molten salts electrolyte (LiCl-NaCl-KCl: 61-3-36 mol.%), however, after cell testing, apparently, the electrolyte composition (especially Li and Na) changed.

Electrolyte after cell testing presents a clear decrease in the mole fraction of Li and a distinct increment in the mole fraction of Na while the mole fraction of K only increased a little. The change in electrolyte composition indicates the occurrence of the exchange reaction between Na and the cations of electrolyte, especially Li (see Equation 5.1) [161].

Exchange reaction between Li-ions and Na:



The exchange reaction between Na and Li-ions (Equation 5.1) occurs in both cells without foam and cells with Ni-foam, therefore, as a result, the actual active negative electrode of Na-based LMB cells turns into the mixture of Li and Na.

Additionally, in Na-based LMB cells with Al<sub>2</sub>O<sub>3</sub>-ceramic insulating sheath, according to the Ellingham diagram for oxides [162, 163], the line for Li-oxide formation is below the line for Al-oxide formation while the line for Al-oxide formation is below that for Na-oxide formation, hence Li is oxidized to Li-ions. The side reaction between Li and Al<sub>2</sub>O<sub>3</sub>-ceramic can be expressed as:



Laser-induced breakdown spectroscopy (LIBS) examination was conducted on both the darkened area and bright area of Al<sub>2</sub>O<sub>3</sub> in order to get further information. The selection of measurement point for the LIBS examination is totally arbitrary and each measurement point was continuously measured 15 times to collect information of deeper region. The results on the darkened area (seen in Figure 5.7 and Table 5.2) clarify that the original constituents (Al and O) were distinctly

depleted, a large number of Li was detected in both near-surface and deeper region while a small amount of K was only found in the near-surface region. By contrast, a large amount of Al and O can still be found in the bright area while Li can only be detected in the near-surface region. Moreover, a small amount of K can be measured in the near-surface region of the bright area as well, however, its content increased drastically in the deeper region (Figure 5.8 and Table 5.3).

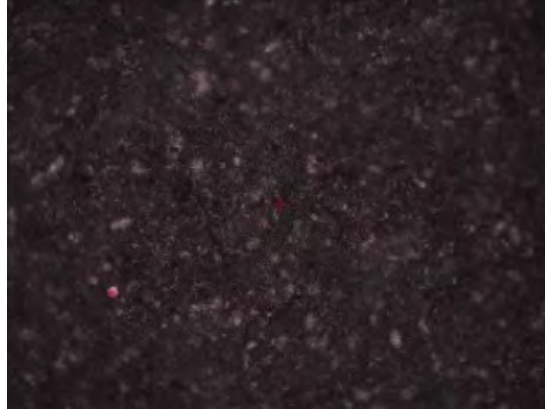


**Figure 5.7:** Image of LIBS analysis on darkened area of  $\text{Al}_2\text{O}_3$ -ceramic in Na-based LMB cells.

**Table 5.2:** Results of LIBS analysis on darkened area of  $\text{Al}_2\text{O}_3$ -ceramic in Na-based LMB cells (in wt.%).

Measurement number	Li	O	Al	K	Si
1	82.3	11.3	5.1	1.0	–
2	83.5	11.0	4.8	0.7	–
3	74.9	16.0	8.7	0.4	–
4	53.1	33.3	13.1	0.5	–
5	45.8	39.7	13.5	0.7	0.3
6	67.0	22.7	9.7	0.6	–
7	61.4	26.9	10.4	0.8	0.5
8	55.3	32.8	11.0	0.6	0.3
9	51.3	38.3	10.0	0.4	–
10	56.5	34.3	8.8	0.4	–
11	52.0	38.7	9.0	–	0.3
12	61.4	30.9	7.7	–	–
13	67.0	24.5	8.5	–	–
14	50.5	40.4	9.1	–	–
15	49.3	39.7	9.4	–	1.6



**Figure 5.8:** Image of LIBS analysis on bright area of  $\text{Al}_2\text{O}_3$ -ceramic in Na-based LMB cells.

**Table 5.3:** Results of LIBS analysis on bright area of  $\text{Al}_2\text{O}_3$ -ceramic in Na-based LMB cells (in wt.%).

Measurement number	Li	O	Al	Na	K	Si
1	33.7	40.8	18.7	1.3	4.4	1.1
2	24.5	48.8	20.6	1.0	3.9	1.2
3	17.3	53.0	24.1	0.8	3.6	1.2
4	14.3	55.5	25.9	0.8	2.8	0.7
5	10.0	50.0	31.4	0.5	2.7	1.2
6	–	44.1	22.3	0.5	22.7	0.4
7	–	50.9	23.0	0.5	25.2	0.4
8	–	48.6	27.4	–	23.2	0.8
9	–	48.1	27.8	–	22.8	1.3
10	–	65.5	31.5	–	2.0	1.0
11	–	53.4	26.8	–	19.2	0.6
12	–	48.2	27.4	–	24.4	–
13	–	50.1	28.5	–	20.8	0.6
14	–	52.3	31.1	16.0	0.6	
15	–	43.4	24.4	32.2	–	

Therefore, the darkening on the  $\text{Al}_2\text{O}_3$  might be attributable to the synergistic effect of both above-mentioned side reactions (see Equation 5.1 and 5.2). Pieces of different ceramics were tested and the spinel-ceramic ( $\text{MgAl}_2\text{O}_4$ , 70 %  $\text{Al}_2\text{O}_3$  + 30 %  $\text{MgO}$ , inner  $\varnothing$ : 56 mm, outer  $\varnothing$ : 58 mm, bottom thickness: 2 mm, height: 40 mm, Gieß-Technische-Sonderkeramik GmbH & Co. KG), which should be accordingly to the manufacturer be entirely stable in Na, showed the slowest reaction and was therefore selected as the ceramic insulating sheath instead of  $\text{Al}_2\text{O}_3$ -

ceramic for LMB cells without foam.

### 5.4.2 Short-circuit

For the first cell tests, Ni-foams with a diameter of 50 mm were applied as Na-host in Na || SbBi<sub>9</sub> cells. However, short-circuit occurred very often on those cells and made the implementation of long-term electrochemical tests almost impossible. The unexpected short-circuit might be owing to the short range between foam side edge and the inner wall of cell case. As a result, Na accumulates on the side wall and forms a “Na-bridge” between the foam and side wall of cell case, which finally leads to the short-circuit. Therefore the diameter of Ni-foams was reduced to 40 mm, and the short-circuit issue disappeared after the adjustment on Ni-foam’s diameter.

To get a clear insight into the electrolyte from another perspective, current density distribution in electrolyte was simulated by COMSOL Multiphysics software. The simulation was performed in 2D dimension, only half of the cross-section of cell active components was utilized to build the model in order to reduce the computing time (Figure 5.9). In all cases, the vertical distance and the  $\Delta E$  between the negative electrode and positive electrode was set as 10 mm and 0.80 V, respectively. In addition, in Figure 5.9 (a) and (b), the side wall was set to have the same potential as positive electrode while the boundary condition was set as dielectric in Figure 5.9 (c).

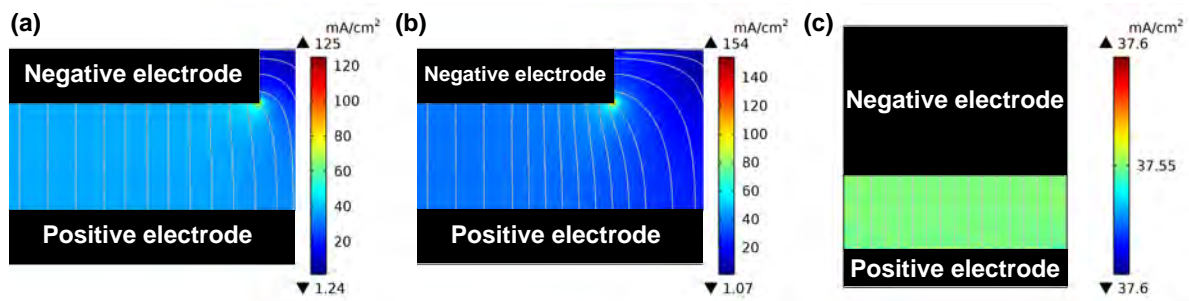


**Figure 5.9:** The current density distribution in electrolyte of (a) Na || SbBi<sub>9</sub> cell with 50 mm-foam, (b) with 40 mm-foam and (c) without foam.

It can be seen from Figure 5.9 (a) and (b) that as long as a foam is applied as Na-host in LMB cells, a large perturbation of current distribution can be observed at the bottom edge of the foam, regardless of the foam size. Moreover, by comparison with Figure 5.9 (a) and (b), Figure 5.9 (c) illustrates that the LMB cell without foam possess the most uniform and most even current density distribution in electrolyte.

## 5.5 Electrochemical performance

### 5.5.1 GITT measurements

The Galvanostatic Intermittent Titration Technique (GITT) test was first performed in cells with Ni-foam under the potential range between 0.60 V and 1.05 V to investigate the thermodynamic and kinetic properties of Na-atoms in Na || SbBi<sub>9</sub> cell during cell operation. The voltage and current vs. time during the GITT test for Na || SbBi<sub>9</sub> cell with Ni-foam at 500 °C is shown in Figure 5.10. The cell was first discharged under the current pulse of  $-0.5$  A for 1000 s, followed by a 2000 s relaxation to make the cell achieve electrochemical equilibrium, these steps were repeated consecutively until the cell voltage reached 0.60 V. After that the cell was forced to start to charge with the same settings as the previous discharging process: each step consists of a charging step under the current pulse of 0.5 A for 1000 s and followed by a relaxation step for 2000 s.

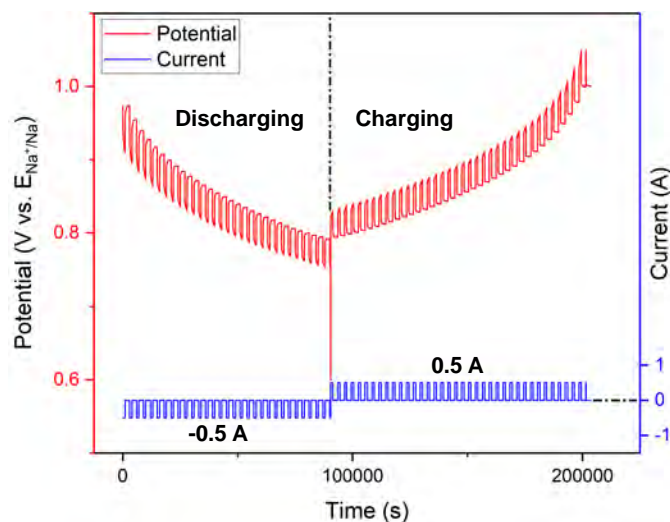


**Figure 5.10:** The voltage and current vs. time during the GITT test for Na || SbBi<sub>9</sub> cell with Ni-foam at 500 °C.

As described in Section 3.4.1, the diffusion coefficients of Na-atoms in Na || SbBi<sub>9</sub> cells at different discharging and charging states were calculated on the basis of Equation 3.15 and 3.16. Since the transient response of the voltage vs. the square root of the current pulse time shows a line behavior (seen in Figure 5.11), combined with the fact that both the applied current pulse and the time interval for the GITT tests are sufficiently small, despite the intrinsically errors brought by Equation 3.16, it can be applied to calculate the diffusion coefficients of Na-atoms in Na || SbBi<sub>9</sub> cell with Ni-foam at different discharging and charging states and itself can be

re-written into:

$$D = \frac{4}{\pi\tau} \left( \frac{mV_M}{M_M S} \right)^2 \left( \frac{\Delta E_s}{\Delta E_t} \right)^2 \quad (5.3)$$

In this case (Na || SbBi<sub>9</sub> cell with Ni-foam),  $\tau$  is the duration of the current pulse (1000 s),  $m$  is the mass of SbBi<sub>9</sub> positive electrode (130 g),  $M_M$  is the molar mass of SbBi<sub>9</sub> (200.258 g/mol) and  $S$  is the electrode/electrolyte contact area ( $S = \text{active reaction area} = \pi R^2 = 28.27 \text{ cm}^2$ ). Therefore, the diffusion coefficients of Na-atoms in cell with Ni-foam at different discharging and charging states at 500 °C are calculated and shown in Figure 5.12.

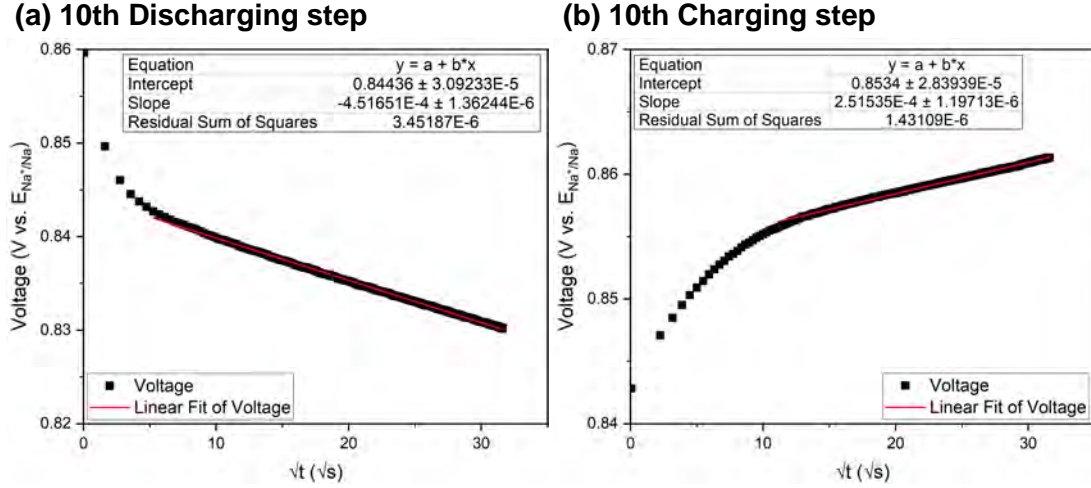


**Figure 5.11:** Line behavior of  $dE/d\sqrt{t}$  at the (a) 10<sup>th</sup> discharging step and (b) 10<sup>th</sup> charging step of GITT test in Na || SbBi<sub>9</sub> cell with Ni-foam at 500 °C.

It can be seen from Figure 5.12 that as the discharging proceeds, the Na-atoms diffused a little bit slower, which might be owing to change in Na-atoms concentration in the cell caused by the reaction of Na with positive electrode. Besides, the reaction of Na with positive electrode may as well simultaneously lead to the formation of a solid intermetallic phase at top of positive electrode. Consequently, the further diffusion of Na-atoms was hindered by the solid intermetallic layer. As the charging process goes on, the speedup of Na-atoms' diffusion and recovery of diffusion coefficient to that of initial discharging state can be attributed to the synergistic effect of the change in Na-atoms concentration with the dissolution of the solid intermetallic layer.

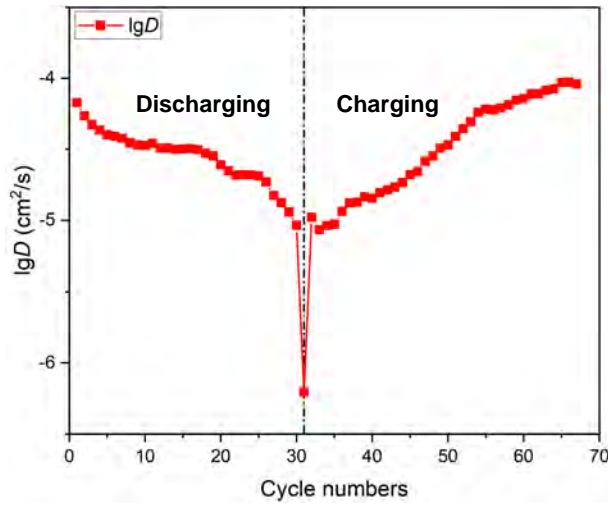


**Figure 5.12:** The diffusion coefficient of Na-atoms in Na || SbBi<sub>9</sub> cell with Ni-foam during discharging and charging at 500 °C.

Figure 5.13 shows the electromotive force (EMF) curves of Na || SbBi<sub>9</sub> cell with Ni-foam plotted as function of the mole fraction of Na inside the positive electrode. For the presentation of results in Figure 5.13, the initial amount of Na in the positive electrode is unknown and a guess is used.

As shown in Figure 5.13 (a), the charge curve deviates from the discharge curve, which is due to the self-discharge of LMB cell during the whole GITT process (discharging, charging and relaxation). If we take the self-discharge into consideration (seen in Figure 5.13 (b)), the charge curve and the discharge curve overlap with each other precisely.

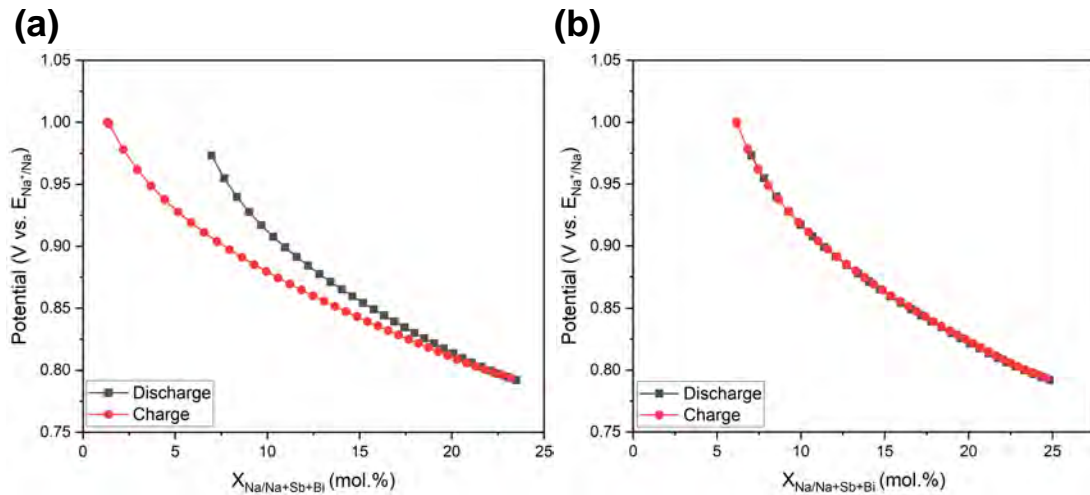


**Figure 5.13:** The EMF curves of Na || SbBi<sub>9</sub> cell with Ni-foam obtained by GITT at 500 °C, where (a) ignore the influence of self-discharging and (b) take self-discharging into consideration.

The self-discharge current  $I_{\text{self-discharge}}$  of Na || SbBi<sub>9</sub> cell with Ni-foam, which can be mainly

contributed to the solubility of Na in molten salts electrolyte, can be calculated by the following equation:

$$I_{\text{self-discharge}} = \frac{Q_{\text{Charge}} - Q_{\text{discharge}}}{\Delta t} = 0.0164134 \text{ A} \quad (5.4)$$

Considering that the electrode/electrolyte contact area of the cell (active reaction area =  $\pi r^2 = 28.27 \text{ cm}^2$ ), the self-discharge current density  $J_{\text{self-discharge}}$  during the GITT test was calculated according to the following formula:

$$J_{\text{self-discharge}} = \frac{I_{\text{self-discharge}}}{S} = 0.5808 \text{ mA/cm}^2 \quad (5.5)$$

Moreover, no flat voltage plateau (Na are not able to continuously react with the positive electrode and continually form a new intermetallic compounds) can be observed during charging and discharging in Figure 5.13. This indicates a high state of charge (SoC) or a low depth of discharge (DoD) during GITT test owing to the low ratio of negative electrode to positive electrode, or rather, the small sum of Na absorbed in foam in comparison with the large amount of positive electrode in cell case. The Na was already consumed at the initial discharging state hence the cell are not able to discharge further. As a result, the utilization rate of positive electrode is quite low.

Later the GITT test was carried out in LMB cells without foam under a broader potential range (0.5 – 1.10 V). The discharge and charge current was selected as  $-0.7 \text{ A}$  and  $0.7 \text{ A}$ , respectively while both the current pulse time and the relaxation time remain the same (1000 s and 2000 s, respectively). The voltage and current vs. time during the GITT test for cell without foam at  $500 \text{ }^\circ\text{C}$  is plotted in Figure 5.14.

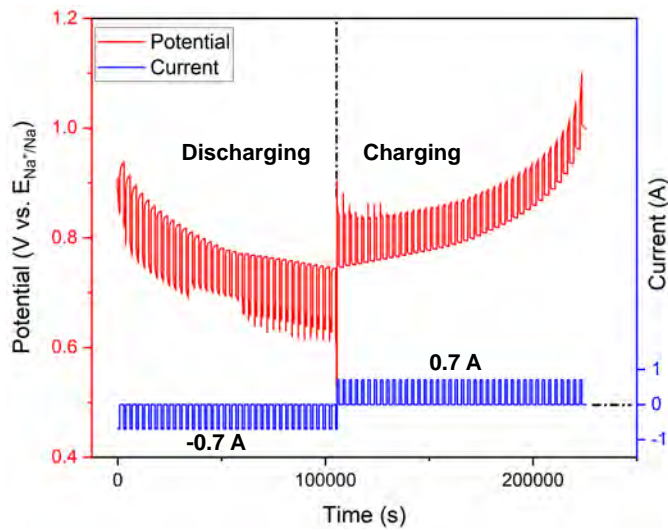


**Figure 5.14:** The voltage and current vs. time during the GITT test for Na || SbBi<sub>9</sub> cell without foam at 500 °C.

The same as Na || SbBi<sub>9</sub> cell with Ni-foam, Figure 5.15 shows the linear relationship between the transient response of the  $E$  and  $\sqrt{t}$  for Na || SbBi<sub>9</sub> cell without foam. Therefore, Equation 5.3 can be applied to calculate the the diffusion coefficients of Na-atoms in cell without foam as well, and the results are shown in Figure 5.16.

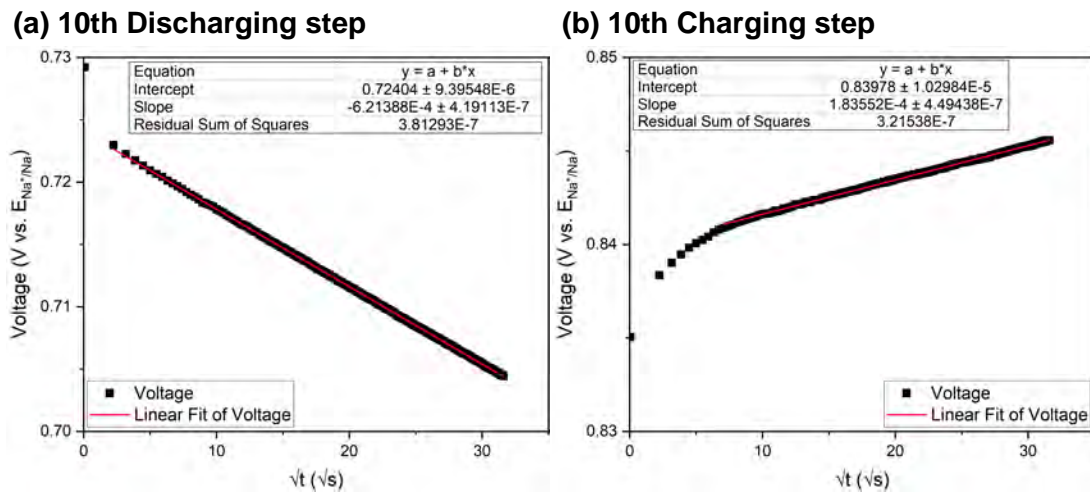


**Figure 5.15:** Line behavior of  $dE/d\sqrt{t}$  at the (a) 10<sup>th</sup> discharging step and (b) 10<sup>th</sup> charging step of GITT test in Na || SbBi<sub>9</sub> cell without foam at 500 °C.

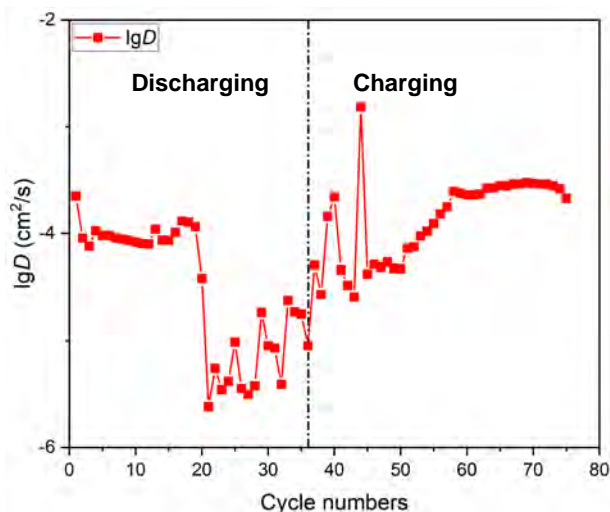


**Figure 5.16:** The diffusion coefficient of Na-atoms in Na || SbBi<sub>9</sub> cell without foam during discharging and charging at 500 °C.

It is easy to find out that Figure 5.16 exhibits close similarity to Figure 5.12: the diffusion of Na-atoms became slower as the discharging process proceeds, when charging starts, the diffusion of Na-atoms accelerated and gradually returned to its initial value. However, unlike Na || SbBi<sub>9</sub> cell with Ni-foam (see Figure 5.12), in Na || SbBi<sub>9</sub> cell without foam, a strong fluctuation in diffusion coefficient can be observed at deep discharging states and at the beginning of charging process (also seen the voltage curve in Figure 5.14). The fluctuation reflects the instability in Na || SbBi<sub>9</sub> cell without foam during this time period, which might be contributed to the imperfect cell assembly or unsuitable test parameters.

When compared with sodium-ion batteries (SIBs), the diffusion coefficients of Na-ions in SIBs with Na<sub>0.44</sub>MnO<sub>2</sub> cathode were calculated to be in the range of  $1.08 \times 10^{-13}$  to  $9.15 \times 10^{-12} \text{ cm}^2 \text{ s}^{-1}$  in aqueous system and in the range of  $5.75 \times 10^{-16}$  to  $2.14 \times 10^{-14} \text{ cm}^2 \text{ s}^{-1}$  in non-aqueous system [164]. Besides, for SIBs with vanadium phosphate cathode materials, at 300 K, the diffusion coefficient of Na-ions was calculated as  $5.1 \times 10^{-11} \text{ cm}^2 \text{ s}^{-1}$  in Na<sub>4</sub>VO(PO<sub>4</sub>)<sub>2</sub> cathode [165] and in the range of  $10^{-11}$  to  $10^{-12} \text{ cm}^2 \text{ s}^{-1}$  in NaVOPO<sub>4</sub> cathode, respectively [166].

Moreover, the diffusion coefficients of Na-ions in other Na-ions cathode materials were determined to be  $10^{-11} \text{ cm}^2 \text{ s}^{-1}$  in Na<sub>x</sub>CoO<sub>2</sub> [167],  $10^{-11} \text{ cm}^2 \text{ s}^{-1}$  in Na<sub>x</sub>MnO<sub>2</sub> [168] and  $10^{-12} \text{ cm}^2 \text{ s}^{-1}$  in Na<sub>2</sub>CoSiO<sub>5</sub> [169].

Apparently, the diffusion of Na in Na-based LMBs is at least five orders of magnitude faster than that of SIBs, which demonstrates the superior mass transport properties of LMB cells,

which can be attributed to the liquid electrode and higher operating temperature of LMBs.

The electromotive force (EMF) curves of Na || SbBi<sub>9</sub> cell without foam are shown in Figure 5.17. Obviously, in contrast to cell with Ni-foam (Figure 5.13), a flat voltage plateau can be observed on discharge curve at  $\sim 0.77$  V, which might be attributed to the further reaction (between negative electrode and positive electrode) and the continuous formation of intermetallic compounds. This plateau coincides with Zhou's results [63]. More interestingly, unlike Figure 5.13 (b), the charge curve and the discharge curve do not overlap with each other in Figure 5.17 (b). In this case, the gap between the discharge curve and the charge curve indicates that when the cell was discharged under 0.80 V, the discharge process is not 100 % reversible, some products generated by the discharging process might not be completely decomposed by the subsequent charging process.

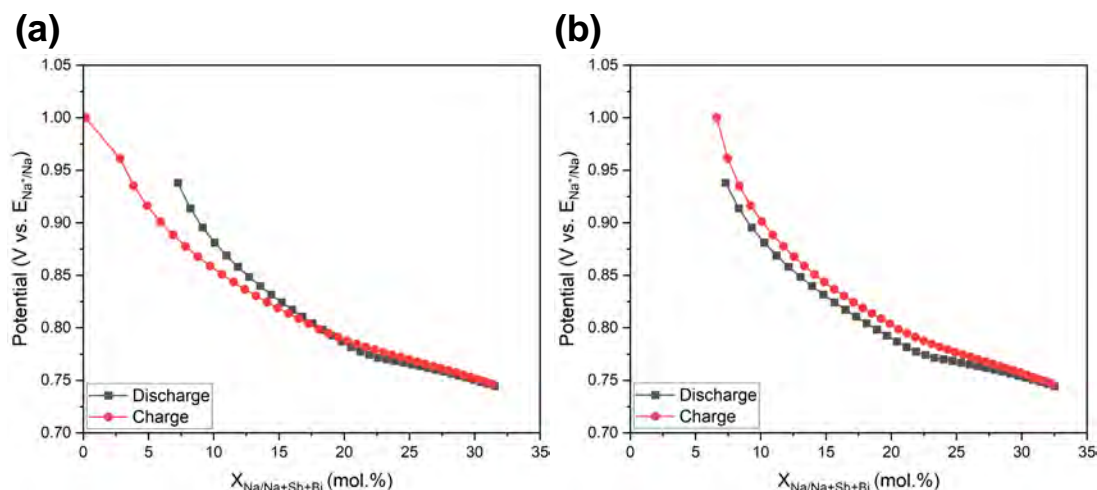


**Figure 5.17:** The EMF curves of Na || SbBi<sub>9</sub> cell without foam obtained by GITT at 500 °C, where (a) ignore the influence of self-discharging and (b) take self-discharging into consideration.

Additionally, in order to compare the Na || SbBi<sub>9</sub> cell with Ni-foam and without foam, Figure 5.13 (b) and Figure 5.17 (b) were plotted in one diagram (see Figure 5.18).

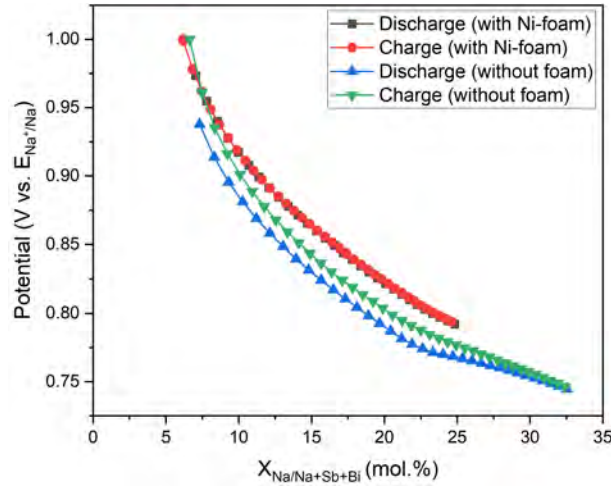


**Figure 5.18:** Comparison of EMF curves of Na || SbBi<sub>9</sub> cell with Ni-foam (Figure 5.13 (b)) and without foam (Figure 5.17 (b)) obtained by GITT at 500 °C, both taking self-discharging into consideration.

Since the EMF of Na || SbBi<sub>9</sub> cells was solely determined by the mole fraction of Na inside the positive electrode, regardless of the cell constructions (cells with Ni-foam or without foam), so long as the mole fraction of Na inside the positive electrode of different cells keep the same value, the OCV of those cells should maintain the same as well. However, as shown in Figure 5.18, the curves of cell with Ni-foam and of cell without foam do not coincide with each other, which is probably due to the fact that before GITT tests start, some Na was already diffused into positive electrode and the amount of Na into positive electrode in cell with Ni-foam differs from the value in cell without foam, which has been described in the aforementioned text. The initial values of Na in positive electrode can be individually adjusted to obtain a better consistency between the data from those two cells.

The self-discharge current  $I_{\text{self-discharge}}$  and self-discharge current density  $J_{\text{self-discharge}}$  in Na || SbBi<sub>9</sub> cell without foam (active reaction area =  $\pi r^2 = 21.24 \text{ cm}^2$ ) were calculated by the following formulas:

$$I_{\text{self-discharge}} = \frac{Q_{\text{Charge}} - Q_{\text{discharge}}}{\Delta t} = 0.0132919 \text{ A} \quad (5.6)$$

$$J_{\text{self-discharge}} = \frac{I_{\text{self-discharge}}}{S} = 0.6261 \text{ mA/cm}^2 \quad (5.7)$$

When compared with LMB cell with Ni-foam, the smaller self-discharge current in cell without foam might be attributed to the smaller amount of molten salts electrolyte as well as the elongated distance between the negative electrode and positive electrode (around 20 mm). The former factor limits the total amount of Na which can be dissolved in electrolyte while the

latter leads to a smaller Na concentration gradient, which slows down the Na-atoms diffusion and the self-discharge as well. Nevertheless, the increased self-discharge current density is owing to the reduced active reaction area (electrode/electrolyte contact area within the ceramic-crucible).

### 5.5.2 GCPL tests

The cycling stability and rate performance are determinant factors for practical application. Hence, the rate performance of Na || SbBi<sub>9</sub> cell has been first investigated at various current densities.

Figure 5.19 (a) and (b) exhibit the rate performance of of Na || SbBi<sub>9</sub> LMB cell with Ni-foam at 500 °C at current densities of 100, 200, 400, 500 and 1000 mA/cm<sup>2</sup> and the discharge-charge curves at corresponding current densities, respectively.

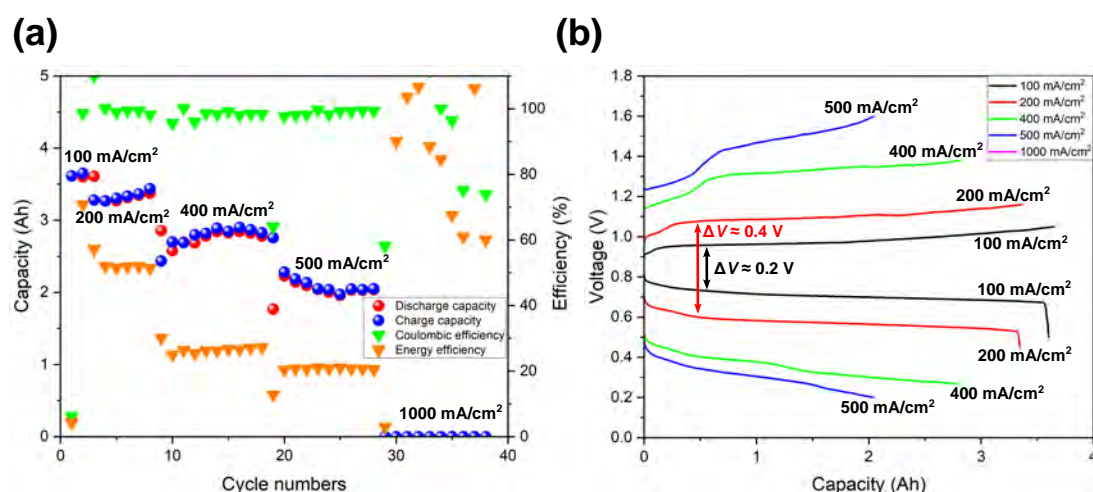


**Figure 5.19:** (a) Rate performance of Na || SbBi<sub>9</sub> cell with Ni-foam at 500 °C at current densities of 100, 200, 400, 500 and 1000 mA/cm<sup>2</sup> and (b) the discharge-charge curves at corresponding current densities.

It can be seen from Figure 5.19 (a) that the higher the applied current densities, the lower the capacity and the efficiency of the cell. This can be explained by Figure 5.19 (b) that the higher the applied current density is, the stronger the polarization. For instance, the polarization at the current density of 100 mA/cm<sup>2</sup> was only  $\approx 0.20$  V, with the doubled current density (200 mA/cm<sup>2</sup>), doubled the polarization ( $\approx 0.40$  V). As shown in Figure 5.19 (b), this kind of cell has proper rate performance: when the current density increases from 100 to 500 mA/cm<sup>2</sup>, both discharge capacity and charge capacity maintain more than 50 % of the initial value.

Nevertheless, obviously, the discharge-charge curves at the current density of 1000 mA/cm<sup>2</sup> are missing in Figure 5.19 (b) due to the enormous polarization brought by the huge current, so the cell voltage reaches the lower and upper limit of the safety voltage for the test (0.10 V and 1.80 V, respectively) immediately.

Therefore, later the current densities for rate performance were adjusted to 100, 200, 400, 500 and 600 mA/cm<sup>2</sup> (see Figure 5.20). The voltage and current used in the last two cycles at the current density of 200 mA/cm<sup>2</sup> is plotted in Figure 5.21 as an example.

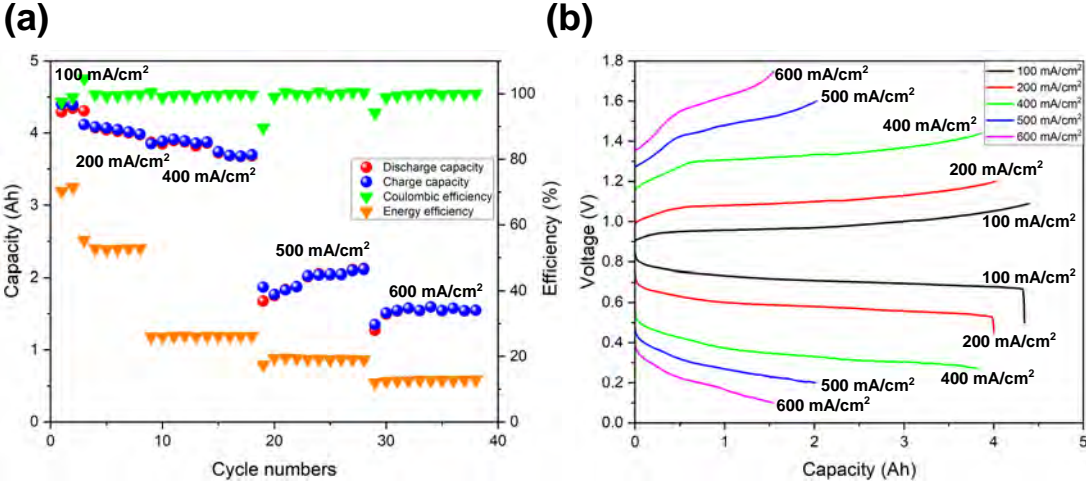


**Figure 5.20:** (a) Rate performance of Na || SbBi<sub>9</sub> cell with Ni-foam at 500 °C at current densities of 100, 200, 400, 500 and 600 mA/cm<sup>2</sup> and (b) the discharge-charge curves at corresponding current densities.

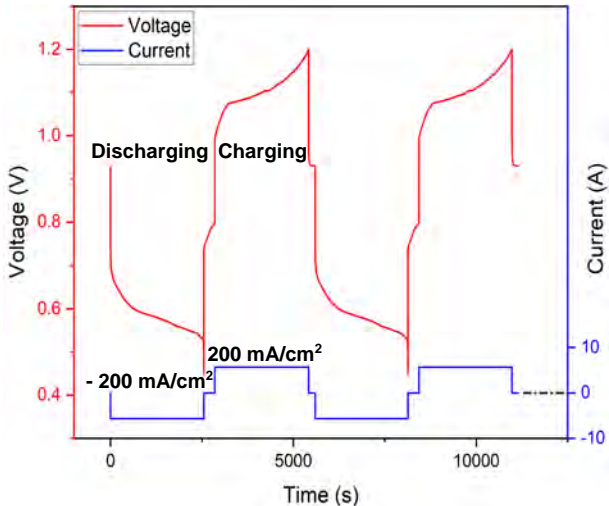


**Figure 5.21:** The voltage and current vs. time during the last two cycles at the current density of 200 mA/cm<sup>2</sup>.

After the investigation in rate performance, in order to get a brief insight into the cycle stability

of LMB cells, both Na || SbBi<sub>9</sub> cells with Ni-foam and without foam were cycled at 500 °C for a shorter time.

Figure 5.22 illustrates the cycle performance of Na || SbBi<sub>9</sub> cell with Ni-foam under the voltage range between 0.50 V and 0.98 V. The cell was discharged under the constant current density of  $-100 \text{ mA/cm}^2$  while the charging process consists of two steps: first is charging under the constant current density of  $100 \text{ mA/cm}^2$  until the voltage reached 0.98 V, after that the cell was further charged under the constant voltage of 0.98 V until the actual current is below 1 A.

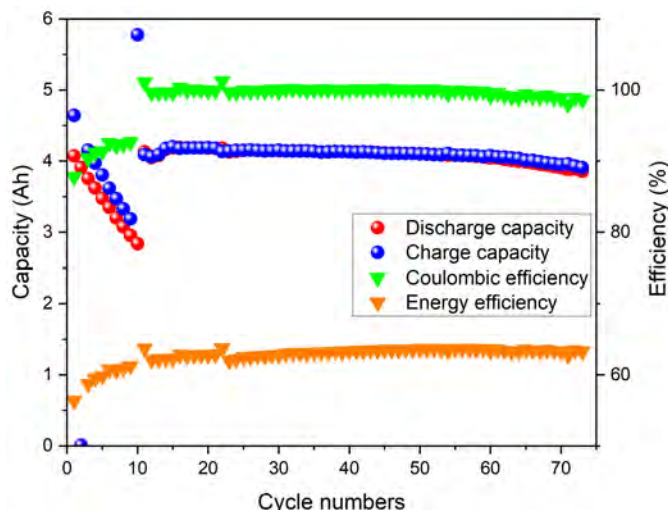


**Figure 5.22:** Cycle performance of Na || SbBi<sub>9</sub> cell with Ni-foam at 500 °C the voltage range between 0.50 V and 0.98 V for 70 cycles.

It can be seen from Figure 5.22 that the cell capacity momentarily decreased at the beginning (first 10 cycles), which is probably due to the remaining solid cell active components (insufficient cell activation). After that, cell capacity increased to around 4.0 Ah and maintained at that value. During the whole test process, the Coulombic efficiency and energy efficiency of this cell are  $> 99.5 \%$  and over  $60 \%$ , respectively. However, as the test proceeds, both discharge capacity and charge capacity declined a little bit: discharge capacity remains around  $98 \%$  of its original value and charge capacity maintains  $\sim 93 \%$  of its initial value.

The cycle performance of Na || SbBi<sub>9</sub> cells without foam is shown in Figure 5.23. The voltage range is 0.55 – 1.20 V and both the discharging and charging were conducted under the constant current of  $\pm 1.8 \text{ A}$ .

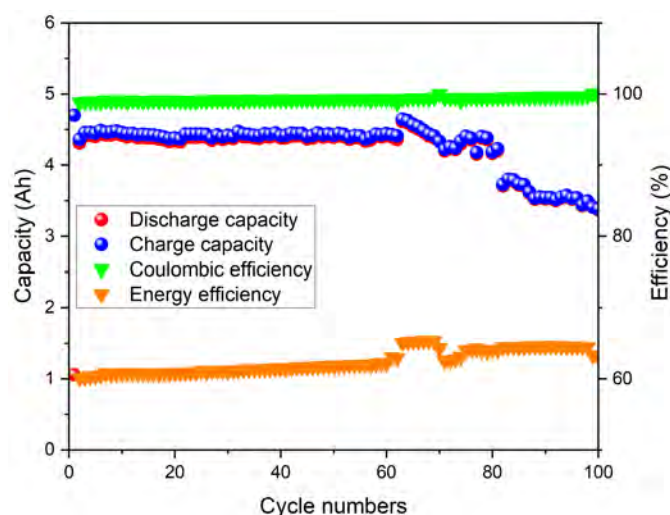


**Figure 5.23:** Cycle performance of Na || SbBi<sub>9</sub> cell without foam at 500 °C the voltage range between 0.55 V and 1.20 V for 100 cycles.

Obviously, the cell capacity maintained stable for the first 60 cycles, after that the capacity became unstable and started to degrade. Nevertheless, the cell exhibits a high Coulombic efficiency of almost 100.0 % or even a little bit higher, which might be caused by the system error of the software (due to its measurement accuracy) and a energy efficiency of over 60 % during the whole test process.

Later, another Na || SbBi<sub>9</sub> cell with Ni-foam was further characterized by GCPL tests with the voltage range of 0.45 V and 1.20 V. The cell performance of Na || SbBi<sub>9</sub> cell with Ni-foam at 500 °C under the current density of 200 mA/cm<sup>2</sup> is shown in Figure 5.24.

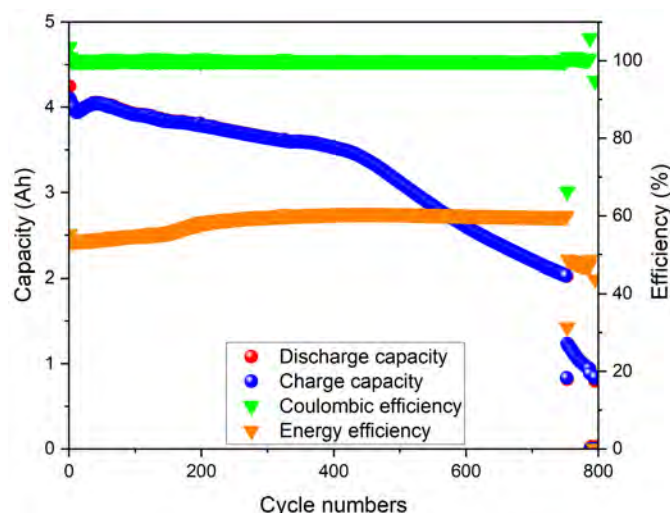


**Figure 5.24:** Cycle performance of Na || SbBi<sub>9</sub> cell with Ni-foam at 500 °C under the current density of 200 mA/cm<sup>2</sup>.

It can be seen from this figure that the cell capacity fluctuated at the very beginning, then it kept degrading during the whole GCPL test until around the 750<sup>th</sup> cycle (more than 1004 h), when the capacity suddenly fell under 2.0 Ah. Then the cell was gradually out of operation before the 800<sup>th</sup> cycle (around 1021 h). The distinct capacity degradation is probably attributed to the corrosion attack on PCC (in this case, cell case).

For comparison, Na || SbBi<sub>9</sub> cells with Ni-foam equipped with a Mo-crucible (as corrosion-resistant inner case for PCC) were built and tested as well. Figure 5.25 exhibits the cell performance of this cell at 500 °C under the same current density (200 mA/cm<sup>2</sup>).

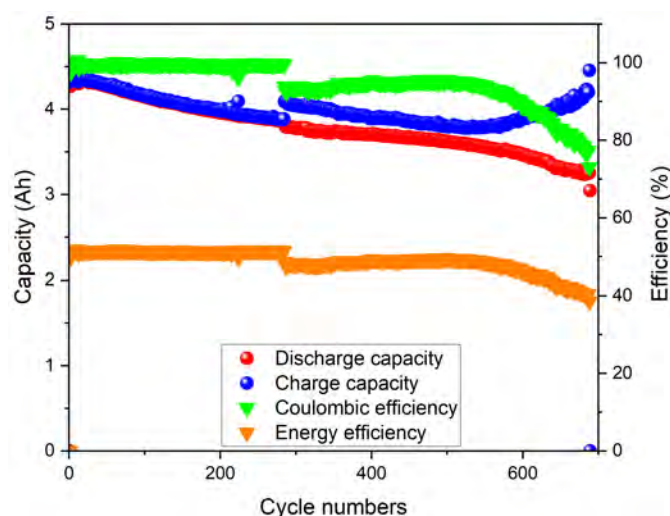


**Figure 5.25:** Cycle performance of Na || SbBi<sub>9</sub> cell with Ni-foam equipped with a Mo-crucible at 500 °C under the current density of 200 mA/cm<sup>2</sup>.

It can be seen from Figure 5.25 that the capacity of the cell with Mo-crucible also faded. Compared with the previous cell without Mo-crucible (see Figure 5.24), whose discharge capacity decreased from 4.25 Ah to about 3.64 Ah after 300 cycles (a decrease of 0.61 Ah), to around 3.53 Ah after 400 cycles (a decrease of 0.72 Ah) and to approximately 2.60 Ah after 600 cycles (a decrease of 1.65 Ah), the discharge capacity of Na || SbBi<sub>9</sub> cell with Ni-foam and with a Mo-crucible fell from almost 4.37 Ah to about 3.78 Ah after 300 cycles (a decrease of 0.59 Ah), to around 3.71 Ah after 400 cycles (a decrease of 0.66 Ah) and to approximately 3.47 Ah after 600 cycles (a decrease of 0.90 Ah).

The different mass of Na combined with the different applied current in these two cells due to the different active reaction areas results in different duration for each cycle for these two cells, to get a clear insight into the capacity degradation rate, the cycle performance of those two cells (Figure 5.24 and 5.25) are plotted versus time instead of the cycle number, as shown in

Figure 5.26 and 5.27.

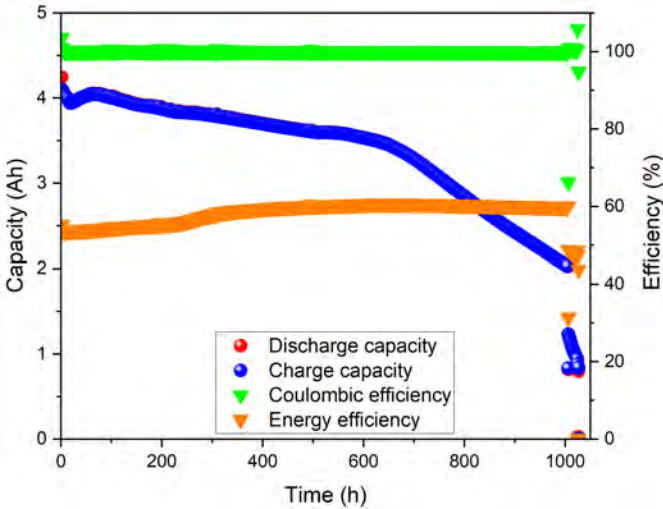


**Figure 5.26:** Cycle performance of Na || SbBi<sub>9</sub> cell with Ni-foam at 500 °C under the current density of 200 mA/cm<sup>2</sup> versus time.

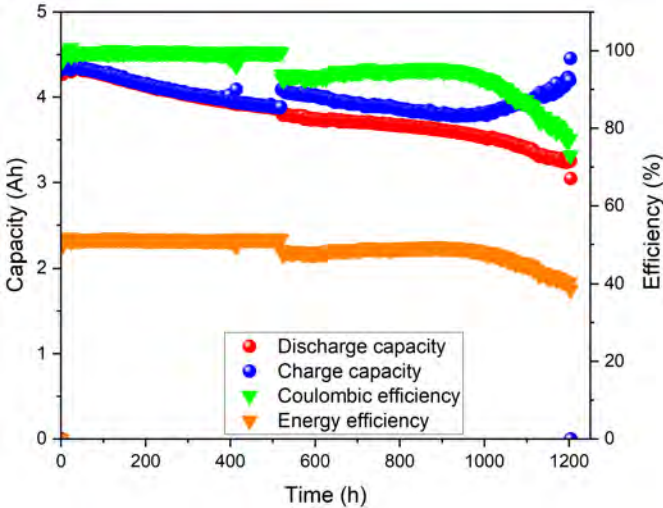


**Figure 5.27:** Cycle performance of Na || SbBi<sub>9</sub> cell with Ni-foam equipped with a Mo-crucible at 500 °C under the current density of 200 mA/cm<sup>2</sup> versus time.

According to Figure 5.26 and 5.27, it is easy to find out that for the Na || SbBi<sub>9</sub> cell without Mo-crucible, the discharge capacity degradation is 15 % (0.64 Ah) after 500 h, this value increases to 43 % (1.82 Ah) after 900 h. In contrast, the discharge capacity loss of the Na || SbBi<sub>9</sub> cell with a Mo-crucible is 11 % (0.50 Ah) after 500 h, the loss only becomes to 17 % (0.75 Ah) after 900 h.

The capacity loss until around 600 h is owing to the loss of Na due to evaporation and precipitation at cell cover see below, the severe capacity loss afterwards is mainly attributed to

the corrosion attack on PCC materials, which leads to the intrusion of impurities and depletion of positive electrode.

Therefore the capacity degradation rate of cell equipped with Mo-crucible is much slower. However, both Figure 5.25 and 5.27 illustrate that some abnormal phenomena happened in the cell equipped with Mo-crucible at around 250<sup>th</sup> cycles, which leads to a sudden rise in charge capacity hence results in an abrupt decline on Coulombic efficiency.

The comparison between cells without Mo-crucible and with Mo-crucible indicates that the corrosion attack on cell case (PCC) is not the only reason for cell capacity degradation, therefore, those cells were disassembled for further investigation.

After cell disassembly, as we expected, a large amount of condensed Na can be found on the inner surface of cell cover for all cells (Figure 5.28), which definitely contributes to the capacity degradation.

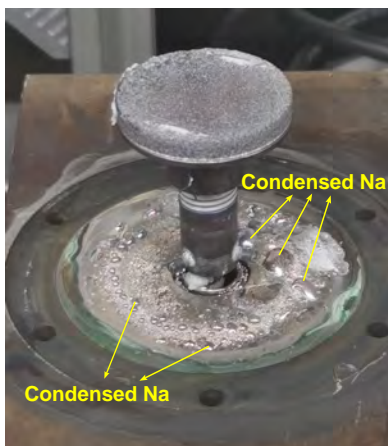


**Figure 5.28:** Condensed Na on the inner surface of cell cover.

This issue might be owing to the temperature gradient between the bottom of cell case and cell cover, some liquid Na in electrolyte partially vaporized due to the higher ambient temperature, after the Na vapor arrived at the inner surface of cell cover, it condensed there and became small Na droplets because of the temperature gradient. Those droplets gradually accumulated and fell into liquid electrolyte due to the gravity. However, some small Na droplets remained attached there, which results in Na lost hence more or less contributes to the cell capacity degradation.

Due to the fact that this temperature gradient is imputed to the applied heating facility for cell testing (see Section 5.3): heating coils of the heating sleeve are only located at bottom, although thermal insulation was laterally added, only the bottom part of the cells can be sufficiently heated. Therefore, unfortunately, this issue is inevitable for all of the cells.

### 5.5.3 EIS measurements

Electrochemical Impedance Spectroscopy (EIS) was employed under the frequency range of 0.01 Hz – 10 kHz by applying a sine AC current with an amplitude of 20 mA.

Figure 5.29 illustrates the EIS data of Na || SbBi<sub>9</sub> cell with Ni-foam at different states of charge (SoC) at 500 °C. The cell was charged under a constant current (1.0 A) to each SoC, rest for 15 min, then the open-circuit voltage (OCV) was measured and EIS data were collected.

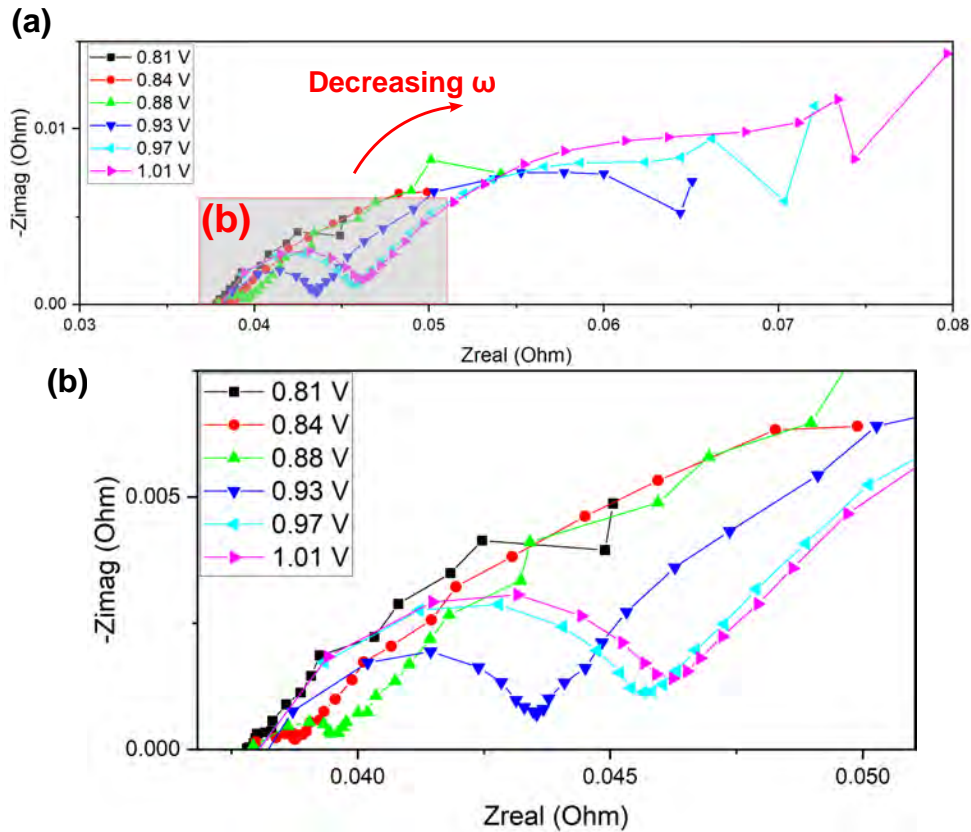


**Figure 5.29:** (a) Nyquist plots of cell with Ni-foam at different states of charge (SoC) at 500 °C, obtained by applying a sine AC current with an amplitude of 20 mA in the frequency range of 0.01 Hz to 10 kHz and (b) Zoom-in shows the enlarged high- and medium-frequency region of the Nyquist plots.

It can be seen from Figure 5.29 that all EIS curves are composed of a semi-circle in the high- and medium-frequency region and a sloping line in the low-frequency region.

As described in Section 3.4.3 (see Figure 3.8), the sloping line in low-frequency region represents the Na-atoms' diffusion in electrode materials (so-called Warburg impedance  $Z_W$ ) while the intercept of the semi-circle at the  $Z_{real}$  axis in high-frequency region corresponds to the ohmic resistance  $R_{ohm}$  of the cell (as described in Figure 3.8), which is mainly provided by

the molten salts electrolyte  $R_S$  (in this case,  $\sim 37 \text{ m}\Omega$ ). Moreover, the diameter of the semi-circle is approximately equal to the charge-transfer resistance  $R_{ct}$  of the Na redox reaction at the electrode-electrolyte interface [105–107, 170–177]. In this case, although the charge-transfer resistance  $R_{ct}$  fluctuates at different states of charge (SoC), its value remains in the range of  $0.6 \text{ m}\Omega - 9 \text{ m}\Omega$ , which is still much lower than that of LIBs and SIBs (ranging from several Ohms to hundreds of Ohms) [171–180]. The low charge-transfer resistance  $R_{ct}$  demonstrates the superior charge-transfer kinetics of electrode-electrolyte interface of LMB cells once again, which is coincident with the results from Galvanostatic Intermittent Titration Technique (GITT) tests.

The EIS data collected from cell with Ni-foam at the OCV of 1.01 V was further analysed by fitting the impedance data to a simplified equivalent electrical circuit (EEC) model with the help of Gamry Echem Analyst software. As described in Section 3.4.3, Randles circuit (seen in Figure 3.8) and its variation (without Warburg impedance but with CPE instead of an ideal capacitance) was selected to build the EEC model for this cell to more precisely simulate the cell with two electrode-electrolyte interfaces. The Nyquist plot of original EIS data with the fitting curve and the applied equivalent circuit are illustrated in Figure 5.30, all impedance parameters obtained from this EEC model are listed in Table 5.4.

As shown in Figure 5.30 (b), the molten salts resistance  $R_S$  was set as  $37 \text{ m}\Omega$ . The other values were calculated and fitted by the software, where the resistor  $R_{Na}$  paralleled with the CPE represents the charge-transfer resistance and double layer capacitance at negative electrode while the resistor  $R_{Sb-Bi}$  paralleled with capacitor  $C_{Sb-Bi}$  accounts for the charge-transfer resistance and double layer capacitance at positive electrode. The Na-ion diffusion in the positive electrode is described by the Warburg impedance element  $Z_W$ .

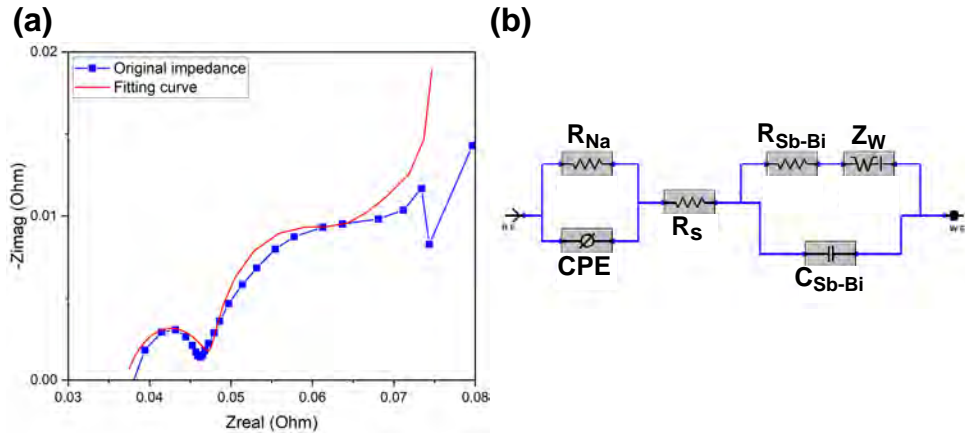


**Figure 5.30:** (a) Nyquist plot of cell with Ni-foam at the OCV of 1.01 V at 500 °C with the fitted curve and (b) the simplified equivalent electrical circuit (EEC) model for fitting the impedance data.

**Table 5.4:** Impedance parameters obtained from the simplified equivalent electrical circuit (EEC) model in Figure 5.30 (b).

Parameter	Value	± Error	Units
$R_{Na}$	$11.04 \times 10^{-3}$	$977.4 \times 10^{-6}$	Ohm
$R_S$	$37.00 \times 10^{-3}$	0.00	Ohm
$R_{Sb-Bi}$	$14.26 \times 10^{-3}$	$4.733 \times 10^{-3}$	Ohm
$C_{Sb-Bi}$	21.23	4.889	F
$B_{Warburg}$	6.553	$230.6 \times 10^{-3}$	$s^{1/2}$
$Y_{0\_Warburg}$	152	47.88	$S \cdot s^{1/2}$
$Y_{0\_Na}$	$769.9 \times 10^{-3}$	$678.4 \times 10^{-3}$	$S \cdot s^a$
$n_{Na}$	$657.8 \times 10^{-3}$	$114.4 \times 10^{-3}$	
Goodness of Fit	$512.1 \times 10^{-6}$		

It is important to note that the simplified EEC model which shows a good fit to the impedance data is not unique, same impedance data can be well fitted by small adjustments in the EEC model. Figure 5.31 is cited as an example, in which the EEC model based on Randles circuit was slightly adjusted for the same impedance data illustrated in Figure 5.30 (a) and its results are shown in Table 5.5. Clearly, the parameters shown in Table 5.5 exhibit very small difference from the parameters in Table 5.4, a good fit was achieved in Table 5.5 as well.

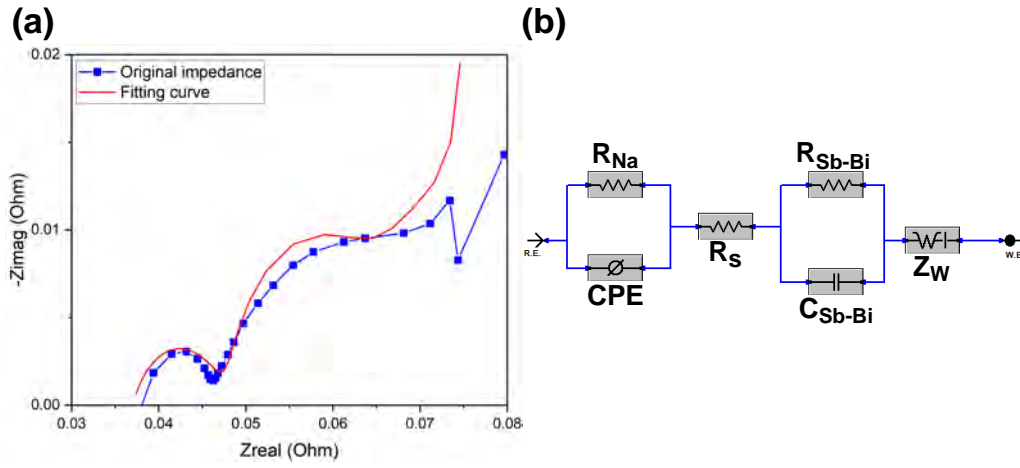


**Figure 5.31:** (a) Nyquist plot of cell with Ni-foam at the OCV of 1.01 V at 500 °C with the fitted curve and (b) another simplified equivalent electrical circuit (EEC) model for fitting the impedance data.

**Table 5.5:** Impedance parameters obtained from this simplified equivalent electrical circuit (EEC) model in Figure 5.31 (b).

Parameter	Value	± Error	Units
$R_{Na}$	$10.18 \times 10^{-3}$	$1.005 \times 10^{-3}$	Ohm
$R_S$	$37.00 \times 10^{-3}$	0.00	Ohm
$R_{Sb-Bi}$	$12.01 \times 10^{-3}$	$1.939 \times 10^{-3}$	Ohm
$C_{Sb-Bi}$	38.01	8.271	F
$B_{Warburg}$	6.924	$27.55 \times 10^{-3}$	$s^{1/2}$
$Y_{0\_Warburg}$	141.9	24.74	$S \cdot s^{1/2}$
$Y_{0\_Na}$	$575.6 \times 10^{-3}$	$553.4 \times 10^{-3}$	$S \cdot s^a$
$n_{Na}$	$696.0 \times 10^{-3}$	$131.1 \times 10^{-3}$	
Goodness of Fit	$531.4 \times 10^{-6}$		

As shown in Figure 5.32, the EIS data of some Na || SbBi<sub>9</sub> cells with Ni-foam at 500 °C exhibit totally different characteristics as the curves in Figure 5.29.

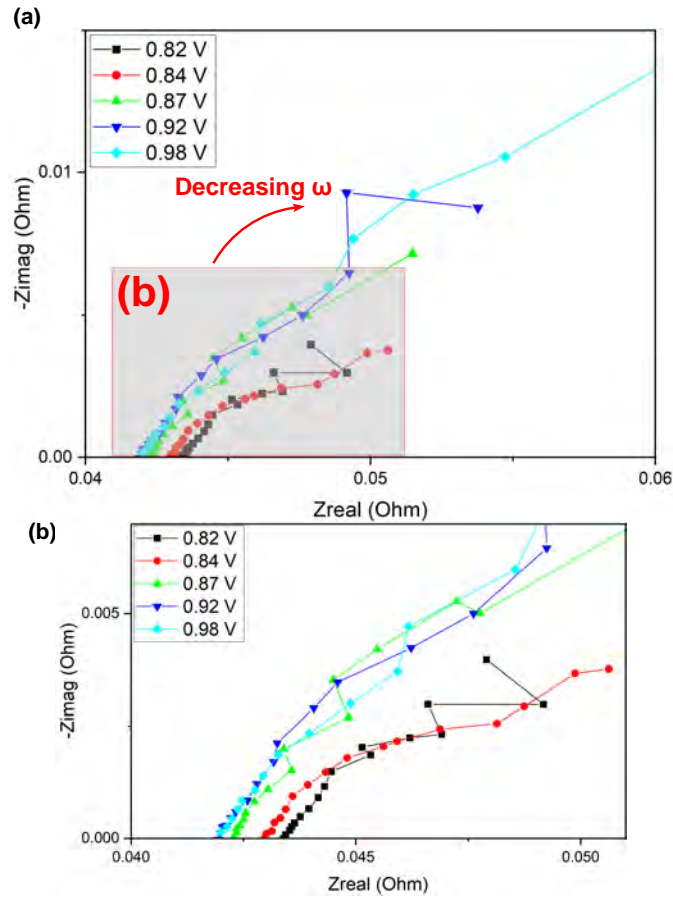


**Figure 5.32:** (a) Nyquist plots of cell with Ni-foam at different states of charge (SoC) at 500 °C with totally different characteristics, obtained by applying a sine AC current with an amplitude of 20 mA in the frequency range of 0.01 Hz to 10 kHz and (b) Zoom-in shows the enlarged high- and medium-frequency region of the Nyquist plots.

Obviously, all EIS curves in Figure 5.32 consist of an intercept at the  $Z_{\text{real}}$  axis in the high-frequency region and an inclined line in the medium- and low-frequency region.

In contrast to Figure 5.29, no semi-circle can be observed between the intercept and the inclined line in Figure 5.32, which might be attributed to the extremely small charge-transfer resistance  $R_{\text{ct}}$  in this cell, so that the diameter of this semi-circle is invisible at the given resolution. Besides, in this cell, owing to the slightly longer distance between the negative electrode and positive electrode, the resistance of molten salts electrolyte  $R_{\text{S}}$  is a little bit larger (approximately 43 m $\Omega$ ).

After one month operation at 500 °C, EIS measurements were performed on the Na || SbBi<sub>9</sub> cell with Ni-foam (same cell shown in Figure 5.32) at different states of charge (SoC) at 500 °C, the results are exhibited in Figure 5.33.

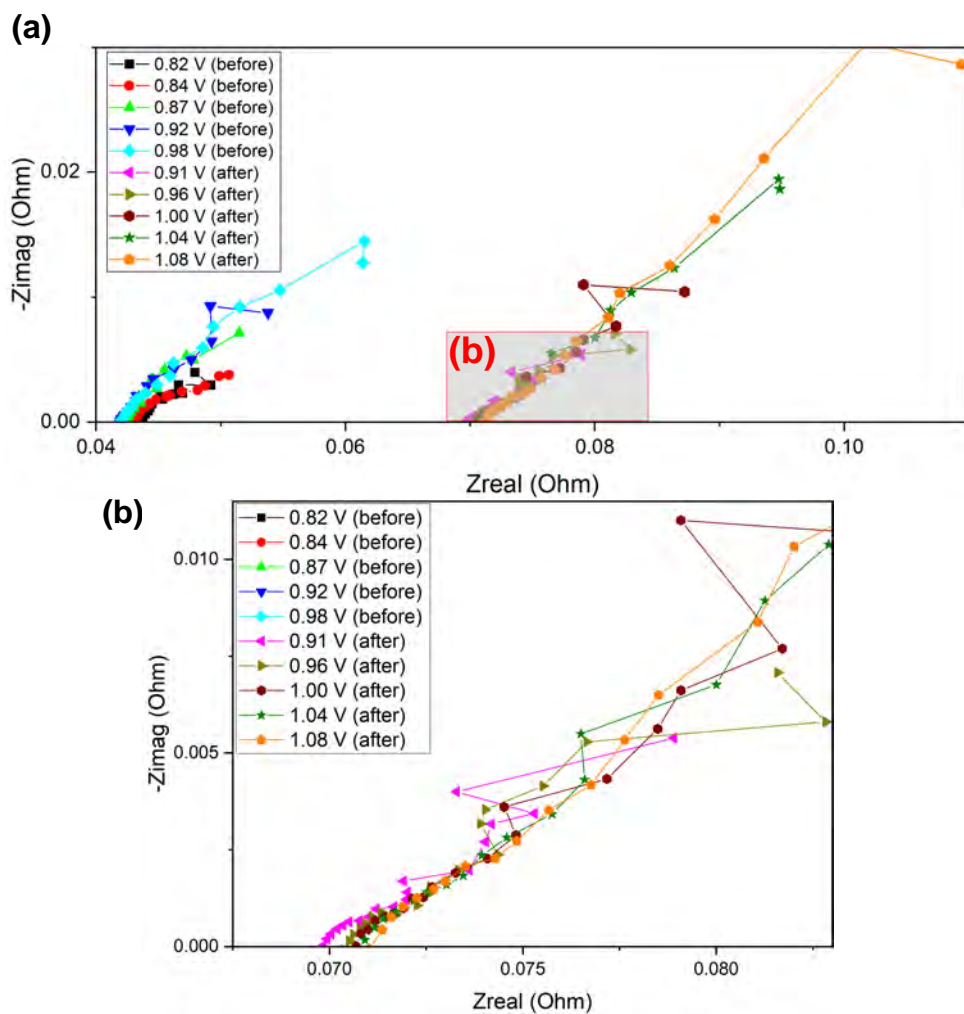


**Figure 5.33:** (a) Nyquist plots of cell with Ni-foam at 500 °C with totally different characteristics before and after 1 month operation and (b) Zoom-in shows the enlarged high- and medium-frequency region of the Nyquist plots.

It can be seen from Figure 5.33 that all EIS curves maintain a similar shape before and after one month operation. However, the intercept at the  $Z_{\text{real}}$  axis increased significantly, the sudden but huge variation of molten salts electrolyte resistance (ohmic resistance) might be attributed to some of the connection problems during cell operation.

EIS was measured on Na || SbBi<sub>9</sub> cell without foam at different states of charge (SoC) at 500 °C (see Figure 5.34) as well.

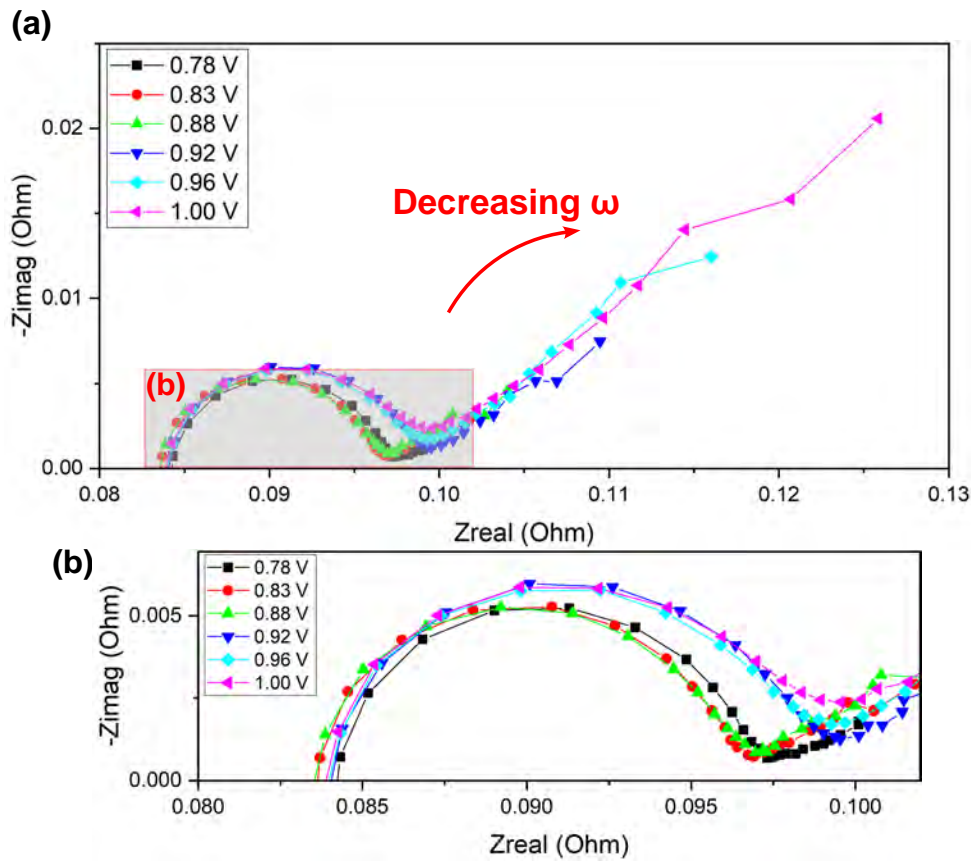


**Figure 5.34:** (a) Nyquist plots of cell without foam at different states of charge (SoC) at 500 °C, obtained by applying a sine AC current with an amplitude of 20 mA in the frequency range of 0.01 Hz to 10 kHz and (b) Zoom-in shows the enlarged high- and medium-frequency region of the Nyquist plots.

Comparing Figure 5.34 with Figure 5.29, it is easy to find out that the cell without foam exhibits the same characteristics as the cell with Ni-foam. The difference in the molten salts electrolyte resistance  $R_S$  is due to the significantly increased distance between the negative electrode and positive electrode. Besides, a distinct variation can be observed in the charge-transfer resistance  $R_{ct}$  in the cell with foam (up to approximately 15 m $\Omega$ ).

The EIS measurements were applied on the Na || SbBi<sub>9</sub> cell without foam EIS at different state of charge (SoC) at 500 °C before and after one month operation, the data are illustrated in see Figure 5.35.

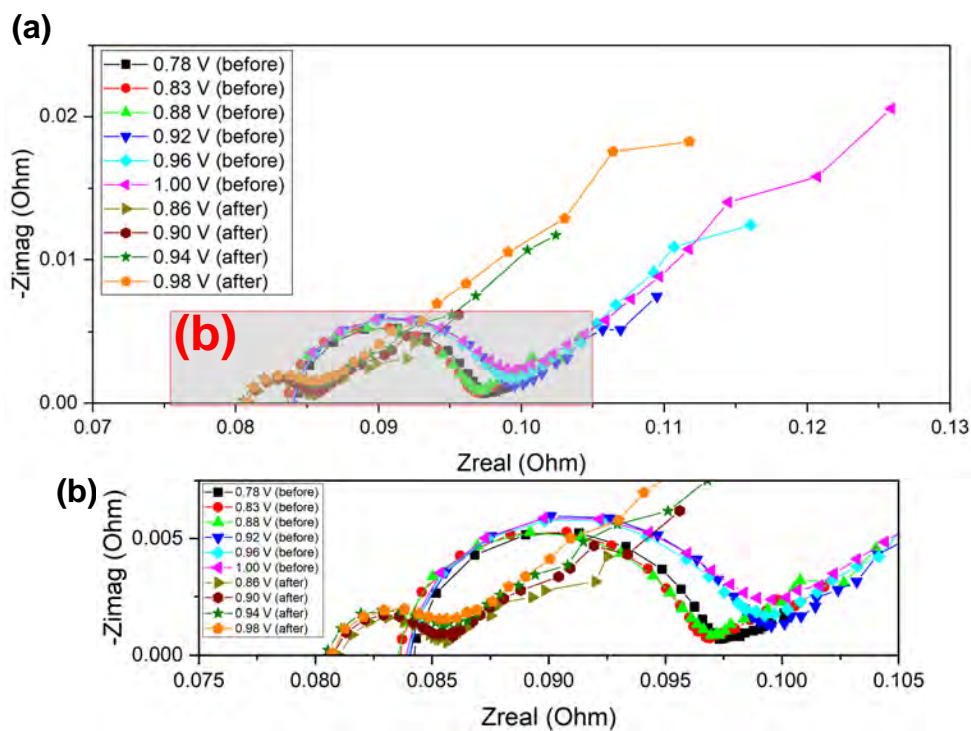


**Figure 5.35:** (a) Nyquist plots of cell without foam at 500 °C before and after 1 month operation and (b) Zoom-in shows the enlarged high- and medium-frequency region of the Nyquist plots.

As can be observed from Figure 5.35, the same as the Na || SbBi<sub>9</sub> cell with Ni-foam, all EIS curves of the Na || SbBi<sub>9</sub> cell without foam exhibit the same characteristics before and after one month operation. Nevertheless, the molten salts electrolyte resistance  $R_S$  decreased slightly and the charge-transfer resistance  $R_{ct}$  declined distinctly when compared with that before cell operation. The decline in the charge-transfer resistance  $R_{ct}$  indicates that the reaction kinetics sped up during cycling.

#### 5.5.4 Discussion

As all cell designs illustrated in Figure 5.1, 5.2 and 5.3, both cells with Ni-foam and without foam were successfully assembled. The assembly procedure of both Na || SbBi<sub>9</sub> cells with Ni-foam and without foam together with the following various electrochemical measurements, including GITT, GCPL and EIS tests on both cell designs forms the heart of this part.

Firstly, the main side reaction in electrolyte, namely the exchange reaction between Li-ions and Na is confirmed, which occurs in both cells with Ni-foam and cells without foam. Hence the actual active negative electrode of the Na-based LMB cells becomes the mixture of Li and Na, which is coincident with Ding's research [161]. Besides, especially for cells without foam,

the application of alumina-ceramic as insulating sheath has been excluded due to another side reaction, i.e. the exchange reaction between the reduced Li and used  $\text{Al}_2\text{O}_3$ -ceramic. For this reason, spinel-ceramic ( $\text{MgAl}_2\text{O}_4$ ) is applied as insulating sheath in this cell design as an alternative to alumina-ceramic.

For cells with Ni-foam, the short-circuit problem occurred on each cell with 50 mm-foam but disappeared on cells with 40 mm-foam, which may be explained by the escape of Na from Ni-foam and accumulation on the side wall of cell case and the formation of “Na-bridge” between NCC and PCC (reason for the short-circuit). This issue may happen during cell assembly when the cell is shaking or when too much liquid Na is attached to the outside of the Ni-foam during cell operation. Besides, the current density distribution in LMB cells was simulated by COMSOL Multiphysics and the results reveal that as long as a foam is applied as Na-host, a small perturbation of current distribution can be observed at the bottom edge of foam. By contrast, cells without foam exhibit the most uniform and most even current density distribution in electrolyte.

When compared with conventional SIBs, the superior mass transport properties of Na-based LMB cells are demonstrated by their at least five orders of magnitude larger diffusion coefficient (in the range of  $10^{-6}$  to  $10^{-4}$   $\text{cm}^2\text{s}^{-1}$ ) obtained from GITT tests, which can be attributed to the synergy between the liquid-liquid electrode-electrolyte interface and higher operating temperature of LMBs. The fast charge-transfer kinetics of electrode-electrolyte interface of Na-based LMB cells is verified by its extremely low charge-transfer resistance (cell with Ni-foam: from not visible due to limited resolution up to approximately 9  $\text{m}\Omega$ ) measured from EIS measurements in comparison to that of LIBs and SIBs.

GITT tests also reveal that both cells with Ni-foam and without foam exhibit a small self-discharge rate during the whole time, the self-discharge current and self-discharge current density are determined to be in the range between 13 and 16.5 mA and circa 0.6  $\text{mA}/\text{cm}^2$ , respectively. Besides, the EMF curves of cells with Ni-foam present no flat voltage plateau due to its low ratio of negative electrode to positive electrode, which indicates a low utilization rate of positive electrode. In contrast, a flat voltage plateau can only be observed on cells without foam, which may be contributed to the further reaction between negative electrode and positive electrode and the continuous formation of intermetallic compounds. According to Zhou’s results, this plateau is generated due to the high voltage of Na-Sb couple [63]. If later the amount of negative electrode (Na) can be increased by increasing the foam volume (increasing the foam thickness or using multiple foams), another flat voltage plateau (Na-Bi couple) might appear.

Moreover, the Na || SbBi<sub>9</sub> cells exhibit proper rate performance, when the applied current density increase from 100 mA/cm<sup>2</sup> to 500 mA/cm<sup>2</sup>, both discharge capacity and charge capacity still maintain a high level (around 50 % of the initial value under 100 mA/cm<sup>2</sup>). However, due to the large  $iR$  drop or more generally, due to the large internal cell resistance of Na || SbBi<sub>9</sub> cells, an applied current density of 1000 mA/cm<sup>2</sup> is too large, which results in a stronger polarization and hence ends the discharging process and charging process immediately. The maximal applied discharged current density in the tests is 600 mA/cm<sup>2</sup>, therefore the application of this type of LMB cell in the field of power supply might be restricted.

In addition, both cell designs with foam and without foam are only stable for short-term cycling (less than 100 cycles). In comparison to cells with Ni-foam, the cycling of cells without foam is more erratic, which indicates the assembly of cells without foam is not ideal and still needs to be improved.

Furthermore, the long-term cycling of cells with Ni-foam exhibit a clear capacity degradation, this issue can be facilitated by applying a corrosion-resistant inner case in cell, for instance, a Mo-crucible. Nevertheless, the capacity degradation cannot be totally eliminated in this way. The disassembly of the cells reveal that some of the liquid Na are vaporized and condensed on the inner surface of cell cover, those Na droplets can be regarded as lost of cell active components (negative electrode). Hence the cell capacity degradation might be owing to the synergy between the vaporization of Na and the corrosion attack on PCC (in this case, cell case), which is mainly triggered by the positive electrode (already discussed in Section 4.2).

Finally, EIS measurements combined with GITT and GCPL tests clarify that cell with Ni-foam and cell without foam have different molten salts electrolyte resistance  $R_S$ . The molten salts electrolyte resistance  $R_S$  depends on the distance between the negative electrode and positive electrode: the longer the distance, the larger the electrolyte resistance  $R_S$ . Since the cell's energy efficiency strongly depends on the cell resistance and thus on the distance between the electrodes, regardless of the cell with Ni-foam or cell without foam, the distance between negative electrode and positive electrode need to be further investigated and adjusted in order to achieve better cell performance.

### 5.5.5 Short summary

In summary, both cell designs with foam and without foam are successfully assembled. However, both cell types could only maintain normal operation for short term (at least for around 1000 h).

The capacity degradation might be owing to the synergy between the vaporization of Na and the corrosion attack on PCC (cell cases), which is mainly triggered by the most aggressive cell active component, i.e. the positive electrode (Section 4.2).

When considering about the above-mentioned merits of cells without foam including milder corrosion attack on NCC materials, higher cell capacity, higher positive electrode utilization and the most even current density distribution, this type of cell design is worthy to be further investigated and improved.

## 5.6 Post-evaluation of cell cases

After cell tests, the cells with Ni-foam were disassembled, then certain areas of cell case (seen in Figure 5.36) were cut with or without cell active components, embedded in epoxy resin, ground and polished. Scanning electron microscope (SEM) with energy-dispersive X-ray spectroscopy (EDS) was used for the characterization. Especially, for cell cases without cell active components, after the cell cover with Ni-foam was disassembled from the cell case, all cell active components were first poured out of the cell case directly.

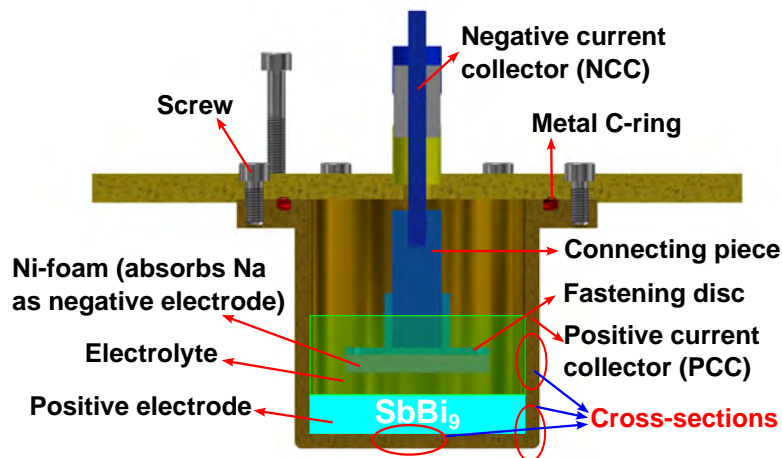


**Figure 5.36:** Selection of cross-sections on cell case after cell operation.

Considering about the distinct capacity degradation during the GCPL tests of Na || SbBi<sub>9</sub> LMB cells without corrosion mitigation method, combined with the results from the static corrosion tests for PCC materials (Section 4.2), the reason for the capacity degradation in LMB cells might be the corrosion attack on PCC materials. Therefore, to shed further light on this issue, post-mortem examination on cell case from cells which has been operated for at least one month, was accomplished.

It is important to note that the a thin Ni-layer was first coated on the cross-sections of Mo-crucible by an electro bath. After that, certain areas of Mo-crucible without cell active components were embedded, ground and polished the same as the stainless steel cell cases.

### 5.6.1 Results

#### Cells with foam but without Mo-crucible

First, a cell case without cell components were investigated. As shown in Figure 5.37, after cell operation, some parts of the surface on cell case bottom became bumpy while some other parts were covered by a thin layer of Sb-Bi alloy (brighter parts in this figure). Besides, some Sb-Bi alloy can be found attached on the side wall of cell case (Figure 5.37 (b)) as well. The maximal local corrosion depth at cell case bottom after 1335 h of operation reached around 50  $\mu\text{m}$ , which corresponds to a corrosion rate of 0.037  $\mu\text{m}/\text{h}$ . This is in good agreement with the results obtained on Fe-Cr-Ni steels during the static exposure in Sb-Bi alloys (Section 4.2).

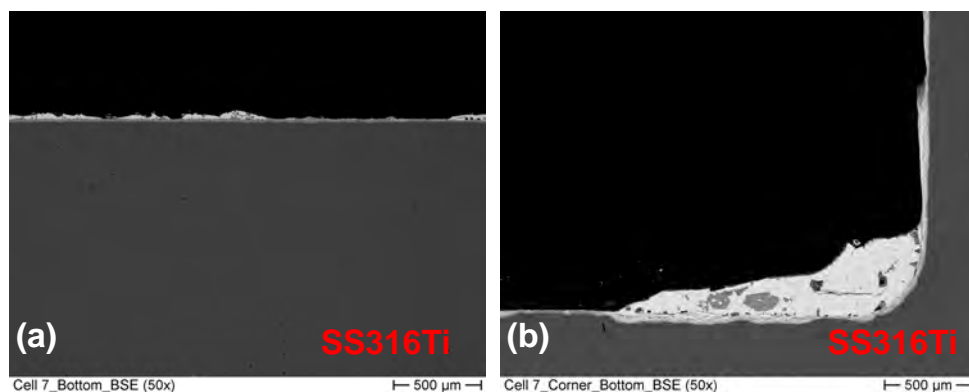


**Figure 5.37:** BSE images of cross-section of (a) the bottom of cell case and (b) the bottom with side wall of cell case after cell operation.

The BSE image and EDS element mapping images of cross-section of the cell case bottom are shown in Figure 5.38. It can be seen from this figure that the bottom of the cell case was attacked by the positive electrode, all main constituents (Fe, Cr and Ni) of SS316Ti are depleted while both Sb and Bi penetrated into SS316Ti. Besides, a Sb-, Fe- and Cr-rich layer can be seen at the outer interface. Moreover, Sb is only in combination with Fe, Cr and/or Ni but is only very little in combination with Bi. In addition, when compared with Sb, the penetration of Bi into SS316Ti is significantly reduced or almost even missing.

All those observations are consistent with the results from the static corrosion tests in PCC materials at fully-charged state (Section 4.2.3) but show significant differences with the results

at fully-discharged state (Section 4.3.3).

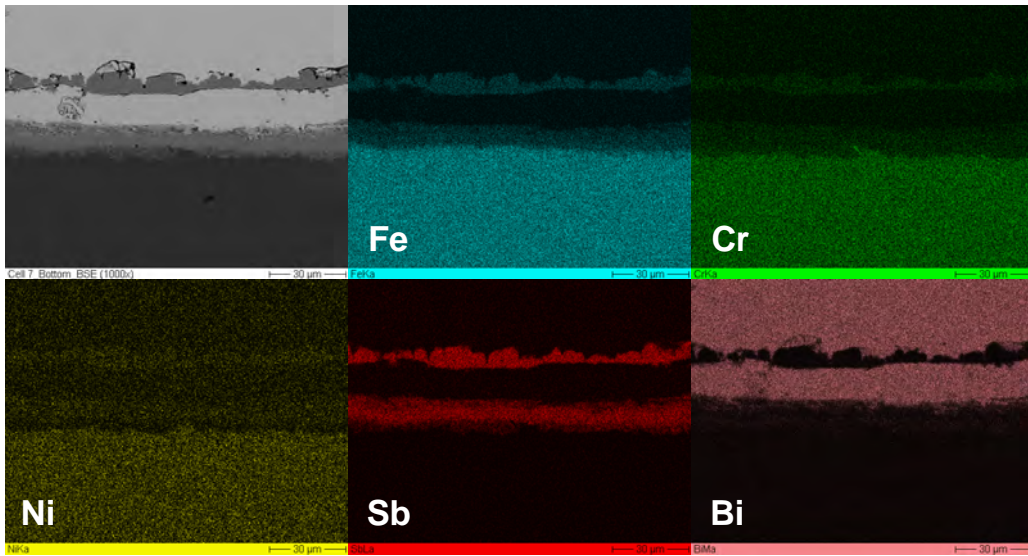


**Figure 5.38:** BSE image and EDS element mapping images of cross-section of cell case bottom after cell operation.

The line scan (Figure 5.39) manifests that two Fe-Cr-Ni-Sb-Bi layers with different elemental compositions can be observed as corrosion products. All Fe, Cr and Ni in SS316Ti are depleted at the corrosion front layer (zone ② in Figure 5.39) while Sb is enriched in this region. A Fe-Cr-Ni-Sb layer (zone ④ in Figure 5.39) is formed at the outer corrosion region, which presents almost the same Cr and Ni contents as zone ② but a slightly higher Sb content with a slightly lower Fe content. Besides, the formation of a Bi-rich layer can be observed in between those two layers, in which almost no Bi can be observed.

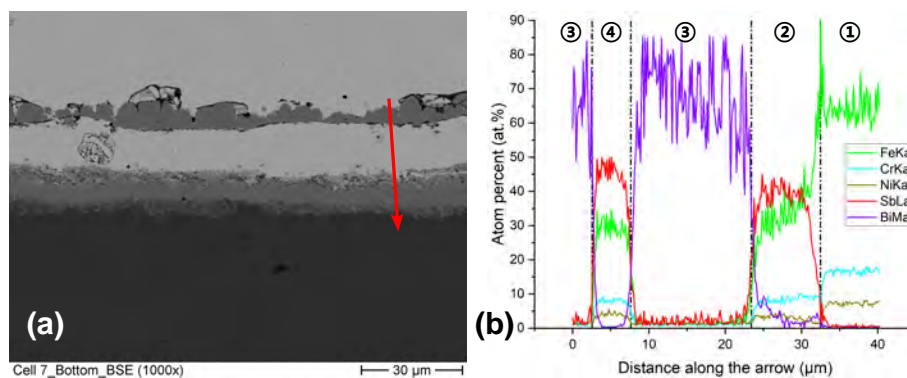


**Figure 5.39:** (a) Line scan across cell case bottom after cell operation with (b) results of composition analysis, where ① is the unmodified SS316Ti, ② is the corrosion layer at the corrosion front, ③ is the attached Sb-Bi alloy and ④ is the outer Fe-Cr-Ni-Sb layer.

Figure 5.40 shows the BSE image of cross-section of side wall of the cell case, where (a) is

the upper region where contacts the molten salts electrolyte but has no direct contact to the positive electrode and (b) is the bottom area where it only contacts the positive electrode due to the fact that the height of positive electrode (SbBi<sub>9</sub> alloy) in cell is calculated to be around 5 mm. Obviously, the upper part of side wall, where should have no direct contact to the positive electrode, was attached by a thin layer of Sb-Bi alloy and hence corroded as well, and the corrosion rate in this region is approximately the same as that in the region where contacts the positive electrode.

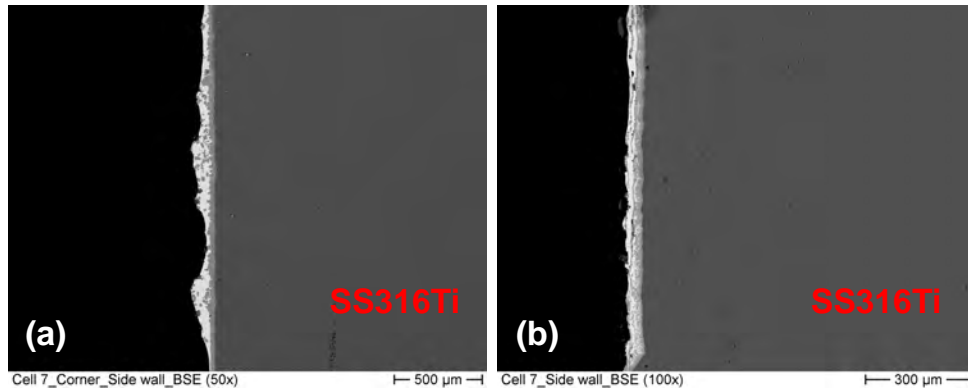


**Figure 5.40:** BSE image of cross-section of side wall of cell case bottom after cell operation, where (a) is the upper region where contacts the molten salts electrolyte but has no direct contact to the positive electrode and (b) is the bottom area where only contacts the positive electrode.

As shown in Figure 5.41, the corrosion attack occurred on the side wall of cell case is very similar to that on the cell case bottom.

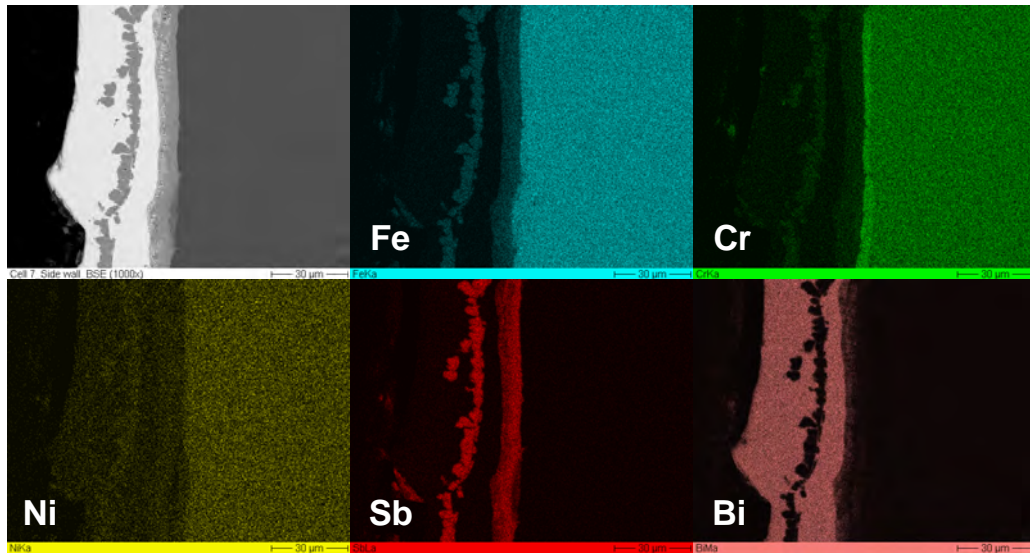


**Figure 5.41:** BSE image and EDS element mapping images of cross-section of the upper part of side wall of cell case after cell operation.

The line scan of side wall (Figure 5.42) exhibits close similarity to the line scan of cell case bottom, in which three Fe-Cr-Ni-Sb-Bi layers with different elemental compositions are formed as corrosion products. The layer formed at the corrosion front (zone ② in Figure 5.42) possesses a higher Cr content but a lower Ni content than the unmodified steel substrate. The intermediate Fe-Cr-Ni-Sb-Bi layer (zone ③ in Figure 5.42) shows an obvious increase on Sb content while all main constituents of steel (Fe, Cr and Ni) decrease distinctly. A layer with dendrites (zone ⑤ in Figure 5.42) can be observed in the outer corrosion region, which exhibits almost the same Fe, Cr and Ni content as zone ③ but a little higher Sb content. Moreover, a Bi-rich layer (zone ④) is formed between zone ③ and zone ⑤.

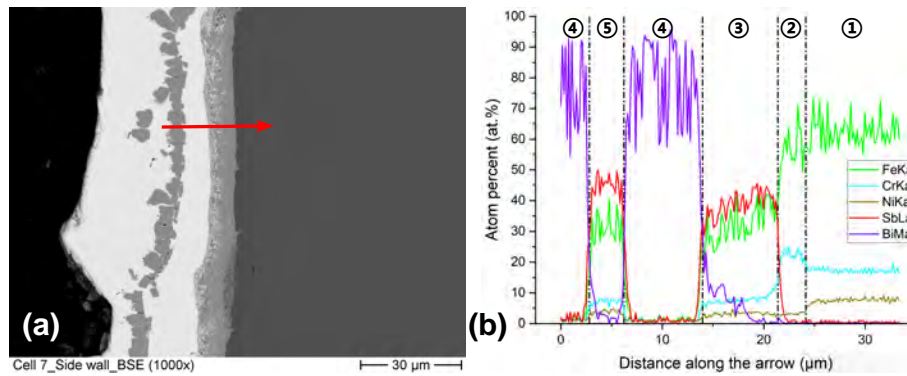


**Figure 5.42:** (a) Line scan across side wall of cell case after cell operation with (b) results of composition analysis, where ① is the unmodified SS316Ti, ② is the Cr-rich layer at the corrosion front, ③ is the intermediate Fe-Cr-Ni-Sb-Bi layer, ④ is the attached Sb-Bi alloy and ⑤ is the outer Fe-Cr-Ni-Sb-Bi layer with dendrites.

After cell operation, the cell case was strongly attacked, all main constituents (Fe, Cr and Ni) of SS316Ti are intensively depleted in the corrosion region. Those dissolved steel constituents may diffuse into the positive electrode and take part in the electrochemical reactions in cell or result in other side reactions. In addition, a large amount of Sb and Bi are found penetrated into the cell case. As a result, both the composition and the voltage potential of positive electrode are most likely to change. Therefore, the cell case bottom with positive electrode was further analysed to get a comprehensive understanding. Most importantly, I would like to emphasize that due to the safety concerns, after cell operation, the cell was first fully-charged to ensure that all sodium could de-alloy out of the positive electrode and be removed before cutting.

The BSE image and EDS element mapping images of cross-section of cell case bottom with solidified positive electrode (see Figure 5.43) exhibits great consistency with the previous results.

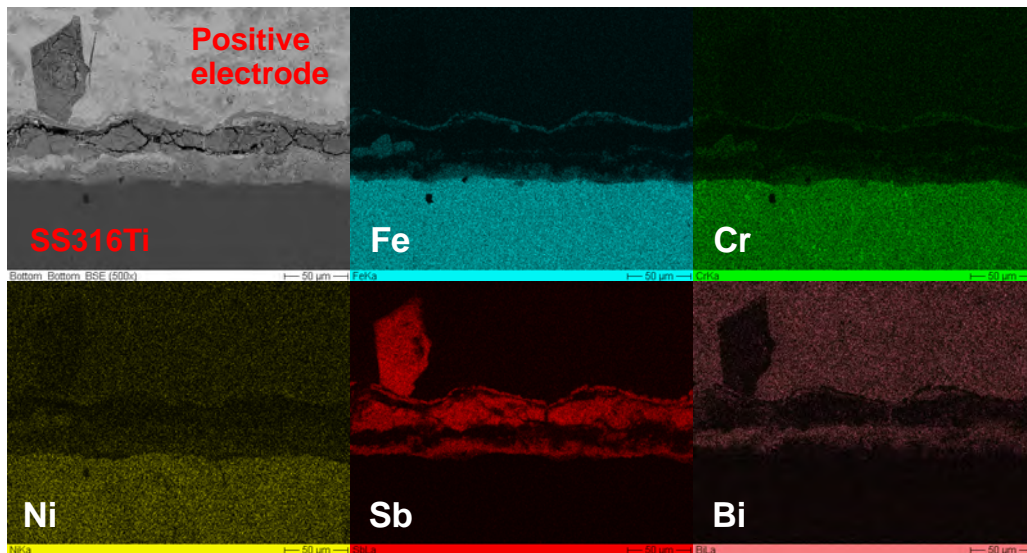


**Figure 5.43:** BSE image and EDS element mapping images of cross-section of cell case bottom with attached positive electrode after cell operation.

As expected, the constituents (Fe, Cr and Ni) of cell case were detected on the upper part of the attached positive electrode by point measurement (see Figure 5.44 and Table 5.6, 5.7 and 5.8). It can be seen from Figure 5.44 (a), (b) and (c) that two different phases exist in the positive electrode region. The darker phase is mainly composed of Fe and Sb with a small amount of Cr and Ni, which might be the intermetallic Fe-Cr-Ni-Sb compounds while the brighter phase contains an extremely high number of Bi, which is probably the original positive electrode ( $\text{SbBi}_9$  alloy).

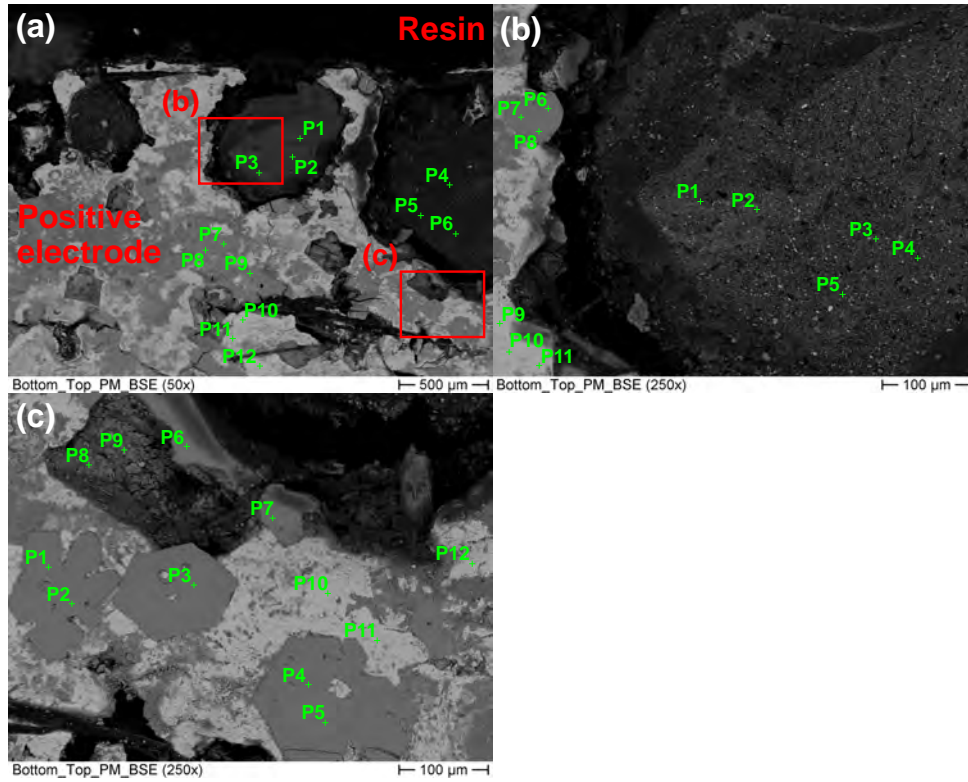


**Figure 5.44:** (a) BSE image of EDS point measurement of the upper part of attached positive electrode after cell operation with Zoom-in images (b) and (c) of point measurement at higher magnification in different regions.

**Table 5.6:** Results of EDS point measurement of the upper part of attached positive electrode shown in Figure 5.44 (a) (in wt.%).

Point number	Fe	Cr	Ni	Sb	Bi	Na	K	Cl
1	9.49	2.39	1.38	2.88	36.08	0.82	0.22	0.15
2	6.79	1.72	1.00	2.73	50.43	0.66	0.17	0.21
3	14.33	3.57	2.06	1.94	27.45	0.52	0.18	0.12
4	6.01	1.46	0.91	13.29	10.76	2.65	3.52	0.10
5	1.60	0.30	0.14	8.01	11.61	1.43	2.51	0.00
6	0.66	0.18	0.14	11.21	12.31	2.83	3.94	0.19
7	20.58	4.43	3.28	63.84	0.74	0.10	0.00	0.04
8	19.59	4.36	3.08	62.08	2.74	0.47	0.17	0.15
9	20.29	3.96	2.82	63.65	3.44	0.00	0.00	0.00
10	0.00	0.00	0.00	0.00	89.58	0.00	0.00	0.00
11	0.30	0.01	0.04	0.60	88.10	1.62	0.04	0.45
12	0.00	0.00	0.03	1.24	85.26	0.12	0.00	0.20

**Table 5.7:** Results of EDS point measurement of positive electrode shown in Figure 5.44 (b) (in wt.%).

Point number	Fe	Cr	Ni	Sb	Bi	Na	K	Cl
1	20.32	4.96	3.30	2.93	24.32	1.10	0.32	0.29
2	16.61	4.93	1.92	3.46	44.82	0.24	0.18	0.19
3	15.58	3.61	2.35	7.30	35.21	0.43	0.07	0.00
4	10.92	2.51	1.43	2.43	48.80	0.00	0.00	0.00
5	10.55	2.59	1.60	2.90	41.34	0.35	0.13	0.12
6	21.75	3.21	3.01	64.59	2.01	0.00	0.00	0.00
7	21.06	4.02	3.07	65.09	1.89	0.00	0.00	0.00
8	20.58	4.00	3.08	63.26	3.09	0.00	0.00	0.00
9	0.06	0.03	0.08	0.41	88.92	0.50	0.13	0.43
10	0.00	0.00	0.00	0.00	91.52	0.00	0.00	0.00
11	0.00	0.00	0.01	0.00	90.33	0.00	0.00	0.00

**Table 5.8:** Results of EDS point measurement of positive electrode shown in Figure 5.44 (c) (in wt.%).

Point number	Fe	Cr	Ni	Sb	Bi	Na	K	Cl
1	20.98	4.24	2.63	64.76	2.83	0.00	0.00	0.00
2	20.77	3.85	2.97	64.53	2.75	0.00	0.00	0.00
3	18.48	4.18	2.96	59.81	3.32	0.68	0.28	0.21
4	18.09	3.63	2.99	58.10	5.38	0.34	0.24	0.04
5	19.17	3.42	2.57	59.52	8.43	0.00	0.00	0.00
6	21.20	4.30	3.08	65.00	1.11	0.00	0.00	0.00
7	18.63	3.95	2.81	59.65	3.25	0.03	0.00	0.00
8	0.08	0.02	0.05	3.97	49.47	2.83	3.56	0.17
9	0.32	0.06	0.12	3.02	53.76	1.32	1.13	0.03
10	0.00	0.00	0.00	0.00	91.80	0.00	0.00	0.00
11	0.00	0.00	0.00	0.00	91.43	0.00	0.00	0.00
12	0.04	0.01	0.07	0.05	88.24	0.32	0.04	0.34

Obviously, the depletion of active electrode compositions (Sb and Bi) and the introduction of impurity elements (Fe, Cr, Ni, etc.) may result in cell capacity degradation and other issues. Besides, when taking the high melting point of Fe-Sb compounds FeSb (melting point: 1025 °C)

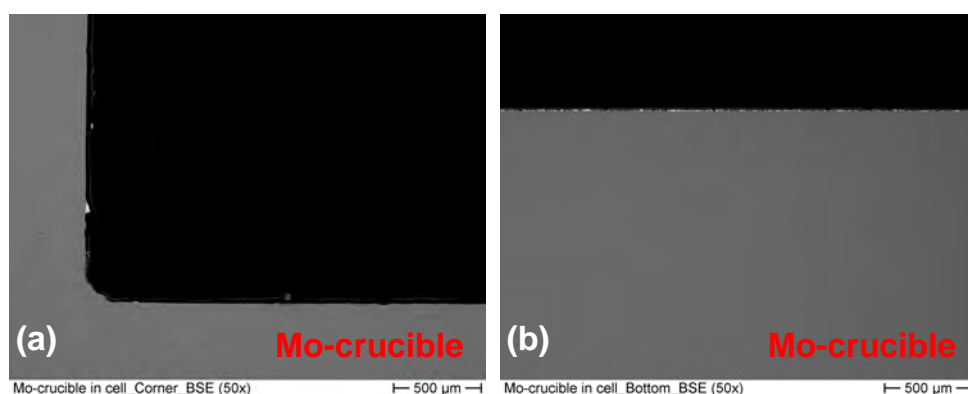
and  $\text{FeSb}_2$  (melting point:  $750\text{ }^\circ\text{C}$ ) into consideration, the formation of those solid intermetallic compounds slows down the diffusion of Na-ions by gradually reducing and blocking the effective area: the more solid intermetallic compounds is generated, the less effective diffusion area are available for Na-ions.

Additionally, a small amount of Na, K and Cl can also be found in the attached positive electrode by those point measurements, which is probably due to the remaining molten salts electrolyte on positive electrode after cell disassembly.

### Cells with foam and with Mo-crucible

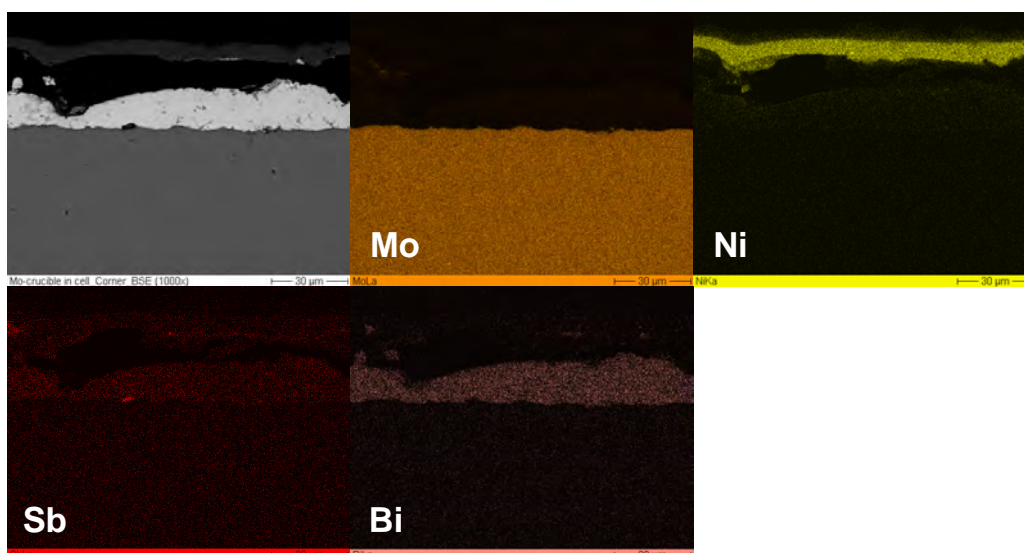
As mentioned in Section 5.5.2, for comparison, cells with Mo-crucible were disassembled and the applied Mo-crucible were analysed.

As shown in Figure 5.45, in contrast to stainless steel cell case, after cell operation, only very little Sb-Bi alloy can be found attach on the bottom of Mo-crucible, the surface of Mo-crucible bottom remained smooth and intact.



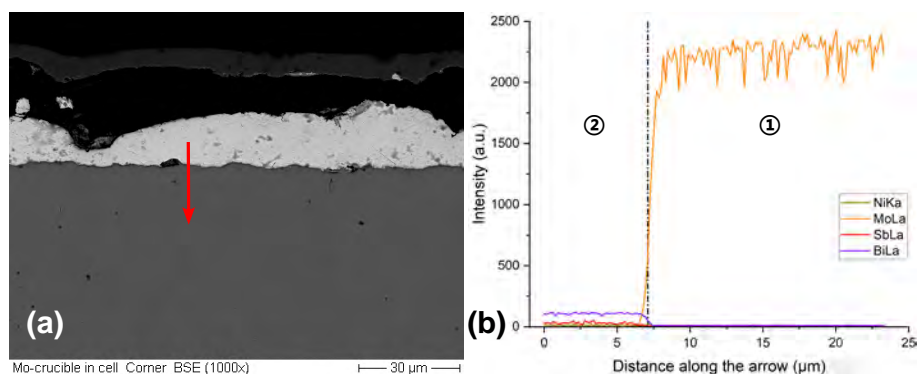
**Figure 5.45:** BSE images of cross-section of (a) the bottom with side wall of Mo-crucible and (b) the bottom of Mo-crucible after cell operation.

The BSE image and EDS element mapping images of cross-section of Mo-crucible bottom (Figure 5.46) illustrate that after cell operation, although the surface of Mo-crucible was attached by a thin layer of positive electrode, Mo-crucible still preserved its original shape. In addition, neither penetration of positive electrode nor destruction of Mo-crucible can be observed.



**Figure 5.46:** BSE image and EDS element mapping images of cross-section of Mo-crucible bottom after cell operation.

The results of the line scan (Figure 5.47) manifest that no penetration of positive electrode (SbBi<sub>9</sub> alloy) into Mo-crucible can be found and no enrichment of Mo in the positive electrode can be observed, which is coincident with the results of static exposure in Sb-Bi alloys (Section 4.2). Therefore, after cell operation, no visible corrosion attack can be observed on Mo-crucible.



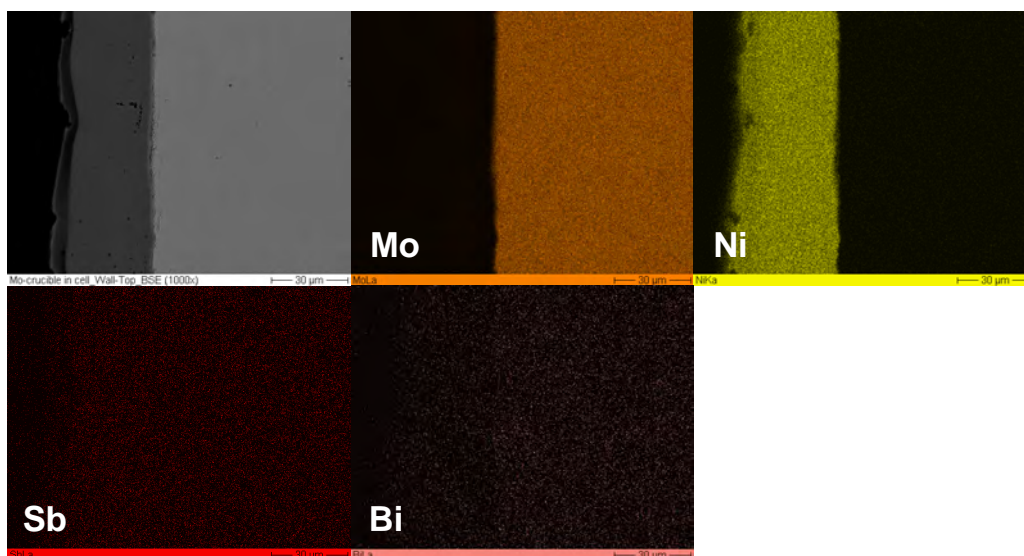
**Figure 5.47:** (a) Line scan across Mo-crucible bottom after cell operation with (b) results of composition analysis, where ① is the unmodified Mo-crucible and ② is the attached positive electrode.

Figure 5.48 presents the BSE images of cross-section of the upper region of side wall of Mo-crucible, where only contacts the molten salts electrolyte but has no direct contact to the positive electrode. It is quite clear that in contrast to the side wall of stainless steel cell case (seen in Figure 5.40), neither attached positive electrode nor corrosion attack can be observed on the side wall of Mo-crucible.

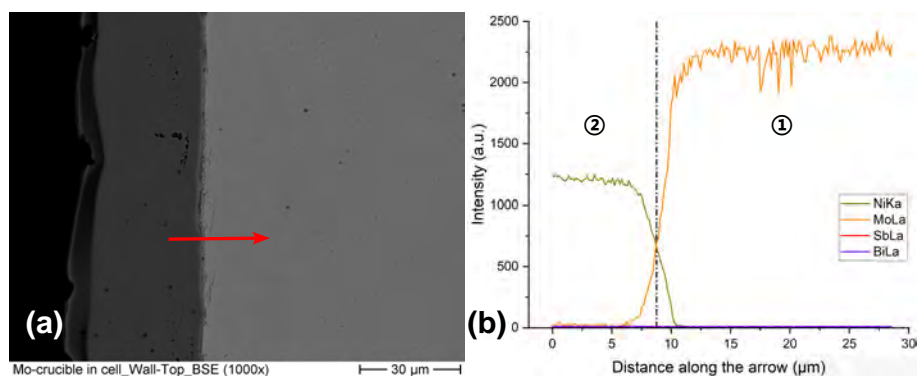


**Figure 5.48:** BSE image of cross-section of the upper region of side wall of Mo-crucible after cell operation.

Figure 5.49 exhibits the BSE image and EDS element mapping images of the upper part of side wall of Mo-crucible, the line scan of this area is presented in Figure 5.50. Both Figure 5.49 with Figure 5.50 further verify that on contrary to stainless steel cell case, the upper part of Mo-crucible, where only contacts the molten salts electrolyte suffered no corrosion attack from the positive electrode.

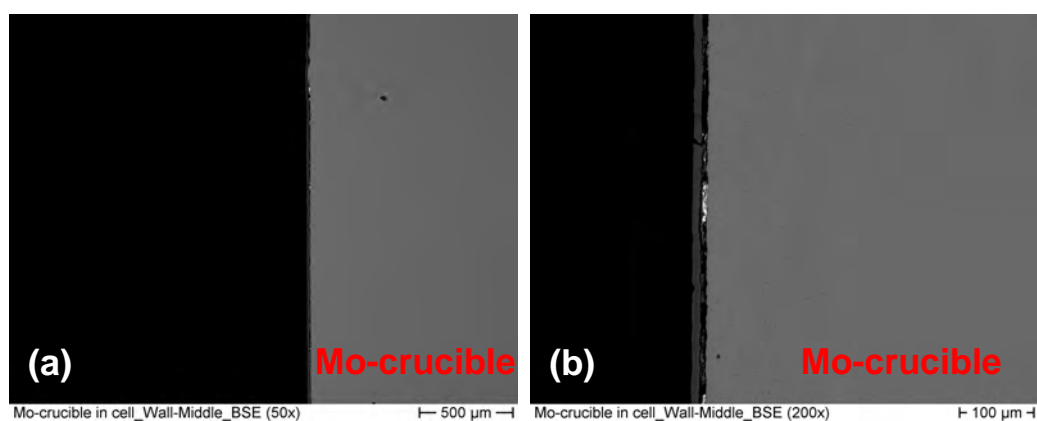


**Figure 5.49:** BSE image and EDS element mapping images of the upper part of side wall of Mo-crucible after cell operation.



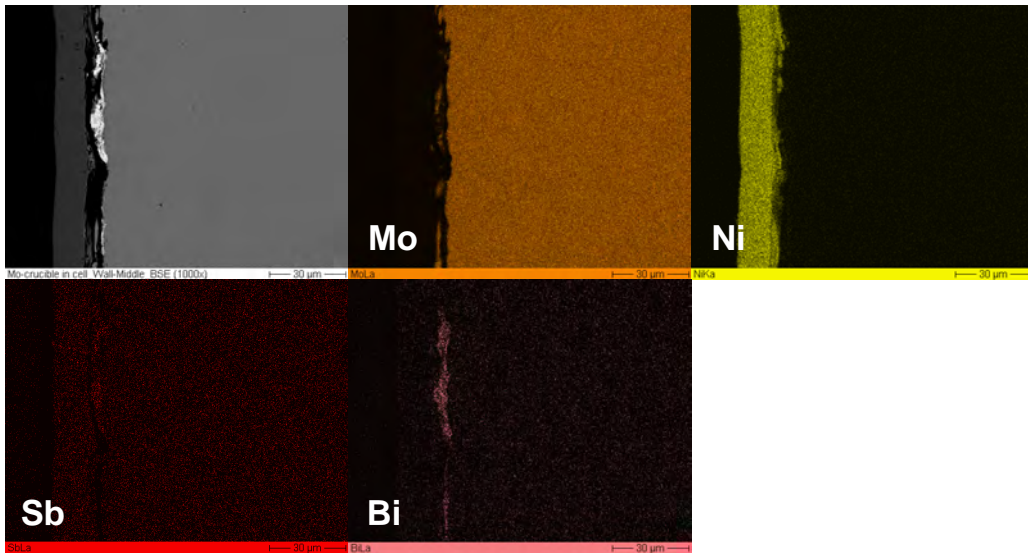
**Figure 5.50:** (a) Line scan across upper part of side wall of Mo-crucible after cell operation with (b) results of composition analysis, where ① is the unmodified Mo-crucible and ② is the Ni-coating layer.

Figure 5.51 presents the BSE images of the middle region of side wall of Mo-crucible, where has no direct contact to the positive electrode as well. However, it can be seen from Figure 5.51 (b) that some positive electrode can still be found attached on the surface of Mo-crucible.



**Figure 5.51:** BSE image and EDS element mapping images of cross-section of the middle region of side wall of Mo-crucible after cell operation.

Hence, EDS element mapping and line scan of this region were conducted (see Figure 5.52 and Figure 5.53). The results illustrate that no corrosion attack can be observed on the side wall of Mo-crucible despite the attached Sb-Bi alloy. Therefore, the attached Sb-Bi alloy might be generated when the active cell components were voided after disassembly and remained attached on the side wall.



**Figure 5.52:** BSE image and EDS element mapping images of the middle part of side wall of Mo-crucible after cell operation.

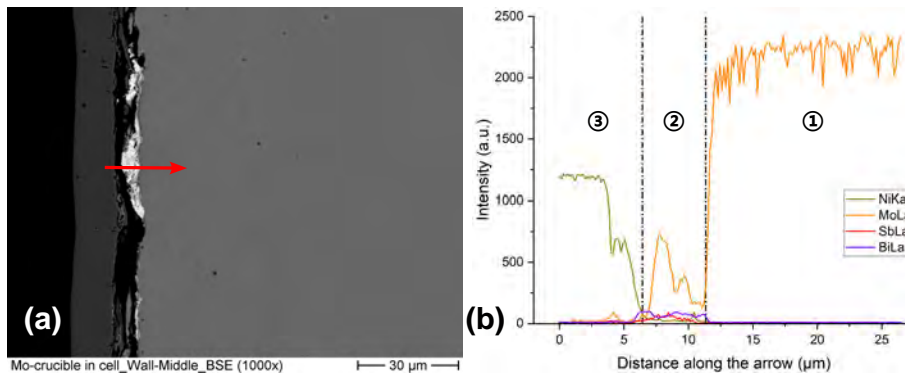


**Figure 5.53:** (a) Line scan across middle part of side wall of Mo-crucible after cell operation with (b) results of composition analysis, where ① is the unmodified Mo-crucible, ② is the attached Sb-Bi alloy and ③ is the Ni-coating layer.

## 5.6.2 Discussion

In this part, two types of LMB cells with Ni-foam: without and with corrosion mitigation method (Mo-crucible as inner case) were disassembled and further analysed in order to figure out the corrosion attack and maybe speculate about its influence on the cell performance, which was investigated in Section 5.5.

Firstly, after cell operation, not surprisingly, the bottom of cells without corrosion mitigation method, which directly contacts the positive electrode, was corroded by the positive electrode.

Both the corrosion rate ( $0.037 \mu\text{m/h}$ ) and the corrosion products on cell case bottom are in coincidence with the results on Fe-Cr-Ni steels during static exposure in Sb-Bi alloys (Section 4.2).

After cell operation, due to the fact that the altitude of positive electrode is approximately 5 mm, the upper part of side wall has no direct contact to the positive electrode. However, cells without corrosion mitigation method show that the upper part of side wall was fully covered by a thin layer of Sb-Bi alloy and corroded as well. In addition, the corrosion on side wall is very similar to the corrosion attack on cell case bottom. Hence, the corrosion attack in a cell is much more complicated. The corrosion attack on side wall might be attributed to the transport of Sb-Bi alloy due to the magnet-hydraulic effect. Additionally investigation is required to clarify this effect.

Results from cell cases without corrosion mitigation method exhibit that the corrosion attack (mainly from the positive electrode) on stainless steel cell case (PCC) results in adverse consequences on LMB cell performance owing to the depletion of positive electrode composition and introduction of impurity elements. Hence the corrosion on PCC material of LMB cells should be avoided by technical corrosion protection methods for long-term industrial application.

Moreover, due to the fact that no corrosion attack can be observed on cells with Mo-crucible and cells with a Mo-crucible exhibit a much slower capacity degradation rate when compared with cells without Mo-crucible, Mo has been verified as one of the appropriate solutions to PCC materials. However, as mentioned in Section 4.2, considering about the high price of Mo, the application of corrosion-resistant Mo-crucible as inner case or a thin Mo-coating layer on the inner bottom and inner wall of cell case might be the most cost-effective and appropriate method.

### 5.6.3 Short summary

To conclude, as we suspected in Section 5.5.2, the cell capacity degradation might be attributed to the synergistic effect between Na vaporization (limited to the applied heating facility for cell testing) and the corrosion attack on PCC materials, which is mainly triggered by the positive electrode ( $\text{SbBi}_9$ ).

The cross-section analysis verifies when compared with the cells without Mo-crucible, cells equipped with a Mo-crucible exhibit a much slower capacity degradation rate, hence the

corrosion attack on PCC materials is one of the main factor which may result in capacity degradation in LMB cells. Besides, the capacity degradation rate can be distinctly decelerated by inserting a Mo-crucible as a corrosion-resistant inner case for PCC. The application of MAX-phases as corrosion-resistant inner layer for PCC materials is feasible and still needs further investigation.

In addition, the vaporization of Na might be facilitated or eliminated by utilizing heating facilities which can evenly heat the cells in an all-around way.

## 6 Conclusion and outlook

### 6.1 Conclusion

In the present work, the material compatibility of construction materials on Na-based LMB cells with cell active components were systematically studied. This includes the compatibility of NCC and electrical insulator (oxide and nitride ceramics) materials in Na vapor and in molten salts (LiCl-NaCl-KCl) vapor, respectively and the material compatibility of PCC materials with positive electrode at fully-charged state (Sb-Sn/Sb-Bi alloys), with positive electrode at fully-discharged state (Na-Sb-Bi alloy) and with molten salts electrolyte (LiCl-NaCl-KCl).

The static corrosion tests of NCC and electrical insulator materials in Na vapor and in molten salts show that when compared with Na vapor, molten salts vapor is more aggressive on metallic specimens (Cu and 4J33 Kovar alloy), which leads to pitting corrosion on the surface of NCC materials. In contrast, no such pitting corrosion can be detected on the surface of electrical insulator materials after exposure in molten salts vapor, which verifies their better corrosion resistance under this circumstance. In addition, despite the appearance of pitting corrosion on NCC materials, it is relatively marginal and only exists at the near-surface region, which confirms that all test specimens exhibit promising corrosion resistance against Na vapor and molten salts vapor. Considering about the cost factor,  $\text{Al}_2\text{O}_3$  and MgO might be the most appropriate candidates for electrical insulator materials while Cu and Invar alloy are regarded as the best selection for NCC materials.

The static corrosion tests of PCC materials in positive electrode at fully-charged state (Sb-Sn/Sb-Bi alloys) illustrate that when compared with Sb-Bi alloys, Sb-Sn alloys are more aggressive and corrosive. Besides, the results also exhibit that the corrosion rate of steels in Sb-Bi alloys is acceptable for its application as PCC for short term while Fe-Co-Ni alloys are definitely unsuitable to be applied as PCC for either Sb-Sn alloy or Sb-Bi alloy as positive electrode. Among all test specimens, only pure Mo metal and MAX-phases coatings ( $\text{Cr}_2\text{AlC}$ ,  $\text{Ti}_2\text{AlC}$  and  $\text{Ti}_3\text{AlC}_2$ ) present outstanding corrosion resistance against both Sb-Sn and Sb-Bi alloys. Despite that, considering about the cost factor, coating of pure Mo metal or MAX-phases on a suitable substrate (conductive metallic materials, e.g., steels or alloys) might be the most economically reasonable and feasible method.

Good corrosion resistance of all test specimens (steels, Mo metal and MAX-phases) has been

proven by the static corrosion tests of PCC materials in positive electrode at fully-discharged state (Na-Sb-Bi alloy), when As impurity is excluded from the heavy metals and 30 mol.% Na is added into SbBi<sub>9</sub> alloy.

The static corrosion tests of PCC materials in molten salts electrolyte (LiCl-NaCl-KCl) present that when compared with the corrosion attack from positive electrode at fully-charged state, the corrosion attack by molten salts electrolyte is almost negligible, all test specimens (steels and Mo metal) exhibit good material compatibility with molten salts electrolyte. Besides, the results also indicate the existence of side reaction between molten salts electrolyte and liquid Na, which results in the decomposition of alumina sample holder.

For the performance of Na-based LMB cells, both Na || SbBi<sub>9</sub> cells with Ni-foam as Na-host and without foam were successfully assembled, tested and analysed.

The main side reaction in electrolyte, namely the exchange reaction between Li-ions and Na, which occurs in both cell with Ni-foam and without foam, is confirmed. As a result, the actual active negative electrode becomes the mixture of Li and Na. Besides, for cells without foam, the application of alumina-ceramic as insulating sheath has been excluded due to another side reaction of itself with reduced Li, in contrast, spinel-ceramic (MgAl<sub>2</sub>O<sub>4</sub>) can be used as an alternative for insulating sheath.

When compared with conventional SIBs, the GITT tests prove the superior mass transport properties of Na-based LMB cells by their at least five orders of magnitude larger diffusion coefficient (in the range of 10<sup>-6</sup> to 10<sup>-4</sup> cm<sup>2</sup>s<sup>-1</sup>). The fast charge-transfer kinetics of electrode-electrolyte interface of Na-based LMB cells is verified by its extremely low charge-transfer resistance (maximum value: 9 mΩ) obtained from EIS measurements in comparison to that of LIBs and SIB.

GCPL tests reveal that both cells with Ni-foam and without foam exhibit a small self-discharge rate (self-discharge current density in the range between 0.58 and 0.63 mA/cm<sup>2</sup>) during the whole test time. Besides, by comparison with cells without foam, the EMF curves of cells with Ni-foam indicates a low utilization rate of positive electrode due to the low ration of negative electrode to positive electrode.

In addition, Na || SbBi<sub>9</sub> cells exhibit proper rate performance at relatively smaller current density range (between 100 and 500 mA/cm<sup>2</sup>). However, a current density of 1000 mA/cm<sup>2</sup> is too large for this cell, which results in a stronger polarization. According to the tests, the maximal applied current density on this cell is 600 mA/cm<sup>2</sup>, therefore the application of this LMB cell in the

field of power supply might be restricted.

Furthermore, both cell designs (cells with Ni-foam and without Ni-foam) could only maintain normal operation for short term (at least for around 1000 h). A clear capacity degradation can be observed on the results of long-term GCPL tests for both cell designs, which is probably due to the synergistic effect of the vaporization of Na with the corrosion attack on PCC (in this case, cell case).

Hence the corrosion attack on cell cases after cell operation and its influence on the cell performance is investigated.

It can be seen from the post-evaluation of cell cases after cell operation that the corrosion attack on cell cases is mainly caused by the positive electrode. Beside, both the corrosion rate ( $0.037 \mu\text{m}/\text{h}$ ) and the corrosion products on cell case bottom coincide with the results on Fe-Cr-Ni steels during static corrosion tests in Sb-Bi alloys.

The post-evaluation of the side wall of cell case illustrates that the side wall, where has no direct contact to the positive electrode was fully covered by a thin layer of Sb-Bi alloy and corroded as well. This phenomenon might be attributed to the transport of Sb-Bi alloy with the help of electric field and electromagnetic field.

When compared the cell performance and cell case post-evaluation of cells without Mo-crucible with that of cells with Mo-crucible as corrosion mitigation method, it is easy to find out that the corrosion attack on PCC results in adverse consequences on cell performance (much faster capacity degradation rate). Therefore, the corrosion on PCC materials of LMB cells should be avoided by technical corrosion protection methods for long-term industrial application.

## 6.2 Outlook

Experiments and results presented in my work have not only proven the feasibility of NCC, electrical insulator and PCC, to be utilized as construction materials for Na-based LMB cells for long-term application, but also verified that Na-based LMB cells have the potential to be a promising alternative to ion-batteries for deployment as large-scale stationary energy storage system.

However, due to the time limitation and shortage of MAX-phases coatings, some other experiments including the material compatibility of MAX-phases coatings on steel substrate

with positive electrode at fully-charged state (Sb-Sn/Sb-Bi alloys) and with molten salts electrolyte have not been implemented.

With regards to the two cell designs, compared with cells with foam as Na-host, cells without foam possess several merits including milder corrosion attack on NCC materials, higher cell capacity, higher positive electrode utilization and most even current density distribution, therefore it is worthy to be further investigated and improved.

Regardless of cell with Ni-foam or without foam, up to now, the assembled cells have not achieved a stable performance or a good reproducibility/repeatability. Hence not only the cell assembly procedures but also the cell design could be further improved.

To avoid the capacity degradation due to Na evaporation and precipitation at cell cover, the temperature management must be improved to eliminate the temperature gradient inside the cell.

In addition, the cell performance strongly depends on the distance between the negative electrode and positive electrode, this influencing factor should be further investigated.

In summary, Na-based LMBs are worthy to be further studied, in order to meet the increasingly serious challenge to find proper alternatives for electrical energy storage system in grid-scale.

## References

- [1] Steven Chu and Arun Majumdar. “Opportunities and challenges for a sustainable energy future”. In: *nature* 488.7411 (2012), pp. 294–303. DOI: 10.1038/nature11475.
- [2] Ronald Lee. “The Outlook for Population Growth”. In: *Science* 333.6042 (2011), pp. 569–573. DOI: 10.1126/science.1208859.
- [3] United Nations Department of Economic and Social Affairs, Population Division. *World Population Prospects 2022: Summary of Results*. Research report. 2022.
- [4] International Energy Agency. *World Energy Outlook 2022*. Research report. 2022.
- [5] V.S. Arunachalam and E.L. Fleischer. “The Global Energy Landscape and Materials Innovation”. In: *MRS Bulletin* 33.4 (2008), pp. 264–288. DOI: 10.1557/mrs2008.61.
- [6] John P. Holdren. “Energy and Sustainability”. In: *Science* 315.5813 (2007), pp. 737–737. DOI: 10.1126/science.1139792.
- [7] Zhenguo Yang et al. “Electrochemical Energy Storage for Green Grid”. In: *Chemical Reviews* 111.5 (2011), pp. 3577–3613. DOI: 10.1021/cr100290v.
- [8] David Ginley, Martin A. Green, and Reuben Collins. “Solar Energy Conversion Toward 1 Terawatt”. In: *MRS Bulletin* 33.4 (2008), pp. 355–364. DOI: 10.1557/mrs2008.71.
- [9] Emilio Ghiani and Giuditta Pisano. “Chapter 2 - Impact of Renewable Energy Sources and Energy Storage Technologies on the Operation and Planning of Smart Distribution Networks”. In: *Operation of Distributed Energy Resources in Smart Distribution Networks*. Ed. by Kazem Zare and Sayyad Nojavan. Elsevier, 2018, pp. 25–48. ISBN: 978-0-12-814891-4. DOI: 10.1016/B978-0-12-814891-4.00002-3.
- [10] Haisheng Chen et al. “Progress in electrical energy storage system: A critical review”. In: *Progress in Natural Science* 19.3 (2009), pp. 291–312. DOI: 10.1016/j.pnsc.2008.07.014.

- [11] International Electrotechnical Commission. *Electrical Energy Storage*. White paper. 2011.
- [12] M.A. Hannan et al. “Review of energy storage systems for electric vehicle applications: Issues and challenges”. In: *Renewable and Sustainable Energy Reviews* 69 (2017), pp. 771–789. DOI: 10.1016/j.rser.2016.11.171.
- [13] Bruno Scrosati and Jürgen Garche. “Lithium batteries: Status, prospects and future”. In: *Journal of Power Sources* 195.9 (2010), pp. 2419–2430. DOI: 10.1016/j.jpowsour.2009.11.048.
- [14] Bruce Dunn, Haresh Kamath, and Jean-Marie Tarascon. “Electrical Energy Storage for the Grid: A Battery of Choices”. In: *Science* 334.6058 (2011), pp. 928–935. DOI: 10.1126/science.1212741.
- [15] David Linden and Thomas B. Reddy. *Handbook of Batteries*. 3rd Edition. McGraw-Hill, 1995. ISBN: 978-0-07-135978-8.
- [16] Bruno Scrosati et al. *Lithium Batteries: Advanced Technologies and Applications*. John Wiley & Sons, Inc., 2013. ISBN: 978-1-118-18365-6. DOI: 10.1002/9781118615515.
- [17] Jürgen Garche et al. *Encyclopedia of electrochemical power sources*. Elsevier B.V., 2009. ISBN: 978-0-444-52093-7.
- [18] Jeff Tollefson. “Charging up the future”. In: *Nature* 456.7221 (2008), pp. 436–441. DOI: 10.1038/456436a.
- [19] Naoki Nitta et al. “Li-ion battery materials: present and future”. In: *Materials Today* 18.5 (2015), pp. 252–264. DOI: 10.1016/j.mattod.2014.10.040.
- [20] Reiner Korthauer. *Lithium-Ion Batteries: Basics and Applications*. Springer, 2018. ISBN: 978-3-662-53069-6. DOI: 10.1007/978-3-662-53071-9.
- [21] Sergio Vazquez et al. “Energy Storage Systems for Transport and Grid Applications”. In: *IEEE Transactions on Industrial Electronics* 57.12 (2010), pp. 3881–3895. DOI: 10.1109/TIE.2010.2076414.
- [22] William M. White. *Encyclopedia of Geochemistry. A Comprehensive Reference Source on the Chemistry of the Earth*. Springer, 2018. ISBN: 978-3-319-39311-7. DOI: 10.1007/978-3-319-39312-4.

- [23] U.S. Geological Survey. *Mineral commodity summaries 2022*. Research report. 2022. DOI: 10.3133/mcs2022.
- [24] Hanna Vikström, Simon Davidsson, and Mikael Höök. “Lithium availability and future production outlooks”. In: *Applied Energy* 110 (2013), pp. 252–266. DOI: 10.1016/j.apenergy.2013.04.005.
- [25] Paul W. Gruber et al. “Global Lithium Availability”. In: *Journal of Industrial Ecology* 15.5 (2011), pp. 760–775. DOI: 10.1111/j.1530-9290.2011.00359.x.
- [26] Camille Grosjean et al. “Assessment of world lithium resources and consequences of their geographic distribution on the expected development of the electric vehicle industry”. In: *Renewable and Sustainable Energy Reviews* 16.3 (2012), pp. 1735–1744. DOI: 10.1016/j.rser.2011.11.023.
- [27] Jamie Speirs et al. “The future of lithium availability for electric vehicle batteries”. In: *Renewable and Sustainable Energy Reviews* 35 (2014), pp. 183–193. DOI: 10.1016/j.rser.2014.04.018.
- [28] M. Armand and J.-M. Tarascon. “Building better batteries”. In: *Nature* 451.7179 (2008), pp. 652–657. DOI: 10.1038/451652a.
- [29] V.Z. Barsukov et al. “On the faradaic and non-faradaic mechanisms of electrochemical processes in conducting polymers and some other reversible systems with solid-phase reagents”. In: *Electrochimica Acta* 46.26-27 (2001), pp. 4083–4094. DOI: 10.1016/S0013-4686(01)00715-0.
- [30] P.M. Biesheuvel, S. Porada, and J.E. Dykstra. “The difference between Faradaic and non-Faradaic processes in Electrochemistry”. 2018. DOI: 10.48550/arXiv.1809.02930.
- [31] Martin Winter and Ralph J. Brodd. “What are Batteries, Fuel Cells, and Supercapacitors?” In: *Chemical Reviews* 104.10 (2004), pp. 4245–4270. DOI: 10.1021/cr020730k.
- [32] Christian Julien et al. *Lithium Batteries. Science and Technology*. Springer, 2016. ISBN: 978-3-319-319107-2. DOI: 10.1007/978-3-319-19108-9.

- [33] Kejie Zhao et al. “Fracture of electrodes in lithium-ion batteries caused by fast charging”. In: *Journal of Applied Physics* 108.7 (2010). 073517. DOI: 10.1063/1.3492617.
- [34] Candace K. Chan et al. “High-performance lithium battery anodes using silicon nanowires”. In: *Nature Nanotechnology* 3.1 (2008), pp. 31–35. DOI: 10.1038/nano.2007.411.
- [35] Hojong Kim et al. “Liquid Metal Batteries: Past, Present, and Future”. In: *Chemical Reviews* 113.3 (2013), pp. 2075–2099. DOI: 10.1021/cr300205k.
- [36] William Hoopes. “Electrolytically-refined Aluminium and Articles Made Therefrom”. Pat. US Patent 1,534,315. 1925.
- [37] Helena L. Chum and Robert A. Osteryoung. *Review of Thermally Regenerative Electrochemical Systems. Volume 1: Synopsis and Executive Summary*. Technical report SERI/TR-332-416-Vol.1. Solar Energy Research Institute (SERI), Golden, CO (United States), 1980. DOI: 10.2172/5030338.
- [38] Helena L. Chum and Robert A. Osteryoung. *Review of Thermally Regenerative Electrochemical Systems. Volume 2*. Technical report SERI/TR-332-416-Vol.2. Solar Energy Research Institute (SERI), Golden, CO (United States), 1981.
- [39] Norbert Weber et al. “Current-driven flow instabilities in large-scale liquid metal batteries, and how to tame them”. In: *Journal of Power Sources* 265 (2014), pp. 166–173. DOI: 10.1016/j.jpowsour.2014.03.055.
- [40] Takanari Ouchi et al. “Calcium-Antimony Alloys as Electrodes for Liquid Metal Batteries”. In: *Journal of The Electrochemical Society* 161.12 (2014), A1898. DOI: 10.1149/2.0801412jes.
- [41] Takanari Ouchi et al. “Calcium-based multi-element chemistry for grid-scale electrochemical energy storage”. In: *Nature Communications* 7.1 (2016), pp. 1–5. DOI: 10.1038/ncomms10999.
- [42] Junli Xu et al. “Na–Zn liquid metal battery”. In: *Journal of Power Sources* 332 (2016), pp. 274–280. DOI: 10.1016/j.jpowsour.2016.09.125.

- [43] David J. Bradwell et al. “Magnesium–Antimony Liquid Metal Battery for Stationary Energy Storage”. In: *Journal of the American Chemical Society* 134.4 (2012), pp. 1895–1897. DOI: 10.1021/ja209759s.
- [44] Kangli Wang et al. “Lithium–antimony–lead liquid metal battery for grid-level energy storage”. In: *Nature* 514.7522 (2014), pp. 348–350. DOI: 10.1038/nature13700.
- [45] Xiaohui Ning et al. “Self-healing Li–Bi liquid metal battery for grid-scale energy storage”. In: *Journal of Power Sources* 275 (2015), pp. 370–376. DOI: 10.1016/j.jpowsour.2014.10.173.
- [46] David R. Lide. *CRC Handbook of Chemistry and Physics*. 85th Edition. CRC Press, Boca Raton, FL, 2004. ISBN: 978-0-8493-0485-9.
- [47] Brian L. Ellis and Linda F. Nazar. “Sodium and sodium-ion energy storage batteries”. In: *Current Opinion in Solid State and Materials Science* 16.4 (2012), pp. 168–177. DOI: 10.1016/j.cossms.2012.04.002.
- [48] Michael D. Slater et al. “Sodium-Ion Batteries”. In: *Advanced Functional Materials* 23.8 (2013), pp. 947–958. DOI: 10.1002/adfm.201200691.
- [49] Naoaki Yabuuchi et al. “Research Development on Sodium-Ion Batteries”. In: *Chemical Reviews* 114.23 (2014), pp. 11636–11682. DOI: 10.1021/cr500192f.
- [50] T. Weier et al. “Liquid metal batteries - materials selection and fluid dynamics”. In: *IOP Conference Series: Materials Science and Engineering*. Vol. 228. 1. IOP Publishing, 2017, p. 012013. DOI: 10.1088/1757-899X/228/1/012013.
- [51] Haomiao Li et al. “Liquid Metal Electrodes for Energy Storage Batteries”. In: *Advanced Energy Materials* 6.14 (2016), p. 1600483. DOI: 10.1002/aenm.201600483.
- [52] E. Peled and S. Menkin. “Review–SEI: Past, Present and Future”. In: *Journal of The Electrochemical Society* 164.7 (2017), A1703. DOI: 10.1149/2.1441707jes.
- [53] Weidong Zhou et al. “Rechargeable Sodium All-Solid-State Battery”. In: *ACS Central Science* 3.1 (2017), pp. 52–57. DOI: 10.1021/acscentsci.6b00321.

- [54] Byeongyong Lee et al. “Sodium Metal Anodes: Emerging Solutions to Dendrite Growth”. In: *Chemical Reviews* 119.8 (2019), pp. 5416–5460. DOI: 10.1021/acs.chemrev.8b00642.
- [55] Shuai Ma et al. “Temperature effect and thermal impact in lithium-ion batteries: A review”. In: *Progress in Natural Science: Materials International* 28.6 (2018), pp. 653–666. ISSN: 1002-0071. DOI: 10.1016/j.pnsc.2018.11.002.
- [56] Xiaochuan Lu et al. “Sodium-beta Alumina Batteries: Status and Challenges”. In: *The Journal of The Minerals, Metals & Materials Society* 62.9 (2010), pp. 31–36. DOI: 10.1007/s11837-010-0132-5.
- [57] Xiaochuan Lu et al. “High energy density Na-S/NiCl<sub>2</sub> hybrid battery”. In: *Journal of Power Sources* 224 (2013), pp. 312–316. DOI: 10.1016/j.jpowsour.2012.09.108.
- [58] Charles A. Eckert, Robert B. Irwin, and Jeffery S. Smith. “Thermodynamic Activity of Magnesium in Several Highly-Solvating Liquid Alloys”. In: *Metallurgical Transactions B* 14.3 (1983), pp. 451–458. DOI: 10.1007/BF02654364.
- [59] A.G. Morachevskii, E.B. Bochagina, and M.A. Bykova. “Thermodynamic Properties of Liquid Alloys in the System Bismuth-Sodium-Antimony”. In: *Russian Journal of Applied Chemistry* 73.10 (2000), pp. 1699–1703.
- [60] Haomiao Li et al. “High Performance Liquid Metal Battery with Environmentally Friendly Antimony-Tin Positive Electrode”. In: *ACS Applied Materials & Interfaces* 8.20 (2016), pp. 12830–12835. DOI: 10.1021/acsami.6b02576.
- [61] W. Weppner and R.A. Huggins. “Thermodynamic Properties of the Intermetallic Systems Lithium-Antimony and Lithium-Bismuth”. In: *Journal of the Electrochemical Society* 125.1 (1978), p. 7. DOI: 10.1149/1.2131401.
- [62] Tao Dai et al. “Capacity extended bismuth-antimony cathode for high-performance liquid metal battery”. In: *Journal of Power Sources* 381 (2018), pp. 38–45. DOI: 10.1016/j.jpowsour.2018.01.048.

- [63] Hao Zhou et al. “A sodium liquid metal battery based on the multi-cationic electrolyte for grid energy storage”. In: *Energy Storage Materials* 50 (2022), pp. 572–579. DOI: 10.1016/j.ensm.2022.05.032.
- [64] E.J. Cairns et al. *Galvanic Cells with Fused-Salt Electrolyte*. Technical report ANL-7316. Argonne National Laboratory (ANL), Argonne, Ill (United States), 1967. DOI: 10.2172/4543889.
- [65] E. A. Ukshe and N.G. Bukun. “THE DISSOLUTION OF METALS IN FUSED HALIDES”. In: *Russian Chemical Reviews* 30.2 (1961), p. 90. DOI: 10.1070/RC1961v030n02ABEH002955.
- [66] J. Songster and A.D. Pelton. “Thermodynamic Calculation of Phase Diagrams of the 60 Common-Ion Ternary Systems Containing Cations Li, Na, K, Rb, Cs and Anions F, Cl, Br, I”. In: *Journal of Phase Equilibria* 12.5 (1991), pp. 511–537. DOI: 10.1007/BF02645064.
- [67] George J. Janz et al. *Physical Properties Data Compilations Relevant to Energy Storage. I. Molten Salts: Eutectic Data*. Technical report NSRDS-NBS 61, Part I. Rensselaer Polytechnic Institute, Troy, New York (USA). Cogswell Laboratory, 1978.
- [68] G.J. Janz et al. *Physical Properties Data Compilations Relevant to Energy Storage. II. Molten Salts: Data on Single and Multi-Component Salt Systems*. Technical report NSRDS-NBS 61, Part II. Rensselaer Polytechnic Institute, Troy, New York (USA). Cogswell Laboratory, 1979.
- [69] Takanari Ouchi and Donald R. Sadoway. “Positive current collector for Li||Sb–Pb liquid metal battery”. In: *Journal of Power Sources* 357 (2017), pp. 158–163. DOI: 10.1016/j.jpowsour.2017.04.104.
- [70] Kaixuan Cui et al. “Feasibility Research of SS304 Serving as the Positive Current Collector of Li||Sb–Sn Liquid Metal Batteries”. In: *The Journal of Physical Chemistry C* 125.1 (2021), pp. 237–245. DOI: 10.1021/acs.jpcc.0c09629.
- [71] Hans Ulrich Borgstedt and Cezary Guminski. “Solubilities and Solution Chemistry in Liquid Alkali Metals”. In: *Monatshefte für Chemie/Chemical Monthly* 131.9 (2000), pp. 917–930. DOI: 10.1007/s007060070046.

- [72] R.L. Eichelberger. *The Solubility of Oxygen in Liquid Sodium: A Recommended Expression*. Technical report AI-AEC-12685. Atomics International, 1968. DOI: 10.2172/4808140.
- [73] K. Vignarooban et al. “Corrosion resistance of Hastelloys in molten metal-chloride heat-transfer fluids for concentrating solar power applications”. In: *Solar Energy* 103 (2014), pp. 62–69. DOI: 10.1016/j.solener.2014.02.002.
- [74] C.C. Addison. *The Chemistry of the Liquid Alkali Metals*. John Wiley & Sons, Inc., 1984. ISBN: 978-0-471-90508-9.
- [75] LeRoy R. Kelman, Wilkinson D. Wilkinson, and Frank L. Yaggee. *Resistance of Materials to Attack by Liquid Metals*. Technical report ANL-4417. Argonne National Laboratory (ANL), Argonne, Ill (United States), 1950. DOI: 10.2172/4419134.
- [76] A. Ravi Shankar, A. Kanagasundar, and U. Kamachi Mudali. “Corrosion of Nickel-Containing Alloys in Molten LiCl-KCl Medium”. In: *Corrosion* 69.1 (2012), pp. 48–57. DOI: 10.5006/0627.
- [77] Alexander V. Abramov et al. “Spectroelectrochemical Study of Stainless Steel Corrosion in NaCl-KCl Melt”. In: *ECS Transactions* 33.7 (2010), p. 277. DOI: 10.1149/1.3484785.
- [78] George Y. Lai. “Molten Salts Corrosion”. In: *High-Temperature Corrosion and Materials Applications*. Materials Park, OH: ASM International, 2007. Chap. 15, pp. 409–421. ISBN: 978-0-87170-853-3.
- [79] J. Porcayo-Calderon et al. “Electrochemical Performance of Ni20Cr Coatings Applied by Combustion Powder Spray in ZnCl<sub>2</sub>-KCl Molten Salts”. In: *International Journal of Electrochemical Science* 7.2 (2012), pp. 1134–1148.
- [80] Y.S. Li, M. Spiegel, and S. Shimada. “Corrosion behaviour of various model alloys with NaCl–KCl coating”. In: *Materials Chemistry and Physics* 93.1 (2005), pp. 217–223. DOI: 10.1016/j.matchemphys.2005.03.015.
- [81] Takaaki NAGAOKA, Ken’ichiro KITA, and Naoki KONDO. “Hot corrosion of Al<sub>2</sub>O<sub>3</sub> and SiC ceramics by KCl-NaCl molten salt”. In: *Journal of the Ceramic Society of Japan* 123.1440 (2015), pp. 685–689. DOI: 10.2109/jcersj2.123.685.

- [82] J.R. Weeks. “Lead, bismuth, tin and their alloys as nuclear coolants”. In: *Nuclear Engineering and Design* 15 (1971), pp. 363–372. DOI: 10.1016/0029-5493(71)90075-6.
- [83] J. Pacio and Th. Wetzel. “Assessment of liquid metal technology status and research paths for their use as efficient heat transfer fluids in solar central receiver systems”. In: *Solar Energy* 93 (2013), pp. 11–22. DOI: 10.1016/j.solener.2013.03.025.
- [84] Annette Heinzl et al. “Liquid Metals as Efficient High-Temperature Heat-Transport Fluids”. In: *Energy Technology* 5.7 (2017), pp. 1026–1036. DOI: 10.1002/ente.201600721.
- [85] A. Fritsch et al. “Conceptual Study of Central Receiver Systems with Liquid Metals as Efficient Heat Transfer Fluids”. In: *Energy Procedia* 69 (2015), pp. 644–653. DOI: 10.1016/j.egypro.2015.03.074.
- [86] Richard N. Lyon. *Liquid-Metals Handbook*. Technical report NAVEXOS-P-733 (Rev.3). USAEC and Department of the Navy, 1952.
- [87] Wilhelm Timmerhoff. “Die Löslichkeit verschiedener Stähle in Bleischmelzen”. In: *International Journal of Materials Research* 34.5 (1942), pp. 102–104. DOI: 10.1515/ijmr-1942-340503.
- [88] Alfons Weisenburger, Fabian Lang, and Georg Müller. “Material and Experimental Issues Related to the Use of Liquid Metals as Heat Transfer Media for CSP Tower Receivers”. In: *AIP Conference Proceedings* 2033.1 (2018), p. 080005. DOI: 10.1063/1.5067094.
- [89] A. Heinzl, A. Weisenburger, and G. Müller. “Corrosion behavior of austenitic steel AISI 316L in liquid tin in the temperature range between 280 and 700 °C”. In: *Materials and Corrosion* 68.8 (2017), pp. 831–837. DOI: 10.1002/maco.201609211.
- [90] Thomas Emmerich and Carsten Schroer. “Corrosion in austenitic steels and nickel-based alloys caused by liquid tin at high temperature”. In: *Corrosion Science* 120 (2017), pp. 171–183. DOI: 10.1016/j.corsci.2017.02.025.

- [91] E.L. Reed. “Stability of Refractories in Liquid Metals”. In: *Journal of the American Ceramic Society* 37.3 (1954), pp. 146–152. DOI: 10.1111/j.1151-2916.1954.tb14013.x.
- [92] Wei Liu et al. “Corrosion Behaviors of Iron, Chromium, Nickel, Low-Carbon Steel, and Four Types of Stainless Steels in Liquid Antimony-Tin Alloy”. In: *Corrosion* 77.11 (2021), pp. 1192–1202. DOI: 10.5006/3820.
- [93] D.A.J. Swinkels. “Molten Salt Batteries and Fuel Cells”. In: *Advances in Molten Salt Chemistry: Volume 1*. Ed. by J. Braunstein, Gleb Mamantov, and G.P. Smith. Springer US, 1971. Chap. 4, pp. 165–223. ISBN: 978-1-4757-0504-1. DOI: 10.1007/978-1-4757-0504-1\_4.
- [94] Klaus J. Vetter. *Electrochemical Kinetics: Theoretical Aspects*. Academic Press, 1967. ISBN: 978-1-4832-2936-2. DOI: 10.1016/C2013-0-12183-6.
- [95] W. Wang et al. “Chapter 1 - Electrochemical cells for medium- and large-scale energy storage: fundamentals”. In: *Advances in Batteries for Medium and Large-Scale Energy Storage*. Ed. by Chris Menictas, Maria Skyllas-Kazacos, and Tuti Mariana Lim. Woodhead Publishing, 2015, pp. 3–28. ISBN: 978-1-78242-013-2. DOI: 10.1016/B978-1-78242-013-2.00001-7.
- [96] Jocelyn Marie Newhouse. “Modeling the Operating Voltage of Liquid Metal Battery Cells”. PhD thesis. Massachusetts Institute of Technology, 2014. URL: <http://hdl.handle.net/1721.1/89840>.
- [97] Paolo Personnettaz et al. “Mass transport induced asymmetry in charge/discharge behavior of liquid metal batteries”. In: *Electrochemistry Communications* 105 (2019), p. 106496. DOI: 10.1016/j.elecom.2019.106496.
- [98] B. Agruss. “The Thermally Regenerative Liquid-Metal Cell”. In: *Journal of The Electrochemical Society* 110.11 (1963), p. 1097. DOI: 10.1149/1.2425597.
- [99] Jocelyn M. Newhouse and Donald R. Sadoway. “Charge-Transfer Kinetics of Alloying in Mg-Sb and Li-Bi Liquid Metal Electrodes”. In: *Journal of The Electrochemical Society* 164.12 (2017), A2665. DOI: 10.1149/2.1571712jes.

- [100] C. John Wen et al. “Thermodynamic and Mass Transport Properties of “LiAl””. In: *Journal of The Electrochemical Society* 126.12 (1979), p. 2258. DOI: 10.1149/1.2128939.
- [101] W. Weppner and R.A. Huggins. “Determination of the Kinetic Parameters of Mixed-Conducting Electrodes and Application to the System  $\text{Li}_3\text{Sb}$ ”. In: *Journal of The Electrochemical Society* 124.10 (1977), p. 1569. DOI: 10.1149/1.2133112.
- [102] Yujie Zhu and Chunsheng Wang. “Galvanostatic Intermittent Titration Technique for Phase-Transformation Electrodes”. In: *The Journal of Physical Chemistry C* 114.6 (2010), pp. 2830–2841. DOI: 10.1021/jp9113333.
- [103] Zheng Shen et al. “Least Squares Galvanostatic Intermittent Titration Technique (LS-GITT) for Accurate Solid Phase Diffusivity Measurement”. In: *Journal of The Electrochemical Society* 160.10 (2013), A1842. DOI: 10.1149/2.084310jes.
- [104] B.C. Han et al. “Electrochemical modeling of intercalation processes with phase field models”. In: *Electrochimica Acta* 49.26 (2004), pp. 4691–4699. DOI: 10.1016/j.electacta.2004.05.024.
- [105] Xuming Yang and Andrey L. Rogach. “Electrochemical Techniques in Battery Research: A Tutorial for Nonelectrochemists”. In: *Advanced Energy Materials* 9.25 (2019), p. 1900747. DOI: 10.1002/aenm.201900747.
- [106] Allen J. Bard and Larry R. Faulkner. *Electrochemical Methods: Fundamentals and Applications*. 2nd Edition. John Wiley & Sons, Inc., 2001. ISBN: 978-0-471-04372-0.
- [107] Christopher M.A. Brett and Maria Oliveira Brett. *Electrochemistry: Principles, Methods, and Applications*. Oxford University Press, 1993. ISBN: 978-0-198-55388-5. DOI: 10.1002/bbpc.19940981033.
- [108] B.D. Cullity. *Elements of X-ray Diffraction*. Addison-Wesley Publishing Company, Inc., 1956. ISBN: 978-0-201-01230-9.
- [109] Douglas A. Skoog, F. James Holler, and Stanley R. Crouch. *Principles of Instrumental Analysis*. Thomson Brooks/Cole, 2007. ISBN: 978-0-495-01201-6.
- [110] A. Guinier. *X-ray Diffraction in Crystals, Imperfect Crystals, and Amorphous Bodies*. Dover Publications, Inc., 1994. ISBN: 978-0-486-68011-8.

- [111] Xiandeng Hou et al. “Inductively Coupled Plasma Optical Emission Spectrometry”. In: *Encyclopedia of Analytical Chemistry: Applications, Theory and Instrumentation*. Ed. by Robert A. Meyers. John Wiley & Sons, Ltd, 2021, pp. 1–29. ISBN: 978-0-470-02731-8. DOI: 10.1002/9780470027318.a5110.pub4.
- [112] Charles B. Boss and Kenneth J. Fredeen. *Concepts, Instrumentation and Techniques in Inductively Coupled Plasma Optical Emission Spectrometry*. Perkin-Elmer Corporation, 1997.
- [113] David A. Cremers and Leon J. Radziemski. *Handbook of Laser-Induced Breakdown Spectroscopy*. John Wiley & Sons, Ltd, 2013. ISBN: 978-1119971122. DOI: 10.1002/9781118567371.
- [114] Andrzej W. Miziolek, Vincenzo Palleschi, and Israel Schechter. *Laser-Induced Breakdown Spectroscopy*. Cambridge University Press, 2006. ISBN: 978-0-511-54126-1. DOI: 10.1017/CB09780511541261.
- [115] Jagdish P. Singh and Surya N. Thakur. *Laser-Induced Breakdown Spectroscopy*. Elsevier, 2007. ISBN: 978-0-444-51734-0. DOI: 10.1016/B978-0-444-51734-0.X5001-7.
- [116] Celio Pasquini et al. “Laser Induced Breakdown Spectroscopy”. In: *Journal of the Brazilian Chemical Society* 18.3 (2007), 463—512. DOI: 10.1590/S0103-50532007000300002.
- [117] Anwar Ul-Hamid. *A Beginners’ Guide to Scanning Electron Microscopy*. Springer, 2018. ISBN: 978-3-319-98481-0. DOI: 10.1007/978-3-319-98482-7.
- [118] R.F. Egerton. *Physical Principles of Electron Microscopy. An Introduction to TEM, SEM, and AEM*. Springer, 2016. ISBN: 978-3-319-39877-8. DOI: 10.1007/978-3-319-39877-8.
- [119] Daisuke Shindo and Tetsuo Oikawa. “Energy Dispersive X-ray Spectroscopy”. In: *Analytical Electron Microscopy for Materials Science*. Tokyo: Springer Japan, 2002. Chap. 4, pp. 81–102. ISBN: 978-4-431-66988-3. DOI: 10.1007/978-4-431-66988-3\_4.
- [120] O.M. Akselsen. “Advances in brazing of ceramics”. In: *Journal of Materials Science* 27.8 (1992), pp. 1989–2000. DOI: 10.1007/BF01117909.

- [121] M.B. Uday et al. “Current Issues and Problems in the Joining of Ceramic to Metal”. In: *Joining Technologies*. Ed. by Mahadzir Ishak. IntechOpen, 2016. Chap. 8, pp. 159–217. ISBN: 978-953-51-2596-9. DOI: 10.5772/64524.
- [122] X.S. Ning et al. “Effect of oxide additive in silicon nitride on interfacial structure and strength of silicon nitride joints brazed with aluminium”. In: *Journal of Materials Science* 24.8 (1989), pp. 2865–2870. DOI: 10.1007/BF02385639.
- [123] A. Wu. “26 - Ceramic/metal bonding”. In: *Microjoining and Nanojoining*. Ed. by Y.N. Zhou. Woodhead Publishing, 2008, pp. 758–785. ISBN: 978-1-84569-179-0. DOI: 10.1533/9781845694043.3.758.
- [124] J. Lemus and R.A.L. Drew. “Diffusion bonding of silicon nitride to titanium”. In: *British Ceramic Transactions* 99.5 (2000), pp. 200–205. DOI: 10.1179/096797800680947.
- [125] Samuel J. Schneider. *Engineered Materials Handbook, Volume 4: Ceramics and Glasses*. ASM International, 1991. ISBN: 978-0871702821.
- [126] David W. Richerson and William E. Lee. *Modern Ceramic Engineering: Properties, Processing, and Use in Design*. 4th Edition. CRC Press, 2018. ISBN: 978-1-4987-1691-8. DOI: 10.1201/9780429488245.
- [127] Osgood J. Whittemore Jr. and Neil N. Ault. “Thermal Expansion of Various Ceramic Materials to 1500°C”. In: *Journal of the American Ceramic Society* 39.12 (1956), pp. 443–444. DOI: 10.1111/j.1151-2916.1956.tb15619.x.
- [128] H. Beisswenger and S. Dorner. “Solubility of oxygen in liquid sodium”. In: *Journal of Nuclear Materials* 28.3 (1968), pp. 297–302. DOI: 10.1016/0022-3115(68)90196-7.
- [129] J.K. Fink and L. Leibowitz. *Thermodynamic and Transport Properties of Sodium Liquid and Vapor*. Technical report ANL/RE-95/2. Argonne National Laboratory (ANL), Argonne, Ill (United States), 1995. DOI: 10.2172/94649.
- [130] D.L. Hildenbrand et al. “Vapor Pressures and Vapor Thermodynamic Properties of Some Lithium and Magnesium Halides”. In: *The Journal of Chemical Physics* 40.10 (1964), pp. 2882–2890. DOI: 10.1063/1.1724921.

- [131] Curtis T. Ewing and Kurt H. Stern. “Equilibrium Vaporization Rates and Vapor Pressures of Solid and Liquid Sodium Chloride, Potassium Chloride, Potassium Bromide, Cesium Iodide, and Lithium Fluoride”. In: *The Journal of Physical Chemistry* 78.20 (1974), pp. 1998–2005. DOI: 10.1021/j100613a005.
- [132] Joseph E. Mayer and Irmgard Hölder Wintner. “Measurements of Low Vapor Pressures of Alkali Halides”. In: *The Journal of Chemical Physics* 6.6 (1938), pp. 301–306. DOI: 10.1063/1.1750255.
- [133] E.N. Hoffman et al. “MAX phase carbides and nitrides: Properties for future nuclear power plant in-core applications and neutron transmutation analysis”. In: *Nuclear Engineering and Design* 244 (2012), pp. 17–24. DOI: 10.1016/j.nucengdes.2011.12.009.
- [134] N.C. Ghosh and S.P. Harimkar. “3 - Consolidation and synthesis of MAX phases by Spark Plasma Sintering (SPS): a review”. In: *Advances in Science and Technology of  $M_{n+1}AX_n$  Phases*. Ed. by I.M. Low. Woodhead Publishing, 2012, pp. 47–80. ISBN: 978-1-84569-991-8. DOI: 10.1533/9780857096012.47.
- [135] G. Coen et al. “Investigation of the effect of lead–bismuth eutectic on the fracture properties of T91 and 316L”. In: *Journal of Nuclear Materials* 398.1 (2010), pp. 122–128. DOI: 10.1016/j.jnucmat.2009.10.021.
- [136] Chongchong Tang et al. “Textured growth of polycrystalline MAX phase carbide coatings via thermal annealing of M/C/Al multilayers”. In: *Journal of Vacuum Science & Technology A* 38.1 (2020), p. 013401. DOI: 10.1116/1.5131544.
- [137] H. Okamoto. “Sb-Sn (Antimony-Tin)”. In: *Journal of Phase Equilibria and Diffusion* 33.4 (2012), p. 347. DOI: 10.1007/s11669-012-0054-8.
- [138] H. Okamoto. “Bi-Sb (Bismuth-Antimony)”. In: *Journal of Phase Equilibria and Diffusion* 33.6 (2012), pp. 493–494. DOI: 10.1007/s11669-012-0092-2.
- [139] Klaus W. Richter and Herbert Ipser. “Reinvestigation of the binary Fe-Sb phase diagram”. In: *Journal of Alloys and Compounds* 247.1 (1997), pp. 247–249. DOI: 10.1016/S0925-8388(96)02597-2.
- [140] H. Okamoto. “Fe-Sb (Iron-Antimony)”. In: *Journal of Phase Equilibria* 20.2 (1999), p. 166. DOI: 10.1007/s11669-999-0017-x.

- [141] Benyan Pei et al. “A thermodynamic assessment of the iron — antimony system”. In: *Calphad* 19.1 (1995), pp. 1–15. DOI: 10.1016/0364-5916(95)00001-U.
- [142] Ortrud Kubaschewski von Goldbeck. “Fe–Sb Iron–Antimony”. In: *IRON—Binary Phase Diagrams*. Berlin, Heidelberg: Springer Berlin Heidelberg, 1982, pp. 128–130. ISBN: 978-3-662-08024-5. DOI: 10.1007/978-3-662-08024-5\_59.
- [143] K.C. Hari Kumar, P. Wollants, and L. Delaey. “Thermodynamic evaluation of Fe–Sn phase diagram”. In: *Calphad* 20.2 (1996), pp. 139–149. DOI: 10.1016/S0364-5916(96)00021-1.
- [144] H. Okamoto. “Cr-Sb (Chromium-Antimony)”. In: *Journal of Phase Equilibria* 13.4 (1992), pp. 438–439. DOI: 10.1007/BF02674996.
- [145] M. Venkatraman and J.P. Neumann. “The Cr-Sn (Chromium-Tin) System”. In: *Bulletin of Alloy Phase Diagrams* 9.2 (1988), pp. 159–162. DOI: 10.1007/BF02890556.
- [146] H. Okamoto. “Ni-Sb (Nickel-Antimony)”. In: *Journal of Phase Equilibria and Diffusion* 30.3 (2009), pp. 301–302. DOI: 10.1007/s11669-009-9513-2.
- [147] P Nash and A Nash. “The Ni-Sn (Nickel-Tin) System”. In: *Bulletin of Alloy Phase Diagrams* 6.4 (1985), pp. 350–359. DOI: 10.1007/BF02880521.
- [148] H. Okamoto. “Co-Sb (Cobalt-Antimony)”. In: *Journal of Phase Equilibria and Diffusion* 26.2 (2005), p. 198. DOI: 10.1007/s11669-005-0156-7.
- [149] H. Okamoto. “Co-Sn (Cobalt-Tin)”. In: *Journal of Phase Equilibria and Diffusion* 27.3 (2006), p. 308. DOI: 10.1361/154770306X109999.
- [150] L. Brewer et al. “The As-Mo system (Arsenic-Molybdenum)”. In: *Bulletin of Alloy Phase Diagrams* 1.2 (1980), pp. 76–78. DOI: 10.1007/BF02881194.
- [151] J.-Q. Yan et al. “Flux growth in a horizontal configuration: An analog to vapor transport growth”. In: *Phys. Rev. Materials*. 1 (2017), p. 023402. DOI: 10.1103/PhysRevMaterials.1.023402.
- [152] L. Brewer and R.H. Lamoreaux. “The Mo-Sn (Molybdenum-Tin) System”. In: *Bulletin of Alloy Phase Diagrams* 1.2 (1980), pp. 96–97. DOI: 10.1007/BF02881202.

- [153] J.R. Weeks. “Liquidus Curves of Nineteen Dilute Binary Alloys of Bismuth”. In: *ASM Trans. Quart.* 58 (1965), pp. 303–322.
- [154] Ortrud Kubaschewski von Goldbeck. “Fe–Bi Iron–Bismuth”. In: *IRON–Binary Phase Diagrams*. Berlin, Heidelberg: Springer Berlin Heidelberg, 1982, pp. 22–23. ISBN: 978-3-662-08024-5. DOI: 10.1007/978-3-662-08024-5\_11.
- [155] M. Venkatraman and J.P. Neumann. “The Bi–Cr (Bismuth–Chromium) System”. In: *Bulletin of Alloy Phase Diagrams* 9.3 (1988), pp. 271–273. DOI: 10.1007/BF02881279.
- [156] H. Okamoto. “Bi–Ni (Bismuth–Nickel)”. In: *Journal of Phase Equilibria and Diffusion* 29.2 (2008), p. 203. DOI: 10.1007/s11669-008-9268-1.
- [157] H. Okamoto. “Bi–Ni (Bismuth–Nickel)”. In: *Journal of Phase Equilibria and Diffusion* 33.6 (2012), p. 492. DOI: 10.1007/s11669-012-0091-3.
- [158] J. Sangster and Pelton A.D. “The Na–Sb (Sodium–Antimony) System”. In: *Journal of Phase Equilibria* 14.2 (1993), pp. 250–255. DOI: 10.1007/BF02667822.
- [159] J. Sangster and Pelton A.D. “The Bi–Na (Bismuth–Sodium) System”. In: *Journal of Phase Equilibria* 12.4 (1991), pp. 451–456. DOI: 10.1007/BF02645967.
- [160] Peter Dömstedt, Jesper Ejenstam, and Peter Szakálos. “High Temperature Corrosion of a Lean Alloyed FeCrAl-steel and the Effects of Impurities in Liquid Lead”. In: *2020 IEEE International Conference on Environment and Electrical Engineering and 2020 IEEE Industrial and Commercial Power Systems Europe (EEEIC / ICPS Europe)*. 2020, pp. 1–6. DOI: 10.1109/EEEIC/ICPSEurope49358.2020.9160504.
- [161] Wenjin Ding et al. “Multi-cationic molten salt electrolyte of high-performance sodium liquid metal battery for grid storage”. In: *Journal of Power Sources* 553 (2023), p. 232254. DOI: 10.1016/j.jpowsour.2022.232254.
- [162] J.J. Moore. *Chemical Metallurgy*. 2nd Edition. Butterworth-Heinemann, 1990. ISBN: 978-0-408-05369-3. DOI: 10.1016/C2013-0-00969-3.
- [163] Mohammad Shamsuddin. *Physical Chemistry of Metallurgical Processes*. 2nd Edition. Springer, 2021. ISBN: 978-3-030-58068-1. DOI: 10.1007/978-3-030-58069-8.

- [164] Dong Jun Kim et al. “Diffusion behavior of sodium ions in  $\text{Na}_{0.44}\text{MnO}_2$  in aqueous and non-aqueous electrolytes”. In: *Journal of Power Sources* 244 (2013), pp. 758–763. DOI: 10.1016/j.jpowsour.2013.02.090.
- [165] Pablo A. Aparicio and Nora H. de Leeuw. “Electronic structure, ion diffusion and cation doping in the  $\text{Na}_4\text{VO}(\text{PO}_4)_2$  compound as a cathode material for Na-ion batteries”. In: *Phys. Chem. Chem. Phys.* 22 (12 2020), pp. 6653–6659. DOI: 10.1039/C9CP05559B.
- [166] Pablo A. Aparicio et al. “Computational Study of  $\text{NaVOPO}_4$  Polymorphs as Cathode Materials for Na-Ion Batteries: Diffusion, Electronic Properties, and Cation-Doping Behavior”. In: *The Journal of Physical Chemistry C* 122.45 (2018), pp. 25829–25836. DOI: 10.1021/acs.jpcc.8b07797.
- [167] Takayuki Shibata, Wataru Kobayashi, and Yutaka Moritomo. “Sodium Ion Diffusion in Layered  $\text{Na}_x\text{CoO}_2$ ”. In: *Applied Physics Express* 6.9 (2013), p. 097101. DOI: 10.7567/APEX.6.097101.
- [168] Takayuki Shibata, Wataru Kobayashi, and Yutaka Moritomo. “Sodium ion diffusion in layered  $\text{Na}_x\text{MnO}_2$  ( $0.49 \leq x \leq 0.75$ ): Comparison with  $\text{Na}_x\text{CoO}_2$ ”. In: *Applied Physics Express* 7.6 (2014), p. 067101. DOI: 10.7567/APEX.7.067101.
- [169] Joshua C. Treacher et al. “ $\text{Na}_2\text{CoSiO}_4$  as a cathode material for sodium-ion batteries: structure, electrochemistry and diffusion pathways”. In: *Phys. Chem. Chem. Phys.* 18.48 (2016), pp. 32744–32752. DOI: 10.1039/C6CP06777H.
- [170] Y.-J. Kang et al. “The effect of  $\text{Al}(\text{OH})_3$  coating on the  $\text{Li}[\text{Li}_{0.2}\text{Ni}_{0.2}\text{Mn}_{0.6}]\text{O}_2$  cathode material for lithium secondary battery”. In: *Electrochimica Acta* 50.24 (2005), pp. 4784–4791. DOI: 10.1016/j.electacta.2005.02.032.
- [171] Ho Chul Shin, Won Il Cho, and Ho Jang. “Electrochemical properties of carbon-coated  $\text{LiFePO}_4$  cathode using graphite, carbon black, and acetylene black”. In: *Electrochimica Acta* 52.4 (2006), pp. 1472–1476. DOI: 10.1016/j.electacta.2006.01.078.
- [172] Baohua Li et al. “Facile synthesis of  $\text{Li}_4\text{Ti}_5\text{O}_{12}/\text{C}$  composite with super rate performance”. In: *Energy Environ. Sci.* 5 (11 2012), pp. 9595–9602. DOI: 10.1039/C2EE22591C.

- [173] Yujie Zhu et al. “Comparison of electrochemical performances of olivine  $\text{NaFePO}_4$  in sodium-ion batteries and olivine  $\text{LiFePO}_4$  in lithium-ion batteries”. In: *Nanoscale* 5 (2 2013), pp. 780–787. DOI: 10.1039/C2NR32758A.
- [174] Zhe Hu et al. “ $\text{Li}_2\text{MnSiO}_4$ @C nanocomposite as a high-capacity cathode material for Li-ion batteries”. In: *J. of Mater. Chem. A* 1.40 (2013), pp. 12650–12656. DOI: 10.1039/C3TA12106B.
- [175] Weixin Song et al. “A promising  $\text{Na}_3\text{V}_2(\text{PO}_4)_3$  cathode for use in the construction of high energy batteries,” in: *Phys. Chem. Chem. Phys.* 16.7 (2014), pp. 3055–3061. DOI: 10.1039/C3CP54604G.
- [176] Huawei Song et al. “Enhanced storage capability and kinetic processes by pores- and hetero-atoms-riched carbon nanobubbles for lithium-ion and sodium-ion batteries anodes”. In: *Nano Energy* 4 (2014), pp. 81–87. DOI: 10.1016/j.nanoen.2013.12.017.
- [177] Yingchang Yang et al. “Lithium Titanate Tailored by Cathodically Induced Graphene for an Ultrafast Lithium Ion Battery”. In: *Advanced Functional Materials* 24.27 (2014), pp. 4349–4356. DOI: 10.1002/adfm.201304263.
- [178] Wenpei Kang et al. “Porous  $\text{CuCo}_2\text{O}_4$  nanocubes wrapped by reduced graphene oxide as high-performance lithium-ion battery anodes”. In: *Nanoscale* 6.12 (2014), pp. 6551–6556. DOI: 10.1039/C4NR00446A.
- [179] Yao Lu et al. “Preparation and characterization of carbon-coated  $\text{NaVPO}_4\text{F}$  as cathode material for rechargeable sodium-ion batteries”. In: *Journal of Power Sources* 247 (2014), pp. 770–777. DOI: 10.1016/j.jpowsour.2013.09.018.
- [180] Yang Xu et al. “Enhancement of Sodium Ion Battery Performance Enabled by Oxygen Vacancies”. In: *Angewandte Chemie* 54.30 (2015), pp. 8768–8771. DOI: 10.1002/anie.201503477.

## List of publications

- [1] Tianru Zhang et al. “Corrosion Investigations of Materials in Antimony–Tin and Antimony–Bismuth Alloys for Liquid Metal Batteries”. In: *TMS 2021 150th Annual Meeting & Exhibition Supplemental Proceedings*. Cham: Springer International Publishing, 2021, pp. 605–614. ISBN: 978-3-030-65261-6.
- [2] Wenjin Ding et al. “Multi-cationic molten salt electrolyte of high-performance sodium liquid metal battery for grid storage”. In: *Journal of Power Sources* 553 (2023), p. 232254. DOI: 10.1016/j.jpowsour.2022.232254.